UNIVERSITY OF SÃO PAULO
ENGINEERING SCHOOL OF SÃO CARLOS
DEPARTMENT OF STRUCTURAL ENGINEERING

ARTHUR ÁLAX DE ARAÚJO ALBUQUERQUE

A POSITIONAL FORMULATION OF THE EMBEDDED BAR WITH UNIAXIAL, SHEAR AND FLEXURAL STIFFNESS FOR THE REINFORCED CONCRETE ANALYSIS CONSIDERING PHYSICAL NONLINEARITIES

UMA FORMULAÇÃO DE BARRA EMBUTIDA COM RIGIDEZES UNIAXIAIS, FLEXÃO E DE CISALHAMENTO PARA ANÁLISES DE CONCRETO ARMADO CONSIDERANDO NÃO LINEARIDADES FÍSICAS

São Carlos
2019

ARTHUR ÁLAX DE ARAÚJO ALBUQUERQUE

A POSITIONAL FORMULATION OF THE EMBEDDED BAR WITH UNIAXIAL, SHEAR AND FLEXURAL STIFFNESS FOR THE REINFORCED CONCRETE ANALYSIS CONSIDERING PHYSICAL NONLINEARITIES

VERSÃO CORRIGIDA
(A versão original encontra-se na Escola de Engenharia de São Carlos)

Text presented to the São Carlos School of Engineering of the University of São Paulo as one of the requisites for obtaining the degree of Doctor in Science (Structural Engineering).

Advisor: Prof. Dr. Vladimir Guilherme Haach

São Carlos
2019

Ficha catalográfica elaborada pela Biblioteca Prof. Dr. Sérgio Rodrigues Fontes da EESC/USP com os dados inseridos pelo(a) autor(a).

de Araújo Albuquerque, Arthur Álax
D658a A POSITIONAL FORMULATION OF THE EMBEDDED BAR WITH UNIAXIAL, SHEAR AND FLEXURAL STIFFNESS FOR THE REINFORCED CONCRETE ANALYSIS CONSIDERING PHYSICAL NONLINEARITIES / Arthur Álax de Araújo Albuquerque; orientador Vladimir Guilherme Haach. São Carlos, 2019.

Tese (Doutorado) - Programa de Pós-Graduação em Engenharia Civil(Engenharia de Estruturas) e Área de Concentração em Estruturas -- Escola de Engenharia de São Carlos da Universidade de São Paulo, 2019.

1. Embedded reinforcement. 2. Fracture Mechanic. 3. Crack Models. 4. Damage model. 5. Finite Elements. 6. Dowel Action. 7. Shear mechanism. I. Título.

Eduardo Graziosi Silva - CRB - 8/8907

FOLHA DE JULGAMENTO

Candidato: Engenheiro **ARTHUR ÁLAX DE ARAUJO ALBUQUERQUE.**

Título da tese: "Uma formulação de barra embutida com rigidezes uniaxiais, flexão e de cisalhamento para análises de concreto armado considerando não linearidades físicas".

Data da defesa: 18/06/2019.

Comissão Julgadora: **Resultado:**

Prof. Associado **Vladimir Guilherme Haach** APROVADO
(Orientador)
(Escola de Engenharia de São Carlos/EESC)

Prof. Titular **Humberto Breves Coda** Aprovado
(Escola de Engenharia de São Carlos/EESC)

Prof. Dr. **Caio Gorla Nogueira** Aprovado
(Universidade Estadual Paulista "Júlio de Mesquita Filho"/UNESP- Bauru)

Prof. Titular **Túlio Nogueira Bittencourt** APROVADO
(Escola Politécnica/EP-USP)

Prof. Dr. **Gustavo Henrique Siqueira** Aprovado
(Universidade Estadual de Campinas/UNICAMP)

Coordenador do Programa de Pós-Graduação em Engenharia Civil (Engenharia de Estruturas):
Prof. Associado **Vladimir Guilherme Haach**

Presidente da Comissão de Pós-Graduação:
Prof. Titular **Murilo Araujo Romero**

AGRADECIMENTOS

Aos meus pais Ruberval e Zenilda pelo suporte, apoio, confiança e educação que me fizeram tornar a pessoa que sou hoje.

Aos meus irmãos Alessandro e Alanna que se preocupam com o meu bem estar.

A voinha (Lenita) por me propiciar horas de lazer e conversas leves.

Ao meu orientador Vladimir G. Haach, pelos conhecimentos passados, pela paciência, motivação e convivência durante os anos de realização não só do doutorado mas também do mestrado. Gostaria de frisar este agradecimento de maneira intensa pois o respeito e a crença que sinto que o professor deposita no trabalho torna objeto de apreciação para qualquer orientando.

A todas amizades feitas em São Carlos dentro e fora do ambiente do campus universitário que levarei para toda a vida e que fizeram companhia em alguns momentos do doutorado: Fernanda, Matheus, Rodrigo, Pablo, Geovanne, Danilo, Lorena, Hugo, Carolina, Jesus, Uziel, Karoline, Margot, Lorenzo, Thaís, Morkis, Fernando Gilio, Heider, André, Carlinhos, Ketson, Emerson, Rafael El Nino, Sérgio; companheiros de café e na busca de conhecimentos científicos.

Aos professores do Departamento de Engenharia de Estruturas, que facilitaram o entendimento de conceintos teóricos que ajudaram no fomento desta pesquisa.

Em especial agradeço ao professor Humberto B. Coda pelas sugestões e contribuições em diversas etapas da pesquisa.

Ao professor Rodrigo R. Paccola pelo conhecimento e orientações passadas durante o desenvolvimento desta pesquisa.

Ao professor Lukasz Kaczmarczyk que foi o meu orientador no período do sanduíche que realizei na Universidade de Glasgow (Escócia). Com ele tive a oportunidade de aprender não só conhecimentos científicos mas também o que é ser um pesquisador.

Aos professores da graduração de Engenharia da Universidade Federal do Rio Grande do Norte - UFRN, os quais se dedicam diariamente no ensino de engenheria com o intuito de sempre formarem bons profissionais. Em especial agradeço a professora Selma H. Shimura pelas oportunidades de bolsa de monitoria que muito me incentivou e despertou a paixão pela Engenharia Estrutural. À professora Maria das Vitória V. A. de Sá que acredtiou e confiou na minha capacidade enquanto aluno. Ao professor Joel A. do Nascimento Neto que se dedicou ao ensino das primeiras disciplinas que tive relacionadas com a Engenharia de Estruturas.

Aos funcionários do SET Masaki, Dorival e Melina e ao pessoal da secretaria Clayton, Silvia, Toninho, Nadir, Rosi e Dani pela atenção e o suporte prestado.

Ao Depatamento de Engenharia de Estruturas - SET pelas instalações físicas e ambiente adequado que propiscia a realização de trabalhos científicos.

A Coordenação de Aperfeiçoamento de Pessoal de Nível Superior - Brasil (CAPES) - Código de Financiamento 001 e da agência de fomento CNPq que subsidiáram as bolsas e a taxa de bancada para a realização da presente pesquisa

Enfim, todos aqueles que contribuíram de forma indireta e direta na minha formação quanto pessoa e também profissional, eu veemente agradeço.

“Se hoje estou no lugar em que me encontro é porque todas as outras alternativas deram errado. ”

(Arthur Álax de Araújo Albuquerque)

RESUMO

ALBUQUERQUE, A. A. A., **Uma formulação de barra embutida com rigidez uniaxiais, flexão e de cisalhamento para análises de concreto armado considerando não linearidades físicas**. 2019. 226p. Tese (Doutorado) – Escola de Engenharia de São Carlos, Universidade de São Paulo, São Carlos, 2019.

Na análise numérica via método dos elementos finitos (MEF) à adequada representação do aço (fibras) em materiais compósitos como o concreto (matriz) é de fundamental importância para que o modelo seja avaliado de forma apropriada. Por esta razão, pesquisas direcionadas a diferentes maneiras de representações numéricas de fibras em compósitos têm sido comumente exploradas. Atualmente, no concreto armado apenas a rigidez uniaxial da barra de aço têm sido considerada nas análises numéricas. Entretanto, para estruturas cujo mecanismo de colapso está relacionado com o efeito pino as fibras a serem consideradas nas análises utilizando elementos finitos devem apresentar rigidezes: uniaxial, à flexão e ao cisalhamento. O uso de elementos finitos de pórtico é uma opção para a solução deste problema. Neste contexto, a proposta da presente pesquisa visa em desenvolver um código computacional usando o MEF com formulação posicional considerando a formulação de fibras embutidas para simular as estruturas que apresentam o risco de colapso anteriormente mencionado. Desta maneira, o código computacional permite a análise de estruturas cujo efeito ao cisalhamento da barra de aço determina um comportamento global relevante. As não linearidades físicas para os elementos da matriz e da fibra são consideradas para a melhor discussão dos efeitos das rigidezes adicionais consideradas. Modelos de plasticidade unidimensional e bidimensional, aplicados aos elementos finitos de barra e pórtico, respectivamente, são estudados e implementados no código desenvolvido. Dois modelos de dano com a aproximação de modelos de fissuração distribuída são desenvolvidos para representar a degradação dos elementos da matriz. Exemplos são explorados para investigar e comprovar a formulação proposta. Por fim, mostra-se que para a análise de estruturas, as quais o mecanismo de cisalhamento não é um efeito preponderante, a consideração de fibras com as rigidezes a flexão e cisalhamento produzem resultados semelhantes quando comparados com as análises realizadas com fibras com apenas a rigidez uniaxial. Entretanto, para os casos em que o efeito pino é significante a avaliação da estrutura se adequa mais ao comportamento real quando os elementos das fibras são representados com os elementos que apresentam as rigidezes adicionais.

Palavras-chaves: Armadura embutida. Mecânica da Fratura. Modelos de fissuração. Modelo de dano. Elementos finitos. Efeito pino. Mecanismo de cisalhamento.

ABSTRACT

ALBUQUERQUE, A. A. A., **A positional formulation of the embedded bar with uniaxial, shear and flexural stiffness for the reinforced concrete analysis considering physical nonlinearities**. 2019. 226p. Thesis (Ph.D.) – School of Engineering of São Carlos, University of São Paulo, São Carlos, 2019.

Nowadays, the representation of reinforcement bars in composite materials, such as the reinforced concrete, is an important role that needs to be properly evaluated in numerical analysis with the finite element method. For this reason, researches that supply useful information about different ways to represent such reinforcements has commonly been explored. The matrix and fibers terminology is frequently adopted in numerical research to refers to the two materials: concrete and steel, respectively. Currently, only bars with the uniaxial stiffness have been assumed to the analysis of the reinforced concrete. However, some structures, in which the collapse mechanism is related to the dowel action phenomenon, must be evaluated with fibers represented by finite elements that take into account the uniaxial, flexural and shear stiffnesses. The use of frame finite element is an option to the solution of this problem. In this context, this research addresses a computational code using FEM with positional formulation approach to simulate the structures mentioned with embedded bar formulation. Thus, this code enables the analysis of structural elements whose shear effects in the fibers produce a global relevant behavior. The physical nonlinearities for the matrix and fibers elements are taken into account to better discuss the effects of such additional stiffnesses. The one-dimensional and plane-stress plasticity theories are studied and implemented in the developed code, being used by the bar and the frame elements, respectively. Two damage models related to the smeared crack models approach are suggested to represent the degradation of the matrix elements. Several examples are explored to investigate the theory proposed. It is showed that for the analysis of structures in which the shear mechanism is not a preponderant effect the consideration of the fiber with additional flexural and shear stiffnesses produce similar results when compared with analysis performed by fibers with only uniaxial stiffness. However, for the cases in which the dowel action is significant, a more appropriate analysis is carried out when the fiber elements present such additional stiffnesses.

Keywords: Embedded reinforcement. Fracture Mechanic. Crack Models. Damage model. Finite Elements. Dowel Action. Shear mechanism.

LIST OF CONTENT

LIST OF FIGURES

LIST OF TABLES

1 INTRODUCTION AND RESEARCH SIGNIFICANCE

The *reinforced concrete* is a material vastly used in structural elements responsible for providing stability and equilibrium of the civil engineering constructions. It is composed of two materials, the concrete and the steel, also called *matrix* and *fibers*, respectively. The combination of the properties related to the two elements are the most significant advantage of the final product. Innumerous studies were and continue to be published to describe the real behavior, while structural elements, of such material. From the point of view of the computational mechanics, this reinforced material embraces a significant set of aspects that constitute an area of extensive exploration.

Computational mechanics covers a field of study that applies numerical methods to solve the mathematical models representing real physical phenomena. In the last three decades, its development and applicability have exponentially increased. The demand for quick answers of complex structures subject to different kind of actions, among other factors, has been the primary motivations of this trend. Nowadays, the application of the computational mechanics can be viewed in the more diverse areas such as *solid and structural mechanics*, *fluid mechanics*, *fluid-structure interactions*, *biomechanics and mechanics in medicine*, *fracture mechanics and others*. The reason for such a broad application is the viability of a sophisticated, safe and relatively rapid analysis.

One alternative of representation of reinforced concrete in the computational mechanics area can be performed with the use of the *finite element method* (FEM). Within the numerical models, the FEM and its variations have proved to be a powerful technique to solve a vast number of problems. The FEM suitably allows the representation of any geometry with appropriate boundary conditions and load applications as well as facilitates the resolution of issues associated with the physical nonlinearities of the materials. The nonlinear physical behavior is an intrinsic characteristic of each material, and it is directly associated with its mechanism of stresses transference.

Concerning the representation of the physical behavior of the reinforced concrete, one option is the simulation of such a mechanism within the framework of continuum mechanics. In this context, the constitutive laws are mathematically expressed with the stress-strain relationship that represents the real answer of the material. The constitutive laws associate their expressions with rheological models, which in turn approximate the performance of materials under application of external actions. The *plasticity theory* and *the damage and smeared crack models* are examples of continuum models approach.

The articles and books already published about the *plasticity theory* compose a substantial material collection that represents by itself the importance of the theme to the study of the materials and consequently to society. The plasticity theory associates the nonlinear behavior of the stress-strain curve of any material with the dissipation of energy due to the accumulation of plastic strain. Such mathematical approach describes the phenomenological behavior that happens in microscopical level with the changing of the configuration of the atomic arrangement of the polycrystals that compound the materials.

The *damage and smeared crack models* arose in the 1960s, and since then the researchers have performed several contributions due to the importance of the subject. Such models associate the loss of energy with the degradation of the material caused by arising of micro-fissures and consequently opening cracks. These two models use criterions to specify the initial process of deterioration that once started its progression is controlled with the fracture energy and a numerical parameter called characteristic length or bandwidth.

The application of the FEM involves other circumstances beyond the adequate representation of the materials with appropriate nonlinear physical law. A suitable association among all finite elements used, such as the same degrees of freedom and the connection between their nodes is one of them. Three different approaches to perform the analysis of reinforced materials can be adopted. The first one, concern the representation with both materials, the matrix and the fibers, represented by the same two-dimensional finite elements. The second one, the finite elements used to represent the matrix and fibers are differents. The matrix is described with two-dimensional elements and the fibers with truss elements. The third case, the embedded theory is used to inserting the fibers in the finite elements that represent the matrix of the material.

In the context of the embedded theory to representation of the steel reinforcement, a mathematical procedure to coupling bars with uniaxial, transversal and flexural stiffness is

proposed in this thesis. The performance of such formulation consist in the analysis of structures under the dowel action effects.

The Dowel action is a component of shear mechanical behavior that occurs in the steel reinforcement of the structures. The adequate evaluation of the shear mechanism in the structures is an important aspect because its neglection involves dangerous characteristics such as the sudden and brittle collapse of the structural elements. The risk of human life is a consequence of these features once unsafe civil structures can be constructed. Several experimental and analytical research to understand the complex mechanical behavior of dowel action have been developed over the years. However, due to its complexity, the results published with numerical simulation shows that such field still comprehends an area that needs to be better developed.

1.1 Aims

The primary objective of this study is the development of a computational code based on the finite element method with the positional formulation approach. Such code will allow the analysis of two-dimensional structures with dowel action phenomenon. The physical and geometrical nonlinearities, as well as the embedded steel reinforcement theories, are subjects explored and implemented in the code.

To reach the main purpose of this thesis some specific objectives must be performed as follow presented.

a) Studying and application of the finite element concept with positional formulation approach to evaluating two-dimensional structures. In such a context, it is indispensable a literature review of themes as the kinematic of the elements as well as the strain energy and constitutive laws considered.
b) Implementing two-dimensional finite elements as well as the bars and frame elements for the nonlinear geometrical analysis of elastic solids.
c) Literature review of different representations of steel reinforcement bars in numerical simulation.
d) Coupling of bar and frame elements (also called as stell reinforcement bars or fibers) in two-dimensional finite elements (matrix) to simulate composite materials, more specifically the reinforced concrete.

e) Studing of one/two-dimensional plasticity models to represent the material physic nonlinearities of the reinforcement bars. The one-dimensional plasticity model is implemented for the bar element while the two-dimensional model is employed for the frame element.
f) Studing and development of a damage constitutive relationship to represent the nonlinear physical degradation of the matrix finite elements.
g) Analysis of structures to perform the validation of the code developed.
h) Investigation of two-dimensional reinforced structures in which the uniaxial, flexural and shear stiffness of steel reinforcement bar have a relevant effect to strength distribution.

1.2 Justifications

The research addresses significant subjects that in the literature review have never been discussed in this way. The applicability of the damage model and embedded model through the finite element method with positional formulation approach. Being, the embedded model used to simulate the steel reinforcement bars. The damage constitutive relationship employed to represent the physical nonlinearity of the matrix of the reinforced materials. All characteristics mentioned are some aspects that define the originality of the idea proposed in this research and therefore represent the justification of the present thesis.

1.3 Methodology

The following four steps were accomplished to produce the present thesis: *literature review*, *analytical development of the models*, *implementation of the formulation proposed* and *validation of the code developed*. The above-described steps were not necessarily performed separately and in sequence. They were made according to the demand of the research. However, they are presented here in topics to improve understanding this work.

The *literature review* provided a background about the different numerical procedures already used to represent the steel reinforcement bars into two-dimensional structures. The study of the finite element method with the positional formulation was also part of the

bibliographic review. The plasticity and the damage models used to characterize the materials physical nonlinearity behavior, also compound the topic explored in the literature.

The *analytical development* concern to the description of the finite elements used and the constitutive relationship established to simulate the physical nonlinearities of the materials. The coupling between fibers and matrix elements also constitute another important topic. It stands out the coupling is performed with the summation of the total strain energy associated with the elements and posterior differentiation of these terms about the global positions of the matrix elements. Such method constitutes a novel coupling technique recently developed and used with the finite element method with the positional formulation. The coupling between the frame elements, which possess the uniaxial, flexural and shear stiffness, and matrix constitute one of the contributions of the present work.

The *implementation* of the expressions studied resulted in a computational code that is compound by the three steps specified in Figure 1.1. The pre-processing stage, which corresponds to the definition of the geometrical dimensions, boundary conditions, load setting, and the meshing discretization, is performed with the Gmesh program, available in *http://gmsh.info/*. The Gmesh exports the data of the structure in a .txt format file that is read with the reading algorithm implemented in the Fortran language. Next, the calculation process of the structure is executed and the results of the analysis are performed with the post-processing done into AcadView, available in *http://www.set.eesc.usp.br/portal/pt/softwares*.

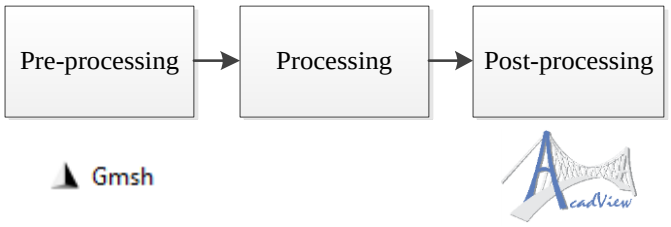

Figure 1.1 – Overview of the program.

Table 1 details the followed steps to develop the processing environment of the code. First, the two-dimensional isoparametric finite elements were implemented. Such elements are quadrangular with four and eight nodes and the triangular with ten nodes. Next, the one-dimensional element was coupled with the previous elements. The one-dimensional element is often called as bar finite element in this work. Such element correspond to the representation

of the steel reinforcement bar with only the uniaxial stiffness. The flexural and shear stiffness was taken into account with the implementation of the frame element that was also coupled in the two-dimensional element. The verifications of the numerical implementation of these finite elements were performed with some examples. For these first examples, the initial analyzes concern the materials assumed with the elastic behavior.

Table 1 – Phases to development of the code.

STEPS	IMPLEMENTATION
1	Two-dimensional finite elements
2	Embedded reinforcement finite elements
3	Elastoplastic models for the reinforcement bars
4	Damage model
5	Validation examples

After, two elastoplastic models were implemented to govern the physical nonlinearity of the steel reinforcement bars. The one and two-dimensional plasticities are employed for the bar and frame finite elements, respectively. For both cases, the Von Mises Criterion is the plastic surface adopted with linear hardening. To validate such models some examples were properly investigated.

Finally, two damaging models were developed to describe the physical nonlinearity of the two-dimensional finite elements. A first damage model is an approach of the well-known smeared crack models. Such model calculate the stiffness penalization in a preferential direction once the limited strength of the material is reached. The second model uses numerical development to the first one to enhance the penalization calculation of the material taking into account the traction and compression behavior. It emphasizes that the two damage models developed compound one of the main contributions of the present work. Analogous to the previous implementations both models are discussed and tested with examples.

At last, some numerical analysis was accomplished to evaluate the performance of the code.

1.4 Outline of the thesis

The present thesis is composed of six chapters. All chapters discuss themes indispensable to the development of the work such as the finite element method with a positional approach, plasticity models and damage model.

Chapter 2 presents a literature review about dowel action, positional finite element, the numerical representation of fibers, plasticity theory, and damage models.

Chapter 3 details the two-dimensional, the bar and the frame finite elements implemented on the code. Some aspects such as the positional approach in the technique of finite element method, the kinematic configuration, the elastic constitutive laws adopted and the construction of the internal forces vector and Hessian matrix for all elements are presented. Such chapter also shows the strategy used to the coupling the bar and frame elements in the two-dimensional element. To the end of each numerical model presented, the programming strategy is illustrated with flowcharts.

Chapter 4 discusses the physical nonlinearity models employed. The mathematical description of the one and two-dimensional plasticity is expressed. The equations related to the one and two-dimensional plasticity models are written for the bar and frame elements. Next, the chapter also describes the mathematical formalism of two damage models. The first model takes into account only the degradation of the material due to traction requested in a preferential direction of cracking formation. The second one enlarges the concepts used to the previous model to accomplish the stiffness penalization due to compression and traction situations.

Chapter 5 presents the analysis of the numerical simulation performed with the formulation discussed in the preceding sections 3 and 4. The examples validate the mathematical expressions as well as their implementation on the code developed.

Chapter 6 discusses the more significant conclusions evaluated during the process of development of this thesis.

2 LITTERATURE REVIEW

This chapter addresses the literature review of the subjected explored in the present research. Firstly, the dowel action problem is discussed, following by the positional finite element method and the matrix-fiber coupling technique. The nonlinearities of the material are briefly presented from plasticity and damage and smeared crack models approach.

2.1 Dowel Action

By definition, dowel action is a mechanism of transfer of shear forces between concrete and steel bar (Fédération Internationale du Béton-fib 2008). The inclusion of dowel action effects in the analysis is relevant for problems in which the transference of shear force has a significant influence, such as the casting joints and connections. In concrete structures, such mechanism occurs locally and can take place in a bar that connects two elements or even when the bar is completely immersed in the concrete. For the first case, this phenomenon is commonly observed in precast structures that assure the connection between the elements with dowel connectors. For the second case, the dowel action mechanism occurs in the regions that the reinforcing bars crossing the concrete cracks.

In accordance with Fédération Internationale du Béton-fib (2008) three different failure modes are associated to the collapse of the structures under dowel action mechanism: (a) Steel shear failure; (b) Concrete splitting failure and (c) Steel flexural failure (combined steel/ concrete failure). The strengths and dimensions of the bar and concrete are the factors that determine how will follow the collapse of the structure.

The flexural behavior of the concrete members is more predictable if compared with the structural members subjected to the shear mechanism (Kwan and Ng 2013). The failure of a structural member under shear mechanism action is sudden and brittle (Wight and MacGregor 2012). According to El-Ariss (2007) in experimental tests, the shear force transferred by the dowel action is quite difficult to measure because it is embedded with other shear transfer

components. Park and Paulay (1975) and He and Kwan (2001) define the shear transfer mechanism in the concrete as complex behaviour. Such mechanism is associated with: direct transfer of shear force by uncracked concrete, tensile force of the stirrups crossing the shear cracks, aggregate interlocking, and the dowel action of the reinforcement bars crossing the shear cracks, Figure 2.1.

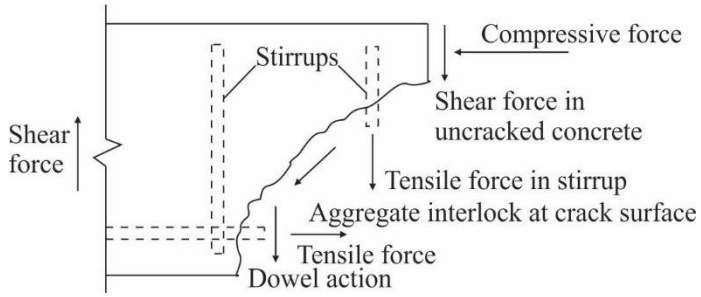

Figure 2.1 – Internal forces in a cracked beam. Source: Kwan and Ng (2013).

The geometry of the member, the arrangement of the applied load, the reinforcement layout and the crack pattern are variables that when changed has direct influence with the contribution of the shear transfer mechanism (Singh and Chintakindi 2012, He and Kwan 2001).

Several experimental, analytical, and numerical studies were already developed over the years to understand and describe the influence on the structures of the physical phenomenon of the dowel force. In agreement with Moradi et al. (2012) the investigation of such shear mechanism can be found on the literature from three different points of view: direct dowel test setups, divided beam test, and beam end test. The first two groups the dowel action mechanism is studied with little or no tension on the reinforcement (He et al. 2017, Randl 2007, Ashour 1997), while the last one enables the analysis with the interactions between the tensile and dowel forces (Li et al. 2018).

The proper experimental direct dowel test setup is the biggest challenge that the researchers have been found to carry out an appropriate shear mechanical representation. The first investigations performed with the direct dowel test concerned in the analysis of the characteristic of shear planes, characteristic of the reinforcements, and the influence of the concrete strength under different types of possible failures. The main proposal of such tests is the reduction of the effect of bending on the specimens and hence to achieve a pure state of shear. Commonly, the following three main configurations of specimens are used to represent such a phenomenon, Figure 2.2.

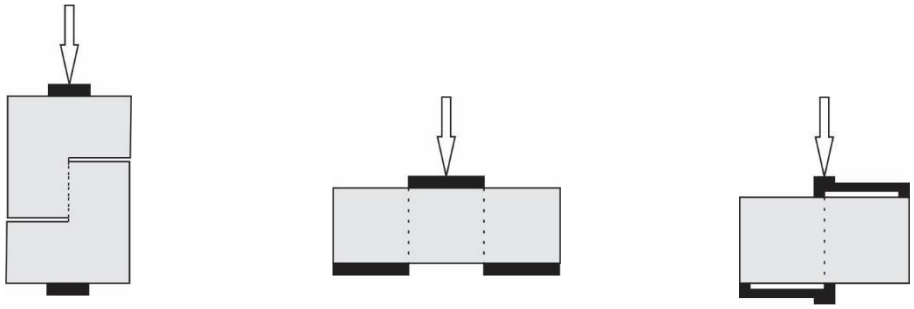

(a) (b) (c)

Figure 2.2 – Some test setups used to investigate the direct shear behavior. (a) Z-type, (b) JSCE-type and (c) FIP-type. Adapted from Soetens and Matthys (2017).

Other variations of the geometrical configurations shown in Figure 2.2 are found in the literature. For the so-called "push-off test" (Figure 2.2a), Mattock and Hawkins (1972), Soroushian et al. (1987) and Foster et al. (2016) discuss among other aspects the influence of the dimensions of the specimens and the load application configuration with the position of the shear plan formation. To avoid the residual of other possible mechanisms, as flexural behavior, Echegaray-Oviedo et al. (2017) proposed a methodology to cracked concrete specimens before the push-off test. Thus, the test is carried out in two stages: pre-cracking and push-off. The authors showed that such methodology avoided possible damage and undesired displacements on the shear plane in the handling stage of the specimen. As a consequence of this, the experimental validation of crack dilatancy models was possible. For the experimental test setup presented in Figure 2.2b, Vintzeleou and Tassios (1987) propose a practical recommendation for the interfaces between the blocks that transfer the shear force. Husain et al. (2009) following such advice carried out a similar experimental test and the results were used to performed a numerical simulations. The beam-type specimens, Figure 2.2c, is extensively debated with the studies produced by Maekawa and Qureshi (1996a), Maekawa and Qureshi (1996b), Maekawa and Qureshi (1997), Maekawa et al. (2006) and Moradi et al. (2012). Beyond the experimental apparatus, the researches also discuss the dowel action under cyclic and repeating load conditions.

Among the three experimental test configurations previously presented the push-off test is preferably employed by the researchers to correlate the failure of structures under shear mechanism with design parameters. At this context, Table 2 presents some researches performed in the last years.

Table 2 – Some researches developed with the experimental "push-off "test.

Authors	Research carried out
Frenay et al. (1992a) and Frenay et al. (1992b)	Performed the push-off test with the application of the load during a specific time to verify the time-dependent shear transfer mechanism.
Sagaseta and Vollum (2011)	Use two sets of push-off tests to investigate the effect of aggregate fracture on shear transfer through cracks. Marine dredged gravel and limestone were used in differents specimens. It was observed that the cracks passed through the limestone aggregate but passed around the gravel aggregate. However, despite this fracturing for the limestone aggregate, the crack dilatancy was almost identical for both specimens.
Xu et al. (2015)	Apply the finite element method to simulate the push-off tests, to provide a relationship between the shear stress and slip for a range of design parameters, such as concrete strength, percentage of dowel and variation of normal lateral pressure on RC members.
Jongvivatsakul et al. (2016)	Presents the shear behavior and a crack-shear slip model of high-strength steel fiber-reinforced concrete based on a push-off test. The test results indicated that the shear strength increased by approximately 1.5–2 times due to the presence of steel fibers and the ductility effectively increased when using steel fibers and stirrups.
Rahal et al. (2016)	Carried out a Fifteen non-precracked push-off specimens test to investigate the shear-transfer behavior of normal strength and high strength self-compacting concrete (SCC). The reported results include the cracking stresses, the yielding stresses, the ultimate strengths and the post-ultimate residual strengths.
Figueira et al. (2016)	Performed push-off tests in the study of cyclic behavior of interfaces between concretes cast at different times.

Authors	Research carried out
Ahmad et al. (2018)	Presented a simple analytical model for the estimation of shear transfer strength (STS) of uncracked (UC) interfaces. The combination of cohesion resistance offered by concrete and frictional resistance offered by the reinforcement provided across the interface are the bases of the model.
Waseem and Singh (2018)	Developed analytical formulation based on the truss analogy to predict the shear capacity in uncracked push-off speciemens with natural concrete and recycled aggregate concrete.

Many other research investigates the shear mechanism and the dowel action with different experimental test setups. Ashour (1997) compared eight reinforced concrete continuous deep beams. The main parameter considered was shear span-to-depth ratio, amount and type of web reinforcement, and amount of main longitudinal reinforcement. Yang and Ashour (2007) performed the experimental test to investigate the failure of ten reinforced-concrete continuous deep beams with openings. Aguiar (2010) and Aguiar et al. (2012) studied the behavior of grouted dowels used in beam-to-column connections in precast concrete structures. Xia et al. (2015) examined the influence of dowel action in the ultra-high performance fiber reinforced concrete. Li et al. (2018) investigated the mechanical properties of dowel action under fatigue loads.

According to Sørensen et al. (2017), a dowel action mechanism is most clearly observed when rebar has part of its length embedded in a large block of concrete while being loaded by a transverse force at the concrete surface. From the point of view of analytical expressions development, such experimental configuration is represented by a beam transversely supported on springs (Timoshenko 1956). To increase the accuracy of this model the nonlinear elastic behavior for both the beam and the springs must be considered. Several authors have embraced this approach to obtain the load-displacement curves (Vintzeleou and Tassios 1986, Vintzeleou and Tassios 1987, Hsu et al. 1987, Dei Poli et al. 1992, He and Kwan 2001, Randl 2007, El-Ariss 2007, Mansur et al. 2008, Kwan and Ng 2013). In a few words and consistent with Sørensen et al. (2017), the load-displacement curves or trajectory of equilibrium of the dowel

action mechanism describes beyond the load carrying capacity a nonlinear behaviour. Such characteristic is associated with the plastic hinge formation in the rebar followed by the local crushing of the concrete.

Figure 2.3 shows a typical final configuration after subjected for a load F, of a casting joint constituted by two different concretes. In accordance with Sørensen et al. (2017), the collapse due to the shear mechanism developed in the structure from the dowel action is compound by different stages. Initially, it observes the plastic hinge formation. In such a step, the casting joint is subjected to pure dowel action. The plastic hinge on the rebar happens simultaneously on the two blocks, and its position of formation is associated with the characteristic of the concrete, such as its strength. As long as the displacement (u) increase, the dowel action is accompanied by a uniaxial tension represented by the elongation (Δ) in the plastic hinges formed. At this instance, the structural behavior is established by the combination of these two actions. At the final stage, the mechanical behavior of the casting joint is described by the uniaxial tensions, which defines a configuration of the catenary effect of the rebar. In brief words, the trajectory of equilibrium and the posterior collapse of the casting joint directly depends on the diameter of the steel rebar and the strength capacity of the two blocks.

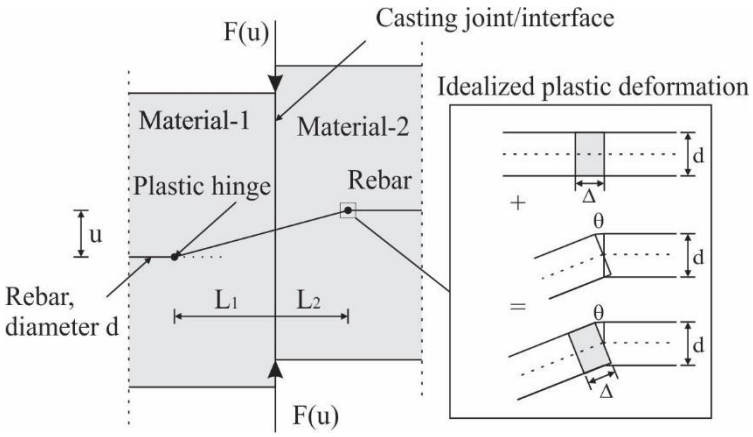

Figure 2.3 – Casting joint between two diferente concretes subjected to shear diaplacements and crossed by a rebar. Adapted from Sørensen et al. (2017).

As demonstrated, the mechanism of the dowel action involves several aspects that turn it on a complicated configuration to be described and consequently analyzed. El-Ariss (2007) points out that for the analysis of the dowel action with the use of the finite element methods (FEM), the steel bars need to be individually modeled by finite elements and a considerably dense mesh has to be used for the concrete. To circumvent such issues, a dowel action

formulation was developed to be applied with a program that uses the displacement method and the initial stiffness procedure to perform the calculation.

He and Kwan (2001) use the beam-on-elastic-foundation theory (BoEFT) and proposes the change of the constitutive law to enable the analysis with the application of the finite element method. Both the dowel action and the reinforcement bar are considered with a smeared representation approach. Kwan and Ng (2013) also derived a dowel action formulation based on the BoEFT to be applied with the FEM. However, the reinforcement bars are represented with the discrete approach. Sanches Júnior and Venturini (2007) proposed a damage modeling of reinforced concrete beams that takes into account the stiffness reductions and determines the ultimate loads with the consideration of non-linear effects due to the shear components. A finite element reinforced concrete is the final product of such an approach. For all researches, over-reinforced beams are used to prove the coherence of the strategies proposed.

As verified, many types of research associated with shear effects and related explicitly to the dowel action mechanism have been developed over the years. The sudden and brittle failure are dangerous characteristics that provide sufficient reasons to justify the engagement of several works in this field. In general, for all papers cited in this section that applies the FEM in the investigations the bar finite elements with only the uniaxial stiffness are considered in the analysis, i.e., the shear and flexural stiffness are neglected, as commented by Kwan and Ng (2013). At this context, the present work embraces this lack, proposing an embedded bar formulation that takes into account such stiffnesses.

2.2 Positional Finite element method and equilibrium

The finite element method used in this work calls positional because it is based on position, not displacements as a traditional FEM. The first works that discuss such method were carried out by Bonet et al. (2000), Coda and Greco (2004), and Coda and Paccola (2007, 2008, 2010). The development and use of the positional theory has an important role to Computational Mechanics group at the Department of Structures (SET) at São Carlos School of Engineering (EESC) at the University of São Paulo (USP).

Table 3 shows some of latest works developed with such positional formulation.

Table 3 - The use of the positional finite element formuation in some researchs.

Authors	Research carried out
Maciel (2008)	Development a plane frame and 3D solids elements to investigates nonlinear geometric problems
Marques (2006) and Sánchez (2013)	Development and posterior aplication of positional formulation in dynamic applications.
Sanches (2006 and 2011)	Aplication in analysis of problems that involves fluid-structure interaction.
Silva (2010 and 2014)	Investigation of problems with soil-structure interaction.
Sampaio (2014);	Development of formulation of laminated shells reinforced with fibers.
Carrazedo (2009)	Evaluation of Thermoelastic and Thermoplastic behaviors in the impact analysis.
Pascon (2012) and Reis (2012)	Study of the elastic and elastoplastic constitutive models.
Moura (2015)	Applications in particulate composites problems.
Nogueira (2015)	Development of laminated finite elements.
(Ramírez 2018)	Biomechanical analysis to simulate the skeletal muscles behavior
(Felix 2018)	Investigation of the reinforced concrete strain as a consequence of corrosion products formation.

The development of the present formulation is based on a change of the configuration function. Thus, the actual configuration (equilibrium) is determined from a fixed domain represented by the initial configuration. Such methodoly is defined as a Total Lagrangian formulation. The Green strain is the measure adopted and consequently, the Saint-Venant-Kirchhoff stress is the energetic conjugate.

The Lagrange polynomials define the interpolation of nodal positions. The mechanical problem applies the principle of stationary total mechanical energy to reach the equilibrium of

the structure. In such a context, the minimum energy obtained with the first variation of the total mechanical energy about the positions must be null. The equilibrium configuration results in a system of nonlinear equations and the Newton-Raphson method is adopted as the solution process.

So, the total potential energy $\Pi(Y)$ associated to the structure in the static equilibrium is mathematically expressed as:

$$\Pi(Y) = U(Y) + \Omega(Y) \tag{2.1}$$

where Y is the current position vector, while U and Ω are the elastic strain energy and external forces potential, respectively. Note that the kinetic energy is not considered because all problems proposed in the present work are static. The second parcel Ω is defined as:

$$\Omega = -F_j Y_j \tag{2.2}$$

where F_j is the vector of external forces, Y_j is the current position vector and the index j the degree of freedom of the finite element. The equilibrium position performed with the Principle of Stationary Total Mechanical Energy in the equation (2.1) gives:

$$g_j = \frac{\partial \Pi}{\partial Y_j} = \frac{\partial U}{\partial Y_j} - F_j = F_j^{\text{int}} - F_j = 0 \tag{2.3}$$

which g_j represent the residual or unbalanced force vector of the equilibrium between internal and external forces F_j^{int} and F_j, respectively.

The equilibrium equation written in (2.3) is a set of nonlinear equations solved with any numerical procedure. Newton-Raphson method, Line search method and Arc-Length method are some examples of numerical procedure that could be applied (Bonet and Wood 2010, Crisfield 1991, Crisfield 1997). In this thesis, the Newton-Raphson strategy is the method used.

The Newton-Raphson method is extensively employed in the solution of nonlinear problems. The strategy consists of an incremental-iterative process, which the linearization of the function on the incremental step is performed and the answer is obtained with an iterative process. In the iterative process, an initial trial solution is adopted. When the convergence criterion is found the iterative procedure finishes.

Equation (2.3) is therefore developed in Taylor series truncated in the first order derivative term, as follows is described:

$$g_j\left(Y\right)=g_j\left(Y^0\right)+\left.\frac{\partial g_j}{\partial Y_k}\right|_{\left(Y^0\right)}\Delta Y_k+\vartheta_j^2=0 \tag{2.4}$$

where ϑ_j^2 are the neglected terms. It is possible rewrite Eq. (2.4) as:

$$\Delta Y_k=-\left(\left.\frac{\partial g_j}{\partial Y_k}\right|_{Y^0}\right)^{-1}g_j\left(Y^0\right)=-\left(\left.\frac{\partial^2 U}{\partial Y_k\partial Y_j}\right|_{Y^0}\right)^{-1}g_j\left(Y^0\right)=-\left(H_{kj}\right)^{-1}g_j\left(Y^0\right) \tag{2.5}$$

where H_{kj} is the Hessian matrix numerically calculated in the trial position Y^0 whose dimension is equal the total number of degrees of freedom of the model in analysis. Regarding that the terms to second derivative of external forces vector are nulls and therefore the Hessian Matrix is calculated only with the second derivative of the strain energy. Thus, the accuracy of the procedure is reached as long the value of Y^0 is close the solution. For this, successively new values of Y is updated from accumulation of ΔY, calculated in each iteration (m), as follow presented:

a) Computing: $\Delta Y_{(\mathrm{m})}=-\left(H_{kj}\right)^{-1}_{(\mathrm{m})}g_j\left(Y^0\right)_{(\mathrm{m})}$.

b) Computing the new value of $Y_{(m+1)}=Y^0{}_{(m)}+\Delta Y_{(m)}$. (2.6)

The end of iterative procedure is obtained when the relative error, Eq. (2.7), in position, force or energy is sufficiently smaller than tolerance defined by the user.

$$\frac{\left\|\Delta Y^{(m)}\right\|}{\left\|\Delta Y_m\right\|}<tolerence,\quad \frac{\left\|g^{(m)}\right\|}{\left\|g_m\right\|}<tolerence,\ \text{and}\ \left|\frac{g^{(m)T}\Delta Y^{(m)}}{g_m{}^T\Delta Y_m}\right|<tolerence \tag{2.7}$$

The parenthesis under the index (m) indicates that the value of vector refers to the iteration (m) while the index m without parenthesis refers to the accumulated value in the step load in analysis as follow expressed:

$$\Delta Y_m=\sum_{i=1}^{m}\Delta Y^{(i)}\ \text{ and }\ \Delta g_m=\sum_{i=1}^{m}\Delta g^{(i)} \tag{2.8}$$

Figure 2.4 shows the steps adopted during the solution of the Newton Raphson Method. First, at the beginning of each increment, the error is always assumed bigger than tolerance.

Thus, it is performed the calculus of the internal force (F_j^{int}) showed in Eq.(2.3), the Hessian matrix ($\partial^2 U / \partial Y_k \partial Y_j$) and the unbalanced force vector (g_j), both defined in Eq.(2.5). After, the incremental of the trial position is performed from the solution of the operation between the inverse of the Hessian matrix and the unbalanced force vector (Eq.(2.6)a). Next, the new positions are updated with Eq.(2.6)b. Finally, the relative error (2.7) is calculated and, if the error assumes values smaller than tolerance, the increment is finished. Otherwise, with the news position values the procedure previously described is repeated.

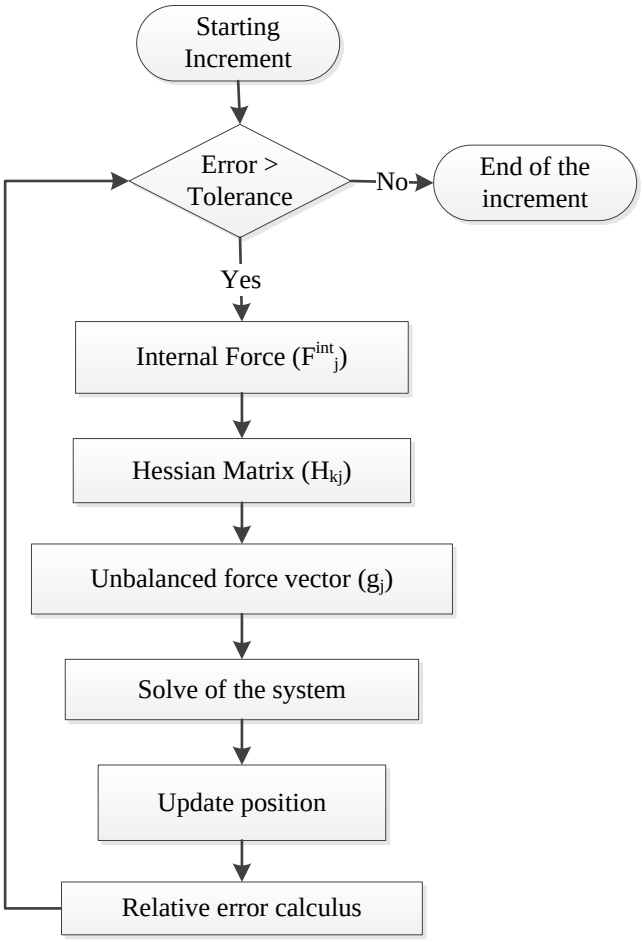

Figure 2.4 - Newton-Raphson's method.

The finite element method with the positional formulation approach is the calculation procedure adopted to compound the basis of the computational code developed in this research.

2.3 Numerical representation of the steel reinforcement bars

Analysis by the finite element method (FEM) of reinforced concrete (RC) structures is performed by taking into account the two mains materials used in this composite: concrete and steel. In the literature review the terminology "concrete elements" or "matrix elements" are commonly used to associate the finite elements employed to simulate the behavior of the material concrete. On the other hand, the terms “reinforcement bars” or “fibers” are reserved to designate the steel material. In the present topic both terminologies associated with each material are employed.

The numerical representation of reinforcement bar in the analysis of concrete structures with the finite element method can be performed following three approaches, (Barzegar and Maddipudi 1994, Markou and Papadrakakis 2012): (i) discrete model, (ii) distributed or smeared model and (iii) Embedded model, Figure 2.5.

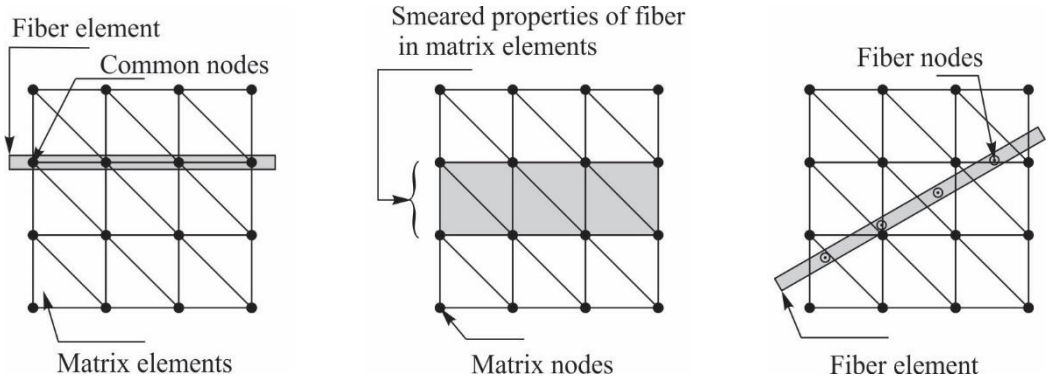

(i) Discrete Model (ii) Smeared Model (iii) Embedded Model

Figure 2.5 – Representation of the matrix and fiber elements.

The discrete model is the simplest case used for the representation of the bar into the concrete. The reinforcement (fiber) is only placed in the borders of the concrete finite element (matrix). In such model the combination between of nodal point of the matrix and fiber elements must be done. The one-dimensional truss finite element with two degrees of freedom in each node is commonly employed. For this element, only the longitudinal stiffness is taken into account in the study. Alernatively, still in the discrete conception, the reinforcement with beam finite elements can also be used to perform the investigation of structures. In such case, three degrees of freedom are associated per node of element.

The distributed or smeared model is more suitable to be applied in the analysis of surface-type structures even tough could be applied in plane analysis. This representation can be performed in accord with any principal angle θ. The constitutive relationship for the composite material, concrete-steel for example, is assumed to develop the model.

In the embedded model, the reinforcement (fiber) is inserted on the concrete finite element (Matrix), such as is presented in the real case. In this model, the nodal points between fiber and matrix do not need to be the same. Thus, to perform the analysis the mesh of matrix elements are first defined. Next, the reinforcement bars are inserted independently from the mesh of the matrix elements. The embedment is done with the contribution of the stiffness of the fibers in the elements of the matrix in which presents the concrete elements.

The first works destinated to analysis of structures with the numerical representation of the reinforced concrete using the discrete conception to simulate the steel were perfomed by Ngo and Scordelis (1967) followed by Nilson (1968). The application of the discrete conception in the development of the codes is relatively straightforward once the finite elements used are the classical finite elements widely employed in the literature. Due to this characteristic, structural analysis with the employment of the discrete model is perfectly available with commercial software, such as DIANA® 10.2 (2017), ABAQUS® 6.13 (2013), ATENA® (5.6 2016) and others.

Over the years, several works based on the simulation of structures from the discrete model were developed (Yankelevsky 1985, Girard and Bastien 2002, Qin et al. 2017, Özcan et al. 2009, Kwan and Ng 2013, Dawari and Vesmawala 2014, Hawileh 2015 Kwan and Ma 2016, Yu et al. 2018, Džolev et al. 2018, Mousa et al. 2018, Piscesa et al. 2018).

As previously affirmed the nodal points between the matrix and fiber elements must be superimposed in the discrete model. Therefore, the discrete representation is preferably applied in the simulation that the use of simple mesh is sufficient to represent the structures adequately in the analysis. If the mesh is refined and the geometry of the structure is complex the connection between the nodes of the matrix and fibers can become a laborious task, especially for the 3D-models. Another aspect is that the discrete model increases the degrees of freedom of the numerical model with the number of reinforcements.

To circumvent the limitation of the method, El-Mezaini and Citipitioglu (1991) developed isoparametric elements with mobile nodes to until use the discrete model approach for the bar representation. The basic idea of the formulation consists of shifting the edge nodes

of the concrete elements to coincide with nodal points of the reinforcement bars. The nodal points of the bars are previously defined in the intersection between the reinforcement bars and the border of the concrete elements, Figure 2.6.

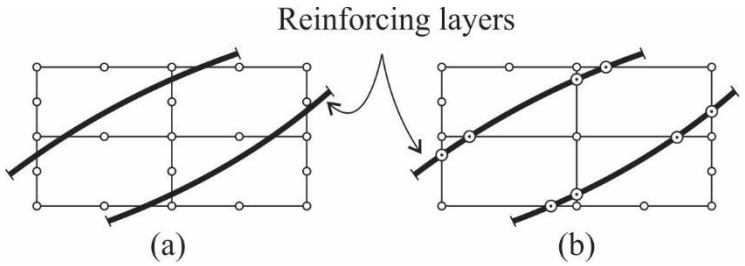

Figure 2.6 – Finite element mesh configuration: (a) Initial mesh and (b) Shifted egde nodes. (El-Mezaini and Citipitioglu 1991).

Still accordding to El-Mezaini and Citipitioglu (1991) in the present formulation the spaced location between the vertex nodes of the standard and the modified isoparametric finite elements must remain the same, as represented in Figure 2.7a and c. Numerically, this is performed by changing the shape functions and their derivatives of the standard isoparametric element. For the case that such an assumption is not obeyed a node mapping distortion could appear in the model, as presented Figure 2.7a and b.

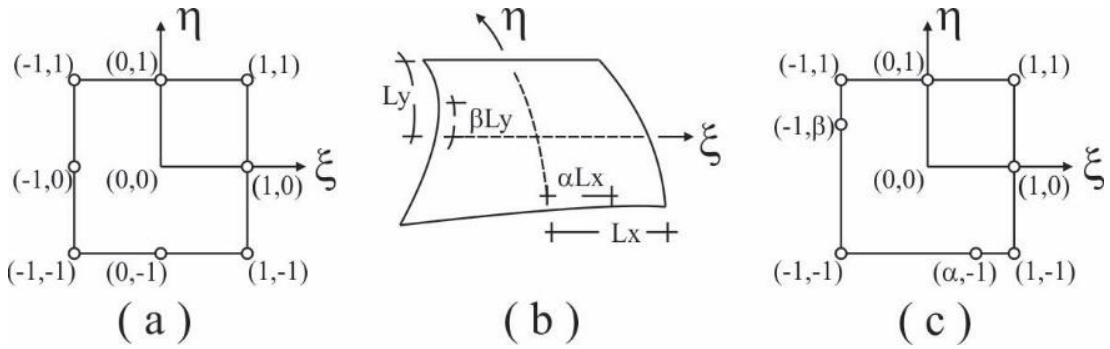

Figure 2.7 – Quadratic elements: (a) Standard isoparatmetric element; (b) Twisted isoparametric element and (c) Modified isoparametric element. Source: El-Mezaini and Citipitioglu (1991)

With the modified isoparametric element, fictitious springs were assumed in the nodal connection between the concrete and steel elements to include also the bond slip effect. The shortcoming of this procedure is when more than one fiber trespass the same matrix finite element, as commented in Barzegar and Maddipudi (1994).

From smeared model conception Barzegar (1988) and Barzegar (1989) proposed finite elements modeled as membrane layer approach with an equivalent cross-section area to represent the reinforcement distribution. Such an approach was performed to the plane-stress and plate bending finite elements, Figure 2.8.

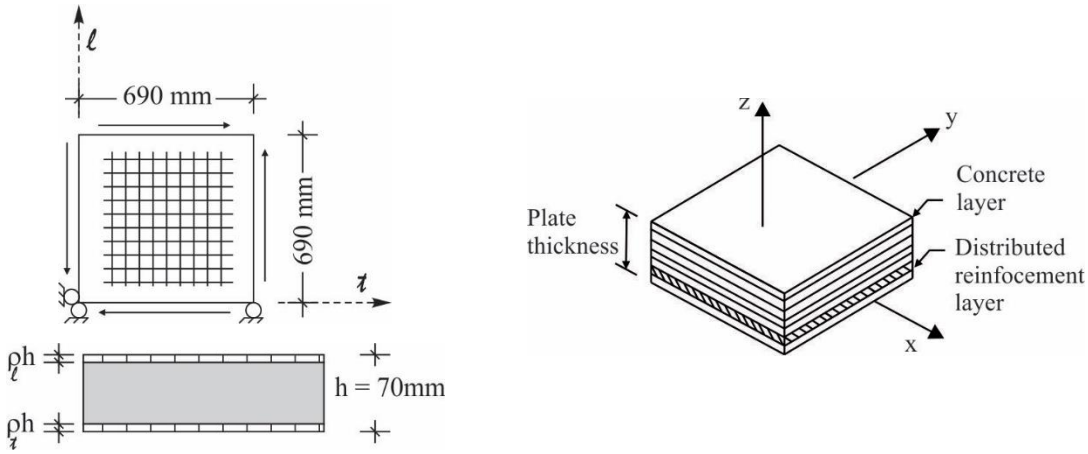

Figure 2.8 – Finite element model (a) Plane stress element and (b) Plate bending element. Adapted from Barzergar (Barzegar 1988) and (Barzegar 1989).

Although the smeared model be less used if compared with the discrete model, several works that use the distributed formulation to analysis reinforced structures can be found in the literature, such as Owen et al. (1983), Vecchio (1990), Kim and White (1999), Zhang et al. (1994), Hu et al. (2004), Barbato (2009) and Heiza (2013).

He and Kwan (2001) developed a numerical model for the dowel action of steel reinforcement bar crossing cracks in concrete to be applied with the finite element method. In such a study, a constitutive relationship, representing both the cracks of concrete and the bars in the smeared form, is developed. The numerical model is verified with experimental test of reinforced concrete beams. The comparision was perfomed with and neglecting the dowel action modeling. It was concluded that, in certain cases, the results from numerical analysis done with the consideration of the dowel action model developed generally agree better with experimental values.

Others works combined the discrete and the smeared conception at the same analysis. For example, Saatci and Vecchio (2009) performed tests and numerical simulations of a set of RC beams to introduce a methodology to evaluate the structures under impact loads. The

longitudinal reinforcement was simulated with truss using the discrete model conception. The transversal bars were considered with smeared model because the stirrups were evenly distributed along the specimen. Another application can be found in Arafa and Mehlhorn (1998) and Bouziadi et al. (2018) that uses the discrete model to the steel reinforcements and smeared model to simulate the steel fibres.

The embedded conception was provided by Phillips and Zienkiewicz (1976) on the condition that the reinforcements necessarily must be aligned with the one axle of the local isoparametric element which represents the concrete. In the same context, Elwi and Murray (1980) expose the embedded model formulation. Chang et al. (1987) take into account the inclination of straight bars in the formulation. Balakirshnan and Murray (1986) and Assan (2003) present the effect of bond-slip on the straight bar. Filippou (1990) uses truss elements to represent the bar with the consideration of the bond-slip effect. More recently Simão (2003) implemented the curve and axisymmetric finite elements with the embedded model developed by Elwi and Hrudey (1989) and Liu and Foster (1998), respectively, considering the bond-slip effect. In all papers cited, the numerical formulations proposed were validating with examples compared with experimental results and the differences were satisfactory.

To still facilitate the input-data of the structures simulated with the embedded model, Barzegar and Maddipudi (1994) and Markou and Papadrakakis (2012) developed an automatic procedure for the inclusion of reinforced bars in the three-dimension solid elements.

For the method proposed by Barzegar and Maddipudi (1994) the embedded bars are represented by straight segments, which are identified by only the coordinates of its end two points. The intersections between the bars and the surfaces of the solids elements are automatically determined. The authors suggest that such procedure reduce the task of generating the input data with embedded elements, principally when remeshs or refinements need to be performed. The developed formulation was applied in the subsequent works: Barzegar and Maddipudi (1997a), Barzegar and Maddipudi (1997b) and Sato and Naganuma (2007)

Jendele and Cervenka (2006) enhanced the embedded formulation considering a mathematical description simulate a arbitrary bond between the fiber and the matrix. Satisfactory results were obtained from the validation of the model performed with the pull out test and shear failure of beam.

Based in enrichment functions on the bond behaviour between Matrix-fiber Radtke et al. (2010a, 2010b, 2011), Hettich et al. (2008), Chudoba et al. (2009) and Oliver et al. (2008) use the conception of partition of unity to represent the composite materials.

Also using the embedded model idea, Vanalli et al. (2008) proposed a simple way to introduce short and long fibers into finite element modelling. The fibers were placed arbitrarily inside a continuum domain called matrix represented by plane stress finite elements. Numerical and experimental results were confronted and the model developed showed to be a satisfactory numerical representation.

Taking into account the last approach and the positional finite element formulation, the distribution of the contact stress between fiber and matrix is studied and available by Paccola et al. (2014). Sampaio et al. (2015) enhances the application of this numerical model for the analysis of fiber reinforced laminated plates and shells. In the same way Pereira (2015) present this theory applied in tri-dimensional finite elements and Friedel (2016) consider the active viscoelastic fiber to analyse biomechanical problems.

At this point, it emphasizes that the structures investigated in the present thesis takes the embedded reinforcement formulation analogous to the last previous studies described. And as one of the contributions of this thesis, additionally to the uniaxial effect, is the considerantion of the flexural and shear effects in the fibers elements.

The use of the embedded formulation boosted many investigations for the behaviour of cementicious and composite materials. Table 4 sumerizes some recent researchs.

Table 4 - The use of the embedded formulation in some researchs.

Authors	Research carried out
Spiliopoulos and Lykidis (2006)	The steel bars are modelled as uniaxial elements and embedded formulation is used to perform a three-dimensional dynamic analysis of reinforced concrete structures.
Cunha et al. (2012)	A numerical approach is presented to simulate the behavior of the steel fibre reinforced concrete.

Authors	Research carried out
Santos and Henriques (2015)	A bond-slip relationship between the concrete and steel is proposed, also including the steel strain effect. The fiber is considered with the embedded model formulation.
Bencardino et al. (2016)	A numerical and analytical study of concrete beams with steel, FRP and hybrid FRB-steel reinforcement is performed.
Mourlas et al. (2017)	Authors use the embedded ideia and propose a computational model to analysis the behavior of the concrete under cyclic action.
Dashti et al. (Dashti et al. 2017)	The paper uses the reinforcement bar of DIANA® (2017) software with the shell finite elements to predict the behavior of the rectangular reinforced concrete structural walls.
Eftekhari et al. (2018)	Multi-scale modelling is applied to analysis concrete columns subjected to service loads. The simulation taking into accout the concrete reinforced with nano material called carbon nanotubes (CNTs). The incorporation of the CNTs is performed in accord with the embedded formulation with truss elements
Piscesa et al. (2018)	FRP confined reinforced concrete columns are investigated using the truss bar embedded in the hexaedral elements.

As demonstrated in the present section the use of reinforcement bars in the numerical analysis is a common practice. Two lines of research have been developed over the years: the first is related to the mathematical development of the formulation and another one is concerned to the application of these numerical models in case analyzes.

2.4 Plasticity

Nowadays, plasticity models have been widely used in many applications in engineering. The studies of the theory can be reported in classical literature (Chen 2007, Lubliner 2006). The famous book of Simo and Hughes (1998) discuss the numerical algorithm implementation while Owen and Hinton (1980), Dunne and Petrinic (2005) and de Souza Neto et al. (2008) debate this theory applied directly with the finite element method.

The theory of plasticity concerns to represent materials answer for which permanent strains are developed after reach a certain yield strength (Belytschko et al. 2014). In Lemaitre and Chaboche (2000) the plasticity phenomenon is discussed under the optic of thermodynamics of irreversible process. Such phenomenological model appears beyond the elastic regime. The yield strength defines the boundary between the elastic and plastic regimes, which combined defines the called elastoplastic models. Mathematically, according to Lemaitre and Chaboche (2000), to describe a plastic regime it is necessary the definitions of the internal variables known as plastic strain tensor and hardening parameters. The plastic strain tensor represents the permanent strain parcels while the hardening parameters describe the gain of material strength related to the increase of plastic strain. Two classical phenomenological hardening models are known: the isotropic and the kinematic hardening. In the isotropic models, the expansion of the initial yield surface is symmetric from its center. For the kinematic model the initial yield surface does not change of size; however, change of position in the stress axles with the plastic process evolution.

Two elastoplastic models were implemented in the code developed in the present work. One for the bar finite element which characterizes the one-dimensional plasticity and another for the frame finite element which corresponds to the plane stress plasticity. Both models are described according to the irreversible process of thermodynamics. Chapter 3 discusses the formulation and consequently the implementation strategy adopted to carry out the numerical simulations presented in chapter 5.

2.5 Damage and Smeared crack model

Physically, the collapse of materials under the action of a set of loads is understood as a mechanism which is initiated with micro-cracks diffuses that undergoes by coalescence process

and forms a macrocrack, (Lemaitre and Desmorat 2005). In the last stage, the material present collapse mechanic and therefore it verifies the crack propagation.

The concepts commonly used in the numerical analysis of structures to study the failure of materials can be divided into following two branches (Oliver and Huespe 2004):

(a) The discrete approach, which is based on the modeling of the cohesive surface, guided by the traction-separation law, located between two continuum materials.

(b) The Continuum approach, which the formulation is associated with the continuum mechanics (Smeared cracks and damage models) or refined theories as well the enriched continuum (non-local approaches, gradient enrichment).

The two previously assumptions, when applied with the finite element method (FEM), demands distinguished algorithms. For the first case the discrete approach, the failure surface is in the boundary between the finite elements. The nodal connectivity changes during the process of the crack propagation what is also already pre-established with the finite element mesh. Such characteristic induced algorithm researchers about automatic re-meshing to become this model a practical method (Ingraffea and Saouma 1985, Azócar et al. 2010, Chiaruttini et al. 2013, Areias et al. 2016), Figure 2.9a. For the Continuum approach, the crack is assumed by Stress-Strain relation evaluated at the integration point of the finite elements of the mesh. In this case once established the discretization no remeshing algorithm is required, Figure 2.9b.

(a) (b)

Figure 2.9 – Model conceptions for: (a) Discrete approach (b) Continuum approach.

Several computational finite elements codes, such as ATENA® 5.6 (2016), DIANA® 10.2 (2017) and Abaqus® 6.13 (2013), have implemented the Smeared crack and Damage models for nonlinear analysis of the structures. Independently of the mathematical formalism adopted both theories associate the loss of stability, provided by the crack mechanism formation, with the stiffness degradation of the material. Next, the failure of materials is reviewed under the continuum conceptions.

The Continuum Damage Mechanics is addressed to the study of the macroscopic level representation of degradation phenomena occurring in materials at the microscopic level. For engineering structures, such degradations are associated with any type of action that acts under the material used, such as physical loads, temperature variations and others. So, as results of these actions, the material presents microcracks, microvoids, and similar defects that lead to the degradation of material stiffness on the macroscale.

Nowadays, Lemaitre (1996), Lemaitre and Desmorat (2005), Lemaitre and Chaboche (2000) are the classical books that present the discussion of damage mechanics in the thermodynamic sense. According to Lemaitre and Desmorat (2005) the term "Continuum Damage Mechanics" was firstly introduced by Hult in 1972 but the concept of damage was initially discussed in the studies published by Kachanov in 1958 and further developed by Rabotnov in 1968, Hayhurt in 1972, Leckie and Hayshurt in 1974.

The difference between the plasticity and damage models concern in the fact that the plasticity theory is an irreversible process associated to the plastic strain accumulation while the damage theory is elated to the stiffness degradation, Figure 2.10. Phenomenologically, the strain accumulation of plasticity model is caused by the relative displacement of the atoms and the stiffness degradation results of breaks of bond and debonding because of the appearance of cracks.

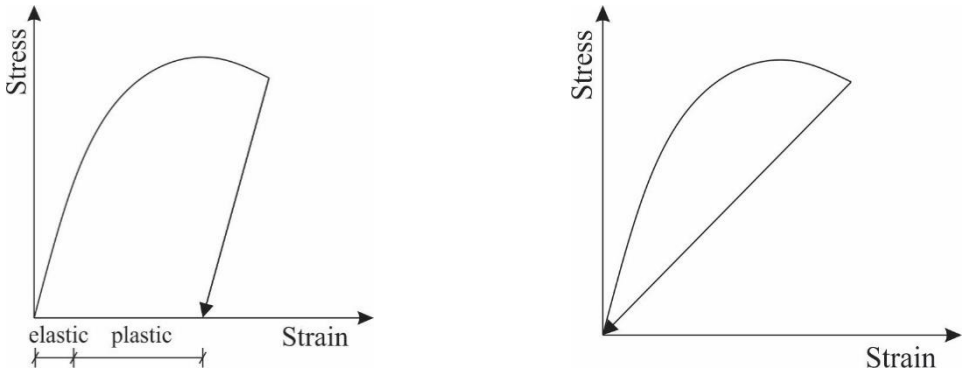

(a) (b)

Figure 2.10 – Basic representation for: (a) Plasticity model and (d) Damage model

Lemaitre and Desmorat (2005) show several versions of damage models that have been developed. The isotropic damage model defined by only one scalar variable that characterizes material degradation is the simplest version. The improvement of this formulation is considered when the damage parameter is associated with two variables, which determine the different

levels of stiffness degradation for compression and tensile states. More sophisticated damage versions describe the anisotropy of the materials with damage variables associated with vectors, second orders tensors or even with fourth-order tensors.

The smeared crack conception was firstly applied to simulate fracture mechanics in the 1960s by Rashid (1968). The development of this theory concerns application in quasi-brittle materials like concrete and rock. Such model gained popularity being entirely explored in the subsequent years (Cervenka and Gerstle 1971, Suidan and Schnobrich 1973, Bazant and ASCE 1976, Crisfleld and Wills 1989, Cervenka 1996, Jirasek and Zimmermann 1998, Lee et al. 2004, Cervenka and Papanikolaou 2008, Hariri-ardebili et al. 2013, Behbahani and Al. 2015, Thybo et al. 2017).

Despite the difference between the discrete and smeared formulations, both are based on the relationship between stress and strain. The Stress-strain correlation in fracture mechanics defines the cohesive-zone model. Dugdale (1960) introduces the cohesive zone for ductile fracture while Barenblatt (1962) for brittle one. The propagation of pre-existing cracks for quasi-brittle material was first developed by Hillerborg et al. (1976) in accordance with the fictitious crack model. Following this approach, cohesive stress is assumed as a function of the crack opening ($f_{COH}(w)$), i.e. when the crack opens the stress does not suddenly fall to zero, Figure 2.11.

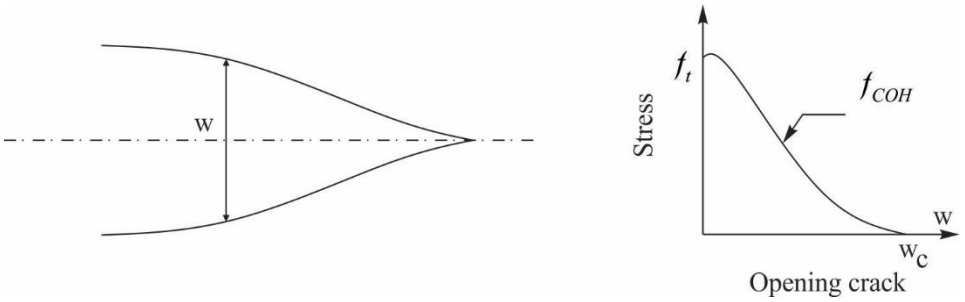

Figure 2.11 – Fictitious crack approach.

The function associated with the gradual decreasing of the stress is called softening function and is considered a material property that can be related to the fracture energy G_f as follow:

$$G_f = \int_0^{w_c} f_{COH}(w)dw \tag{2.9}$$

where w_c is the critical crack opening which indicates the stress are null for larger values and therefore physically a real crack is formed. G_f is defined as the amount of energy required to create one unit of area of a continuous crack.

Based on the fracture mechanics the so-called characteristic length l_{ch} can be derived as:

$$l_{ch} = \frac{\mathbb{E} G_f}{f_t^2} \tag{2.10}$$

where $\mathbb{E}$ and f_t are Young's modulus and the tensile strength, respectively. Generically the characteristic length is a material property, which is assumed as an inverse measurement of its brittleness.

Although the development of the fictitious crack model was applied to the propagation of the pre-existing crack its mathematical formalism is similar to the cohesive crack band approach. The crack band model is directly used with the continuum conception, presented by Bazant in the followings articles: Bazant and oh (1983), Cedolin and Bazant (1980), Bazant and ASCE (1983), Bazant et al. (1983), Bazant (1985) and in the book of Bazant and Planas (1998).

Rots et al. (1985), De Borst and Nauta (1985), De Borst (1986), Rots and De Borst (1987) and Rots (1988) mathematically describes the smeared crack approach by decomposition of total strain into two parcels referred to the elastic and inelastic strain. The inelastic parcel is often called as the crack strain. Successive associations among local coordinates, positioned in the direction of the cracks, and the global coordinates of the system are considered to formulate the constitutive relation for a cracked material. The stiffness of the material cracked is analogous to the prepositions previously taken into account by Bazant in the context of the crack band theory.

More recently, Jirasek (2011) discuss that taking into account the assumptions used to define the constitutive law from the smeared crack models can be observed that this approach differs from the formalism associated with the plasticity and damage theory. Although the decomposition of total strain in elastic and inelastic parts are taken into account, as the plasticity theory, their progress is not defined by a Yielding condition and a respective flow rule. In the smeared crack approach the evolution of the crack strain is directly associated with a traction separation law which is related to the plan of crack.

Figure 2.12 shows the rheological model, represented by a spring, and a unit cohesive crack associated with the crack local coordinates of the smeared crack conception.

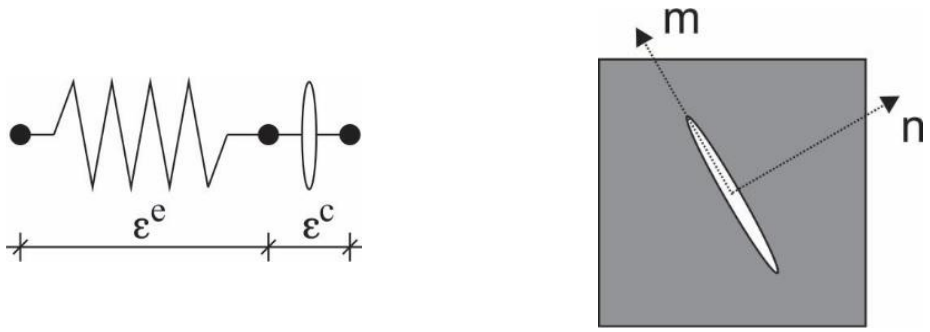

(a) (b)

Figure 2.12 – (a) Rheological model and (b) Local coordinate system aligned with the crack. Withdrawn from (Jirasek 2011).

Initially, three models derivate by the smeared conception are found in the literature:

a) Fixed
b) Rotating
c) Multi-fixed

Summarizing, in the fixed crack model (a) the cracks do not change its direction once they are activated. In the rotating model (b) the inclination of the cracks can be changed and its rotation is established by direction of the principal strain. In the multi-fixed model (c) multiples cracks can arise at the same point of analysis since the principal stress rotation increment exceeds a threshold value.

Softening curves and experimental aspects

The crack opening evolution for the smeared crack model or the damaging process evolution for the damage models is based on the softening curves. Thus, it could be declared that the complete information of the softening curve is an essential input data for performing the numerical simulation.

The softening curve can be determined by experimental tests. Ideally, the direct tensile test it seems the best method to define this. However, they are difficult to be carried out in practice because the fastening devices of the specimens introduce secondary stresses that they cannot be neglected (Mehta and Monteiro 2008).

If in the tensile test it is considered a prismatic or cylindrical specimen the failure can appear as a set of multiplies cracks spread over the volume of the specimen instead of in a localization zone, Figure 2.13a. To circumvent this problem some other shape of specimens were already used, for instance: notched one and dog bone specimens, Figure 2.13b and c, respectively. However as pointed out by Bazant and Planas (1998) the secondary stresses for such cases still persists into the experimental tests. This occurs due to following two reasons:

(1) The specimen tends to shift to an asymmetric mode of fracture due the heterogonous microstructure of the specimen even with a single central crack formed, Figure 2.13d and e.

(2) Imagining that two cracks are growing from both sides of the specimen what occurs is that their extremity tend to avoid each other when they approach and overlap. Therefore, a single crack is not formed in this case, (Figure 2.13f).

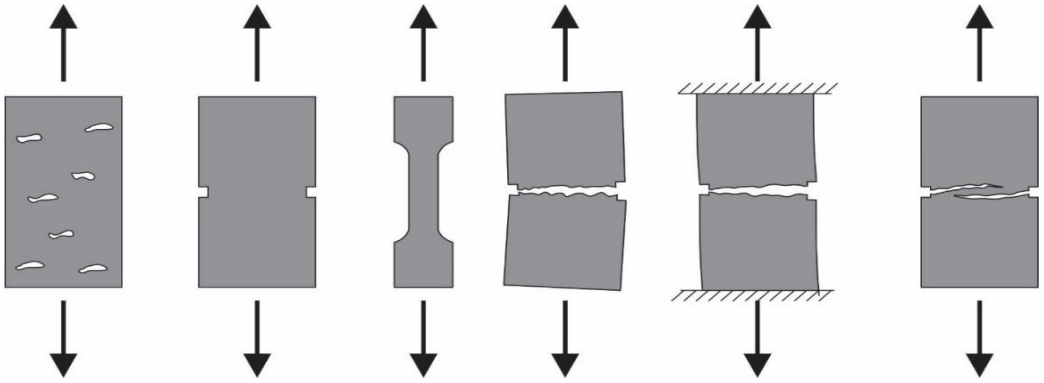

Figure 2.13 – (a) Multiples cracks, (b) Notched specimens, (c) dog bone specimens, (d) rotation in the end of experiment, (e) accommodate by internal deformation and (f) Cracks growing from notched to the center. Adapted from Bazant and Planas (1998).

As the full strain softening curve is difficult to be obtained from the tensile test, alternatively, this descending branch can be estimated by the determination of some parameters, such as tensile strength and fracture energy.

Tensile strength limit

The tensile strength limit (f_t) delimiters the border between the elastic and inelastic regime, i.e. the moment that the crack is activated. In the smeared formulation, such value is assumed constant and equals the tensile strength (f_{ct}).

The splitting cylinder test (or so-called Brazilian test) and four-point bending test can be used to estimate the tensile strength. The Brazilian test is performed with a cylinder specimen with dimensions commonly equal 15x30 cm², (ABNT-NBR 7222:2011). In this test, the compression loading is applied along two axial lines diametrically opposed. Such procedure leads to the failure under tensile in the cross section, Figure 2.14a. The tensile strength by diametrical compression of cylindrical test specimens ($f_{ct,sp}$) is calculated with the follow expression:

$$f_{ct,sp} = \frac{2F}{\pi l d} \tag{2.11}$$

where F is the rupture loading, l and d are the length and the diameter of the specimen, respectively.

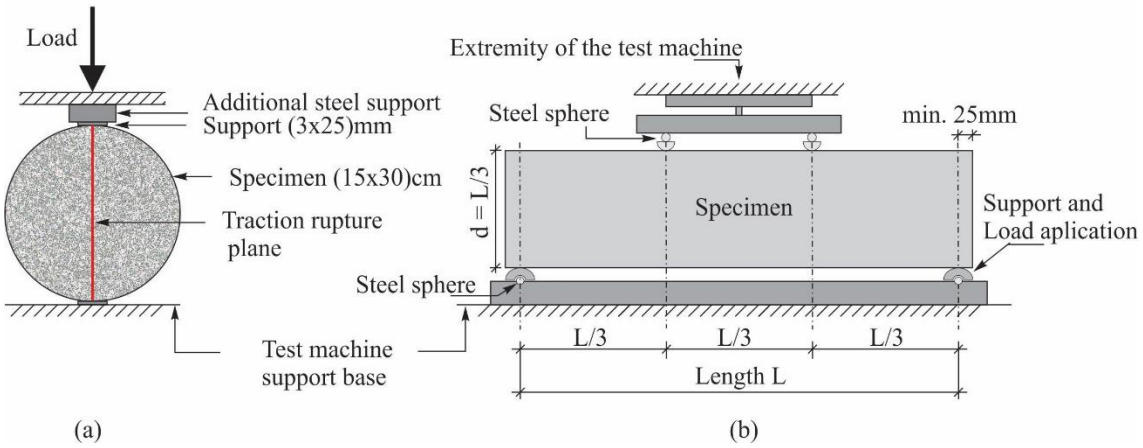

Figure 2.14 – (a) Brazilian test and (b) Four point bending. Adapted from (Mehta and Monteiro 2008).

In the four-point bending test a beam with dimensions 150x150x500mm³ is loaded in the third of the span, Figure 2.14b. The flexural strength ($f_{ct,f}$) is determined with:

$$f_{ct,f} = \frac{FL}{bd^2} \tag{2.12}$$

where F is the rupture loading, L , b and d are the length, width and the height of the specimen, respectively.

ABNT NBR (6118:2014) suggests a reduction of about 30% on the flexural strength as follow defined:

$$f_{ct} = 0.7\, f_{ct,f} \tag{2.13}$$

Similar CEB - FIB Model Code (2010) prescribes the following relationship between mean direct tensile strength (f_{ctm}) and flexural strength ($f_{ct,fl}$):

$$f_{ctm} = f_{ct,fl}\,\frac{0.06h_b^{\,0.7}}{1+0.06h_b^{\,0.7}} \text{ CEB-FIB (2010)} \tag{2.14}$$

where h_b is the beam depth. The strength unities are assumed in MPa.

Alternatively, for the case that there is no experimental data ABNT NBR (6118:2014) and CEB - FIB Model Code (2010) recommends that the tensile direct strength can be estimated as characteristic value (f_{ctm}) from the compressive strength (f_{ck}) according the follow relationships:

$$\begin{aligned} f_{ctm} &= 0.3\left(f_{ck}\right)^{2/3} && \text{concrete grades} \leq \text{C50} \\ f_{ctm} &= 2.12\ln\left(1+0.1\left(f_{ck}+\Delta f\right)\right)^{2/3} && \text{concrete grades} > \text{C50} \end{aligned} \tag{2.15}$$

where $\Delta f = 8MPa$ and all unities that refers to the strength may be considered in MPa.

$$\begin{aligned} f_{ctm} &= 0.3\left(f_{ck}\right)^{2/3} && \text{concrete grades} \leq \text{C50} \\ f_{ctm} &= 2.12\ln\left(1+0.11 f_{ck}\right)^{2/3} && \text{C55} \leq \text{concrete grades} \leq \text{C90} \end{aligned} \tag{2.16}$$

Area under the softening curve

The area under the softening curve (g_f) is mathematically expressed as:

$$g_f = \int_0^{\varepsilon} f_{coh}\left(\varepsilon\right) d\varepsilon \tag{2.17}$$

Such parameter is properly related to the fracture energy (G_f) with the equivalent length also called as characteristic length with the following expression:

$$g_f = \frac{G_f}{h} \tag{2.18}$$

The characteristic length as a crack band approach assures that the energy dissipation does not depends on the finite element size (Cervenka and Papanikolaou 2008). Some authors point out that equivalent length could be associated as a representative dimension of the mesh size (Bazant and Oh 1983, Rots 1988, Oliver 1989, Volokh 2013). However, the value of the characteristic length (h) goes beyond this assumption once depends on the chosen of the element size, element type, element shape, integration scheme and even of the problem considered. In accordance with Feenstra (1993) and De Borst (2002) the equivalent length is written as function of the area of the element as follow:

$$h = \alpha\sqrt{A_e} = \alpha\left(\sum_{i=1}^{NIP} \det(\mathrm{J}_i)\gamma_i\right)^{1/2} \tag{2.19}$$

where the area of element (A_e) is calculating with the numerical integration. NIP is the abbreviation for number of integrations point. The variable γ_i is the weight factors of the numerical integration rule and J_i is the Jacobian transformation between the local, isoparametric coordinates and the global coordinates of the system in integration i. The factor α depends on the element type and the integration scheme. According to Rots (1988) such factor is defined equal 1 for quadratic elements and $\sqrt{2}$ for linear elements.

The three point bending test of a notched concrete beam, Figure 2.15, is the most common experimental test performed to determine the fracture energy (RILEM Committee 50 1985, Guinea et al. 1992, Planas et al. 1992, Elices et al. 1992, Hanson and Ingraffea 2003, Martin et al. 2008, Lee and Lopez 2014).

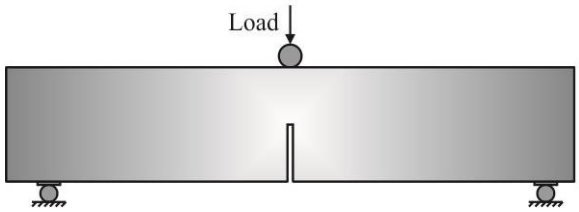

Figure 2.15 – Three point bending test of a notched concrete beam.

According to CEB - FIB Model Code (2010) in the absence of experimental data for ordinary normal weight concrete the fracture energy may be estimated as:

$$G_f = 73 f_{cm}^{0.18} \tag{2.20}$$

where f_{cm} is the mean compressive strength in MPa.

The shape of the softening curve

The shape of the softening relation is another crucial factor to describe the cohesive law adequately, (Bazant and Planas 1998, Morales-alonso et al. 2015). Intrinsically, this relationship is linked to the fracture energy released ratio and the crack opening evolution, as previously mentioned. From the mathematical point of view, the shape of a proper cohesive law point out a gradual process of dissipation of energy and avoid the unrealistic stress jump.

The adoption of strain softening curve in quasi-brittle materials is physically justified by the fact that the formation of a macroscopic stress-free crack in such materials preceded by initiation, growth and coalescence of a network of microcracks (Jirasek 2011).

Over the years some shape of softening curves were proposed, Figure 2.16. The linear softening curve was first suggested by (Hillerborg et al. 1976) as an approximation of the concrete behavior.

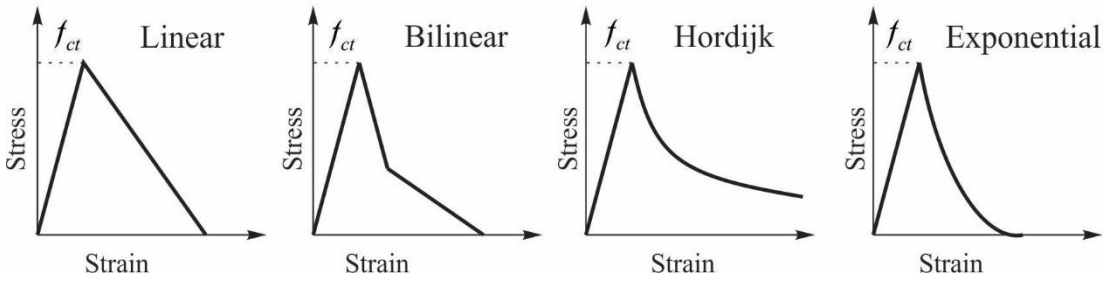

Figure 2.16 – Different softening-curves configurations.

Bazant and Planas (1998) presents that the bilinear curve can be obtained from results of tensile strength and fracture energy provided by the experimental tests, such as the Brazilian test and the three-point bend test. Proposed of bilinear curves can also be found in CEB - FIB Model Code (2010) and JSCE (2010).

The softening curve suggested by Cornelissen et al. (1986) and Hordijk (1991) has the following form:

$$\frac{f(\varepsilon)}{f_{ct}}\begin{cases}\left(1+\left(c_1\frac{\varepsilon}{\varepsilon_{ult}}\right)^3\right)e^{\left(-c_2\frac{\varepsilon}{\varepsilon_{ult}}\right)}-\frac{\varepsilon}{\varepsilon_{ult}}\left(1+c_1^3\right)e^{\left(-c_2\right)} & if\ \left(0<\varepsilon<\varepsilon_{ult}\right)\\ 0 & if\ \left(\varepsilon_{ult}<\varepsilon<\infty\right)\end{cases} \tag{2.21}$$

where C_1 and C_2 are constant parameters respectively equals 3 and 6.93 as suggested by Hordijk (1991). This constants control the shape of the curve. f_{ct} is the uniaxial tensile strength, ε_{ult} is the strain from which the stress are null.

The exponential law is also often used as an approximation of softening curves in Jirásek and Zimmermann (2001) and Jirasek (2011).

It should be emphasized that the concepts discussed in the present topic constitute the basis for the two damage models developed and written at item 4.2 and 4.3 of this thesis.

2.6 Summary

In this chapter, a brief literature review was presented about the themes covered for the development of this work: Dowel action, Positional finite element method, Numerical representation of the reinforcement bars, Plasticity, and Damage and Smeared crack models.

The shear mechanism of Dowel action constitutes an important effect that the steel reinforcement bars of the structures are subjected. Such a mechanism is characterized by actions that occur transversally to the longitudinal axle of the bars. It can occur in casting joints and even in the structures in which the reinforcements completely emerge in the concrete. It was showed that experimental, analytical and numerical researches have been constantly developed over the years. The major challenges found by the researchers consist of the suitable experimental and numerical representation of such a problem. It was presented that the beam-on-elastic-foundation theory is commonly employed for the analytical representation of the dowel action mechanism. However, although such approach results in satisfactory results when compared with experimental test the shear and flexural stiffnesses of the reinforcement bars are neglected with this approach.

Regarding the positional finite element method, it was showed the importance of such formulation to Department of Structures (SET) of the School Engineering of São Carlos (EESC) at the University of São Paulo (USP). Several works were and continue to be published with this methodology. It was also exposed to the mathematical basis for its application.

Following, the progress of the numerical representation of fibers in the context of the finite element method was briefly discussed. The three different approaches discrete, smeared and embedded theories were proposed over the years. Several papers were already published to

shows the mathematical formalities of these three approaches and their applications to investigate reinforced structures. It was presented the advantages and disadvantages of each one. The discrete model is the most realistic representation of the reinforcement bar in the reinforced structures once its contribution occurs exactly at the same position as the reinforcements bars presented in the real case. However, from the numerical point of view, the smeared and embedded theories enable satisfactory analysis with a more practical application.

A brief background about the plasticity theory from the thermodynamics point of view was presented.

At last, from the numerical point of view, it was presented the two ways, Discrete and Continuum approaches, that the problem of failure of material can be treated. Between the possible continuum approach models, the smeared and damage models were briefly presented. Some aspects such as the fracture energy, softening curves, and crack bandwidth or equivalent length was also presented. In the end, the importance of the definition of the three parameters (tensile strength, area, and shape of the softening curves) necessary to determine the crack opening and the damage process evolution was discussed.

Finally, this chapter provided information about dowel action mechanism and suitable numerical formulations available to be used to represent material and structures in order to introduce this thesis and insert it in the context of previous researches.

3 THE NUMERICAL APPROACH

The current chapter addresses the mathematical formulation of the finite elements implemented during the development of this work. The two-dimensional finite element is first presented, followed by the bar and frame. The positional formulation is used to describe the Kinematics of the elements. The chapter also discusses the constitutive laws used as well as the expression that compound the components of the internal forces vector and the Hessian matrix.

The last descriptions concern to the coupling of the bar and frame elements into two-dimensional elements. The coupling technique developed to embedded the frame element into the two-dimensional finite element deserves particular attention because it constitutes one of the contributions of this work.

3.1 Two-dimensional finite element

The present topic concern to the demonstration of the two-dimensional finite element formulation. The theory disposed follow the works developed in Marques (2006) and Sampaio (2014) and more recently the book Coda (2018) entitled as “O Método dos elementos finitos posicional: sólidos e estruturas – não linearidade geométrica e dinâmica”.

Mapping configuration

Two mappings are used to develop the positional formulation. The initial configuration mapping (the non-deformed state) Ω^0 and the current configuration related with deformed state Ω (Figure 3.1).

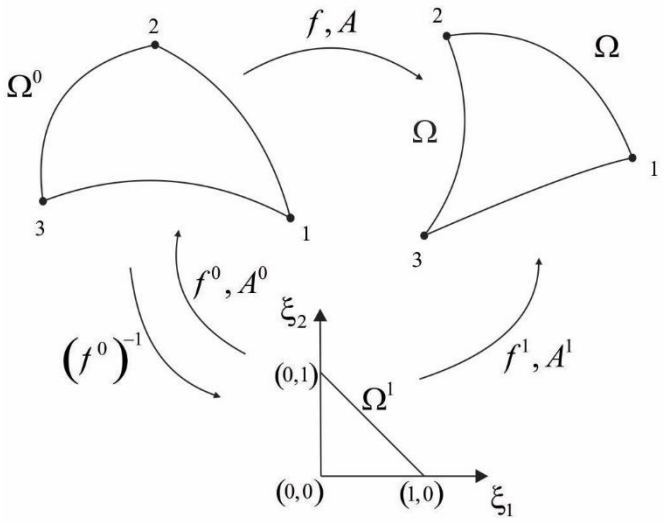

Figure 3.1 – Mapping of initial and current configurations.

Both configurations are described from a system of dimensionless coordinates Ω^1 according to the follow expressions:

$$x_i = f_i^0 = \phi_l(\xi_1, \xi_2) X_i^l \tag{3.1}$$

$$y_i = f_i^1 = \phi_l(\xi_1, \xi_2) Y_i^l \tag{3.2}$$

The coordinates x_i and y_i of the initial and current configurations are respectively mapped on the space Ω^1 using coordinates ξ_i with shape function $\phi_l(\xi_1, \xi_2)$ and the real coordinates nodes X_i^l and Y_i^l at the element. The index i and j represent a certain nodal point while l is the number of nodal coordinates at the element.

f_i^0 and f_i^1 are configuration functions that describe the change of configuration between the initial and current one and the dimensionless coordinates, respectively. The change of configuration at the initial to current is performed with the function f that is calculated from f^0 and f^1 as:

$$f = f^1 \circ (f^0)^{-1} \tag{3.3}$$

The gradient of f, called here as A, is written from the gradient of f^0 and f^1 as:

$$A_{ij}^{0}=\frac{\partial f_i^{\,0}}{\partial \xi_j},\quad A_{ij}^{1}=\frac{\partial f_i^{1}}{\partial \xi_j},\quad A=A\cdot\left(A^{0}\right)^{-1} \tag{3.4}$$

Strain-energy density

The strain energy density at Saint-Venant-Kircchoff is used and defined as:

$$u_e=\frac{1}{2}E:\mathfrak{C}:E \quad \text{or} \quad u_e=\frac{1}{2}E_{ij}\mathfrak{C}_{ijkl}E_{kl} \tag{3.5}$$

where E is the second order Green strain tensor expressed in (3.6) and $\mathfrak{C}$ is the fourth order elastic constitutive tensor (3.7).

$$E=\frac{1}{2}\left(C-I\right)=\frac{1}{2}\left(A^{T}A-I\right) \text{ or } E_{ij}=\frac{1}{2}\left(C_{ij}-\delta_{ij}\right)=\frac{1}{2}\left(A_{ki}A_{kj}-\delta_{ij}\right) \tag{3.6}$$

$$\mathfrak{C}_{ijkl}=\frac{2\mathbb{G}\nu}{1-2\nu}\delta_{ij}\delta_{kl}+\mathbb{G}\left(\delta_{ik}\delta_{jl}+\delta_{il}\delta_{jk}\right) \tag{3.7}$$

With C being the right Cauchy stretch, I the second order identity tensor and δ Kronecker's delta, $\mathbb{G}=\mathbb{E}/\left[2\left(1+\nu\right)\right]$ the transversal elastic modulus, ν the Poisson ration and $\mathbb{E}$ is the longitudinal elastic modulus

For the plane stress case Eq. (3.5) can be conveniently written as:

$$u_e=\frac{\mathbb{G}}{\left(1-\nu^2\right)}\left\{E_{11}^2+E_{22}^2+2\nu E_{11}E_{22}+\left(1-\nu^2\right)\left(E_{12}^2+E_{21}^2\right)\right\} \tag{3.8}$$

Strain Energy

The strain energy for one element U_e is obtained with the volume integration V^0 of the strain-energy density and it is written as:

$$U_e=\int_{V^0}u_e dV^0 \tag{3.9}$$

The specific strain energy written as a function of the dimensionless coordinates results in:

$$U_e=\int_0^1\int_0^1 u_e\left(\xi_1,\xi_2\right)J_0\left(\xi_1,\xi_2\right)d\xi_1 d\xi_2 \tag{3.10}$$

where the domain of the integration is done between 0 and 1 and J_0 is the Jacobian calculated by the determinant of the matrix A^0 as follow showed:

$$J_0\left(\xi_1,\xi_2\right)=\det\left(A^0\right)=A_{11}^0A_{22}^0-A_{12}^0A_{21}^0 \tag{3.11}$$

The numerical integration with the Hammer quadrature is adopted to calculate the integration defined in (3.10). Therefore, the integration is substituted by a summation of the specific strain energy defined for all numerical integration point $\left(\xi_1,\xi_2\right)$ multiplied by its respective weight c_i and Jacobian $J_0\left(\xi_1,\xi_2\right)_i$.

$$U_e=\sum_{i=1}^{nhp}u_e\left(\xi_1,\xi_2\right)_i c_i J_0\left(\xi_1,\xi_2\right)_i \tag{3.12}$$

The index nhp is the number of Hammer's points for one element.

Internal Force

As showed in Eq. (2.3) the internal force is obtained with the first derivative of the strain energy and is written as:

$$F_\alpha^{\beta\,\mathrm{int}}=\frac{\partial U_e}{\partial Y_\alpha^\beta}=\int_{V^0}\frac{\partial u_e}{\partial Y_\alpha^\beta}dV^0=\sum_{i=1}^{nhp}f_\alpha^\beta\left(\xi_1,\xi_2\right)c_i J_0\left(\xi_1,\xi_2\right)_i \tag{3.13}$$

where the index α is the direction of the nodal point β. The development of the term f_α^β gives:

$$f_\alpha^\beta=\frac{\partial U_e}{\partial Y_\alpha^\beta}=\frac{\partial u_e}{\partial E}\frac{\partial E}{\partial C}\frac{\partial C}{\partial Y_\alpha^\beta}=\frac{1}{2}\frac{\partial u_e}{\partial E}\frac{\partial C}{\partial Y_\alpha^\beta}\quad\text{or}\quad f_\alpha^\beta=\frac{\partial U_e}{\partial Y_\alpha^\beta}=\frac{1}{2}\frac{\partial u_e}{\partial E_{ij}}\frac{\partial C_{ij}}{\partial Y_\alpha^\beta} \tag{3.14}$$

The index i and j can be assumed as 1 or 2. By the energy conjugate assumptions, one finds the second Piola-Kirchhoff stress, defined as:

$$S=\frac{\partial u_e}{\partial E}\quad\text{or}\quad S_{ij}=\frac{\partial u_e}{\partial E_{ij}} \tag{3.15}$$

The other term that must be defined is $\partial C/\partial Y_\alpha^\beta$, therefore:

$$\frac{\partial C}{\partial Y_\alpha^\beta}=\left(A^{0^{-t}}\frac{\partial A^{1^t}}{\partial Y_\alpha^\beta}A^1A^{0^{-1}}+A^{0^{-t}}A^{1^t}\frac{\partial A^1}{\partial Y_\alpha^\beta}A^{0^{-1}}\right) \tag{3.16}$$

where $\partial A^1/\partial Y_\alpha^\beta$ for each direction α and a certain node β is:

$$\frac{\partial A^1}{\partial Y_1^\beta}=\frac{\partial}{\partial Y_1^\beta}\begin{bmatrix}\partial Y_1/\partial\xi_1 & \partial Y_1/\partial\xi_2\\ \partial Y_2/\partial\xi_1 & \partial Y_2/\partial\xi_2\end{bmatrix}=\begin{bmatrix}\partial Y_1/\partial\xi_1\partial Y_1^\beta & \partial Y_1/\partial\xi_2\partial Y_1^\beta\\ 0 & 0\end{bmatrix}=\begin{bmatrix}\partial\phi_\beta/\partial\xi_1 & \partial\phi_\beta/\partial\xi_2\\ 0 & 0\end{bmatrix} \tag{3.17}$$

$$\frac{\partial A^1}{\partial Y_2^\beta}=\frac{\partial}{\partial Y_2^\beta}\begin{bmatrix}\partial Y_1/\partial\xi_1 & \partial Y_1/\partial\xi_2\\ \partial Y_2/\partial\xi_1 & \partial Y_2/\partial\xi_2\end{bmatrix}=\begin{bmatrix}0 & 0\\ \partial Y_2/\partial\xi_1\partial Y_2^\beta & \partial Y_2/\partial\xi_2\partial Y_2^\beta\end{bmatrix}=\begin{bmatrix}0 & 0\\ \partial\phi_\beta/\partial\xi_1 & \partial\phi_\beta/\partial\xi_2\end{bmatrix} \tag{3.18}$$

Hessian Matrix

The Hessian matrix definition is performed with the second derivative of the strain energy or with the first derivative of the internal force, as exposed in (2.5), and now rewritten as:

$$H_{\alpha\beta\gamma\tau}=\frac{\partial^2U_e}{\partial Y_\alpha^\beta\partial Y_\gamma^\tau}=\int_{V^0}\frac{\partial^2u_e}{\partial Y_\alpha^\beta\partial Y_\gamma^\tau}dV^0=\sum_{i=1}^{nhp}h_{\alpha\beta\gamma\tau}\left(\xi_1,\xi_2\right)_i c_i J_0\left(\xi_1,\xi_2\right)_i \tag{3.19}$$

where the index α and γ are the direction of the nodes β and τ, respectively. As defined for the internal force the numeric integration is also applied to determine the integration of the second derivative of the specific strain energy.

The development of the term $\partial^2U_e/\partial Y_\alpha^\beta\partial Y_\gamma^\tau$ gives:

$$\frac{\partial^2U_e}{\partial Y_\alpha^\beta\partial Y_\gamma^\tau}=\frac{1}{2}\frac{\partial}{\partial Y_\gamma^\tau}\left(S_{ij}\frac{\partial C_{ij}}{\partial Y_\alpha^\beta}\right)=\frac{1}{2}\left(\frac{\partial S_{ij}}{\partial Y_\gamma^\tau}\frac{\partial C_{ij}}{\partial Y_\alpha^\beta}+S_{ij}\frac{\partial^2C_{ij}}{\partial Y_\alpha^\beta\partial Y_\gamma^\tau}\right) \tag{3.20}$$

where ($\partial C_{ij}/\partial Y_\alpha^\beta$) and S_{ij} were already presented in (3.16) and (3.15), respectively.

The derivative of Piola-Kirchhoff stress is:

$$\frac{\partial S_{ij}}{\partial Y_\gamma^\tau}=\mathfrak{C}\frac{\partial E_{ij}}{\partial Y_\gamma^\tau}=\mathfrak{C}\frac{\partial E_{ij}}{\partial C_{ij}}\frac{\partial C_{ij}}{\partial Y_\gamma^\tau}=\frac{1}{2}\mathfrak{C}\frac{\partial C_{ij}}{\partial Y_\gamma^\tau} \tag{3.21}$$

remembering that $\partial C_{ij}/\partial Y_\gamma^\tau$ is already known in (3.16).

The second derivative of the right Green stretch $\left[\partial^2C_{ij}/\left(\partial Y_\alpha^\beta\partial Y_\gamma^\tau\right)\right]$ is:

$$\frac{\partial^2 C}{\partial Y_\alpha^\beta \partial Y_\gamma^\tau} = \left(A^{0^{-t}} \frac{\partial^2 A^{1^t}}{\partial Y_\alpha^\beta \partial Y_\gamma^\tau} A^1 A^{0^{-1}} + A^{0^{-t}} A^{1^t} \frac{\partial^2 A^1}{\partial Y_\alpha^\beta \partial Y_\gamma^\tau} A^{0^{-1}} \right) + \left(A^{0^{-t}} \frac{\partial A^{1^t}}{\partial Y_\alpha^\beta} \frac{\partial A^1}{\partial Y_\gamma^\tau} A^{0^{-1}} + A^{0^{-t}} \frac{\partial A^{1^t}}{\partial Y_\gamma^\tau} \frac{\partial A^1}{\partial Y_\alpha^\beta} A^{0^{-1}} \right) \tag{3.22}$$

Observing the Eqs. (3.17) and (3.18) the term $\left[\partial^2 A^1 / \left(\partial Y_\alpha^\beta \partial Y_\gamma^\tau\right)\right]$ is null and all the other terms presented in (3.22) are already known.

Chapter 5 shows all simulations of structures performed with this two-dimensional finite element. More specifically, the example 5.1.1 certify this implementation while the exemples 5.2.1, 5.2.2, 5.4.1, 5.5.1, 5.5.2, 5.6.1, 5.6.2, 5.6.3, 5.6.4, 5.7.1, 5.7.2 and 5.8 use this two-dimensional element to validate others theories that will still be discussed in this work.

3.2 Bar finite element

Next, the curved bar finite element formulation developed by Sampaio (2014) and Paccola et al. (2014) is presented. Such an element can be used with straight or curved configuration with any order of approximation.

Kinematic of the bar finite element

Figure 3.2 shows the mapping configuration of the bar finite element. Similar to the two-dimensional element previously discussed the initial (Ω^0) and the current (Ω) configurations are taken into account as well as the system of dimensionless coordinates (Ω^1), which is assumed as the reference for the calculus. It is also defined the configurations functions ${}_f f^0$ and ${}_f f^1$ that describes the change of configuration between Ω^0 and Ω with Ω^1.

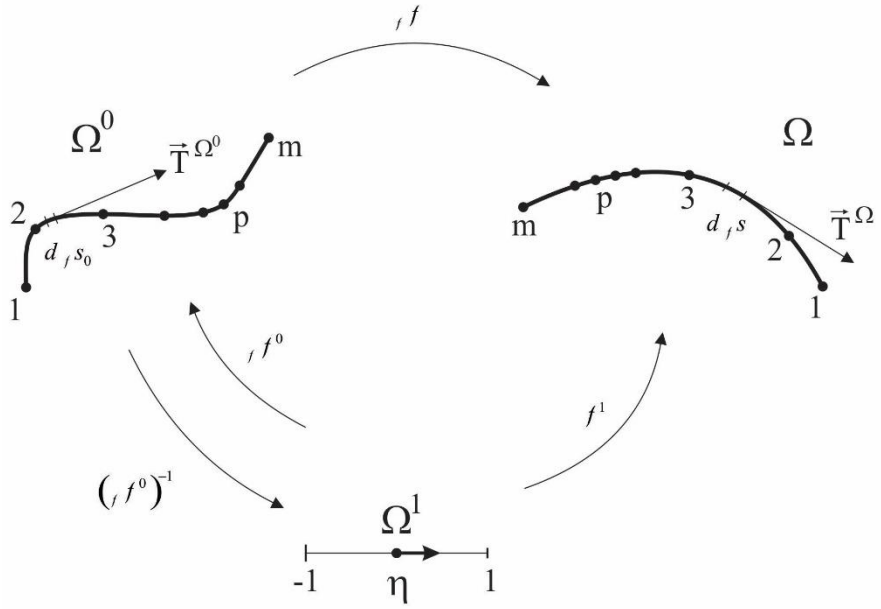

Figure 3.2 – Mapping of initial and current configurations.

So any point p at the initial ($_f X_\alpha^p$) and current ($_f Y_\alpha^p$) coordinates presented in the domains (Ω^0, Ω) are respectively mapped with the shape functions ($_f \phi_p$) and dimensionless coordinates η as follow written:

$$\begin{aligned} {}_f x_\alpha &= {}_f f^0 = {}_f \phi_p(\eta)\, {}_f X_\alpha^p \\ {}_f y_\alpha &= {}_f f^1 = {}_f \phi_p(\eta)\, {}_f Y_\alpha^p \end{aligned} \tag{3.23}$$

where $_f x_\alpha$ and $_f y_\alpha$ are the initial and currents mapped coordinates in the domain of the finite element.

Both the tangent vectors and theirs respective modules for each point of the finite element in the initial and final configurations are respectively defined as:

$$\begin{aligned} {}_f T_\alpha^{\Omega^0} &= \frac{d\, {}_f \phi_p(\eta)}{d\eta}\, {}_f X_\alpha^p \quad \text{and} \quad \left|\vec{T}^{\Omega^0}\right|^2 = \left(\frac{d\, {}_f \phi_p(\eta)}{d\eta}\, {}_f X_1^p\right)^2 + \left(\frac{d\, {}_f \phi_p(\eta)}{d\eta}\, {}_f X_2^p\right)^2 \\ {}_f T_\alpha^{\Omega} &= \frac{d\, {}_f \phi_p(\eta)}{d\eta}\, {}_f Y_\alpha^p \quad \text{and} \quad \left|\vec{T}^{\Omega}\right|^2 = \left(\frac{d\, {}_f \phi_p(\eta)}{d\eta}\, {}_f Y_1^p\right)^2 + \left(\frac{d\, {}_f \phi_p(\eta)}{d\eta}\, {}_f Y_2^p\right)^2 \end{aligned} \tag{3.24}$$

According to the modules expressed in (3.24) the Green strain is assumed as:

$$ {}_f E = \frac{1}{2}\left(\frac{\left| \overrightarrow{{}_f T^{\Omega}} \right|^2 - \left| \overrightarrow{{}_f T^{\Omega^0}} \right|^2}{\left| \overrightarrow{{}_f T^{\Omega^0}} \right|^2} \right) $$

or (3.25)

$$ {}_f E = \frac{1}{2}\frac{\left[\left(\frac{d\,{}_f\phi_p(\eta)}{d\eta} {}_f Y_1^{p} \right)^2 + \left(\frac{d\,{}_f\phi_p(\eta)}{d\eta} {}_f Y_2^{p} \right)^2 \right] - \left[\left(\frac{d\,{}_f\phi_p(\eta)}{d\eta} {}_f X_1^{p} \right)^2 + \left(\frac{d\,{}_f\phi_p(\eta)}{d\eta} {}_f X_2^{p} \right)^2 \right]}{\left[\left(\frac{d\,{}_f\phi_p(\eta)}{d\eta} {}_f X_1^{p} \right)^2 + \left(\frac{d\,{}_f\phi_p(\eta)}{d\eta} {}_f X_2^{p} \right)^2 \right]} $$

The strain-energy density (${}_f u$) definition is:

$$ {}_f u = \frac{1}{2} {}_f \mathbb{E} {}_f E^2 \tag{3.26} $$

where ${}_f \mathbb{E}$ is the tangent elasticity modulus.

Integrating (3.26) over the initial volume gives:

$$ {}_f U = \int_{{}_f V_0} {}_f u \, d\,{}_f V_0 \tag{3.27} $$

The global internal force and the Hessian matrix are obtained, respectively, with the first and second derivative of the strain energy density.

The internal force definition is, therefore:

$$ {}_f F_\alpha^i = \frac{\partial\,{}_f U}{\partial\,{}_f Y_\alpha^i} = \int_{V_0^f} \frac{\partial\,{}_f u}{\partial\,{}_f E_\alpha^i} \frac{\partial\,{}_f E}{\partial\,{}_f Y_\alpha^i} d\,{}_f V_0 \tag{3.28} $$

where:

$$ {}_f S = {}_f \mathbb{E} {}_f E \tag{3.29} $$

$$ \frac{\partial\,{}_f E}{\partial\,{}_f Y_\alpha^i} = \frac{\left(\frac{d\,{}_f\phi_p(\eta)}{d\eta} {}_f Y_\alpha^{p} \right) \frac{d\,{}_f\phi_i(\eta)}{d\eta}}{\left| \overrightarrow{{}_f T^{\Omega^0}} \right|^2} \tag{3.30} $$

The integral solution of the Eq.(3.28) is performed in the dimensioneless coordinates domain. So the integration limits [-1,+1] is assumed and the initial volume of the element (${}_fV_0 = {}_fA\,{}_fL_0$) is defined as function of the isoparametric coordinates η as follow written:

$${}_fF_\alpha^i = \int_{-1}^{1} {}_fS \frac{\partial\, {}_fE}{\partial\, {}_fY_\alpha^i}\, {}_fJ_0(\eta)\, {}_fA\, d\eta \tag{3.31}$$

where ${}_fA$ it is the initial cross-section of the bar and the Jacobian ${}_fJ_0(\eta)$ can be expressed as:

$${}_fJ_0(\eta) = \left|\vec{T}^{\Omega_0}\right| = \sqrt{\left(\frac{dx_1}{d\eta}\right)^2 + \left(\frac{dx_2}{d\eta}\right)^2} \tag{3.32}$$

The Gauss-Legendre quadrature assumed to solve the Eq.(3.31) gives:

$${}_fF_\alpha^i = \sum_{k=1}^{npg} \frac{{}_fS}{\left|{}_f\vec{T}^{\Omega^0}\right|^2} \left(\left.\frac{d\, {}_f\phi_p(\eta)}{d\eta}\right|_{\eta=\eta_k} {}_fY_\alpha^p \right) \left.\frac{d\, {}_f\phi_i(\eta)}{d\eta}\right|_{\eta=\eta_k} {}_fc_k\, {}_fJ_0(\eta_k)\, {}_fA \tag{3.33}$$

where npg are the numbers of Gauss points and ${}_fc_k$ theirs respective weights.

The second derivative of the energy-strain density defines the Hessian matrix as:

$${}_fH_{\alpha\beta}^{ij} = \frac{\partial^2\, {}_fU}{\partial\, {}_fY_\alpha^i \partial\, {}_fY_\beta^j} = \int_{{}_fV_0} \frac{\partial\, {}_fu}{\partial\, {}_fY_\alpha^i \partial\, {}_fY_\beta^j}\, d\, {}_fV_0 = \int_{{}_fV_0} \frac{\partial}{\partial\, {}_fY_\beta^j}\left(\frac{\partial\, {}_fu}{\partial\, {}_fY_\alpha^i}\right) d\, {}_fV_0 \tag{3.34}$$

Applying the chain rule to solve the expression inside the integral defined in (3.34) it is possible to write:

$$\frac{\partial}{\partial\, {}_fY_\beta^j}\left(\frac{\partial\, {}_fu}{\partial\, {}_fE}\frac{\partial\, {}_fE}{\partial\, {}_fY_\alpha^i}\right) = \frac{\partial}{\partial\, {}_fY_\beta^j}\left({}_fS\frac{\partial\, {}_fE}{\partial\, {}_fY_\alpha^i}\right) = \frac{\partial\, {}_fS}{\partial\, {}_fY_\beta^j}\frac{\partial\, {}_fE}{\partial\, {}_fY_\alpha^i} + {}_fS\frac{\partial\, {}_fE}{\partial\, {}_fY_\beta^j \partial\, {}_fY_\alpha^i} \tag{3.35}$$

where ($\partial\, {}_fE / \partial\, {}_fY_\alpha^i$) and (${}_fS$) were already defined in (3.29) and (3.30). The others terms are following expressed:

$$\frac{\partial\, {}_fS}{\partial\, {}_fY_\beta^j} = \frac{\partial}{\partial\, {}_fY_\beta^j}\left({}_f\mathbb{E}\, {}_fE\right) = {}_f\mathbb{E}\frac{\partial\, {}_fE}{\partial\, {}_fY_\beta^j} \tag{3.36}$$

$$\frac{\partial\, {}_f E}{\partial\, {}_f Y_\beta^j \partial\, {}_f Y_\alpha^i} = \frac{\partial}{\partial\, {}_f Y_\beta^j}\left(\frac{\partial\, {}_f E}{\partial\, {}_f Y_\alpha^i}\right) = \frac{\partial}{\partial\, {}_f Y_\beta^j}\left\{\frac{\left[\left(d\, {}_f\phi_p(\eta)/d\eta\right) {}_f Y_\beta^p\right] d\, {}_f\phi_j/d\eta}{\left|{}_f\vec{T}^{\Omega^0}\right|^2}\right\} \tag{3.37}$$

$$\frac{\partial}{\partial\, {}_f Y_\beta^j}\left\{\frac{\left[\left(d\, {}_f\phi_p(\eta)/d\eta\right) {}_f Y_\beta^p\right] d\, {}_f\phi_j/d\eta}{\left|{}_f\vec{T}^{\Omega^0}\right|^2}\right\} = \frac{1}{\left|{}_f\vec{T}^{\Omega^0}\right|^2}\left(\frac{d\, {}_f\phi_p(\eta)}{d\eta}\frac{d\, {}_f\phi_i(\eta)}{d\eta}\delta_{\alpha\beta}\right) \tag{3.38}$$

The integral solution of Hessian matrix (3.34) is also performed with the Gauss-Legendre quadrature. Thus, replacing the expressions (3.29), (3.30), (3.36), (3.37), (3.38) in (3.35) and after into (3.34) the numerical integration is follow specified:

$${}_f H_{\alpha\beta}^{ij} = \sum_{k=1}^{npg}\left(\begin{array}{l} \dfrac{{}_f\mathbb{E}}{\left|{}_f\vec{T}^{\Omega^0}\right|^4}\left(\left.\dfrac{d\, {}_f\phi_p(\eta)}{d\eta}\right|_{\eta=\eta_k} {}_f Y_\beta^p\right)\left.\dfrac{d\, {}_f\phi_j(\eta)}{d\eta}\right|_{\eta=\eta_k} \\ +\left(\left.\dfrac{d\, {}_f\phi_p(\eta)}{d\eta}\right|_{\eta=\eta_k} {}_f Y_\alpha^p\right)\left.\dfrac{d\, {}_f\phi_i(\eta)}{d\eta}\right|_{\eta=\eta_k} \\ +\dfrac{{}_f S}{\left|{}_f\vec{T}^{\Omega^0}\right|^2}\left.\dfrac{d\, {}_f\phi_j(\eta)}{d\eta}\right|_{\eta=\eta_k}\left.\dfrac{d\, {}_f\phi_i(\eta)}{d\eta}\right|_{\eta=\eta_k}\delta_{\alpha\beta} \end{array}\right) {}_f c_k\, {}_f J_0(\eta_k)\, {}_f A \tag{3.39}$$

where $\delta_{\alpha\beta}$ is the Kronecker delta.

Such bar finite element formulation contributes to the analysis of the examples 5.2.1, 5.2.2, 5.3.1, 5.3.2, 5.3.3, 5.5.2, 5.7.1, 5.7.2 and 5.8 performed and written in Chapter 5.

3.3 Frame finite element

Reis and Coda (2014) developed the frame finite element used in the present work. The positions in the directions 1 and 2 and the rotations of the cross-section are the three degrees of freedom considered in its construction. In this work, the element implemented presents four

nodes that correspond to a cubic order element with twelve degrees of freedom. Such two-dimensional element contemplates the Reissner kinematic once the shear stress distribution is included in the formulation and for any deformed configuration, the cross-section does not necessarily remain orthogonal with the longitudinal neutral axle. Next, the formulation of the element is discussed.

Kinematic of the frame finite element

The initial mapping at the reference line of the frame finite element for the dimensionless coordinate system is performed with the shape functions as follow expressed:

$$\overline{f}^{0^m} = x_i^m(\xi) = \phi_l X_{il}^m \tag{3.40}$$

Figure 3.3 illustrates the reference line at a finite element of 4 nodes (cubic approximation).

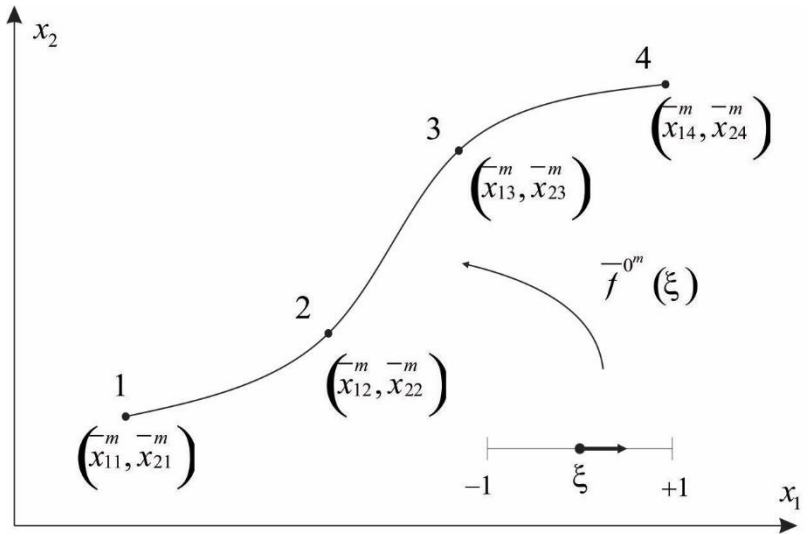

Figure 3.3 – Reference line parameterization for initial configuration. (REIS and CODA, 2014).

The x_i indicates the coordinates for the directions $(i = 1, 2)$ of the nodes mapped at the dimensionless configuration. The subscript *m* is the point in the reference line at the element, X are the nodes coordinates at the element and, the repetition of index l indicates summation.

At nodes, the tangent vector at a reference line, Figure 3.4, can be written as:

$$T_{ik} = \left. \frac{d\phi_l(\xi)}{d\xi} \right|_{\xi_k} X_{il}^{m} \tag{3.41}$$

where ξ_k is the dimensionaless coordinate of node k and T_{ik} is the i_{th} component of the tangent vector at node k.

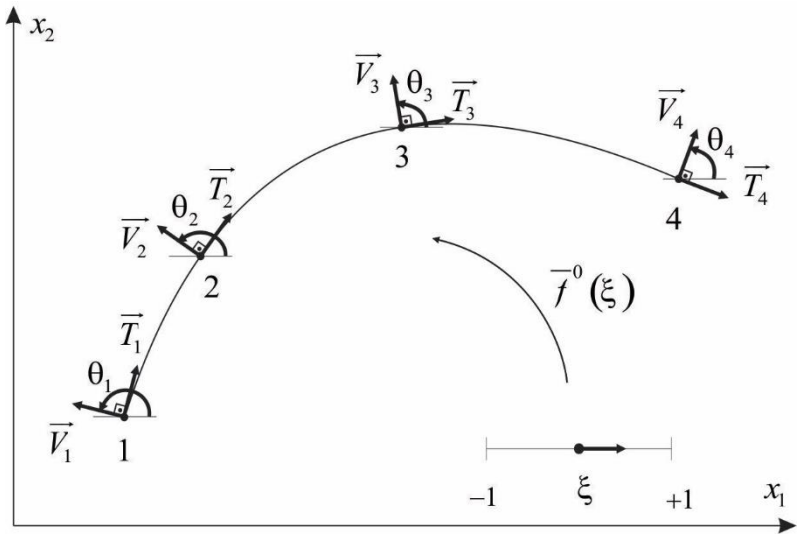

Figure 3.4 – Nodal normal vectors. Adapted from (REIS and CODA, 2014).

The normal vectors at the nodes ilustred in Figure 3.4 is calulcated as:

$$V_{1k} = -T_{2k} \Big/ \sqrt{T_{i(k)} T_{i(k)}} \tag{3.42}$$

$$V_{2k} = T_{1k} \Big/ \sqrt{T_{i(k)} T_{i(k)}} \tag{3.43}$$

The index inside brackets does not mean summation and it could be written as:

$$\sqrt{T_{i(k)} T_{i(k)}} = \sqrt{\left(T_{1(k)}\right)^2 + \left(T_{2(k)}\right)^2} \tag{3.44}$$

The nodal angle θ_k^0 between the normal vector V_{ik} and horizontal direction $\left(x_1\right)$ is determined by:

$$\theta_k^0 = arctg\left(V_{2(k)} \Big/ V_{1(k)}\right) \tag{3.45}$$

The angle θ^0 can be approximate with the shape functions, thus the $\theta^0(\xi)$ for any cross-section along the initial configuration is calculated as:

$$\theta^0(\xi) = \phi_l(\xi)\theta_l^0 \tag{3.46}$$

Any point inside the continuum at the frame finite element presented in Figure 3.5 can be described adding the normal vector $g_i^0(\xi,\eta)$ to a point of the reference line as follow presented:

$$x_i(\xi,\eta) = x_i^m(\xi) + g_i^0(\xi,\eta) \tag{3.47}$$

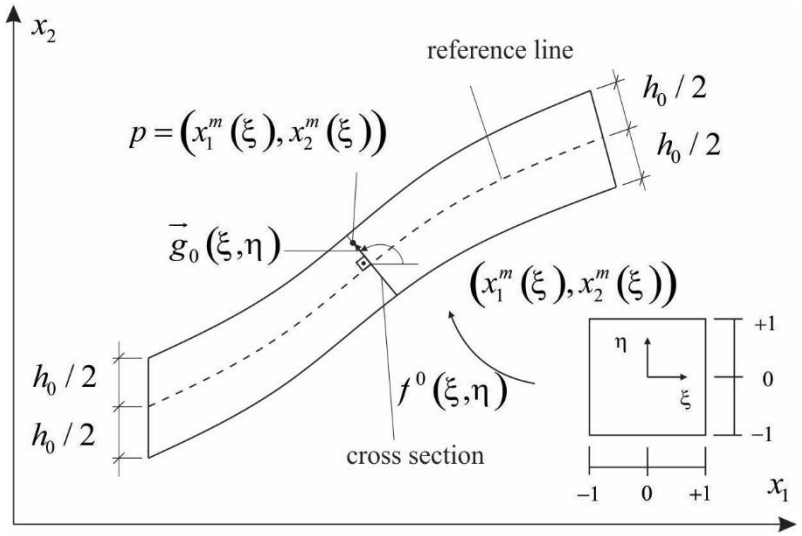

Figure 3.5 – Point P at a general section of the initial element configuration. (REIS and CODA, 2014).

Defining the initial cross-section orthogonal to the reference line, as ilustred in Figure 3.5, it is possible write the normal vector $(g_i^0(\xi,\eta))$ in function of $(\theta^0(\xi))$ as:

$$g_1^0(\xi,\eta) = \frac{h_0}{2}\eta\cos(\phi_l(\xi)\theta_l^0) \tag{3.48}$$

$$g_2^0(\xi,\eta) = \frac{h_0}{2}\eta\sin(\phi_l(\xi)\theta_l^0) \tag{3.49}$$

Therefore, substituting the expressions (3.40), (3.48) and (3.49) into (3.47), the expression that describes the mapping between the initial configuration and the dimensionless coordinate system is defined as:

$$f_1^0(\xi,\eta) = x_1(\xi,\eta) = \phi_l X_{1l}^m + \frac{h_0}{2}\eta\cos\left(\phi_l(\xi)\theta_l^0\right) \tag{3.50}$$

$$f_2^0 = x_2(\xi,\eta) = \phi_l X_{2l}^m + \frac{h_0}{2}\eta\sin\left(\phi_l(\xi)\theta_l^0\right) \tag{3.51}$$

Analogously, the changes function configuration between the current configuration and dimensionless coordinate system can be written as:

$$f_1^1(\xi,\eta) = y_1(\xi,\eta) = \phi_l Y_{il}^m + \frac{h_0}{2}\eta\cos\left(\phi_l(\xi)\theta_l^1\right) \tag{3.52}$$

$$f_2^1(\xi,\eta) = y_2(\xi,\eta) = \phi_l Y_{2l}^m + \frac{h_0}{2}\eta\sin\left(\phi_l(\xi)\theta_l^1\right) \tag{3.53}$$

For the current configuration, the (y_1, y_2) positions and angle (θ) are determined directly at the non-linear solution process.

Figure 3.6 presents the current configuration mapping at the frame finite element. As can be seen from equations (3.52) and (3.53), the cross-section remains straight but not orthogonal to the reference line as the initial configuration. The height h_0 and the width b_0 do not also change for current configuration. This fact allows the constitutive relation for accept any shear elastic modulus but always null poison ration.

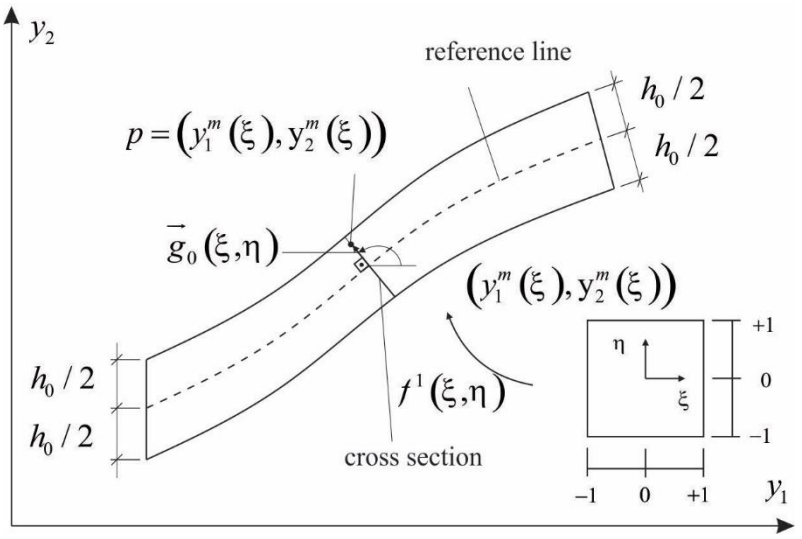

Figure 3.6 – Point P at a general section of the current element configuration. Adapted from (REIS and CODA, 2014).

Similar to the other fintie elements, such one is also based in the two mappings the initial $\left(\Omega^0\right)$ and current $\left(\Omega\right)$ configurations that are mapped according a dimensionless coordinate system $\left(\Omega^1\right)$ as shows Figure 3.7.

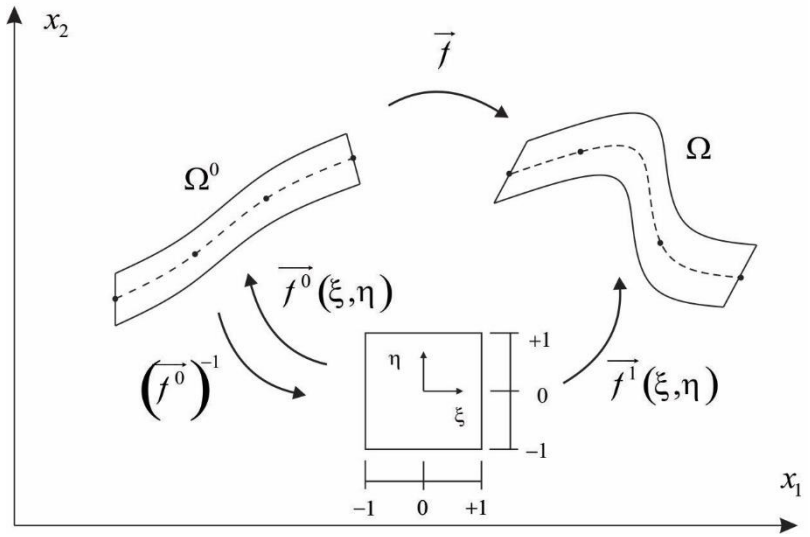

Figure 3.7 – Point P at a general section of the current element configuration. (REIS and CODA, 2014).

The calculus of the function change configuration $\left(\vec{f}\right)$ from initial to current state is done with the decomposition of mappings $\left(\overrightarrow{f^0}\right)$ and $\left(\overrightarrow{f^1}\right)$ as:

$$\vec{f} = \overrightarrow{f^1} \circ \left(\overrightarrow{f^0}\right)^{-1} \tag{3.54}$$

The gradients of $\vec{f}$ is the matrix A with dimensions 2x2 that is determined from the gradient of the initial and current mappings of $\overrightarrow{f^0}$ and $\overrightarrow{f^1}$, as:

$$A = A^1 \cdot \left(A^0\right)^{-1} \tag{3.55}$$

The gradients A^0 and A^1, in index notation A^0_{ij} and A^1_{ij}, are written as:

$$A_{ij}^{0}=\begin{bmatrix}\dfrac{\partial f_1^{0}}{\partial \xi} & \dfrac{\partial f_1^{0}}{\partial \eta}\\ \dfrac{\partial f_2^{0}}{\partial \xi} & \dfrac{\partial f_2^{0}}{\partial \eta}\end{bmatrix}=\begin{bmatrix}\dfrac{\partial x_1}{\partial \xi} & \dfrac{\partial x_1}{\partial \eta}\\ \dfrac{\partial x_2}{\partial \xi} & \dfrac{\partial x_2}{\partial \eta}\end{bmatrix} \tag{3.56}$$

$$A_{ij}^{1}=\begin{bmatrix}\dfrac{\partial f_1^{1}}{\partial \xi} & \dfrac{\partial f_1^{1}}{\partial \eta}\\ \dfrac{\partial f_2^{1}}{\partial \xi} & \dfrac{\partial f_2^{1}}{\partial \eta}\end{bmatrix}=\begin{bmatrix}\dfrac{\partial y_1}{\partial \xi} & \dfrac{\partial y_1}{\partial \eta}\\ \dfrac{\partial y_2}{\partial \xi} & \dfrac{\partial y_2}{\partial \eta}\end{bmatrix} \tag{3.57}$$

The expressions to the parcels of the two gradients (3.56) and (3.57) are determined inserting in such parcels the Eqs. (3.50), (3.51), (3.52) and (3.53), which results in:

$$A_{11}^{0}=\frac{\partial x_1}{\partial \xi}=\frac{\partial \phi_l(\xi)}{\partial \xi}X_{1l}^{m}-\frac{h_0}{2}\eta\sin\left(\phi_l(\xi)\theta_l^{0}\right)\frac{\partial \phi_k(\xi)}{\partial \xi}\theta_k^{0} \tag{3.58}$$

$$A_{12}^{0}=\frac{\partial x_1}{\partial \eta}=\frac{h_0}{2}\cos\left(\phi_l(\xi)\theta_l^{0}\right) \tag{3.59}$$

$$A_{21}^{0}=\frac{\partial x_2}{\partial \xi}=\frac{\partial \phi_l(\xi)}{\partial \xi}X_{2l}^{m}+\frac{h_0}{2}\eta\cos\left(\phi_l(\xi)\theta_l^{0}\right)\frac{\partial \phi_k(\xi)}{\partial \xi}\theta_k^{0} \tag{3.60}$$

$$A_{22}^{0}=\frac{\partial x_2}{\partial \eta}=\frac{h_0}{2}\sin\left(\phi_l(\xi)\theta_l^{0}\right) \tag{3.61}$$

$$A_{11}^{1}=\frac{\partial y_1}{\partial \xi}=\frac{\partial \phi_l(\xi)}{\partial \xi}Y_{1l}^{m}-\frac{h_0}{2}\eta\sin\left(\phi_l(\xi)\theta_l\right)\frac{\partial \phi_k(\xi)}{\partial \xi}\theta_k \tag{3.62}$$

$$A_{12}^{1}=\frac{\partial y_1}{\partial \eta}=\frac{h_0}{2}\cos\left(\phi_l(\xi)\theta_l^{0}\right) \tag{3.63}$$

$$A_{21}^{1}=\frac{\partial y_2}{\partial \xi}=\frac{\partial \phi_l(\xi)}{\partial \xi}Y_{2l}^{m}+\frac{h_0}{2}\eta\cos\left(\phi_l(\xi)\theta_l\right)\frac{\partial \phi_k(\xi)}{\partial \xi}\theta_k \tag{3.64}$$

$$A_{22}^{1}=\frac{\partial y_2}{\partial \eta}=\frac{h_0}{2}\sin\left(\phi_l(\xi)\theta_l\right) \tag{3.65}$$

The Saint-Venant-kirchhoff constitutive relation and the Poisson value null are assumed to define the strain energy density as follow represented:

$$u_e=\frac{\mathbb{E}}{2}\left\{\left(E_{11}^{2}+E_{22}^{2}\right)+\left(E_{12}^{2}+E_{21}^{2}\right)\right\} \tag{3.66}$$

Internal Force

The internal force is obtained from the derivative of strain energy density in a relation to nodal and angular positions as follow defined:

$$F_{\alpha}^{\beta \text{int}} = \frac{\partial U_e}{\partial Y_{\alpha}^{\beta}} = \int_{V_0} \frac{\partial u_e}{\partial Y_{\alpha}^{\beta}} dV_0 = \int_{-1}^{1}\int_{-1}^{1} \frac{\partial u_e(\xi,\eta)}{\partial Y_{\alpha}^{\beta}} J_0(\xi,\eta)\, d\xi d\eta = \frac{\partial u_e\left(\xi_{i_g},\eta_{j_g}\right)}{\partial Y_{\alpha}^{\beta}} w_{i_g} w_{j_g} J_0\left(\xi_{(i_g)},\eta_{(j_g)}\right) \tag{3.67}$$

$$M^{\beta \text{int}} = \frac{\partial U_e}{\partial \theta^{\beta}} = \int_{V_0} \frac{\partial u_e}{\partial \theta^{\beta}} dV_0 = \int_{-1}^{1}\int_{-1}^{1} \frac{\partial u_e(\xi,\eta)}{\partial \theta^{\beta}} J_0(\xi,\eta)\, d\xi d\eta = \frac{\partial u_e\left(\xi_{i_g},\eta_{j_g}\right)}{\partial \theta^{\beta}} w_{i_g} w_{j_g} J_0\left(\xi_{(i_g)},\eta_{(i_g)}\right) \tag{3.68}$$

Taking into account the computational implementation, the two internal forces demonstrated in (3.67) and (3.68) can be refereed as only one vector as:

$$\begin{aligned} F^{\text{int}} &= \left\{ F_1^{1\text{int}} \quad F_2^{1\text{int}} \quad M^{1\text{int}} \quad F_1^{2\text{int}} \quad F_2^{2\text{int}} \quad M^{2\text{int}} \quad \ldots \quad F_1^{\beta\text{int}} \quad F_2^{\beta\text{int}} \quad M^{\beta\text{int}} \right\}^t \\ F^{\text{int}} &= \left\{ F_1^{1\text{int}} \quad F_2^{1\text{int}} \quad F_3^{1\text{int}} \quad F_1^{2\text{int}} \quad F_2^{2\text{int}} \quad F_3^{2\text{int}} \quad \ldots \quad F_1^{\beta\text{int}} \quad F_2^{\beta\text{int}} \quad F_3^{\beta\text{int}} \right\}^t \end{aligned} \tag{3.69}$$

The expression of the derivative of internal force ($\partial U_e / \partial Y_{\alpha}^{\beta}$) is exactly the same equation written in (3.14). However, the second Piola-Kirchhoff stresses is defined for the present element as:

$$S_{11} = \frac{\partial u_e}{\partial E_{11}} = \mathbb{E} E_{11} \tag{3.70}$$

$$S_{22} = \frac{\partial u_e}{\partial E_{22}} = \mathbb{E} E_{22} \tag{3.71}$$

$$S_{12} = \frac{\partial u_e}{\partial E_{12}} = 2\mathbb{G} E_{12} \tag{3.72}$$

$$S_{21} = \frac{\partial u_e}{\partial E_{21}} = 2\mathbb{G} E_{21} \tag{3.73}$$

The derivative of right Cauchy stretch $\left(\partial C / \partial Y_{\alpha}^{\beta}\right)$ is generically defined in (3.16) and the terms $\left(\partial A^1 / \partial Y_{\alpha}^{\beta}\right)$ as:

$$\frac{\partial A^1}{\partial Y_1^\beta}=\frac{\partial}{\partial Y_1^\beta}\begin{bmatrix}\partial Y_1/\partial\xi & \partial Y_1/\partial\eta\\ \partial Y_2/\partial\xi & \partial Y_2/\partial\eta\end{bmatrix}=\begin{bmatrix}\partial Y_1/\partial\xi\partial Y_1^\beta & 0\\ 0 & 0\end{bmatrix}=\begin{bmatrix}\partial\phi_\beta/\partial\xi & 0\\ 0 & 0\end{bmatrix} \tag{3.74}$$

$$\frac{\partial A^1}{\partial Y_2^\beta}=\frac{\partial}{\partial Y_2^\beta}\begin{bmatrix}\partial Y_1/\partial\xi & \partial Y_1/\partial\eta\\ \partial Y_2/\partial\xi & \partial Y_2/\partial\eta\end{bmatrix}=\begin{bmatrix}0 & 0\\ \partial Y_2/\partial\xi\partial Y_2^\beta & 0\end{bmatrix}=\begin{bmatrix}0 & 0\\ \partial\phi_\beta/\partial\xi & 0\end{bmatrix} \tag{3.75}$$

$$\frac{\partial A^1}{\partial Y_3^\beta}=\frac{\partial}{\partial Y_2^\beta}\begin{Bmatrix}\left[-\frac{h_0}{2}\eta\cos\left(\phi_l(\xi)\theta_l\right)\phi_\beta\frac{\partial\phi_k(\xi)}{\partial\xi}\theta_k-\frac{h_0}{2}\eta\sin\left(\phi_l(\xi)\theta_l\right)\frac{\partial\phi_\beta(\xi)}{\partial\xi}\right]\\ \left[-\frac{h_0}{2}\eta\sin\left(\phi_l(\xi)\theta_l\right)\phi_\beta\frac{\partial\phi_k(\xi)}{\partial\xi}\theta_k+\frac{h_0}{2}\eta\cos\left(\phi_l(\xi)\theta_l\right)\frac{\partial\phi_\beta(\xi)}{\partial\xi}\right]\\ \left[-\frac{h_0}{2}\sin\left(\phi_l(\xi)\theta_l\right)\phi_\beta(\xi)\right]\\ \left[\frac{h_0}{2}\cos\left(\phi_l(\xi)\theta_l\right)\phi_\beta(\xi)\right]\end{Bmatrix} \tag{3.76}$$

Hessian Matrix

The Hessian matrix calculation is performed with the second derivative of the strain energy density as:

$$H_{\alpha\beta\gamma\tau}=\frac{\partial^2U_e}{\partial Y_\alpha^\beta\partial Y_\gamma^\tau}=\int_{V^0}\frac{\partial^2u_e}{\partial Y_\alpha^\beta\partial Y_\gamma^\tau}dV^0=\frac{\partial^2u_e\left(\xi_{i_g},\eta_{j_g}\right)}{\partial Y_\alpha^\beta\partial Y_\gamma^\tau}w_{i_g}w_{j_g}J_0\left(\xi_{(i_g)},\eta_{(j_g)}\right)=h_{\alpha\beta\gamma\tau}w_{i_g}w_{j_g}J_0\left(\xi_{(i_g)},\eta_{(j_g)}\right) \tag{3.77}$$

Remembering from (3.20) the second derivative of the strain energy can be defined as:

$$\frac{\partial^2U_e}{\partial Y_\alpha^\beta\partial Y_\gamma^\tau}=\frac{1}{2}\frac{\partial}{\partial Y_\gamma^\tau}\left(S_{ij}\frac{\partial C_{ij}}{\partial Y_\alpha^\beta}\right)=\frac{1}{2}\left(\frac{\partial S_{ij}}{\partial Y_\gamma^\tau}\frac{\partial C_{ij}}{\partial Y_\alpha^\beta}+S_{ij}\frac{\partial^2C_{ij}}{\partial Y_\alpha^\beta\partial Y_\gamma^\tau}\right) \tag{3.78}$$

where the term S_{ij} has been already presented in (3.70) until (3.73) and the term ($\partial C_{ij}/\partial Y_\alpha^\beta$) in (3.16). The derivative of Piola-Kirchhoff stress was also already defined in (3.21) and it is rewritten as:

$$\frac{\partial S_{ij}}{\partial Y_\gamma^\tau}=\mathbb{E}\frac{\partial E_{ij}}{\partial Y_\gamma^\tau}=\mathbb{E}\frac{\partial E_{ij}}{\partial C_{ij}}\frac{\partial C_{ij}}{\partial Y_\gamma^\tau}=\frac{1}{2}\mathbb{E}\frac{\partial C_{ij}}{\partial Y_\gamma^\tau} \tag{3.79}$$

with $\partial C_{ij}/\partial Y_\gamma^\tau$ already kwon in (3.16).

The term $\left[\partial^2 C/\left(\partial Y_\alpha^\beta \partial Y_\gamma^\tau\right)\right]$ is defined in (3.22). All terms with first derivative are already known from (3.74) until (3.76). $\partial^2 A^1/\partial Y_\alpha^\beta \partial Y_\gamma^\tau$ has a relevant computation cost if compare with its contribution for the convergence ratio, therefore, these values are not calculated.

The frame element formulation previously presented was validated with the example 5.1.2, beyond to be used to discuss the cases 5.2.1, 5.2.2, 5.4.1, 5.4.2, 5.4.3, 5.5.2, 5.7.1, 5.7.2 and 5.8 addressed in chapter 5.

3.4 Coupling of the reinforcement bars

In previous sections, all finite elements formulations used in the present research were separately described. Next, the internal forces vector and Hessian matrix at a finite element reinforced by fiber will be presented and discussed. The initial formulation idea showed and used in the present studies was defined by Vanalli et al. (2008). Paccola et al. (2014) and Sampaio et al. (2015) also enhanced the formulation applying to study the stress contact between fiber and matrix.

Total strain energy

The basic idea of the coupling consists in calculate the total strain energy (U) with the sum of matrix (U_{mat}) and fiber (U_f) energy, as:

$$U = U_{mat} + U_f \tag{3.80}$$

Following the natural sequence of the finite element method the next step is calculate the internal force and the Hessian matrix. It is important to note that these terms must be determinate as function of position of the matrix. Therefore, before to present them it is necessary to discuss how this relationship is perfomed.

It considers a point P belong to the bar element and it is inside in the matrix domain as presented in Figure 3.8.

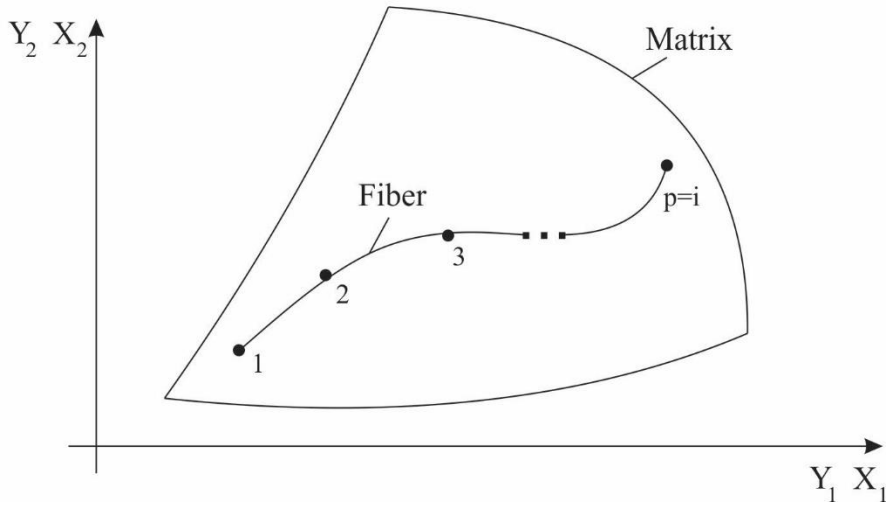

Figure 3.8 – Point P in the matrix domain

The coordinates at a node P $\left(X_{\alpha}^{P};Y_{\alpha}^{P}\right)$ following direction α can be written in function at the shape function matrix element $\left(\phi_{l}^{mat}\right)$ with the isoparametric coordinates known $\left(\xi_{1}^{p},\xi_{2}^{p}\right)$ and the matrix coordinates $\left(X_{i}^{lmat};Y_{i}^{lmat}\right)$ according to:

$$\begin{aligned} X_{\alpha}^{f\,p} &= \phi_{l}^{mat}\left(\xi_{1}^{p},\xi_{2}^{p}\right)X_{\alpha}^{lmat} \\ Y_{\alpha}^{f\,p} &= \phi_{l}^{mat}\left(\xi_{1}^{p},\xi_{2}^{p}\right)Y_{\alpha}^{lmat} \end{aligned} \tag{3.81}$$

where the index l represent a summation of all nodal points of the matrix finite element.

Internal Force

The internal force at a node i following direction α can be expressed as:

$$\frac{\partial U}{\partial Y_{\alpha}^{i}} = \frac{\partial\left(U_{mat}+U_{f}\right)}{\partial Y_{\alpha}^{i}} = \frac{\partial U_{mat}}{\partial Y_{\alpha}^{i}} + \frac{\partial U_{f}}{\partial Y_{\alpha}^{i}} = \frac{\partial U_{mat}}{\partial Y_{\alpha}^{i}} + \frac{\partial U_{f}}{\partial Y_{\kappa}^{f\,P}}\frac{\partial Y_{\kappa}^{f\,P}}{\partial Y_{\alpha}^{i}} = F_{\alpha}^{\mathrm{iint}} \tag{3.82}$$

The first internal force parcel ($\partial U_{mat}/\partial Y_{\alpha}^{i}$) is the same internal force for the two-dimensional finite element presented in (3.13). The chain rule applied for second parcel ($\partial U_{f}/\partial Y_{\alpha}^{i}$) is necessary because as previously discussed the strain energy of the fiber is now derivative as function of the position nodes of the matrix. The term $\left(\partial Y_{\kappa}^{f\,P}/\partial Y_{\alpha}^{i}\right)$ performance

the contribution of the internal force of the bar $\left(\partial U_f / \partial Y_\kappa^P\right)$ and when $k = \alpha$ and the node P is inside at the matrix element the parcel is calculated as $\left(\partial Y^{f\,P}_{\ \kappa} / \partial Y_\alpha^i\right) = \phi_i\left(\xi_1^p, \xi_2^p\right)$.

Hessian Matrix

As already described, the hessian matrix is determined with the second derivative of strain energy. In the present context, such derivation is the relation at position of the matrix finite element as follows:

$$\frac{\partial^2 U}{\partial Y_\alpha^i \partial Y_\beta^j} = \frac{\partial^2\left(U_{mat} + U_f\right)}{\partial Y_\alpha^i \partial Y_\beta^j} = \frac{\partial^2 U_{mat}}{\partial Y_\alpha^i \partial Y_\beta^j} + \frac{\partial^2 U_f}{\partial Y_\alpha^i \partial Y_\beta^j} \tag{3.83}$$

where the first parcel refers to the Hessian of the matrix and the second parcel can be written as:

$$\frac{\partial^2 U_f}{\partial Y_\alpha^i \partial Y_\beta^j} = \frac{\partial}{\partial Y_\alpha^i}\left(\frac{\partial U_f}{\partial Y_\beta^j}\right) = \frac{\partial}{\partial Y_\beta^j}\left(\frac{\partial U_f}{\partial Y_\kappa^p}\frac{\partial Y_\kappa^p}{\partial Y_\alpha^i}\right) = \frac{\partial}{\partial Y_\beta^j}\left(\frac{\partial U_f}{\partial Y_\kappa^p}\right)\frac{\partial Y_\kappa^p}{\partial Y_\alpha^i} + \frac{\partial U_f}{\partial Y_\kappa^p}\left(\frac{\partial^2 Y_\kappa^p}{\partial Y_\beta^j \partial Y_\alpha^i}\right) \tag{3.84}$$

The term of the second derivation is null and therefore the first parcel is:

$$\frac{\partial}{\partial Y_\beta^j}\left(\frac{\partial U_f}{\partial Y_\kappa^p}\right)\frac{\partial Y_\kappa^p}{\partial Y_\alpha^i} = \left(\frac{\partial^2 U_f}{\partial Y_\kappa^p \partial Y_\omega^q}\frac{\partial Y_\omega^q}{\partial Y_\beta^j}\right)\frac{Y_\kappa^p}{\partial Y_\alpha^i} \tag{3.85}$$

The derivation with superior order is the Hessian of the fiber, and the other terms refer to correct contribution of the bar in the global Hessian. So, we can finally write the expression of the hessian as follow:

$$\frac{\partial^2 U}{\partial Y_\alpha^i \partial Y_\beta^j} = H^{mat} + H^f \delta_{\beta\omega}\phi_j\left(\xi_1^p, \xi_2^p\right)\delta_{\alpha\kappa}\phi_i\left(\xi_1^p, \xi_2^p\right) \tag{3.86}$$

Matrix Notation

The contribution of the internal forces and the Hessian matrix of the bar in the matrix component is performed by node of each fiber element. In general, the terms composed by $\left(\partial Y^{f\,l}_{\ \gamma} / \partial Y_\rho^m\right)$ performance the coupling of the fiber elements and theirs values are related to the geometric association between fiber and matrix.

Once determined the internal force vector of the one fiber finite element for each node P it has one pair of internal force $\left[F^{\text{int } f} \right]_2$ and, therefore, its contribution in the matrix domain can be done as follow:

$$\left[F^{\text{int } f} \right]_{2N} = \left[F^{\text{int}}{}_{f} \right]_2 . [B]_{2x2N} \tag{3.87}$$

assuming N equal the number of nodes at one matrix finite element.

The matrix $[B]_{2x2N}$ refers to the therm $\left(\partial Y^{f}{}_{\kappa}^{P} / \partial Y_{\alpha}^{i} \right)$ of Eq. (3.82) and it is composed by the nodal shape functions of the matrix with values calculated with the isoparametric coordinates of the nodal point P.

$$[B]_{2x2N} = \begin{bmatrix} \phi^1\left(\xi_1^P, \xi_2^P\right) & 0 & \phi^2\left(\xi_1^P, \xi_2^P\right) & 0 & \dots & \phi^{10}\left(\xi_1^P, \xi_2^P\right) & 0 \\ 0 & \phi^1\left(\xi_1^P, \xi_2^P\right) & 0 & \phi^2\left(\xi_1^P, \xi_2^P\right) & \dots & 0 & \phi^{10}\left(\xi_1^P, \xi_2^P\right) \end{bmatrix} \tag{3.88}$$

The contribution of the Hessian of the fiber in the Hessian of the matrix, previously calculated from Eq. (3.85), is rewritten in matrix notation as:

$$\left[H^{\text{int } f} \right]_{2Nx2N} = [B]^{T}_{2x2N} . \left[H^{\text{int}}{}_{f} \right]_{2x2} . [B]_{2x2N} \tag{3.89}$$

So, the matrix operations expressed in (3.87) and (3.89) are calculated for each nodal poin P of the fiber element. The results of these two operations constitute the local internal force vector and the local Hessian matrix contributions of the fiber in the matrix elements. The global internal force and the global Hessian matrix of the structure must be determined.

3.4.1 Coupling Matrix and Fiber-Frame Finite element

As already previous emphasized the two-dimensional finite element presents two degrees of freedom per node, which correspond to the nodal translation in the 1 and 2 directions. The frame element has 3 degrees of freedom per node, linked to their translation in the 1 and 2 directions and its angular rotation. The coupling procedure performed between these two elements and adopted in the present work consider the degree of freedom related to the angular rotation free. In other words, only the translation movements of the nodes of the frame elements are coupled with the tow-dimensional elements. The degree of freedom related to the angular

rotation is assumed as an additional variable in the equilibrium of the system. Following the mathematical formulation for this so-called semi coupling procedure is presented.

The equilibrium position is determined with the variation of the Total potential energy in relation with all degree of freedom of the system ($\overline{Y}_{\rho}^{l}$).

$$\frac{\partial U}{\partial \overline{Y}_{\rho}^{l}} = \frac{\partial \left(U_{mat} + U_{f} \right)}{\partial \overline{Y}_{\rho}^{l}} = \frac{\partial U_{mat}}{\partial \overline{Y}_{\rho}^{l}} + \frac{\partial U_{f}}{\partial \overline{Y}_{\rho}^{l}} = \frac{\partial U_{mat}}{\partial \overline{Y}_{\rho}^{l}} + \frac{\partial U_{f}}{\partial Y^{f\,P}_{\kappa}} \frac{\partial Y^{f\,P}_{\kappa}}{\partial \overline{Y}_{\rho}^{l}} = F_{\rho}^{\text{lint}} \tag{3.90}$$

The vector $\overline{Y}$ correspond to all degree of freedom of the system, i.e. the directions 1 and 2 of the matrix elements plus the angular rotation of the frame elements. The index l is the number of nodes of the system. While l be associated with the nodes of the matrix elements (i), the index ρ assume values of α equal 1 and 2 that relate to the directions of such element. On the other hand, as long as the index l relates to the nodes of the frame elements (r) the direction ρ assumes value 3 that connects to the degree of freedom linked with the angular rotation.

The Eq. (3.90) is rewritten in matrix notation as follow:

$$\left\{ F^{\text{int}} \right\}_{(2Nm+Nf)} = \left\{ \begin{matrix} \dfrac{\partial U_{mat}}{\partial Y_{\alpha}^{i}} \\ \dfrac{\partial U_{mat}}{\partial Y_{3}^{r}} \end{matrix} \right\}_{(2Nm+Nf)} + \left\{ \begin{matrix} \dfrac{\partial U_{f}}{\partial Y^{f\,P}_{\kappa}} \dfrac{\partial Y^{f\,P}_{\kappa}}{\partial Y_{\alpha}^{i}} \\ \dfrac{\partial U_{f}}{\partial Y^{f\,P}_{\kappa}} \dfrac{\partial Y^{f\,P}_{\kappa}}{\partial Y_{3}^{r}} \end{matrix} \right\}_{(2Nm+Nf)} = \tag{3.91}$$

$$= \left\{ \begin{matrix} {}_{mat}F^{\text{int}} \\ {}_{mat}F^{\text{int}}_{,(\text{r}3)} \end{matrix} \right\}_{(2Nm+Nf)} + \left\{ \begin{matrix} {}_{f}F^{\text{int}} \\ {}_{f}F^{\text{int}}_{,(r3)} \end{matrix} \right\}_{(2Nm+Nf)}$$

where $(2Nm+Nf)$ determines the size of the internal force vector and Nm and Nf are the number of nodes of the matrix and frame finite elements, respectively.

The second variation of the Total potential energy defines the Hessian matrix as follow:

$$\frac{\partial^2 U}{\partial \overline{Y}^l_\rho \partial \overline{Y}^q_\lambda} = \frac{\partial^2 U_{mat}}{\partial \overline{Y}^l_\rho \partial \overline{Y}^q_\lambda} + \frac{\partial}{\partial \overline{Y}^q_\lambda}\left(\frac{\partial U_f}{\partial Y^{fP}_\kappa}\frac{\partial Y^{fP}_\kappa}{\partial \overline{Y}^l_\rho}\right)$$
$$= \frac{\partial^2 U_{mat}}{\partial \overline{Y}^l_\rho \partial \overline{Y}^q_\lambda} + \frac{\partial^2 U_f}{\partial \overline{Y}^q_\lambda \partial Y^{fP}_\kappa}\frac{\partial Y^{fP}_\kappa}{\partial \overline{Y}^l_\rho} + \frac{\partial U_f}{\partial Y^{fP}_\kappa}\frac{\partial^2 Y^{fP}_\kappa}{\partial \overline{Y}^q_\lambda \partial \overline{Y}^l_\rho} \tag{3.92}$$
$$= \frac{\partial^2 U_{mat}}{\partial \overline{Y}^l_\rho \partial \overline{Y}^q_\lambda} + \frac{\partial^2 U_f}{\partial Y^{ft}_m \partial Y^{fP}_\kappa}\frac{\partial Y^{ft}_m}{\partial \overline{Y}^q_\lambda}\frac{\partial Y^{fP}_\kappa}{\partial \overline{Y}^l_\rho} + \frac{\partial U_f}{\partial Y^{fP}_\kappa}\frac{\partial^2 Y^{fP}_\kappa}{\partial \overline{Y}^q_\lambda \partial \overline{Y}^l_\rho}$$

As the angular rotation is a degree of freedom free the third parcel ($\partial^2 Y^{fP}_\kappa \big/ \partial \overline{Y}^q_\lambda \partial \overline{Y}^l_\rho$) of Eq. (3.92) is null. Thus, the Hessian is summed up as:

$$\frac{\partial^2 U}{\partial \overline{Y}^l_\rho \partial \overline{Y}^q_\lambda} = \frac{\partial^2 U_{mat}}{\partial \overline{Y}^l_\rho \partial \overline{Y}^q_\lambda} + \frac{\partial^2 U_f}{\partial Y^{ft}_m \partial Y^{fP}_\kappa}\frac{\partial Y^{ft}_m}{\partial \overline{Y}^q_\lambda}\frac{\partial Y^{fP}_\kappa}{\partial \overline{Y}^l_\rho} \tag{3.93}$$

In matrix notation, the Hessian defines in (3.93) can be rewritten as:

$$H_{(2Nm+Nf)\text{x}(2Nm+Nf)} = \begin{Bmatrix} {}_{mat}H & {}_{mat}\mathcal{I} \\ {}_{mat}\mathcal{J} & {}_{mat}\mathcal{H} \end{Bmatrix}_{(2Nm+Nf)\text{x}(2Nm+Nf)} + \begin{Bmatrix} {}_{f}H & {}_{f}\mathcal{I} \\ {}_{f}\mathcal{J} & {}_{f}\mathcal{H} \end{Bmatrix}_{(2Nm+Nf)\text{x}(2Nm+Nf)} \tag{3.94}$$

where each term of this such matrix is summarized in Table 5.

Table 5 – Components of the Hessian matrix of Eq.(3.94).

Two-dimensional element	Frame element
${}_{mat}H = \frac{\partial^2 U_{mat}}{\partial Y^i_\alpha \partial Y^j_\beta}$,	${}_{f}H = \frac{\partial^2 U_f}{\partial Y^{ft}_m \partial Y^{fP}_\kappa}\frac{\partial Y^{ft}_m}{\partial Y^j_\beta}\frac{\partial Y^{fP}_\kappa}{\partial Y^i_\alpha}$
${}_{mat}\mathcal{H} = \frac{\partial^2 U_{mat}}{\partial Y^{fr}_3 \partial Y^{fs}_3}$,	${}_{f}\mathcal{H} = \frac{\partial^2 U_f}{\partial Y^{fr}_3 \partial Y^{fs}_3}$
${}_{mat}\mathcal{I} = \frac{\partial^2 U_{mat}}{\partial Y^{fs}_3 \partial Y^i_\alpha}$,	${}_{f}\mathcal{I} = \frac{\partial^2 U_f}{\partial Y^{fs}_3 \partial Y^{fi}_\alpha}$
${}_{mat}\mathcal{J} = \frac{\partial^2 U_{mat}}{\partial Y^{fr}_3 \partial Y^j_\beta}$,	${}_{f}\mathcal{J} = \frac{\partial^2 U_f}{\partial Y^{fr}_3 \partial Y^{fj}_\beta}$

Notes that ${}_{mat}H$ it is the Hessian of the two-dimensional finite elements and the terms ${}_{mat}\mathcal{H}$, ${}_{mat}\mathcal{I}$ and ${}_{mat}\mathcal{J}$ are nulls. On the other hand, ${}_{f}H$ refers to the coupling components of

the Hessian of the frame elements associated with the degree of freedom linked to direction 1 and 2. The components of ${}_f\mathcal{H}$ are the terms of the Hessian of the frame element only related to the degree of freedom associated with the angular rotation. At last, it verifies that the term ${}_f\mathcal{I}$ is the transpose of ${}_f\mathcal{J}$ (${}_f\mathcal{I} = {}_f\mathcal{J}^T$), and they correspond to the terms of the Hessian matrix of the frame element.

3.4.2 Algorithm process solution

Figure 3.9 presents the organizational structure of the code with the frame finite element for the embedded model previously discussed. After the input data, the tangent and normal vector of the fiber are calculated through Eqs. (3.41), (3.42) and (3.43). The initial angle is also determined by Eq.(3.45) and (3.46). Next, it is calculated the location of the fiber nodes. To do so, the central node coordinates of each two-dimensional finite element is determined. The distances between the central node and the node of the fiber element (called as d) is calculated, as long as the distance between the central node and the vertices nodes of two-dimensional element (dc). If d>2dc the node of the fiber is outside of the two-dimensional finite element. Otherwise, d<2dc, the adimensional coordinates of the fiber node in relation to isoparametric coordinates of the two-dimensional element is stored. The last process is done by inverse mapping for local coordinates, technique presented in Elwi and Hrudey (1989).

The procedure of the tangent and normal vector calculation, as well as the initial angle determination, is not necessary for the coupling technique performed with the bar finite element. This occurs because such a step is exclusive for the calculation of the internal force and the Hessian matrix of the frame finite element. Therefore, for the case that the fiber is represented by bar finite elements the structure of the algorithm is similar to Figure 3.9 excepting such step procedure.

The Newton Rapson procedure shows in Figure 3.9 and Figure 2.4 are similar, excepting the equations used to calculate the internal forces (3.82) and matrix hessian (3.86).

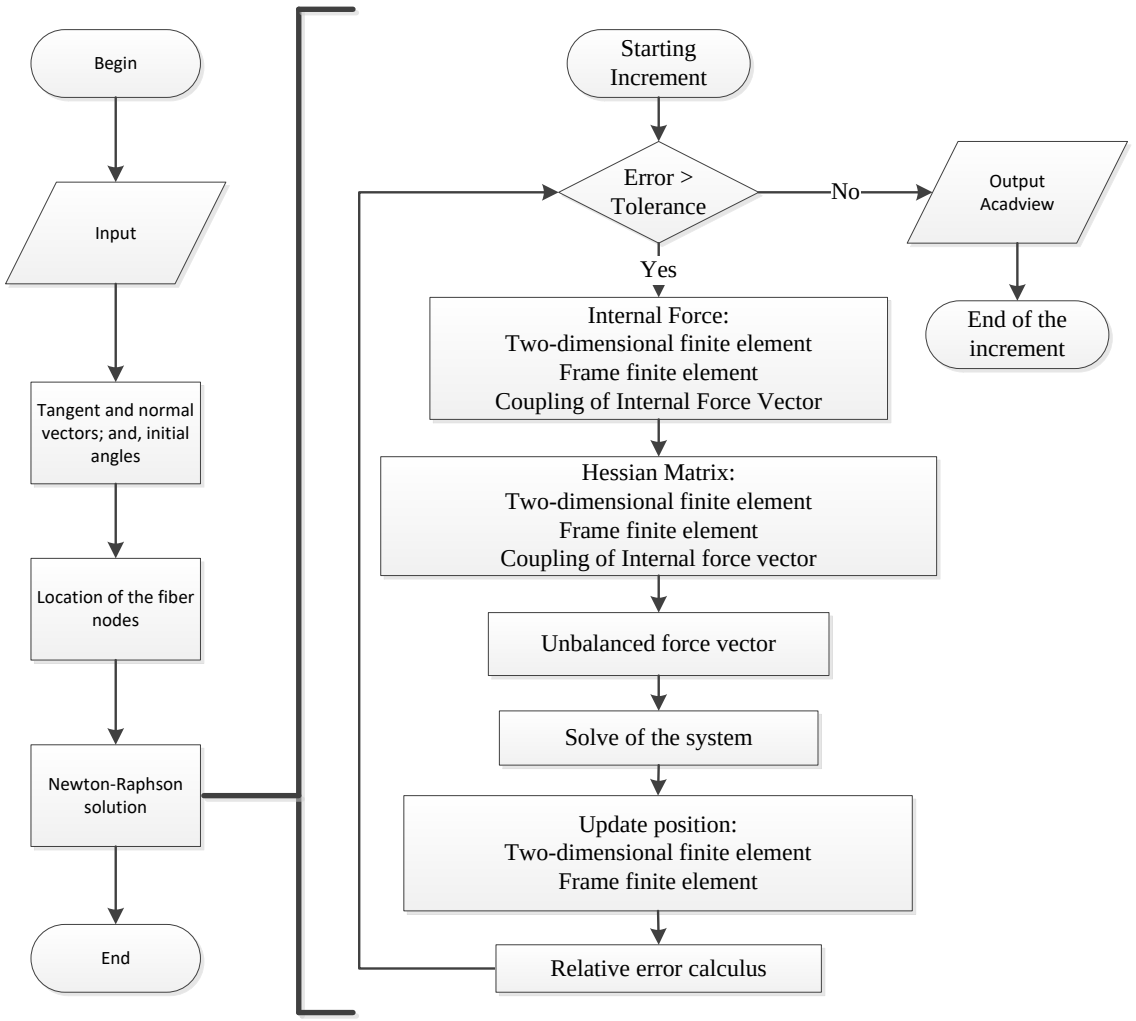

Figure 3.9 – Structural organization of the code nonlinear geometric and with the embedded model.

The coupling technique presented between the fibers and matrix elements is validated with the examples 5.5.1 and 5.5.2, and posterior used to discuss the analysis performed in the topics 5.7.1, 5.7.2 and 5.8.

3.5 Summary

In this chapter, a detailed presentation of the three finite positional elements implemented in the code developed in this work was carried out. The kinematics and the constitutive law of all elements were discussed. The expressions linked to the internal force vector and the Hessian matrix of the elements were obtained. The coupling technique between the two-dimensional

(matrix) and bar/frame (fiber) elements was exposed. The additive composition of the total mechanical energy of the elements and posterior variation of this resultant energy in relation to positions of the matrix elements defines the procedure to perform the coupling technique. The embedded theory defines the strategy adopted. One of the contributions of the present work is presented with the coupling of the frame elements into the matrix elements. The strategy proposed considers the angular rotation of the frame elements as an additional variable of the system. As a result of this, it was showed that the number of equilibrium equations of the system increases proportionally. At last, a flowchart that describes the structural organization of the computational code developed with the formulation presented in this chapter was illustrated.

Regarding the presentation of such subject in this chapter it is possible to remark that:

a) Differently of the traditional finite elements, which is based in displacement, in the positional approach, the internal force vector, as well as the Hessian matrix, are directly obtained from global coordinates. Such characteristic avoids the necessity of the assemblage of matrix rotation for each element.
b) Another advantage of the positional approach can be performed analyzing the expressions which involve the bidimensional elements, such as the two-dimensional and the frame. As showed the expressions consist of operations between matrixes at the same size (2x2). This characteristic facilitate the implementation of such elements.
c) The strategy employed for the application of the embedded theory between elements seems to be a practical and direct procedure that can be applied to the coupling between other finite elements.

4 PHYSICAL NONLINEARITIES

The physical nonlinear theory involves the study of the material behavior beyond the idealized elastic-linear regime. Such physical behavior is related to the stress-strain relationship that the material describes beyond a certain loading level. So, depending on the intensity of the force applied, permanent strains can arise with different characteristics. Additionally, the materials can present degradations associated with diffuses microcracks. The coalescence process between these microcracks results in major cracks. These major cracks can appear locally or spread over all material and can compromise the mechanical stability of the material. All such above process can be described with mathematical models in accordance with the continuum mechanics. At this sense, the one-dimensional and plane-stress plasticity formulations are summarized. The so-called Damage model with the smeared crack approach and the two-dimensional damage model are also discussed. All models are used in the analysis of this work.

4.1 Plasticity

Two elastoplastic models were implemented in the code developed in the present work. One is the one-dimensional plasticity model that was implemented to be used with the bar finite element formulation and another it is the plane stress plasticity which is applied to the frame finite element. The aims to implements such models consist in to approximate the real physical behavior of the steel reinforcement bars in the structures analyzed in this thesis. Both models are described according to the irreversible process of thermodynamics.

4.1.1 Equilibrium equation

Eq. (2.1) showed the total potential energy written to obtain the static elastic equilibrium. Such expression was defined as a function of the potential energy of elastic strain

and the potential energy of external forces. In this context, all energy introduced in the system from the parcel associated with the external forces by a loading process is entirely stored by the elastic strain energy parcel. On the other hand, the elastic strain energy accumulated can be fully recovered since the system is under unloading process.

Differently from the elastic process, the plasticity is thermodynamically associated with irreversible deformation process (Lemaitre and Chaboche 2000). Thus, the energy introduced in a system by a set of external forces applied over a body is not fully recovered for an unloading case. At this sense, a parcel of the energy remains on the body. So to characterize such phenomenon, the total potential energy previously written must be changed. To do so, in place of elastic density energy, the Helmholtz/Density free energy potential can be adopted, once it is a scalar value function, objective and twice differentiable (Holzapfel 2000). Such potential depends on state variables called observable variables, symbolized by total strain (E), and internal variables represented by elastic (E^e) and plastic (E^P) strains. So assuming the symbol (ψ) to the density free energy potential, the Eq. (2.1) can be rewritten to characterize the elastoplastic process as:

$$\Pi(Y) = \int_{V_0} \psi(E, p)\, dV_0 + \Omega(Y) \tag{4.1}$$

where p is a kinematic variable responsible to store the memory history of the material, indispensable to describe the irreversible phenomenon.

The Principle of Stationary Total Potential Energy is applied to obtain the equilibrium position:

$$\delta\Pi = \int_{V_0} \frac{\partial \psi}{\partial E} \frac{\partial E}{\partial Y} dV_0 \delta Y + F \delta Y = 0 \tag{4.2}$$

The parameter p does not increase the number of degree of freedom of the system and it is calculated intrinsically from relation between E and S . The constitutive relationship and the total, elastic and plastic strains correlation determine the elastoplastic model.

Following the uniaxial and plane stress elastoplastic models, used to the bar and frame finite elements, are discussed.

In the present work although the formulation is suitable to large displacement all analysis performed involves small strain. In this case the linear relation between the Green strain and the second Piola-Kirchhoff stress can be adopted in place of the Cauchy stress.

4.1.2 A one-dimensional model of the plasticity

The four assumptions considered to develop the elastoplastic model are: (a) partition hypothesis an additive decomposition of the strain; (b) elastic limit stress; (c) a flow rule to strain plastic; and (d) a flow rule to hardening tensor.

(a) Partition hypothesis

The separation of the elastic and plastic effects for an elastoplastic model composition is suitable according to the physics of the phenomenon observed in experiments. For this work, the additive decomposition of the strain is assumed, as follow:

$$E = E^e + E^p \quad \text{or} \quad E^e = E - E^p \tag{4.3}$$

The elastic (E^e) and plastic (E^p) strains are the internal variables assumed for the elastoplastic process (Lemaitre and Chaboche 2000). The plastic strain is responsible for characterizing the irreversible process of the plasticity.

The results of this decomposition allow writing the free energy in two parcels, elastic and plastic, as follow:

$$\psi = \psi\left(E, p\right) = \psi_e\left(E^e\right) + \psi_p\left(E^p, p\right) = \psi_e\left(E - E^p\right) + \psi_p\left(E^p, p\right) \tag{4.4}$$

The elastic energy (ψ_e) represents the conservative energy of the system, i.e. under an unloading process such energy is recovered. The plastic energy (ψ_p) is associated with irreversible phenomena by internal variable parameter (p) and the plastic strain (E^p).

The free specific potential energy is therefore written as:

$$\psi = \frac{1}{2} E^e \mathbb{E} E^e + \frac{1}{2} php \tag{4.5}$$

where h is a scalar with hardening parameters.

The static variable i.e. the Second Piola-Kirchhoff (S) and the associated thermodynamic force (R) are written as:

$$S = \frac{\partial \psi}{\partial E} = \mathbb{E} E^e = \mathbb{E}\left(E - E^p\right) \tag{4.6}$$

$$R = \frac{\partial \psi}{\partial p} = hp \tag{4.7}$$

(b) Elastic limit

The elastic limit in the elastoplastic models is associated with the yield stress, also called as yield criterion, yielding condition or plasticity criteria, which determines the threshold between the reversible and irreversible phenomenon. In other words, geometrically a plasticity criterion defines a boundary, which identifies a limit elastic or plastic of the material. The differences criteria of this loading surface distinguish the innumerous theories of plasticity developed over the years, as can be reviewed in Simo and Hughes (1998) and de Souza Neto et al. (2008). Mathematically, the yield criteria (f) assume values less or equal to zero. When the value is zero it assumes the domain of problem is plastic, otherwise, it is an elastic domain, i.e:

$f < 0$ (elastic domain) (4.8)

$f = 0$ (plastic domain) (4.9)

Thermodynamically, this yield condition is expressible as a function of the components of the stresses and depends on the hardening state through the internal variables. The internal variables is related with the thermodynamic forces, previously presented as (R) Eq. (4.7).

(c) An hardening flow rule

The hardening can be physically associated with the disagreement accumulation of the crystallographic structures of the material (Dunne and Petrinic 2005). In the plastic models there are two classical formulations to describe the hardening and they are defined as isotropic and kinematic. For the isotropic hardening law once the yielding condition is violated its expansion in the stress spaces occurs symmetrically, Figure 4.1a. The kinematic hardening describes a configuration that the elastic limit is always represented by the same size but the position of its center is changed in accordance with the plastic strain evolution Figure 4.1b.

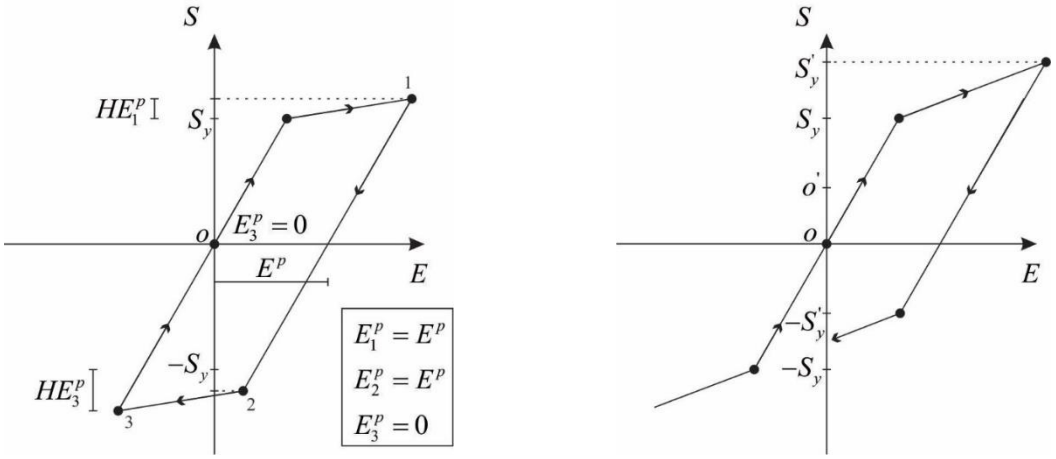

(a) (b)

Figure 4.1 – a) Linear Isotropic Model, and b) Kinematic model.

For the present work, the isotropic model is considered. So, according to Figure 4.1a the stress S_y is the initial size of the yielding condition and once violated its expansion takes a new value equal ($\sigma_y + Hp_1$). For this case, the plastic strain associated to the plasticity criteria expansion is $E_1^p = E^p$. Thus according to the isotropic model for state stress equilibrated in the point 2 the same plastic strain of the point 1 is presented, i.e $E_2^p = E^p$. And in the case where the plasticity criteria is again increased for the point 3 with its new value ($\sigma_y + Hp_3$) it is verified that the plastic strain is null although the value of hardening is changed.

In this terms and taking into account the one-dimensional case the yield criteria defined in accordance with the uniaxial stress space is mathematically written as:

$$f = f(S,R) = |S| - (S_y + R) \tag{4.10}$$

where S_y is the initial size of the yielding condition and once violated its expansion takes a new value equal ($S_y + R$).

(d) An flow rule to strain plastic

The flow rule of plastic strain describes the changing configuration of the yielding surface with the increase of plastic strain and for one-dimension plasticity can be expressed as:

$$dE^p = d\lambda sign(S) \tag{4.11}$$

The Eq. (4.11) shows that the plastic strain has the same signal of the stress. The scalar plastic multiplier $d\lambda$ with the yield condition must comply with the Khun-Tucker complementary conditions and the consistency conditions formally defined as:

$$d\lambda f = 0 \text{ with } d\lambda \geq 0 \text{ and } f \leq 0 \tag{4.12}$$

$$d\lambda df = 0 \quad (\text{with} \quad df \leq 0) \tag{4.13}$$

The both previously conditions assure that the increase of plastic strain occurs only when the plastic criteria is violated and for the new state stress equilibrated the yielding condition is always satisfied. These conditions will be opportunely used to develop the tangent elastoplastic modulus.

The Table 6 summarizes all equations previously discussed for one-dimensional plasticity model implemented in the curved finite element bar of the code.

Table 6 – One-dimensional isotropic plasticity.

i. Additive decomposition
$E = E^e + E^p \Rightarrow E^e = E - E^p$
ii. Elastic stress-strain relantioship
$S = \mathbb{E} E^e \Rightarrow S = \mathbb{E}\left(E - E^p\right)$
iii. Yielding condition
$f(S, p) = \lvert S \rvert - \left(S_y - Hp\right)$
iv. Flow rule and isotropic hardening law
$dE^p = d\lambda sign(\mathrm{S})$ and $dp = d\lambda$
v. Kuhn-Tucker complementarity conditions
$d\lambda \geq 0,\ f(S, p) \leq 0$ and $d\lambda f(S, p) = 0$
vi. Consistency condition
$d\lambda df(S, p) = 0 \quad (\text{If} \quad f(S, p) = 0)$

Newton-Raphson procedure

The Eq. (4.2) as already discussed is nonlinear and can be solved with the Newton Raphson procedure with similar strategy described in the torpic 2.1. The equilibrium of Eq. (4.2) is rewritten as follows:

$$g_j = \frac{\partial \Pi}{\partial Y_j} = \frac{\partial \psi}{\partial Y_j} - F_j = F_j^{\text{int}} - F_j = 0 \tag{4.14}$$

The equilibrium of the system is fulfilled with the equality between the internal and external force. For the internal force calculation it is necessary the determination of the Piola-Kirchhoff stress. The level of this stress must attend the elastoplastic model represented by the yield criteria and the evolution of the plastic strain. So to comply with these conditions, it is required an internal procedure to evaluate if the stresses computed are correct.

In this work, the Return-mapping algorithm was implemented and its execution is based in the elastic or trial prevision and the elastoplastic correction for the case that the criterion is not satisfied. This algorithm is summarized at the end of this topic.

Following the Taylor's series expansion truncated in the first order derivative term of Eq. (4.14) results in:

$$g_j\left(Y\right) = g_j\left(Y^0\right) + \left.\frac{\partial g_i}{\partial Y_k}\right|_{\left(Y^0\right)} \Delta Y_k = 0 \tag{4.15}$$

The derivative of the residual (g) can also be obtained from the second derivative of the free energy potential as follow expressed:

$$\int_{V_0} \frac{\partial^2 \psi}{\partial Y \partial Y} dV_0 = \int_{V_0} \frac{\partial S\left(E, E^p\right)}{\partial E} \frac{\partial E}{\partial Y} \frac{\partial E}{\partial Y} + S\left(E, E^p\right) \frac{\partial^2 E}{\partial Y \partial Y} dV_0 \tag{4.16}$$

The terms $\partial E/\partial Y$ and $\partial^2 E/\partial Y \partial Y$ are similar for the elasticity and plasticity cases. The Piola-Kirchhoff stress ($S\left(E, E^p\right)$) depends on total and plastic strain as already defined with Eq. (4.6) and outcome from the return-mapping algorithm. The term ($\partial S\left(E, E^p\right)/\partial E$) can change during the elastoplastic analysis. If the analysis corresponds to the equilibrium under elastic domain this relation is the elastic modulus; however, for the analysis under a plastic domain, such term is modified. Due to the importance that this term presents in the convergence

of the Newton Raphson method under plastic regime, its nomenclature is defined as the tangent elastoplastic consistent modulus. The next item discusses and formalizes this expression for both elastic/plastic cases.

The tangent elastoplastic consistent modulus

The tangent elastoplastic consistent modulus can be obtained from the linearization of the yielding plasticity function in the level of the stress associated. The linearization of the yielding plasticity function as follow defined as:

$$df = \frac{df}{dS} dS + \frac{df}{dp} dp \tag{4.17}$$

where,

$$\frac{df}{dS} = sign(S) \tag{4.18}$$

$$dS = \mathbb{E}\left(dE - dE^{p}\right) \tag{4.19}$$

$$\frac{df}{dp} = H \tag{4.20}$$

$$dp = d\lambda sign(\mathrm{S}) \tag{4.21}$$

$$d\bar{p}^{p} = d\lambda \tag{4.22}$$

Substituting the Eqs. (4.18), (4.19), (4.20) into (4.17) and after the Eqs. (4.21) and (4.22) is possible to define:

$$df = sign(S)\mathbb{E}dE - \left(\mathbb{E} + H\right)d\lambda \tag{4.23}$$

Note that $df > 0$ cannot hold, thus with the consistency condition $d\lambda$ is nonzero only with:

$$df = 0 \Rightarrow d\lambda = \frac{sign(S)\mathbb{E}dE}{\left(\mathbb{E} + H\right)} \tag{4.24}$$

With the expression written in (4.24) the constitutive relationship (4.19) can be rewritten and the analysis elastic or plastic regime is defined as:

$$dS = \begin{cases} \mathbb{E}\, dE & \text{if } d\lambda = 0 \\ \dfrac{\mathbb{E}\, H}{\left(\mathbb{E} + H\right)} dE & \text{if } d\lambda > 0 \end{cases} \tag{4.25}$$

Thus, in elastic regime $d\lambda = 0$ and the constitutive relationship assumed is calculated with the elastic modulus. Otherwise, in plastic regime $d\lambda > 0$ and the constitutive relationship can be determined with the tangent elastoplastic modulus. Figure 4.2a and b shows the representation of the elastoplastic tangent modulus and the plastic modulus.

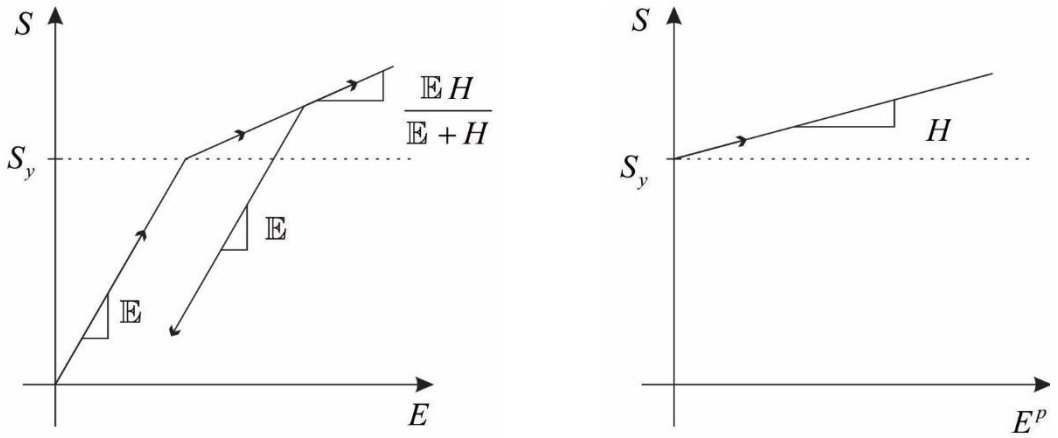

(a) (b)

Figure 4.2 – (a) Tangent modulus and (b) the plastic modulus.

Evolution calculation

Table 7 summarizes the evolution calculation assuming a certain interval $[t_n, t_{n+1}]$ for which n and $n+1$ are the previous equilibrated and the current steps, respectively. Such an algorithm is defined as the return-mapping strategy that consists on the trial/elastic prevision and the elastoplastic correction for the case that the criterion is not fulfilled.

Table 7 – Evolution calculation (return-mapping)

i. Initialization

$${}^{trial}E_{n+1},\ {}^{trial}E^{p}_{n+1} = E^{p}_{n},\ {}^{trial}\lambda_{n+1} = \lambda_{n},\ {}^{trial}R_{n+1} = R_{n}$$

ii. Stress level

$$S_{n+1} = \mathbb{E}\left({}^{trial}E_{n+1} - {}^{trial}E^{p}_{n} - \Delta E^{p}\right) = {}^{trial}S_{n+1} - \mathbb{E}\Delta E^{p}$$

iii. Yielding condition verification

$${}^{trial}f_{n+1} = |S_{n+1}| - \left(S_{y} + {}^{trial}R\right)$$

If ${}^{trial}f_{n+1} \leq 0$ the step is elastic and none plastic correction need to be done,

Else ${}^{trial}f_{n+1} > 0$ the step is elastoplastic go to iv.

iv. Correction

$$\Delta\lambda = \frac{{}^{trial}f_{n+1}}{\mathbb{E} + H} > 0$$

$$S_{n+1} = {}^{trial}S_{n+1} - \Delta\lambda\mathbb{E}sign({}^{trial}S_{n+1})$$

$$E^{p}_{n+1} = E^{p}_{n} + \Delta\lambda sign\left({}^{trial}S_{n+1}\right)$$

$$p^{p}_{n+1} = p^{p}_{n} + \Delta\lambda$$

$$\frac{dS}{dE} = \frac{\mathbb{E}H}{\left(\mathbb{E} + H\right)}$$

End of the return-mapping algorithm

Initializing the procedure the input parameters are updated from the previous step solved, conforming is showed in (i). The input parameters correspond to the total trial strain (${}^{trial}E_{n+1}$), that is calculated with Green Strain Eq. (3.25), the level of plastic strain (${}^{trial}E^{p}_{n+1}$) as well the hardening (${}^{trial}\lambda_{n+1}$) and the thermodynamic forces (${}^{trial}R_{n+1}$). The stress level calculation is directly obtained from the trial stress minus the accumulated plastic stress, written in (ii). If the stress level does not satisfy the yielding condition, see (iii), the analysis is elastic and thus any correction must be performed. Otherwise, in the case where this stress level

violates the yielding condition a correction need to be done. Thus, the incremental of plastic multiplier ($\Delta\lambda$) is computed from the elastic and plastic modulus, ($\mathbb{E}, H$) respectively, and unbalanced force represented by (${}^{trial}f$). Next, the stress is updated in accordance with the evolution law of the plastic strain. Following, the actualization of the plastic strain and the hardening parameter are determined. The tangent consistent elastoplastic modulus is also computed.

The validation and discussion of this one-dimensional plasticity theory applied in the bar finite element are addressed in the examples 5.3.1, 5.3.2 and 5.3.3 in chapter 5. Other examples such as 5.7.1, 5.7.2 and 5.8 also use this theory to perform the analysis.

4.1.3 Plane stress plasticity

The adoption of plasticity in two-dimensional problems in the frame finite element previously discussed is justified because although this element is used to analyse uniaxial structures its formulation is developed as a bi-dimensional problem (plane-stress and plane-strain).

The plasticity in two-dimensional problems can be treated by two different approaches: plane-strain state or plane-stress state. For the first case, the general three-dimensional plasticity formulations can be adopted with the strain out-of-plane constrained. However, for the second one, only constrained the stress out-of-plane, it verifies that once the plastic regime is started the plane-stress condition is violated and therefore such procedure is not suitable. The violation of the plane stress condition occurs because adopting the return-mapping algorithm the stress components initially assumed constrained must be zero for all analysis, which does not happen.

The constitutive relationship of the frame finite element assumes Poisson null, which implies similarities between the plane-strain and plane-stress states formulations. For this work, the plane-stress plasticity was adopted. Thus, taking into account such consideration according to Souza Neto et al. (2008) three main general approaches can be adopted to implement the elastoplastic algorithms:

a) The direct inclusion of the plane-stress constraint into the three-dimensional elastic predictor and plastic corrector algorithm equations applied at the Gauss point level. This approach can also be implemented by means of a nested Newton return-mapping iteration for plane stress enforcement.

b) The use of the standard three-dimensional return mapping at the Gauss point level with the plane-stress condition added as a structural constraint at the global structural level.

c) The use of plane stress-projected constitutive equations where, similarly to the procedure of item (a), the plane-stress constraint is enforced at the Gauss point level.

The latter algorithm topic (c) was implemented and used to analyze the structures reported in this thesis. This choice is justified because still according to Souza Neto et al. (2008) such procedure is more efficient when compared with the two others approaches since the set of involved equations is directly defined in-plane stress components. Therefore all expressions are reduced. Simo and Taylor (1985) and Jetteur (1986) were the precusores to development and application of such algorithm in the computational environment.

Once the formulation involves only in-plane variables the Voigt notion is used in order to simplify the comprehension of the procedure. The total, elastic and plastic strain tensors as well the stress and deviatoric stress tensors are respectively written as:

$$\begin{aligned} &\mathbf{E} = \left\{E_{11}, E_{22}, 2E_{12}\right\}^T, \mathbf{E^e} = \left\{E^e_{11}, E^e_{22}, 2E^e_{12}\right\}^T \text{ and } \mathbf{E^p} = \left\{E^p_{11}, E^p_{22}, 2E^p_{12}\right\}^T \\ &\mathbf{S} = \left\{S_{11}, S_{22}, S_{12}\right\}^T \text{ and } \bar{\mathbf{S}} = \left\{\overline{S_{11}}, \overline{S_{22}}, \overline{S_{12}}\right\}^T \end{aligned} \tag{4.26}$$

The partition hypothesis with the additive decomposition of the strain is therefore considered as follow:

$$\mathbf{E} = \mathbf{E}^e + \mathbf{E}^p \;\Rightarrow\; \mathbf{E}^e = \mathbf{E} - \mathbf{E}^p \tag{4.27}$$

The Helmholtz free energy potential is also used to describe the irreversible phenomenon:

$$\psi = \frac{1}{2}\mathbf{E}^{eT}\,\mathfrak{C}\,\mathbf{E}^e + \frac{1}{2}\bar{E}^p H \bar{E}^p \tag{4.28}$$

where the $\mathfrak{C}$ is the constitutive tensor of the plane-stress case written in voigt notation and $\bar{E}^p$ is a kinematic variable responsible to store the memory history of the material, indispensable to describe the irreversible phenomenon.

The Piola-Kircchhoff stress and the associated scalar thermodynamic forces is defined as:

$$\mathbf{S} = \frac{\partial \psi}{\partial \mathbf{E}^e} = \mathfrak{C}\,\mathbf{E}^e = \mathfrak{C}\left(\mathbf{E}\text{-}\mathbf{E}^p\right) \tag{4.29}$$

$$R = \frac{\partial \psi}{\partial \overline{E}^p} = H\overline{E}^p \tag{4.30}$$

(a) Elastic limit

Differently from the uniaxial force that the elastic limit is defined with the yield stress this threshold for bi-dimensional problems is associated with the yield surface. So, assuming the Von Mises criterion the plasticity surface can be generically written as:

$$\Phi = \sqrt{3J_2} - \Gamma(\overline{E}^p) \tag{4.31}$$

with the second invariant (J_2) defined as $J_2 = \left(\frac{1}{2}S:S\right)^{1/2}$ and $\Gamma(\overline{E}^p)$ being the function that determines the limit of the Von Mises criterion.

The Eq. (4.31) corresponds geometrically to a cylinder in the three-dimensional principal stress space with its axis aligned with the line $S_1 = S_2 = S_3$. The Von Mises criterion is based on the octahedral stress, and the hydrostatic stress does not affect the plastic behavior. For bi-dimensional problems S_3 is null, and therefore the Von Mises criterion is geometrically defined by an elliptical shape

In Voigt notation the Von Mises criterion is directly written in plane-stress space as defined by Simo and Hughes (1998) as:

$$\Phi = \sqrt{\frac{3}{2}\mathbf{S}^T\,\mathbf{PS}} - \Gamma(\overline{E}^p) \tag{4.32}$$

where $\mathbf{P}$ is a constant matrix used to perform the calculation of the deviatory stress ($\mathbf{S}$) from the in-plane stress vector ($\mathbf{S}$) defined as:

$$\mathbf{P} = \frac{1}{3}\begin{bmatrix} 2 & -1 & 0 \\ -1 & 2 & 0 \\ 0 & 0 & 6 \end{bmatrix} \tag{4.33}$$

$$\overline{\mathbf{S}} = \mathbf{PS} \tag{4.34}$$

(b) The hardening flow rule

According to the hardening flow rule adopted two types of plasticity models are classified in the literature, called associative and nonassociative ((Simo and Hughes 1998), (Dunne and Petrinic 2005) and (Lubliner 2006)). To the associated plasticity, the evolution and direction of the plastic strain and the internal variables defined with the equipotential surface are linked to the yield criteria. In other words, the equipotential surface and the yield criteria have the same mathematical dinitition. For this postulation, the evolution of the plastic strain occurs normal to the yield criteria. The classical literature defines this behaviour as the normality hypothesis of plasticty, Figure 4.3.

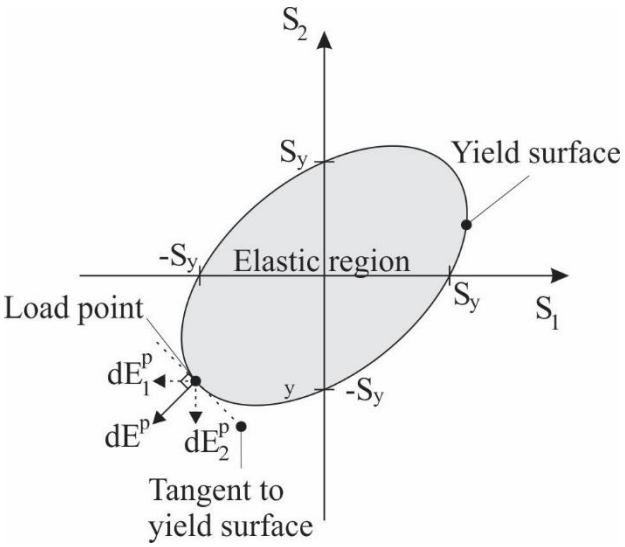

Figure 4.3 – The Von Mises Yield surface for condition of plane stresses. Direction normal to the tangent the surface.

Adopting the associative condition the hardening law explicitly written for the plane-stress space is therefore defined by:

$$d\bar{E}^{p} = d\lambda \frac{\partial \Phi}{\partial \mathbf{S}} = d\lambda \sqrt{\frac{3}{2}} \frac{\mathbf{PS}}{\sqrt{\mathbf{S}^{\mathrm{T}}\mathbf{PS}}} \tag{4.35}$$

$$d\bar{E}^{p} = d\lambda \tag{4.36}$$

Table 8 summarizes the previously expressions used to define the isotropic plane stress-projected Von Mises model.

Table 8 – Isotropic plane stress-projected plasticity.

i. Additive decomposition

$$\mathbf{E}^e = \mathbf{E} - \mathbf{E}^p$$

ii. Elastic stress-strain relantioship

$$\mathbf{S} = \mathfrak{C}\,\mathbf{E}^e \Rightarrow \mathbf{S} = \mathfrak{C}\left(\mathbf{E}^f - \mathbf{E}^{fp}\right)$$

iii. Yielding condition

$$\Phi = \sqrt{\frac{3}{2}\mathbf{S}^T\,\mathbf{PS}} - \Gamma(\bar{E}^p)$$

iv. Flow rule and isotropic hardening law

$$d\bar{E}^p = d\lambda\frac{\partial\Phi}{\partial\mathbf{S}} = d\lambda\sqrt{\frac{3}{2}}\frac{\mathbf{PS}}{\sqrt{\mathbf{S}^{\mathrm{T}}\mathbf{PS}}}$$

$$d\bar{E}^p = d\lambda$$

v. Kuhn-Tucker complementarity conditions

$d\lambda \geq 0$, $\Phi \leq 0$ and $d\lambda\Phi = 0$

vi. Consistency condition

To simplify the expression Simo and Hughes (1998) and de Souza Neto et al. (2008) propose the equations of this model with the square form of the Von Mises criterion, written in Eq. (4.32). In this context, the Von Mises criteria and the hardening evolution law are defined by:

$$\Phi = \frac{1}{2}\mathbf{S}^{\mathrm{T}}\mathbf{PS} - \frac{1}{3}\Gamma^2(\bar{E}^p) \tag{4.37}$$

$$d\,\mathbf{E}^p = d\lambda\,\mathbf{PS} \tag{4.38}$$

$$d\bar{E}^p = d\lambda\sqrt{\frac{2}{3}\mathbf{S}^{\mathrm{T}}\,\mathbf{PS}} \tag{4.39}$$

The evolution calculation

The evolution of the calculation is analogous to the previous procedure describes for the one-dimensional plasticity. The thermodynamic equilibrium is reached with the minimization of the total potential energy, and the Newton Raphson procedure is used to solve the set of nonlinear equations. The Green strain and its conjugate energetic the Piola-Kirchhoff stress

obtained for each integration point are necessary to the constructions of the Hessian and global internal force of the structure. The elastoplastic parameters, as well as the evaluation of the elastoplastic criteria, are performed in an implicit way for each integration point in accordance with the Return-mapping algorithm. The tangent elastoplastic consistent modulus is also required to improve the convergence of the Newton Raphson.

The elastic preditor and the Return-mapping algorithm

The plane stress-projected Return-mapping algorithm involves the resolution of the following set of equations:

$$\mathbf{E}^{e}_{n+1} = \mathbf{E}^{e^{trial}}_{n+1} - \Delta\lambda \mathbf{P}\mathbf{S}_{n+1} \tag{4.40}$$

$$\overline{E}^{p}_{n+1} = \overline{E}^{p}_{n} - \Delta\lambda \sqrt{\frac{2}{3}\left(\mathbf{S}_{n+1}\right)^{T} \mathbf{P}\mathbf{S}_{n+1}} \tag{4.41}$$

$$\frac{1}{2}\left(\mathbf{S}_{n+1}\right)^{T} \mathbf{P}\mathbf{S}_{n+1} - \frac{1}{3}\left(S_y + H\overline{E}^{p}_{n+1}\right)^{2} = 0 \tag{4.42}$$

The Eqs. (4.40), (4.41) and (4.42) can be reduced to an expression with only one variable, the incremental plastic multiplier ($\Delta\lambda$). Before to written such equation firstly consider the inverse of elastic law, the Eq. (4.40), and the substitution of Eq. (4.41) into (4.42) as respectively follow defined:

$$\mathbf{S}_{n+1} = \left[\mathfrak{C}^{-1} + \Delta\lambda \mathbf{P}\right]^{-1} \mathfrak{C}^{-1} \mathbf{S}^{trial}_{n+1} \tag{4.43}$$

$$\frac{1}{2}\mathbf{S}^{T}_{n+1}\mathbf{P}\mathbf{S}_{n+1} - \frac{1}{3}\left[S_y + H\left(\overline{E}^{p}_{n} + \Delta\lambda\sqrt{\frac{2}{3}\left(\mathbf{S}_{n+1}\right)^{T}\mathbf{P}\mathbf{S}_{n+1}}\right)\right]^{2} = 0 \tag{4.44}$$

Following the expression with only the plastic multiplier ($\Delta\lambda$) as variable can be obtained from inserterting Eq. (4.43) into (4.44):

$$\tilde{\Phi}\left(\Delta\lambda\right) = \frac{1}{2}\xi\left(\Delta\lambda\right) - \frac{1}{3}\left[S_y + H\left(\overline{E}^{p}_{n} + \Delta\lambda\sqrt{\frac{2}{3}\xi\left(\Delta\lambda\right)}\right)\right]^{2} = 0 \tag{4.45}$$

where the parameter $\xi\left(\Delta\lambda\right)$ is expressed as:

$$\xi\left(\Delta\lambda\right)=\left(\mathbf{S}_{n+1}^{trial}\right)^{T}\mathbf{A}^{T}\left(\Delta\lambda\right)\mathbf{P}\mathbf{A}\left(\Delta\lambda\right)\mathbf{S}_{n+1}^{trial} \tag{4.46}$$

$$\mathbf{A}\left(\Delta\lambda\right)=\left[\mathfrak{C}^{-1}+\Delta\lambda\mathbf{P}\right]^{-1}\mathfrak{C}^{-1} \tag{4.47}$$

Table 9 summarizes for a certain interval $[t_n,t_{n+1}]$ for which n and $n+1$ are the previous equilibrated and the current steps, respectively, the background of the elastic predictor and the return-mapping algorithm.

Table 9 – Background of the elastic predictor and the return-mappig algorithm.

i. Initialization

$\mathbf{E}_{n+1}^{trial}$, $\overline{E}_{n+1}^{p\ trial}=\overline{E}_{n}^{p}$

ii. Stress level

$\mathbf{S}_{n+1}=\mathfrak{C}\left(\mathbf{E}_{n+1}^{trial}-\mathbf{E}_{n}^{p\ \mathrm{trial}}-\Delta\mathbf{E}^{p}\right)=\mathbf{S}_{n+1}^{trial}-\mathfrak{C}\Delta\mathbf{E}^{p}$

iii. Check the Yielding condition verification ($^{trial}\Phi_{n+1}$):

$a_1=\left(S_{11}^{trial}+S_{22}^{trial}\right)^2;a_2=\left(S_{22}^{trial}-S_{11}^{trial}\right)^2;a_3=\left(S_{12}^{trial}\right)^2$

$\xi^{trial}=\frac{1}{2}a_1+\frac{1}{2}a_2+2a_3$

$\Phi^{trial}=\frac{1}{2}\xi^{trial}-\frac{1}{3}\left(S_y+H\overline{E}_{n+1}^{p\ \mathrm{trial}}\right)^2$

Obtained from Eqs. (4.45), (4.46) and (4.47).

If $^{trial}\Phi_{n+1}\leq 0$ the step is elastic and none plastic correction need to be done,

Else $^{trial}\Phi_{n+1}>0$ the step is elastoplastic go to iv.

iv. Return-mapping algorithm go to Table 10 to enforce:

$\overline{\Phi}\left(\Delta\lambda\right)=0$

with the determination of $\Delta\lambda$ the state variables are updated

$\mathbf{S}_{n+1}=\mathbf{A}\left(\Delta\lambda\right)\mathbf{S}_{n+1}^{trial}$

$\overline{E}_{n+1}^{p}=\overline{E}_{n}^{p}+\Delta\lambda\sqrt{\frac{2}{3}\xi\left(\Delta\lambda\right)}$

End of the return-mapping algorithm

Newton-Raphson algorithm to determine $\Delta\lambda$.

From Eq. (4.45) verifies a nonlinear behavior in the solution of the multiplier plastic increment ($\Delta\lambda$) once it is within of the squared parcel. So differently from one-dimensional plasticity formulation, a closed expression to $\Delta\lambda$ is not possible. The solution is performed with a Newton Raphson procedure, as follow described.

The Taylor series applied at Eq. (4.51) truncated on the linear term results in the follow expression:

$$\tilde{\Phi}\left(\Delta\lambda\right)+\left.\frac{d\tilde{\Phi}}{d\Delta\lambda}\right|_{\Delta\lambda}\delta\Delta\lambda=0 \quad \Rightarrow \quad \delta\Delta\lambda=-\frac{\tilde{\Phi}\left(\Delta\lambda\right)}{\tilde{\Phi}'\left(\Delta\lambda\right)} \tag{4.48}$$

The value $\Delta\lambda$ is therefore determined from the accumulation of $\delta\Delta\lambda$ inside of an iteration procedure. From expression (4.48) it observes that the differentiation in $\Delta\lambda$ of Eq. (4.45) must be perfomed. However such operation can result in a robustness algorithm, as described in de Souza Neto et al. (2008). The equation (4.45) is written in function of the scalar ξ which depends on the matrix $\mathbf{A}$ and finally $\Delta\lambda$. Remembering that $\mathbf{A}$ is associated with matrix operations such as sum, multiplication and even inverse. Therefore to circumvent such robustness Simo and Hughes (1998) propose the diagonalization of $\mathbf{P}$ and $\boldsymbol{\mathcal{C}}$ once these matrixes share the same eigenvectors. Therefore, the follow matrix $\mathbf{Q}$ is defined to excute such transformation:

$$\mathbf{Q}=\begin{bmatrix} \frac{1}{\sqrt{2}} & \frac{1}{\sqrt{2}} & 0 \\ -\frac{1}{\sqrt{2}} & \frac{1}{\sqrt{2}} & 0 \\ 0 & 0 & 1 \end{bmatrix} \tag{4.49}$$

Therefore, the follow orthogonal transformation can be done as:

$$\begin{aligned} \mathbf{P}^{*} &= \mathbf{Q}\mathbf{P}\mathbf{Q}^{T} \\ \boldsymbol{\mathcal{C}}^{*} &= \mathbf{Q}\boldsymbol{\mathcal{C}}\mathbf{Q}^{T} \end{aligned} \tag{4.50}$$

$$\mathbf{A}^{*}\left(\Delta\lambda\right)=\left[\mathfrak{C}^{-1^{*}}+\Delta\lambda\mathbf{P}^{*}\right]^{-1}\mathfrak{C}^{-1^{*}}$$

$$\mathbf{S}_{n+1}^{trial*}=\mathbf{Q}\mathbf{S}_{n+1}^{trial}$$

Thus, Eq. (4.46) is simplified and written as:

$$\begin{aligned}\xi\left(\Delta\lambda\right)&=\left(\mathbf{S}_{n+1}^{trial}\right)^{T}\mathbf{A}^{T}\left(\Delta\lambda\right)\mathbf{P}\mathbf{A}\left(\Delta\lambda\right)\mathbf{S}_{n+1}^{trial}\\&=\left(\mathbf{S}_{n+1}^{trial*}\right)^{T}\left[\mathbf{A}^{*}\left(\Delta\lambda\right)\right]^{2}\mathbf{P}^{*}\mathbf{S}_{n+1}^{trial*}\\&=\frac{\left(S_{11}^{trial}+S_{22}^{trial}\right)^{2}}{6\left[1+\dfrac{\mathbb{E}\Delta\lambda}{3\left(1-\nu\right)}\right]^{2}}+\frac{\dfrac{1}{2}\left(S_{22}^{trial}-S_{11}^{trial}\right)^{2}+2\left(S_{12}^{trial}\right)^{2}}{\left(1+2G\Delta\lambda\right)^{2}}\end{aligned}\tag{4.51}$$

Table 10 summarize the steps and the expression previously defined to determine the plastic multiplier increment.

Table 10 - Newton Raphson algorithm for the determination of the plastic multiplier increment

i. Initial values

$$\tilde{\Phi}\left(\Delta\lambda\right)=\frac{1}{2}\xi\left(\Delta\lambda\right)-\frac{1}{3}\left[S_{y}+H\left(\overline{E}_{n}^{p}+\Delta\lambda\sqrt{\frac{2}{3}\xi\left(\Delta\lambda\right)}\right)\right]^{2};\ \Delta\lambda=0$$

ii. Newton Raphson iteration continues until reaches the convergence

$$H=\left.\frac{dS_{y}}{d\overline{E}^{p}}\right|_{\overline{E}^{p}+\Delta\lambda\sqrt{\frac{2}{3}\xi}}$$

$$\xi^{'}=-\frac{\left(S_{11}^{trial}+S_{22}^{trial}\right)^{2}}{9\left[1+\dfrac{\mathbb{E}\Delta\lambda}{3\left(1-\nu\right)}\right]^{3}}\frac{\mathbb{E}}{\left(1-\nu\right)}-2G\frac{\left(S_{22}^{trial}-S_{11}^{trial}\right)^{2}+4\left(S_{12}^{trial}\right)^{2}}{\left(1+2G\Delta\lambda\right)^{3}}$$

$$\overline{H}=2\left[S_{y}+H\left(\overline{E}_{n}^{p}+\Delta\lambda\sqrt{\frac{2}{3}\xi\left(\Delta\lambda\right)}\right)\right]H\sqrt{\frac{2}{3}}\left(\sqrt{\xi\left(\Delta\lambda\right)}+\frac{\Delta\lambda\xi^{'}\left(\Delta\lambda\right)}{2\sqrt{\xi\left(\Delta\lambda\right)}}\right)$$

$$\tilde{\Phi}' = \frac{1}{2}\xi'(\Delta\lambda) - \frac{1}{3}\overline{H}$$

$$\Delta\lambda = \Delta\lambda - \frac{\tilde{\Phi}}{\tilde{\Phi}'}$$

$$\xi = \frac{\left(S_{11}^{trial} + S_{22}^{trial}\right)^2}{6\left[1 + \frac{\mathbb{E}\Delta\lambda}{3(1-\nu)}\right]^2} + \frac{\frac{1}{2}\left(S_{22}^{trial} - S_{11}^{trial}\right)^2 + 2\left(S_{12}^{trial}\right)^2}{\left(1 + 2G\Delta\lambda\right)^2}$$

$$\tilde{\Phi} = \frac{1}{2}\xi - \frac{1}{3}\left[S_y + H\left(\overline{E}_n^p + \Delta\lambda\sqrt{\frac{2}{3}\xi}\right)\right]$$

iii. Check convergence

IF ($\tilde{\Phi} \leq$ error) EXIT

ELSE return to (ii) with $\Delta\lambda$ updated.

Souza neto et al. (2008) propose the follow simple notation to the matrix $\mathbf{A}(\Delta\lambda)$, defined in (4.47), with the orthogonal transformation performed with ($\mathbf{Q}$):

$$\mathbf{A}(\Delta\lambda) = \mathbf{Q}^T\mathbf{A}^*(\Delta\lambda)\mathbf{Q} \tag{4.52}$$

Opening the matrix $\mathbf{A}(\Delta\lambda)$ we have:

$$\mathbf{A}(\Delta\lambda) = \begin{bmatrix} \frac{1}{2}\left(A_{11}^* + A_{22}^*\right) & \frac{1}{2}\left(A_{11}^* - A_{22}^*\right) & 0 \\ \frac{1}{2}\left(A_{11}^* - A_{22}^*\right) & \frac{1}{2}\left(A_{11}^* + A_{22}^*\right) & 0 \\ 0 & 0 & A_{33}^* \end{bmatrix} \tag{4.53}$$

where the asterisk terms are defined as:

$$A_{11}^* = \frac{3(1-\nu)}{3(1-\nu) + \mathbb{E}\Delta\lambda},\ A_{22}^* = \frac{1}{1+2G\Delta\lambda} \text{ and } A_{33}^* = A_{22}^* \tag{4.54}$$

The tangent elastoplastic consistent modulus

The tangent elastoplastic modulus is defined as:

$$\mathfrak{C}^{ep} = \frac{d\mathbf{S}_{n+1}}{d\mathbf{E}_{n+1}} = \frac{d\mathbf{S}_{n+1}}{d\mathbf{E}_{n+1}^{trial}} \tag{4.55}$$

where the value of $\mathbf{S}_{n+1}$ is resulted from the Return-mapping algorithm.

To obtain the $\mathfrak{C}^{ep}$ it can be started differentiating Eq.(4.40) with the elastic law, which results on:

$$d\mathbf{S}_{n+1} = \mathfrak{E}\left[d\mathbf{E}_{n+1}^{trial} + d\Delta\lambda \mathbf{P}\mathbf{S}_{n+1} \right] \tag{4.56}$$

where $\mathfrak{E}$ is assumed as:

$$\mathfrak{E} = \left[\mathfrak{C}^{-1} + \Delta\lambda \mathbf{P} \right]^{-1} = \begin{bmatrix} \frac{1}{2}\left(E_{11}^{*} + E_{22}^{*}\right) & \frac{1}{2}\left(E_{11}^{*} - E_{22}^{*}\right) & 0 \\ \frac{1}{2}\left(E_{11}^{*} - E_{22}^{*}\right) & \frac{1}{2}\left(E_{11}^{*} + E_{22}^{*}\right) & 0 \\ 0 & 0 & E_{33}^{*} \end{bmatrix} \tag{4.57}$$

with

$$E_{11}^{*} = \frac{3\mathbb{E}}{3(1-\nu) + \mathbb{E}\Delta\gamma}, \quad E_{22}^{*} = \frac{3G}{1 + 2G\Delta\gamma}, \quad E_{33}^{*} = \frac{E_{22}^{*}}{2} \tag{4.58}$$

Following, plastic consistency yield equation (4.45) is differentiated:

$$\begin{aligned} d\tilde{\Phi} &= \frac{1}{2} d\xi - \frac{2}{3} S_y H \sqrt{\frac{2}{3}} \left(d\Delta\lambda \sqrt{\xi} + \frac{\Delta\lambda}{2\sqrt{\xi}} d\xi \right) \\ &= \frac{1}{2} d\xi - \frac{2}{3} H \left(\xi d\Delta\lambda + \frac{1}{2} \Delta\lambda d\xi \right) = 0 \end{aligned} \tag{4.59}$$

From the previously equation the follow expression can be written:

$$d\Delta\lambda = \frac{3}{4H\xi} \left(1 - \frac{2}{3} H\Delta\lambda \right) d\xi \tag{4.60}$$

Taking into account the elastic law and the definition of $\mathfrak{E}$ the scalar term ξ defined by Eq. (4.46) is rewritten as:

$$\xi = \left(\mathbf{E}_{n+1}^{trial}\right)^T \mathfrak{C}\mathbf{P}\mathfrak{C}\mathbf{E}_{n+1}^{trial} \tag{4.61}$$

The defferentiation of the above question gives:

$$\begin{aligned} d\xi &= 2\left(\mathbf{E}_{n+1}^{trial}\right)^T \mathfrak{C}\mathbf{P}\mathfrak{C}d\mathbf{E}_{n+1}^{trial} + 2\left(\mathbf{E}_{n+1}^{trial}\right)^T d\mathfrak{C}\mathbf{P}\mathfrak{C}\mathbf{E}_{n+1}^{trial} \\ &= 2\left(\mathbf{S}_{n+1}^T\mathbf{P}\mathfrak{C}d\mathbf{E}_{n+1}^{trial}\right)^T - \mathbf{S}_{n+1}^T\mathbf{P}\mathfrak{C}\mathbf{P}\mathbf{S}_{n+1}d\Delta\lambda \end{aligned} \tag{4.62}$$

Now, replacing (4.62) into (4.60) and next substituting in (4.56) gives:

$$d\mathbf{S}_{n+1} = \left[\mathfrak{C} - \alpha\left(\mathfrak{C}\mathbf{P}\mathbf{S}_{n+1}\right)\otimes\left(\mathfrak{C}\mathbf{P}\mathbf{S}_{n+1}\right)\right]d\mathbf{E}_{n+1}^{trial} \tag{4.63}$$

where the scalar α is taken as:

$$\alpha = \frac{1}{\mathbf{S}_{n+1}^T\mathbf{P}\mathfrak{C}\mathbf{P}\mathbf{S}_{n+1} + \dfrac{2\xi H}{3-2H\Delta\lambda}} \tag{4.64}$$

From Eq. (4.62) the elastoplastic tangent operator consistent for the Von Mises plane stress-projected Return-mapping is defined as:

$$\mathfrak{C}^{ep} = \mathfrak{C} - \alpha\left(\mathfrak{C}\mathbf{P}\mathbf{S}_{n+1}\right)\otimes\left(\mathfrak{C}\mathbf{P}\mathbf{S}_{n+1}\right) \tag{4.65}$$

Table 11 summarizes and describes the order of the expressions calculation previously developed.

Table 11 - Elastoplastic tangent operator

i. For a certain $\mathbf{S}_{n+1}$, $\bar{\mathbf{E}}_{n+1}^{p}$ and $\Delta\lambda$ (determined from the Return-mapping), it should be computed
$\xi = \mathbf{S}_{n+1}^T\mathbf{P}\mathbf{S}_{n+1}$
$H = \left.\dfrac{dS_y}{d\bar{\bar{\mathbf{E}}}^p}\right\|_{\bar{\bar{\mathbf{E}}}_{n+1}^{p}}$
$\mathfrak{C} = \left[\mathfrak{C}^{-1} + \Delta\lambda\mathbf{P}\right]^{-1}$

$$\mathbf{n} = \mathfrak{C}\mathbf{P}\mathbf{S}_{n+1}$$

$$\alpha = \frac{1}{\mathbf{S}_{n+1}^{T}\mathbf{P}\mathbf{n} + \dfrac{2\xi H}{3 - 2H\Delta\lambda}}$$

ii. The elastoplastic tangent modulus

$$\mathfrak{C}^{ep} = \mathfrak{C} - \alpha\mathbf{n}\otimes\mathbf{n}$$

The validation and discussion of this elastoplastic plane-stress model are performed with examples 5.4.1, 5.4.2 and 5.4.3 addressed in chapter 5. The cases 5.5.1and 5.5.2 certifies the application of such an elastoplastic model accomplished with the embedded matrix-fiber theory. The examples of the topics 5.7.1, 5.7.2 and 5.8 also considered such a model to simulate the global behavior of the structures analyzed.

4.2 Damage model with the smeared crack approach

The present section addresses in the formulation of the damage model with the smeared crack approach applied to the numerical analysis performed in this work. The analytical expressions and the algorithm schedule considered in its implementation are presented.

It should be emphasized that the present damage model is a product of the work developed during the visiting of 6 months of the author of this thesis at the University of Glasgow. During this period the author received scholarship granted by the Capes Foundation, an agency under the Ministry of Education of Brazil. The present model was performed in collaboration with Prof. Dr. Lukasz Kaczmarczyk.

4.2.1 Equilibrium equation

The Principle of Stationary Total Potential Energy is used to solve the mechanical problem. In order to do so, the total potential energy is written as function of Helmoltz free energy (ψ) and the external loads potential (Ω) as follow presented:

$$\Pi(Y) = \int_{V_0} \psi(E,k)\, dV_0 + \Omega(Y) \tag{4.66}$$

where E is the Green strain tensor and k is an internal variable that store the damage history of the material.

The equilibrium position is found when the variation of the equation (4.66) is equal zero. Such variation is performed in function of the position variable (Y) as follow written:

$$\delta\Pi = \int_{V_0} \frac{\partial \psi}{\partial E} \frac{\partial E}{\partial Y} dV_0 \delta Y + F \delta Y = 0 \tag{4.67}$$

In accordance with the energy conjugate assumption it is possible to define:

$$\frac{\partial \psi}{\partial E} = S \tag{4.68}$$

where S is the Saint-Venant-Kirhhoff stress. In the next section an anisotropic damage model is used to stablish the relationship between S and E .

Replacing (4.68) in (4.67) result in:

$$\delta\Pi = \left(\int_{V_0} S \frac{\partial E}{\partial Y} dV_0 + F \right) \delta Y = 0 \tag{4.69}$$

The equilibrium condition is a nonlinear equation, which is solved with the Newton Raphson procedure, as described in the item 2.1.

$$\int_{V_0} S \frac{\partial E}{\partial Y} dV_0 + F = 0 \tag{4.70}$$

4.2.2 Constitutive relationship with damage model

To assume the damage process in the evolution of analysis the constitutive relationship is used in secant format:

$$S = \mathfrak{C}_s E \tag{4.71}$$

where $\mathfrak{C}_s$ is the constitutive tensor of an isotropic material.

Initially, the constitutive relation (4.71) has an elastic isotropic behavior, indicating that $\mathfrak{C}_s = \mathfrak{C}^e$. Such elastic behavior remains until the damage process be started. From the physical

point of view, the damage process is related to the set of micro-defects, which tends to align to a common preferential direction. For the present model, the guidance of these micro-defects is ranged in an orthonormal direction to the maximum principal stress. In accord with the smeared approach this preferential direction of the micro-defects is represented by one single cohesive crack or softening law.

In accordance with the previous assumption hypothesis, the Rankine criterion is taken into account to determine the beginning of the damage process. Rankine criterion evaluates the maximum principal stress with the tensile stress (f_t). The tensile strength is determined by a simple uniaxial tension test. So, if the maximum principal stress is larger than the tensile limit the damage process is initiated. Otherwise, the material remains in the elastic regime.

Once initiated the damage process, its evolution, which describes the stiffness penalization of the material, is governed by a softening curve.

$$f(e_{nn}) \tag{4.72}$$

The softening curve adopted in (4.72) is a function of the local strain (e_{nn}) related to the orthonormal direction (nn) of the preferential damaging plan.

To take into account the loading and partial reloading process the internal variable k is introduced to assure the history of the material. In other words the variable k stores the maximum strain level reached in the analysis in a given time of load t:

$$k(t) = \max_{\tau \leq t} e_{nn}(\tau) \tag{4.73}$$

Following, the expressions that involve the stiffness penalization of the material are presented.

4.2.3 Softening law

Two shapes of softening curves, linear and multilinear, are adopted in the analysis of the structure of this thesis. The expression that defines the stiffness degradation of the material is first developed for the linear softening curve and next it is expanded for the multilinear case.

Linear Softening

At this time, it takes the linear softening law, shown in Figure 4.4, to develop the mathematical expressions considered in the present model.

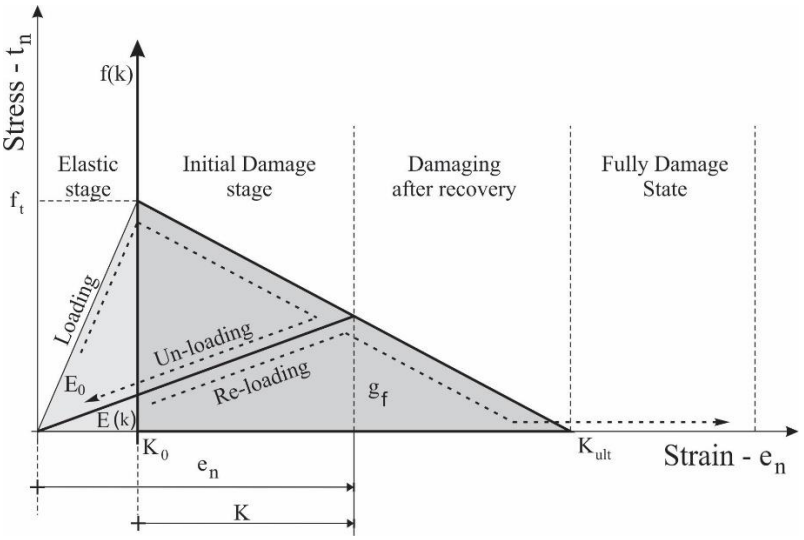

Figure 4.4 - Constitutive law with linear softening.

As previously discussed the initialization of the damaging process occurs when the maximum principal stress reaches the value of the tensile strength of the material (f_t). Until this point, the behavior of the material is considered isotropic elastic. Once achieved such criterion, the initial stiffness of the material (E_0) at the same direction of the principal stress starts to reduce ($E(k)$). The stiffness reduction is performed in accord with the damage evolution, stored indirectly in the internal variable k . Next, the mathematical development of such evolution function of degradation is described.

To do so, first the softening law is written as function of the internal variable k and the properties of the material, such as tensile strength and fracture energy. Afterward, the equation to stiffness penalization into local coordinates is defined. Finally, with the previously expressions the anisotropic constitutive tensor for the damaging material is determined.

Softening law equation

For a plane stress case the stiffness in a direction n is a scalar defined as:

$$E_0 = n \cdot \mathcal{C}^e n \tag{4.74}$$

where $\mathcal{C}^e$ is the elastic constitutive tensor defined for the plane stress case. The vector $n = \left\{\cos^2 \quad \sin^2 \quad 2\sin\cos\right\}$ is the direction orthogonal to the preferential damaging plane.

In the border between the elastic and inelastic regime the parameter k_0 is calculate as:

$$k_0 = \frac{f_t}{E_0} = \frac{f_t}{n \cdot \mathcal{C}^e n} \tag{4.75}$$

The relationship between the area under the softening curve and the fracture energy is performed with the characteristic length or crack bandwidth as follow written:

$$g_f = \frac{G_f}{h} \tag{4.76}$$

The determination of the internal variable (k_{ult}) is associated with the tensile stress, energy fracture and the characteristic length as:

$$g_f = \frac{G_f}{h} = \frac{f_t k_{ult}}{2} \Rightarrow k_{ult} = \frac{2G_f}{h f_t} \tag{4.77}$$

k_{ult} is the internal variable related with the largest value of strain at which the crack still transmit stress. For strain values bigger than k_{ult} the crack is assumed completely open and therefore for this point there is no more rigidity contribution for the global stiffness of the material.

The tangent slope (H) of the softening curve is defined as:

$$H = \frac{f_{ct}}{k_{ult}} = \frac{{f_{ct}}^2 h}{2G_f} \tag{4.78}$$

Therefore, the softening linear equation is written as function of the material properties and the internal variable k as:

$$f(k) = f_t - Hk = f_t - \frac{{f_t}^2 h}{2G_f} k = f_t \left(1 - \frac{f_t h}{2G_f} k\right) \tag{4.79}$$

Stiffness penalization into the local coordinates

From smeared crack models the material damaged is represented schematically with elastic unit coupled in series to a crack unit. So, the inverse of the constitutive law in the local coordinates with the crack plan is defined as:

$$\left(c^{e^{-1}} + c^{d^{-1}}\right) t_{nn} = e_{nn} = k_0 + k \tag{4.80}$$

where $c^{e^{-1}}$ and $c^{d^{-1}}$ are the inverse or compliance of the elastic and damaged material stiffness in the direction n.

Once started the damage process the stress t_{nn} is equivalent to the value of the $f(k)$. Replacing (4.74) and (4.79) into (4.80) and knowing that $c^{e^{-1}} = 1/\left(n \cdot \mathcal{C}^e n\right)$, it is possible to define:

$$\left(\frac{1}{n \cdot \mathcal{C}^e n} + c^{d^{-1}}\right) f_t \left(1 - \frac{f_t h}{2G_f} k\right) = \frac{f_t}{n \cdot \mathcal{C}^e n} + k \tag{4.81}$$

Finally, the scalar term $c^{d^{-1}}$ associated with the stiffness degradation can be expressed as:

$$c^{d^{-1}} = \frac{\left(2G_f n \cdot \mathcal{C}^e n + f_t^{\,2} h\right)}{n \cdot \mathcal{C}^e n f_t \left(2G_f - f_t h k\right)} k \tag{4.82}$$

The constitutive tensor for the damage material

The constitutive law, which describes a material damaged or cracked, is written in global coordinates as follow:

$$S = \mathcal{C}_s E = (\mathcal{C}^{e^{-1}} + \mathcal{C}^{d^{-1}})^{-1} E \tag{4.83}$$

where $\mathcal{C}^{e^{-1}}$ is the inverse of the constitutive tensor and the tensor $\mathcal{C}^{d^{-1}}$ is assumed as:

$$\mathcal{C}^{d^{-1}} = c^{c^{-1}} \left(n \otimes n\right) \tag{4.84}$$

So, replacing (4.84) in (4.83) the constitutive tensor for the damage material is therefore defined as:

$$\mathcal{C}_s^{\bullet} = \mathcal{C}^{\bullet ed} = \mathcal{C}^{\bullet e} - \frac{c^{d^{-1}}}{1 + c^{d^{-1}} Trace\left[\mathcal{C}^{\bullet e}\left(n \otimes n\right)\right]} \mathcal{C}^{\bullet e}\left(n \otimes n\right)\mathcal{C}^{\bullet e} \tag{4.85}$$

As can be observed in (4.86) for the case (a) when $c^{d^{-1}}$ is zero the second term of the expression (4.85) is null, and therefore the constitutive matrix is purely elastic. For the case (b), when $c^{d^{-1}}$ is a value different from zero the stiffness $\mathcal{C}^{\bullet ed}$ is computed by (4.85). For the last case (c), when the term $c^{d^{-1}}$ is a high value the second term of (4.85) is equals the elastic tensor $\mathcal{C}^{\bullet e}$ and consequently the constitutive tensor of the material damaged is null.

$$\begin{cases} (a) \quad c^{d^{-1}} = 0 \Rightarrow \mathcal{C}^{\bullet ed} = \mathcal{C}^{\bullet e} \\ (b) \quad c^{d^{-1}} = c^{cr} \Rightarrow \mathcal{C}^{\bullet ec} = \mathcal{C}^{\bullet e} - \dfrac{c^{d^{-1}}}{1 + c^{d^{-1}} Trace\left[\mathcal{C}^{\bullet e}\left(n \otimes n\right)\right]} \mathcal{C}^{\bullet e}\left(n \otimes n\right)\mathcal{C}^{\bullet e} \\ (c) \quad c^{d^{-1}} = highnumber \Rightarrow \mathcal{C}^{\bullet ed} = 0 \end{cases} \tag{4.86}$$

Multilinear Softening

Two dimensionless parameters $(\alpha \text{ and } \beta)$ are used in the equations to describe the multilinear softening formulation, Figure 4.5. The basic idea consists in to assume values between 0 and 1 for α and β as long as the multilinear softening curve is adequate to the softening curve obtained from the experimental test. The index (n) refers to the total number of linear branch and (H) the tangent of each linear branch.

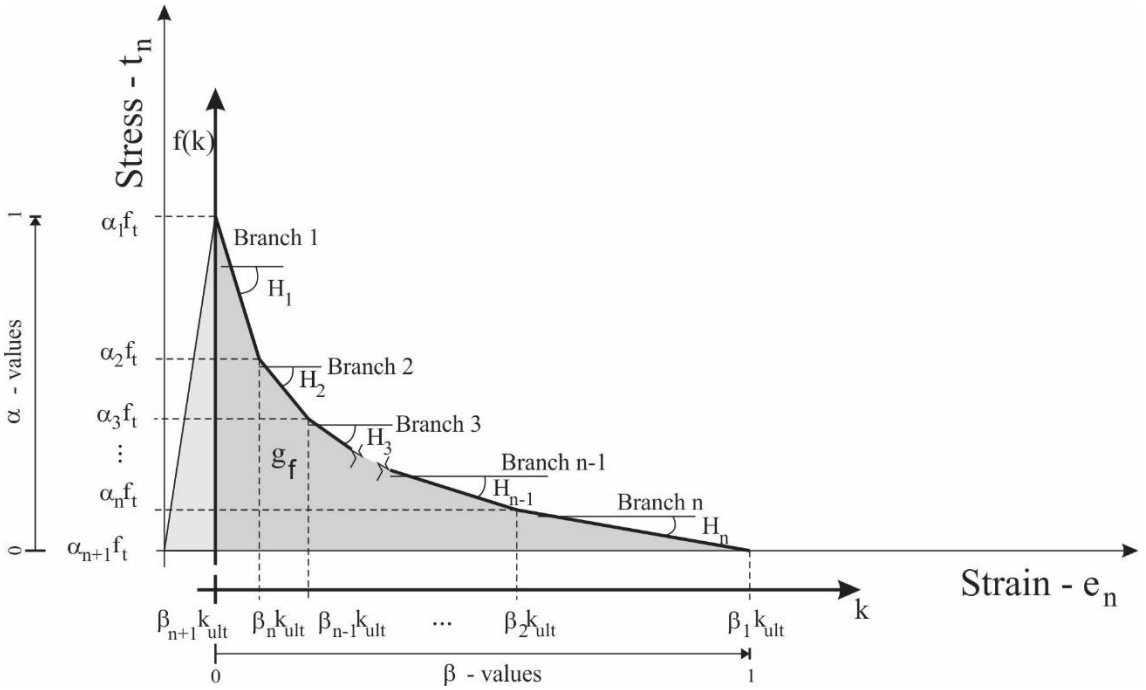

Figure 4.5 – Multilinear Softening.

Therefore, according to Figure 4.5 the tangent of each linear branch softening is calculated as:

$$H_i = \frac{f_t}{k_{ult}}\left(\frac{\alpha_i - \alpha_{i+1}}{\beta_{(n+1)-i} - \beta_{(n+2)-i}}\right); \text{ with } \{i \rightarrow 1,\text{n} \tag{4.87}$$

The index (i) is here used to indicate the linear branch in analysis. Analogously, the general expression to calculate the area under the softening curve is:

$$A_j = \frac{f_t k_{ult}}{2}\left(\alpha_j + \alpha_{j+1}\right)\left(\beta_{(n+1)-j} - \beta_{(n+2)-j}\right); \text{ with } \{j \rightarrow 1,\text{n} \tag{4.88}$$

Taking into account that $g_f = \left(G_f / h\right) = A_j$, with the index (j) varying between 1 and number of linear branch, the internal variable (k_{ult}) associated to the ultimate strain is expressed as:

$$k_{ult} = \frac{2G_f}{f_t h}\left(\frac{1}{\left(\alpha_j + \alpha_{j+1}\right)\left(\beta_{(n+1)-j} - \beta_{(n+2)-j}\right)}\right); \text{ with } \{j \rightarrow 1,\text{n} \tag{4.89}$$

The softening law equation to calculate the stress $\left(f_i(k)\right)$, in the branch (i), in function of the internal variable (k) is:

$$f_i(k) = \alpha_i f_t - H_i\left(k - \beta_{(n+2)-i} k_{ult}\right) \tag{4.90}$$

Replacing (4.87) into (4.90) the softening law is rewritten as follow:

$$f(k) = f_t \frac{\alpha_i + \left[\left(\alpha_i - \alpha_{i+1}\right)\left(-k + k_{ult}\beta_{(n+2)-i}\right)\right]}{k_{ult}\left(\beta_{(n+1)-i} + \beta_{(n+2)-i}\right)} \tag{4.91}$$

Similar to the procedure adopted for the linear softening law, Eq. (4.81), the stiffness degradation into the local coordinates of the crack is resulted from the following expression:

$$f(k)\left(\frac{1}{n \cdot \mathcal{C}^e n} + c^{d^{-1}}\right) = e_n = \frac{\alpha_1 f_t}{n \cdot \mathcal{C}^e n} + k \tag{4.92}$$

Thus, the scalar term c^d is obtained from the replacement of (4.90) into (4.92) and therefore the following expression it can be found:

$$c^{d^{-1}} = \frac{\alpha_i\left(-f_t k + f_t k_{ult}\beta_{(n+1)-i}\right) - \left(\alpha_1 f_t + Ek\right)k_{ult}\left(\beta_{(n+1)-i} - \beta_{(n+2)-i}\right) + f_t\alpha_{i+1}\left(k - k_{ult}\beta_{(n+2)-i}\right)}{Ef_t\left[\alpha_i\left(k - k_{ult}\beta_{(n+1)-i}\right) + \alpha_{i+1}\left(-k + k_{ult}\beta_{(n+2)-i}\right)\right]} \tag{4.93}$$

The general equation defined in (4.86) is also the constitutive matrix for the damaged material determined with the multilinear softening law. The only difference for the analysis performed with the multilinear softening is that the parameter $c^{d^{-1}}$ must be calculated with the expression (4.93).

The expressions presented in this topic although written to the multilinear softening case can be used to calculate structures adopting linear softening. Such procedure can be performed taking into account only one linear branch softening, i.e. $n=1$, and the following dimensionless parameters:

$$\begin{cases} \alpha_1 = 1 \\ \alpha_{1+1} = \alpha_2 = 0 \end{cases}, \text{ and } \begin{cases} \beta_{(1+1)-1} = \beta_1 = 1 \\ \beta_{(1+2)-1} = \beta_2 = 0 \end{cases} \tag{4.94}$$

Assuming the values determined in (4.94) to calculate k_{ult} with Eq. (4.89) and substituting all these values in the Eqs. (4.90) and (4.91) the expressions for $c^{d^{-1}}$ and $f\left(k\right)$ are analogous to those previously written in (4.82) and (4.79), respectively, as rewritten below:

$$c^{d^{-1}} = \frac{\left(2G_f n \cdot \varepsilon^{e} n + {f_{ct}}^2 h\right)}{n \cdot \varepsilon^{e} n f_{ct}\left(2G_f - f_t h k\right)} k \tag{4.95}$$

$$f\left(k\right) = f_t\left(1 - \frac{f_t h}{2G_f} k\right) \tag{4.96}$$

4.2.4 Evolution calculation

The penalization of the constitutive stiffness matrix previously discussed is used to calculation of internal force and the Hessian matrix. Taking into account the Newton Raphson method both terms are constantly calculated in the iterative process as showed in Figure 4.6.

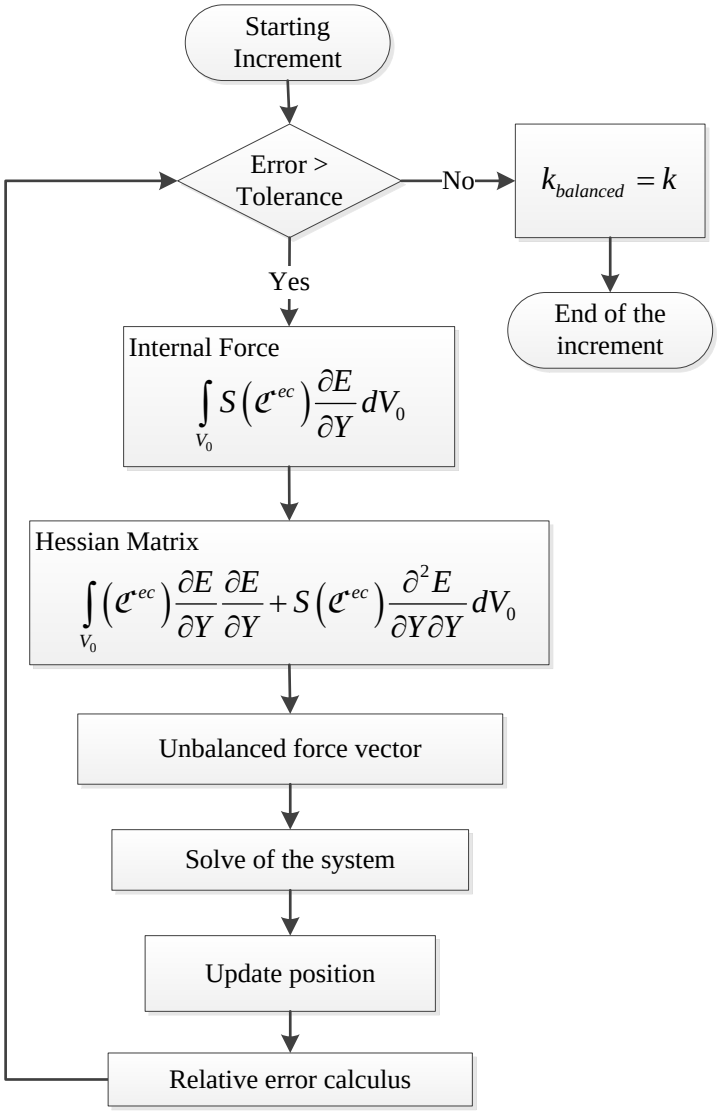

Figure 4.6 – Newton Raphson method

From the schedule of the numerical implementation shown in Figure 4.6, it observes that the internal variable k updates the auxiliary variable $k_{balanced}$ outside the iterative process. $k_{balanced}$ is always used to calculate the Saint-Venant-Kircchhoff stress before the verification of the damage criterion. The variable k is constantly updated into the iterative process since the stress level calculated in the integration point violates the damage criterion.

The damage criterion verification and consequently the evolution of the penalization of the constitutive matrix are performed in the Saint-Venant-Kirchhoff stress calculation.

Figure 4.7 summarizes, for one integration point, the procedure related to the verification of the damage criterion and consequently actualization of the constitutive tensor taking into account a certain iteration (m).

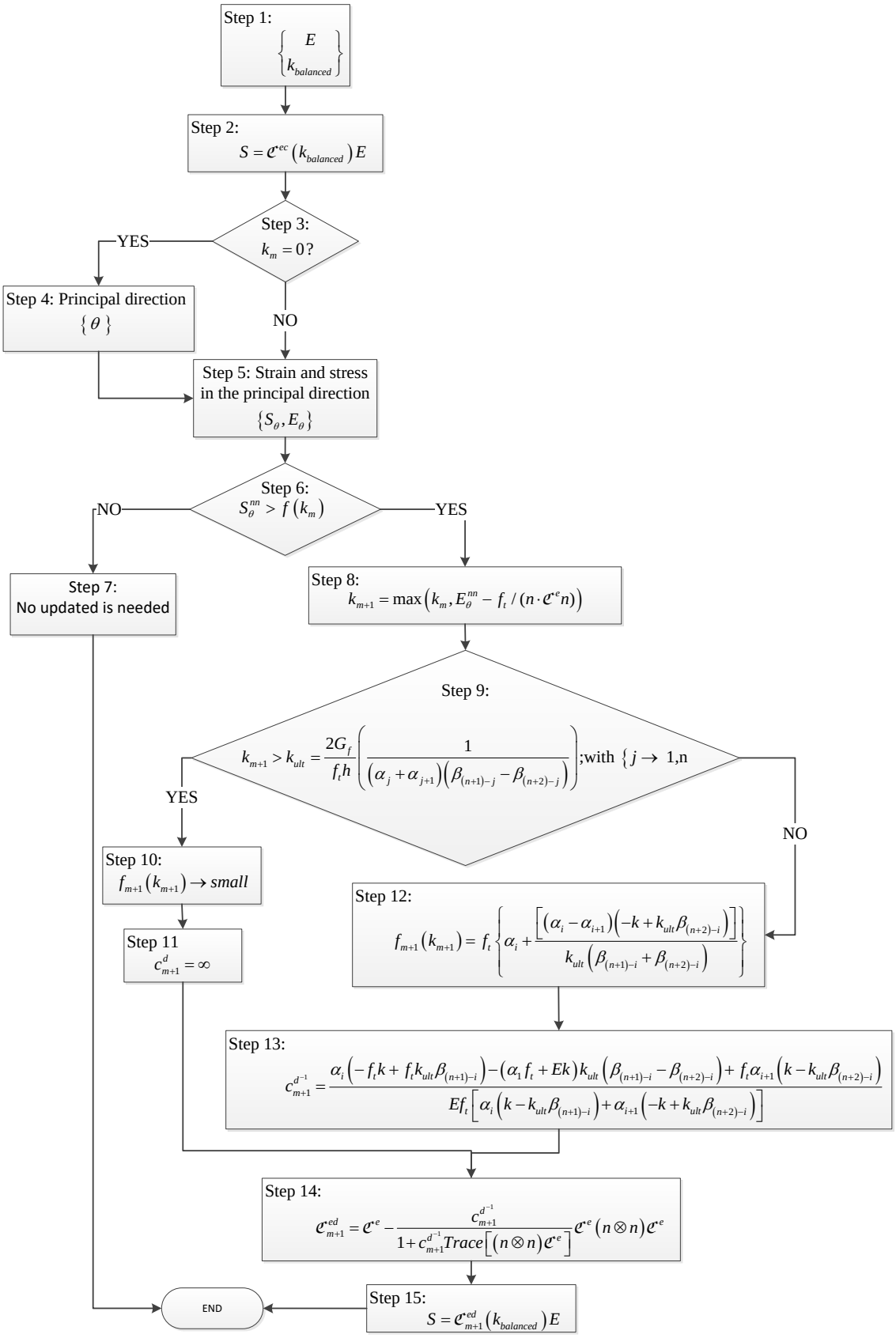

Figure 4.7 – Damage model at integration point level.

For a specific iteration (m) the Green strain (E) and the internal variable balanced ($k_{balanced}$) are known, (Step 1). Next, in the step 2 the stress is obtained with the constitutive matrix updated with the internal variable from the previously balanced increment of load $k_{balanced}$, Eq. (4.86). In the step 3 it is verified if the material is already damaged. Such procedure is performed with the variable k_m, which stores the history of the damaging of the material. For the case in which the material has not yet presented damage k_{m-1} is equal zero and the principal direction of the stress has to be determined (Step 4). Otherwise, the strain and stress in the principal direction are directly calculated in step 5. Following, the stress in the principal direction (θ) is compared with the softening curve adopted $f\left(k_{m-1}\right)$ in the step 6. Note that for the integration point in which the damage process has not started the value of the softening curve is equal to the tensile strength, i.e. $f\left(k_{m-1}\right) = f_t$. So, if the principal stress does not violate the previously criterion no updated is needed. On the other hand, once violates the criterion the internal variable k_m is updated according to the expression written in the step 8. Where k_{m-1} is the previous value of k, E_θ^{nn} is the strain value in the principal direction and k_0 is determined by Eq. (4.75).

Next in the step 9 it is verified if the new value of k_m is bigger than k_{ult}. For the case when such comparison is false the criteria ($f_m\left(k_m\right)$) and $c_m^{d^{-1}}$ are determined according to expression written in step 12 and 13, respectively. Otherwise, when k_m exceeds k_{ult} such integration point does not contribute to strength of the structure. Physically this means the material is fully damage. From numerical point of view, this situation is represented attributing for the function $f_m\left(k_m\right)$ a small value and for $c_m^{d^{-1}}$ a high value, according steps 10 and 11, respectively.

The step 14 refers to the calculation of the constitutive matrix for the material damaged ($\mathcal{C}_m^{ec}$). Lastly, as shows the step 15 the new stress is determined.

The new stress obtained in the iteration is used to calculate the internal forces and stiffness matrix required in the solution of the finite element method.

For numerical reasons, the level of stress is not compared with the softening curve for the first iteration of each increment of load. Thus, the update of stress previously discussed is assumed only from the second iteration.

Once the principal stresses surpass the strength limit of the material (f_t) two damages models can be considered in the analysis: the fixed and rotating damage models.

The so-called fixed damage model stores the direction of the plan in which the damaging is initiated. Such direction remains unchangeable until end of the analysis, and therefore the penalization of the constitutive tensor is continuously associated with the evolution of damage in this direction. On the other hand, for the analysis performed with the rotating damage model the main direction is always calculated for the first iterative process that the damage criterion is verified, independently if the damage process has already been initiated.

In chapter 5, the examples written in the topics 5.6.1, 5.6.2, 5.6.3, 5.7.1 and 5.7.2 shows the application of such damage model with smeared crack approach in the analysis of the structures.

4.3 Bimodular damage model

The previously damage model described was developed only to taking into account the degradation of the material under traction cases. Next, this formulation is enhanced for the compression damage cases, and consequently, a bimodular damage model is presented.

4.3.1 Constitutive relationship

Analogous to the damage model with the smeared approach the constitutive relationship is taken into secant format, as shown in (4.97).

$$S = \mathfrak{C}_s E = \mathfrak{C}^{ed} E \tag{4.97}$$

Once the damage process initialized the penalization of the constitutive tensor ($\mathfrak{C}_s$) is performed with the adoption of any softening curves. Such curves are considered to describe the material behaviour in tension and compression regime.

4.3.2 Damage criteria

Figure 4.8 shows schematically the behaviour of the damage model in the principal direction plan.

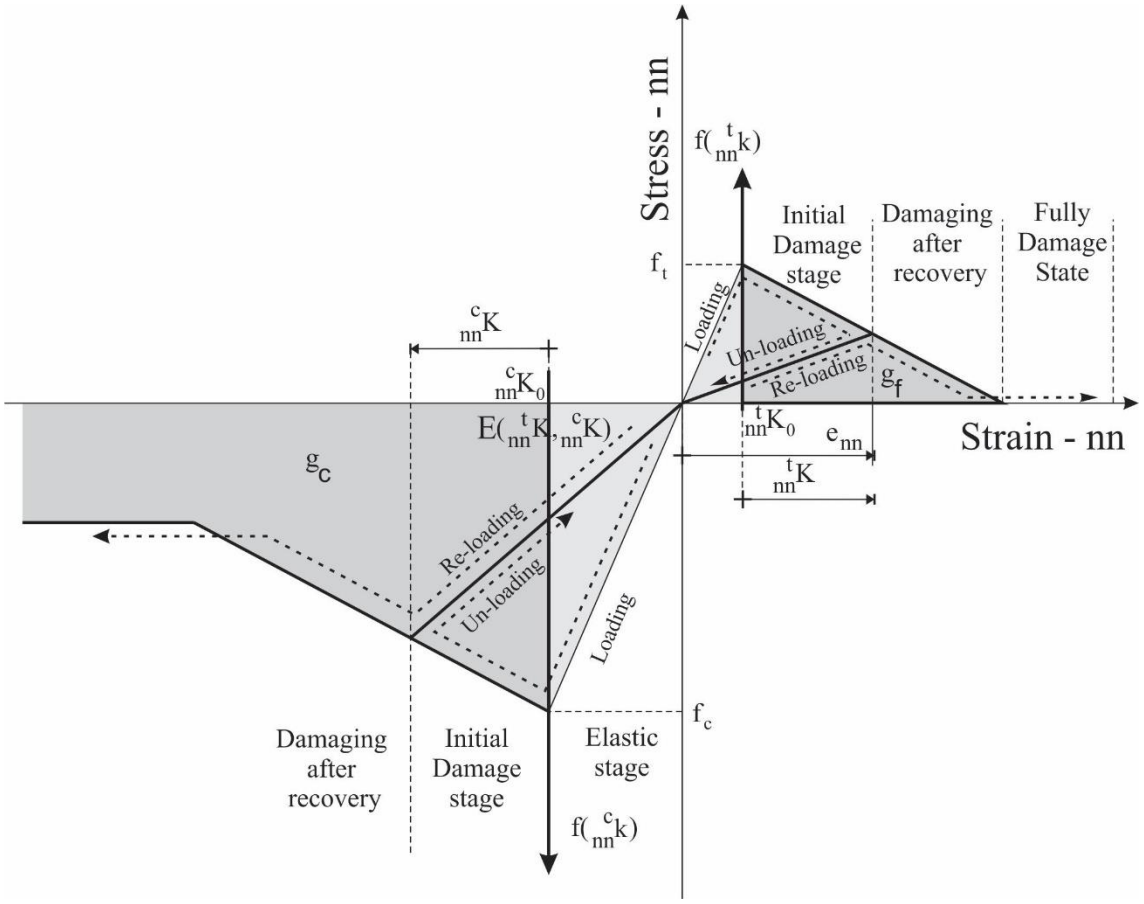

Figure 4.8 – Plane state damage behaviour.

Initially the material is assumed elastic until the damage criteria be violated, which occurs when the principal stresses, in the nn direction, reach the tensile or compression strength of the material $\left(f_t, f_c \right)$. After such point the constitutive relationship follow any softening law function $({}_{nn}^{t} f(e_{nn}), {}_{nn}^{c} f(e_{nn}))$ adopted. The history of the physical non-linearity of the material in such direction is stored at the two internal variable $\left({}_{nn}^{t}k, {}_{nn}^{c}k \right)$ independently from each other. The overwritten t and c is used to differentiate the parameters related to degradation due to traction and compression action, respectively.

The softening curves are written in function of the internal variables as follow:

$$ {}^{t}_{nn}f\left({}^{t}_{nn}k\right) = f_t\left\{{}^{t}\alpha_i + \frac{\left[\left({}^{t}\alpha_i - {}^{t}\alpha_{i+1}\right)\left(-{}^{t}_{nn}k + {}^{t}_{nn}k_{ult}\,{}^{t}\beta_{(n+2)-i}\right)\right]}{{}^{t}_{nn}k_{ult}\left({}^{t}\beta_{(n+1)-i} + {}^{t}\beta_{(n+2)-i}\right)}\right\} \tag{4.98} $$

$$ {}^{c}_{nn}f\left({}^{c}_{nn}k\right) = f_c\left\{{}^{c}\alpha_i + \frac{\left[\left({}^{c}\alpha_i - {}^{c}\alpha_{i+1}\right)\left(-{}^{c}_{nn}k + {}^{c}_{nn}k_{ult}\,{}^{c}\beta_{(n+2)-i}\right)\right]}{{}^{c}_{nn}k_{ult}\left({}^{c}\beta_{(n+1)-i} + {}^{c}\beta_{(n+2)-i}\right)}\right\} \tag{4.99} $$

In plane-stress case, the stress perpendicular to the direction nn is also evaluated and the softening curves are defined at the same similar way as:

$$ {}^{t}_{ss}f\left({}^{t}_{ss}k\right) = f_t\left\{{}^{t}\alpha_i + \frac{\left[\left({}^{t}\alpha_i - {}^{t}\alpha_{i+1}\right)\left(-{}^{t}_{ss}k + {}^{t}_{ss}k_{ult}\,{}^{t}\beta_{(n+2)-i}\right)\right]}{{}^{t}_{ss}k_{ult}\left({}^{t}\beta_{(n+1)-i} + {}^{t}\beta_{(n+2)-i}\right)}\right\} \tag{4.100} $$

$$ {}^{c}_{ss}f\left({}^{c}_{ss}k\right) = f_c\left\{{}^{c}\alpha_i + \frac{\left[\left({}^{c}\alpha_i - {}^{c}\alpha_{i+1}\right)\left(-{}^{c}_{ss}k + {}^{c}_{ss}k_{ult}\,{}^{c}\beta_{(n+2)-i}\right)\right]}{{}^{c}_{ss}k_{ult}\left({}^{c}\beta_{(n+1)-i} + {}^{c}\beta_{(n+2)-i}\right)}\right\} \tag{4.101} $$

where $s = \left\{\sin^2 \quad \cos^2 \quad -2\sin\cos\right\}$ is the vector related to the direction ss which is perpendicular to the direction.

Stiffness penalization into the local coordinates

According to Figure 4.8, the un-loading process happens elastically and the damage of the material under tension and compression actions are independent. In other words, in such model the degradation of the material caused by the tensile forces is not considered when this same material is subjected to compression forces and vice versa. Mathematically, such consideration is assumed when the history of the damage of the material is stored in different internal variables, as previously written. Take advantage of such observation, the scalar terms associated to the stiffness penalization into the local coordinates and in the direction-nn $\left({}^{t}_{nn}c^{d^{-1}}, {}^{c}_{nn}c^{d^{-1}}\right)$ can be obtained following the same steps already described from the previous model. So, rewritten (4.93) with the nomenclature adopted for the present model and taking into account the multilinear softening cases the terms ${}^{t}_{nn}c^{d^{-1}}$ and ${}^{c}_{nn}c^{d^{-1}}$ are defined as follow:

$$ {}^{t}_{nn}c^{d^{-1}} = \frac{{}^{t}\alpha_i\left(-f_{t\,nn}{}^{t}k + f_{t\,nn}{}^{t}k_{ult}\,{}^{t}\beta_{(n+1)-i}\right) - \left({}^{t}\alpha_1 f_t + E\,{}^{t}_{nn}k\right){}^{t}_{nn}k_{ult}\left({}^{t}\beta_{(n+1)-i} - {}^{t}\beta_{(n+2)-i}\right) + f_t\,{}^{t}\alpha_{i+1}\left({}^{t}_{nn}k - {}^{t}_{nn}k_{ult}\,{}^{t}\beta_{(n+2)-i}\right)}{Ef_t\left[{}^{t}\alpha_i\left({}^{t}_{nn}k - {}^{t}_{nn}k_{ult}\,{}^{t}\beta_{(n+1)-i}\right) + {}^{c}\alpha_{i+1}\left(-{}^{t}_{nn}k + {}^{t}_{nn}k_{ult}\,{}^{t}\beta_{(n+2)-i}\right)\right]} \tag{4.102} $$

$$ {}_{nn}^{c}c^{d^{-1}} = \frac{{}^{c}\alpha_i\left(-f_c\,{}_{nn}^{c}k + f_{cc}\,{}_{nn}^{c}k_{ult}\,{}^{c}\beta_{(n+1)-i}\right)-\left({}^{c}\alpha_1 f_c + E\,{}_{nn}^{c}k\right){}_{nn}^{c}k_{ult}\left({}^{c}\beta_{(n+1)-i} - {}^{c}\beta_{(n+2)-i}\right)+ f_c\,{}^{c}\alpha_{i+1}\left({}_{nn}^{c}k - {}_{nn}^{c}k_{ult}\,{}^{c}\beta_{(n+2)-i}\right)}{Ef_c\left[{}^{c}\alpha_i\left({}_{nn}^{c}k - {}_{nn}^{c}k_{ult}\,{}^{c}\beta_{(n+1)-i}\right)+{}^{c}\alpha_{i+1}\left(-{}_{nn}^{c}k + {}_{nn}^{c}k_{ult}\,{}^{c}\beta_{(n+2)-i}\right)\right]} \tag{4.103} $$

For the degradation of the material due to the efforts that acting in the direction ss the terms ${}_{ss}^{t}c^{d^{-1}}$ and ${}_{ss}^{c}c^{d^{-1}}$ are similar to Eqs (4.102) and (4.103), and written as follow:

$$ {}_{ss}^{t}c^{d^{-1}} = \frac{{}^{t}\alpha_i\left(-f_t\,{}_{ss}^{t}k + f_t\,{}_{ss}^{t}k_{ult}\,{}^{t}\beta_{(n+1)-i}\right)-\left({}^{t}\alpha_1 f_t + E\,{}_{ss}^{t}k\right){}_{nn}^{t}k_{ult}\left({}^{t}\beta_{(n+1)-i} - {}^{t}\beta_{(n+2)-i}\right)+ f_t\,{}^{t}\alpha_{i+1}\left({}_{ss}^{t}k - {}_{ss}^{t}k_{ult}\,{}^{t}\beta_{(n+2)-i}\right)}{Ef_t\left[{}^{t}\alpha_i\left({}_{ss}^{t}k - {}_{ss}^{t}k_{ult}\,{}^{t}\beta_{(n+1)-i}\right)+{}^{c}\alpha_{i+1}\left(-{}_{ss}^{t}k + {}_{ss}^{t}k_{ult}\,{}^{t}\beta_{(n+2)-i}\right)\right]} \tag{4.104} $$

$$ {}_{ss}^{c}c^{d^{-1}} = \frac{{}^{c}\alpha_i\left(-f_c\,{}_{ss}^{c}k + f_{cc}\,{}_{ss}^{c}k_{ult}\,{}^{c}\beta_{(n+1)-i}\right)-\left({}^{c}\alpha_1 f_c + E\,{}_{ss}^{c}k\right){}_{ss}^{c}k_{ult}\left({}^{c}\beta_{(n+1)-i} - {}^{c}\beta_{(n+2)-i}\right)+ f_c\,{}^{c}\alpha_{i+1}\left({}_{ss}^{c}k - {}_{ss}^{c}k_{ult}\,{}^{c}\beta_{(n+2)-i}\right)}{Ef_c\left[{}^{c}\alpha_i\left({}_{ss}^{c}k - {}_{ss}^{c}k_{ult}\,{}^{c}\beta_{(n+1)-i}\right)+{}^{c}\alpha_{i+1}\left(-{}_{ss}^{c}k + {}_{ss}^{c}k_{ult}\,{}^{c}\beta_{(n+2)-i}\right)\right]} \tag{4.105} $$

If linear softening is adopted, we have $n=1$ and the dimensionless parameters equal:

$$ \begin{cases} {}^{t}\alpha_1 = 1 \\ {}^{t}\alpha_{1+1} = {}^{t}\alpha_2 = 0 \end{cases}; \quad \begin{cases} {}^{t}\beta_{(1+1)-1} = {}^{t}\beta_1 = 1 \\ {}^{t}\beta_{(1+2)-1} = {}^{t}\beta_2 = 0 \end{cases} \text{ and } \begin{cases} {}^{c}\alpha_1 = 1 \\ {}^{c}\alpha_{1+1} = {}^{c}\alpha_2 = 0 \end{cases}; \quad \begin{cases} {}^{c}\beta_{(1+1)-1} = {}^{c}\beta_1 = 1 \\ {}^{c}\beta_{(1+2)-1} = {}^{c}\beta_2 = 0 \end{cases} \tag{4.106} $$

Therefore, the expressions (4.102) and (4.103) can be reduced for:

$$ {}_{nn}^{t}c^{d^{-1}} = \frac{\left(2G_f n\cdot\mathcal{E}^{e} n + f_t^{\,2}h\right)}{n\cdot\mathcal{E}^{e} n f_t\left(2G_f - f_t h\,{}_{nn}^{t}k\right)}\,{}_{nn}^{t}k \tag{4.107} $$

$$ {}_{nn}^{c}c^{d^{-1}} = \frac{\left(2G_c n\cdot\mathcal{E}^{e} n + f_c^{\,2}h\right)}{n\cdot\mathcal{E}^{e} n f_c\left(2G_c - f_c h\,{}_{nn}^{c}k\right)}\,{}_{nn}^{c}k \tag{4.108} $$

$$ {}_{ss}^{t}c^{d^{-1}} = \frac{\left(2G_f s\cdot\mathcal{E}^{e} s + f_t^{\,2}h\right)}{s\cdot\mathcal{E}^{e} s f_t\left(2G_f - f_t h\,{}_{ss}^{t}k\right)}\,{}_{ss}^{t}k \tag{4.109} $$

$$ {}_{ss}^{c}c^{d^{-1}} = \frac{\left(2G_c s\cdot\mathcal{E}^{e} s + f_c^{\,2}h\right)}{s\cdot\mathcal{E}^{e} s f_c\left(2G_c - f_c h\,{}_{ss}^{c}k\right)}\,{}_{ss}^{c}k \tag{4.110} $$

Note that the energy of fracture (G_f) and the tensile strength (f_t) were replaced to the compressive energy (G_c) and the compressive strength (f_c). The compressive energy is defined as $G_c = g_c h$, where g_c correspond to the area under the stress-strain curve pos-peak load (Figure 4.8). The equivalent strength value (h) is the same for the tension and compression cases. The scalar terms depend directly on its respective internal variable considered ${}_{nn}^{t}k$, ${}_{nn}^{c}k$, ${}_{ss}^{t}k$ or ${}_{ss}^{c}k$.

The constitutive tensor for the two-dimensional damage model

The constitutive law for the plane state damaged model is written in global coordinates as follow:

$$S = \mathcal{C}_s E = (\mathcal{C}^{e^{-1}} + {}_{nn}^{t}\mathcal{C}^{d^{-1}} + {}_{nn}^{c}\mathcal{C}^{d^{-1}} + {}_{ss}^{t}\mathcal{C}^{d^{-1}} + {}_{ss}^{c}\mathcal{C}^{d^{-1}})^{-1} E \tag{4.111}$$

The tensor $\mathcal{C}^{e^{-1}}$ is the inverse of the elastic stiffness and the other terms are the inverse of the tensors related to the degradation of the material:

$$\begin{aligned} {}_{nn}^{t}\mathcal{C}^{d^{-1}} &= {}_{nn}^{t}c^{d^{-1}}\left(n \otimes n\right) \;;\; {}_{ss}^{t}\mathcal{C}^{d^{-1}} = {}_{ss}^{t}c^{d^{-1}}\left(s \otimes s\right) \\ {}_{nn}^{c}\mathcal{C}^{d^{-1}} &= {}_{nn}^{c}c^{d^{-1}}\left(n \otimes n\right) \;;\; {}_{ss}^{c}\mathcal{C}^{d^{-1}} = {}_{ss}^{c}c^{d^{-1}}\left(s \otimes s\right) \end{aligned} \tag{4.112}$$

As described in (4.111) the constitutive tensor $\mathcal{C}_s$ is calculated by the inverse of five tensors:

$$\mathcal{C}_s = \mathcal{C}^{ed} = (\mathcal{C}^{e^{-1}} + {}_{nn}^{t}\mathcal{C}^{d^{-1}} + {}_{ss}^{t}\mathcal{C}^{d^{-1}} + {}_{nn}^{c}\mathcal{C}^{d^{-1}} + {}_{ss}^{c}\mathcal{C}^{d^{-1}})^{-1} \tag{4.113}$$

Setting $C_1 = \mathcal{C}^{e^{-1}}$ and $B_1 = {}_{nn}^{t}\mathcal{C}^{d^{-1}}; B_2 = {}_{nn}^{c}\mathcal{C}^{d^{-1}}; B_3 = {}_{ss}^{t}\mathcal{C}^{d^{-1}}$ and $B_4 = {}_{ss}^{t}\mathcal{C}^{d^{-1}}$ the inverse of Eq.(4.113), according to (Miller 1981), can be finally written as:

$$\mathcal{C}_s = \mathcal{C}^{ed} = C_{k+1}^{-1} = C_k^{-1} - \frac{1}{1 + Trace\left(C_k^{-1} B_k\right)} C_k^{-1} B_k C_k^{-1} \tag{4.114}$$

where the index k ranges from 1 to 4.

The constitutive tensor defined in Eq. (4.114) is used to calculate the internal forces and the Hessian matrix of the finite element method, as already discussed in Figure 4.6.

4.3.3 Evolution calculation

Figure 42 shows the flowchart that describes the routine to the present damage model for a certain iteration (m) implemented for the analysis of stress at the integration point level.

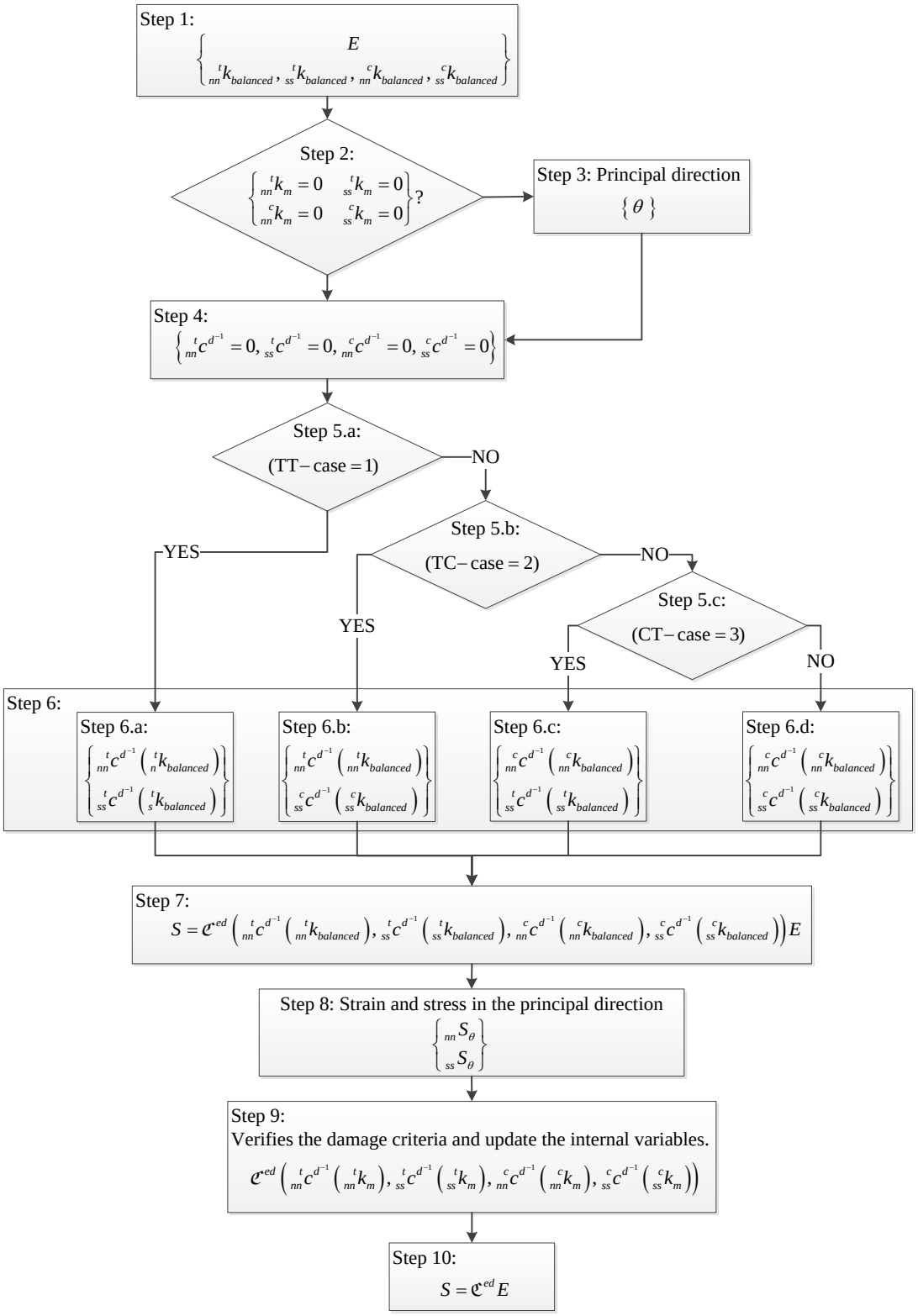

Figure 4.9 – Damage model

The Green strain and the internal variable are known from the step 1. Following, if any damage has initiated, which is verified with the internal variables different to zero, the principal direction is calculated with the strain previously determined. Otherwise, if the damage process

has already started the step 3 is neglected and the procedure goes to the step 4 where all scalar terms are given null values. Next, the plane-state configuration is evaluated. Four different configurations of stress in the plane states are possible, as shows the Figure 4.10, being them: (1) traction-traction (TT); (2) traction-compressive (TC); (3) compressive-traction (CT); and, (4) compression-compression (CC).

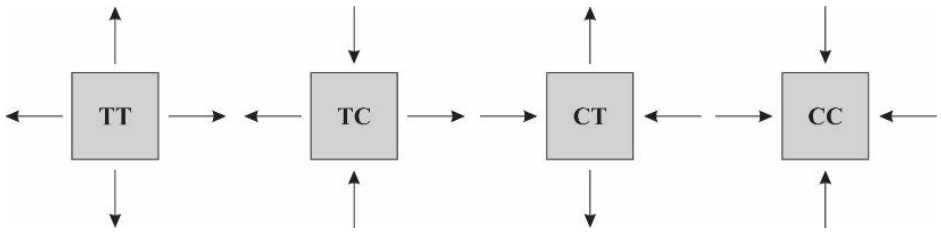

Figure 4.10 - Plane state cases.

Once determined the two-dimensional stress configuration the scalar terms associated with the damage degradation is calculated with their respective internal variable balanced (step 6a, b, c or d). Here, it is important to observe that only the scalar terms associated with the two-dimensional configuration detected are calculated while the others remain null. So, the stresses are calculated in step 7. The stresses previously determined are rotated to the principal direction (step 8), to verify the damage criteria. The step 9 verifies the damage criteria, the internal variables are updated and the constitutive tensor is therefore determined according to the Eq. (4.114). Such routine will be discussed latter. Finally, at the last step, the level of stress is corrected to satisfy the damage criteria.

The verification of the damage criteria at the step 9 is performed with the stresses calculated in n and s directions. It emphasizes that such stresses are analysed independently of each other but in a similar way. Thus, next only one case of stress will be assumed to explain the algorithm proposed to correct the parameters needed.

Figure 4.11 presents the routine calculation for the updating of the stress in the principal direction n when the tensile strength is violated.

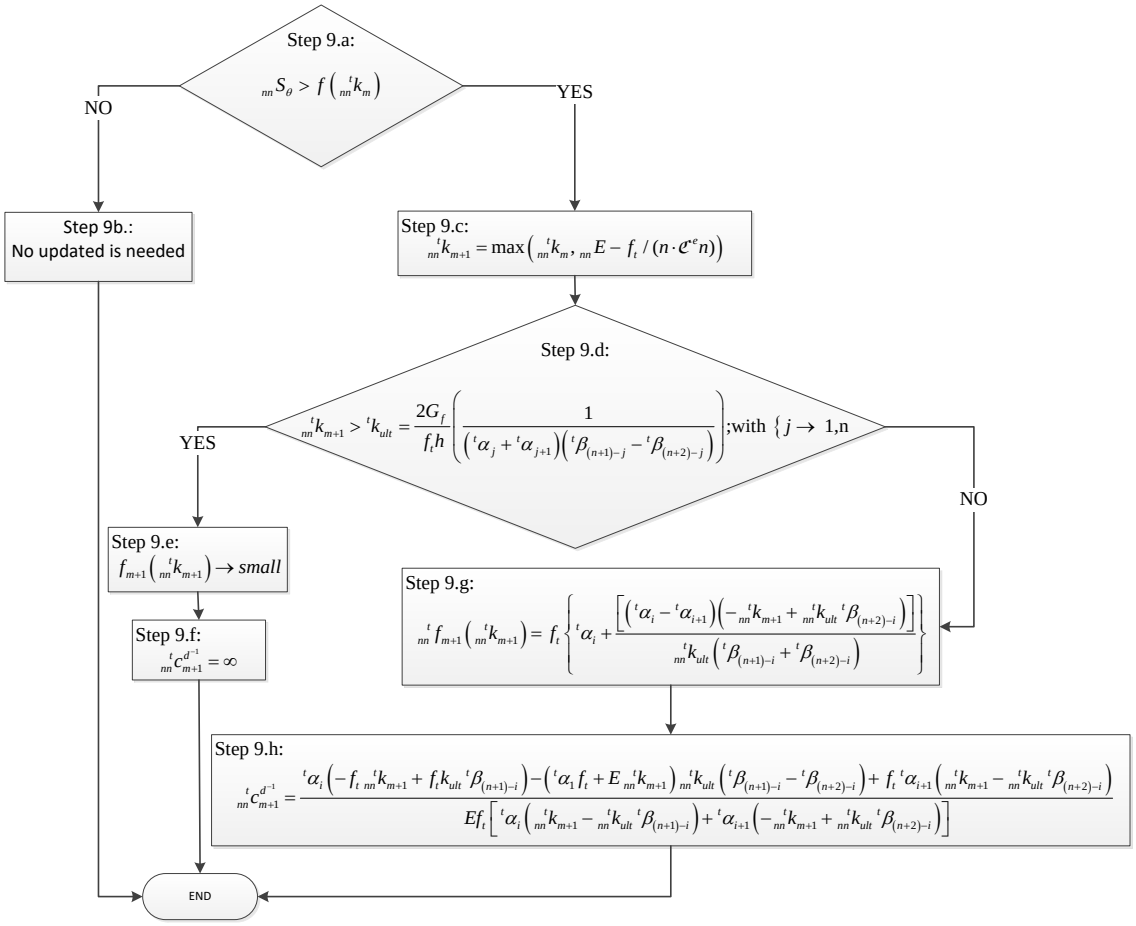

Figure 4.11 – Verification of the damage criteria for the tensile stress cases at the direction n.

The step 9.a verifies if the level of stress surpass the damage criteria. If $_{nn}S_\theta < {}_{nn}^{t}f\left(_{nn}{}^{t}k_m\right)$ the algorithm advances to the step 9.b and no correction is performed, otherwise the internal variable $_{nn}{}^{t}k_m$ is updated in the stage 9.c. Next, the new value of the internal variable is compared with ${}^{t}k_{ult}$, which is variable related to the maximum strain. In one hand, if $_{nn}{}^{t}k_m > {}^{t}k_{ult}$ it means that this point does not contribute any more to the global rigidity of the structure which numerically is assured assuming small values for $_{nn}{}^{t}f_{m+1}\left(_{nn}{}^{t}k_{m+1}\right)$ and a large one for $_{nn}{}^{t}c_{m+1}^{d^{-1}}$, as shown at the steps 9.e and f. In another hand, if $_{nn}{}^{t}k_m < {}^{t}k_{ult}$ the steps 9.g and h are executed and news values for $_{nn}{}^{t}f_{m+1}\left(_{nn}{}^{t}k_{m+1}\right)$ and $_{nn}{}^{t}c_{m+1}^{d^{-1}}$ are determined with Eqs (4.98) and (4.102), respectively.

Assuming compressive stress at the direction nn a similar routine to Figure 4.11 must be implemented with the equations and parameters adapted to this situation. The analysis of stress in the direction ss follows likewise the structure of the flowchart presented.

The global behavior of such *Bimodular damage model* for the situation of loading and unloading configuration is discussed in the example 5.6.4 of chapter 5. On the other hand, beyond the analysis of the structures considered, the examples 5.7.1 and 5.7.2 compare such a model with the *Damage model with the smeared crack approach*. Finally, example 5.8 directly apply the *Bimodular damage model* to represent the degradation of the matrix elements of the structure.

4.4 Summary

In this chapter two physical nonlinearities formulation was described to represent the physical behaviors of the materials: the elastoplastic and the damage models.

The plasticity theory for uniaxial and bidimensional cases was vastly presented. Both cases considered the Von Mises criteria for the border between the elastic and plastic regime. The additive composition between the parcels of elastic and plastic strains constitute the hypothesis of this theory. The expressions defined for the bidimensional plasticity algorithm encompass the plane stress-projected constitutive equations found in the books Simo and Hughes (1998) and de Souza Neto et al. (2008). With the formulation presented, it should be a remark that the additive composition of strains enables the analysis of structures with the materials presenting a small strain.

Two damage models were proposed in this study. The first one considered the degradation of the material only in one preferential direction when the Rankine Criterion is reached. Such a formulation was developed based in the smeared crack approach models. At this sense, two variations of such model were presented. For the first variation, the preferential direction of degradation remains fixed for the first plane of rupture reached, while, the second one considers that this preferred direction rotates, following the rotation of the principal direction of strain. The second damage model, named as *Bimodular damage model*, resulted from the enhancement of the first damage model. In this model, the damaging evolution happens when the compression or the tension stresses surpass the strength limit of the material. The history of the material damage for under compression and tension situations are independently stored from

each other. From the formulations presented it should be stressed that both damage models are classified as anisotropic damage models because the degradation evolution of the structure is not the same for different principal stress directions.

5 NUMERICAL VALIDATION

The examples of validation and analysis related to the formulation discussed and described in the previous chapters are following presented. The order of examples follows the order of presentation of the models described in this thesis.

The results of the analysis are performed with the post-processing program AcadView, available in *http://www.set.eesc.usp.br/portal/pt/softwares.*

5.1 Elastic Nonlinear Analysis

Two geometrical nonlinear analysis are following discussed with the two-dimensional and the frame finite elements.

5.1.1 Tow-dimensional finite element

The follow cantilever beam example was discussed by Mattiasson (1981) who shows the analytical solution with geometrical non-linear effect. Such example is used to verify the implementation of the two-dimensional finite element. The concentrated load of 10kN applied in the free extremity is the only action in the structure. The same 100 load steps adopted in the resolution done by Marques (2006) was adopted as well as the discretization of 120 finite elements. The properties of the material and the geometrical characteristics considered are explicit in the Figure 5.1.

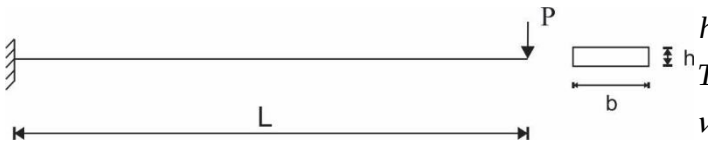

$E = 210x10^9\,Pa$
$L = 10m$
$h = 0.0178m$
$Thickness = 1m$
$\nu = 0.0$

Figure 5.1 – Cantilever beam.

Figure 5.2 shows that the equilibrium trajectories for horizontal and vertical displacement of the free extremity of the numerical solution are the same those obtained by Mattiason (1981) with analytical solution. Therefore, the numerical implementation of the plane stress finite element is consistent.

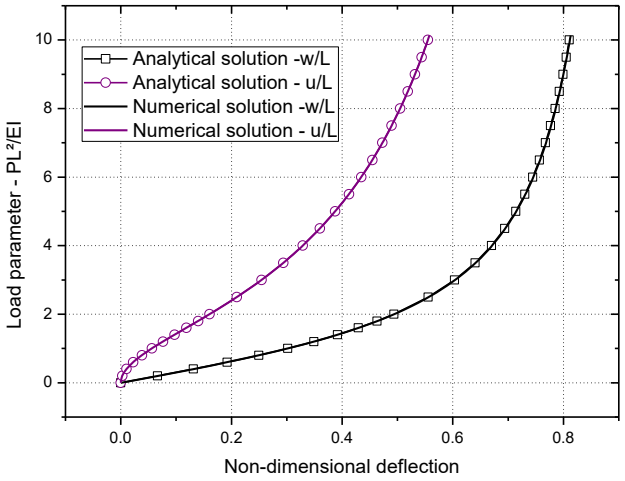

Figure 5.2 – Trajectories of equilibrium.

5.1.2 Frame finite element

Mattiasson (1981) presents an analysis of frame in lozenge shape with elliptic integrals. Figure 5.3 shows such structure requested by different load configurations. In the first load configuration (a) all rods of the structures are under tensile (T) effect, while for the second case (b) the rods are under compression (C) effect. As the frame is double symmetric, the representation of the problem can be analysed by an inclined beam with appropriate boundary conditions. The inclined beam was discretized by 4 finite elements. The geometrical and properties taken into account in the analysis can be viewed in Figure 5.3.

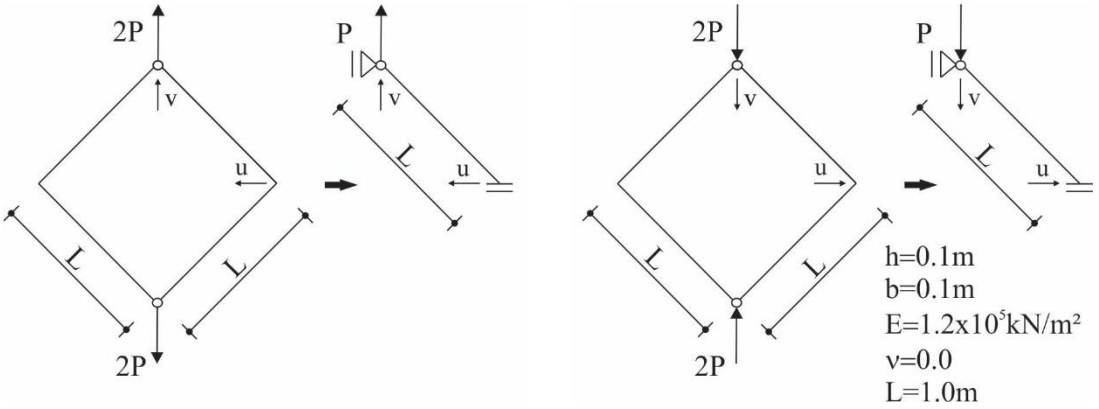

(a) (b)

Figure 5.3 – Lozenge shape structure. (a) Rods under tensile effects and (b) Rods under compression effects

The frame was also studied by Nogueira (2015), which analysed the problem with the positional formulation, considering the frame finite elements with degrees of freedom represented with position vectors.

The equilibrium trajectories with relation the horizontal (u) and vertical (v) displacements for superior and the right extremities of the beams, respectively, are the results analysed in Figure 5.4.

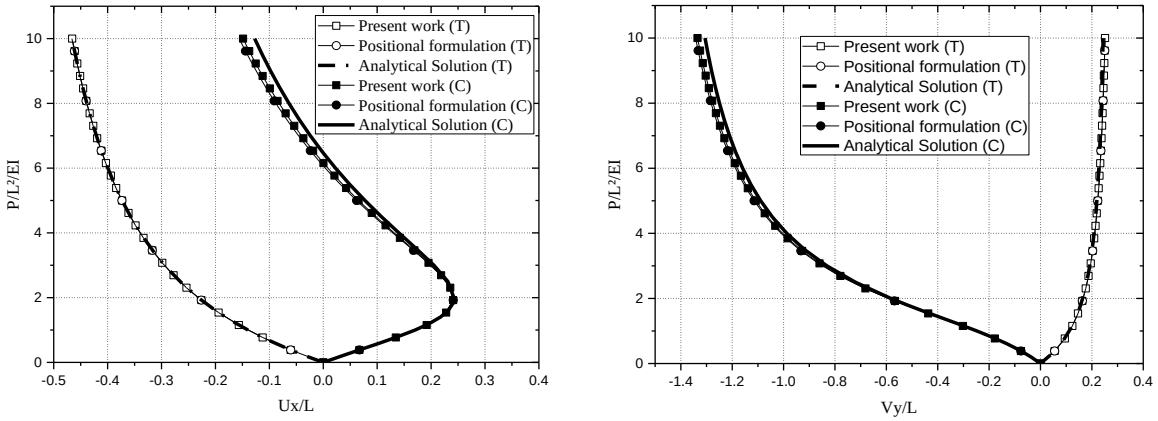

(a) (b)

Figure 5.4 – Equilibrium trajectories for: (a) Force versus Horizontal displacement and (b) Force versus Vertical displacement.

Figure 5.4a and b show the equilibrium trajectories for the cases in which the structure is subjected to tension (T) and compression (C) requesting. As can be seen, curves provided with the simulation performed in the present work are agreed with those picked from the literature.

5.2 Matrix-Fiber coupling

The following two examples validate the matrix-fiber coupling technique, between the two-dimensional finite elements and the bar/frame elements, proposed in chapter 4. The analysis are performed taking into account the elastic regime for all materials. Firstly, a bar axially requested is investigated. Next, a cantilever beam is used to evaluate the matrix-fiber coupling formulation in structures disposed to preferential flexural behavior.

5.2.1 Bar with axial load

A bar under a tension efforts was analysed with the bar and frame finite element embedded in the matrix. Two meshes coarse and refined were used to verify the formulation, Figure 5.5. Both the matrix and fiber materials were represented by cubic finite elements. The analysis was performed with 10 steps of displacement equal 1mm on the top surface of the column. The energy tolerance equal 0.001 was used to check the convergence at each displacement increment. All properties and the dimension description are presented at the same Figure 5.5.

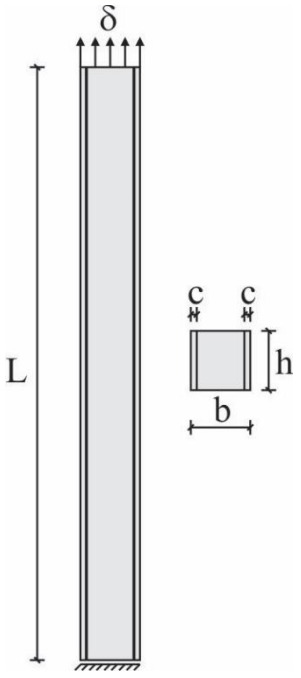

Geometrical configuration

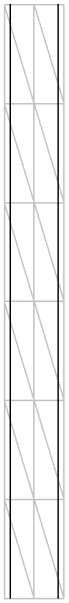

Coarse Mesh

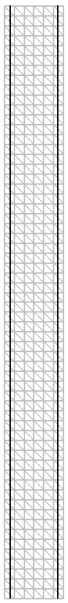

Fine Mesh

Matrix	
Ec	21GPa
Poisson	0.0

Fiber	
Es	210GPa
Diameter	12mm

L	3000mm
b	300mm
h	300mm
c	30mm

Geometry and properties

Figure 5.5 – Geometry and properties of the column studied.

Figure 5.6 shows the displacement resulted in the final configuration of the analysis and the numeration of the fiber elements for the coarse and fine mesh, respectively. The same displacement distribution was obtained for both meshes and for the analysis with the bar and frame embedded.

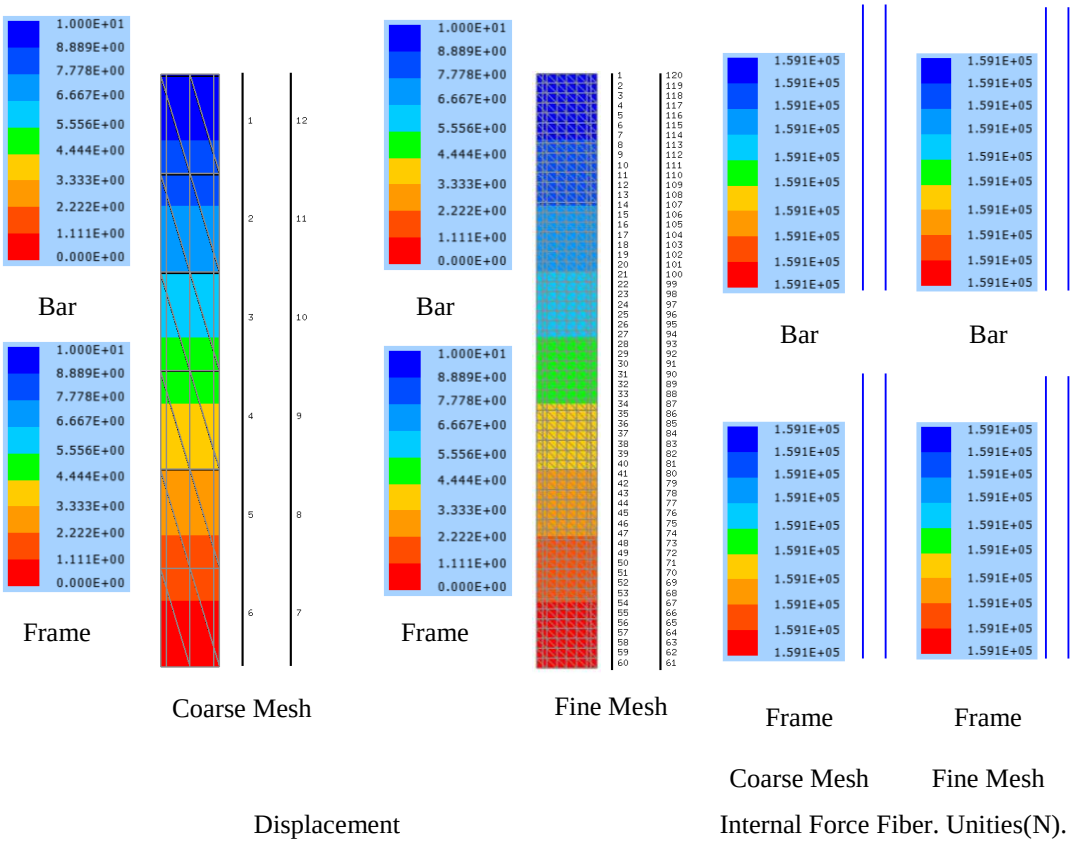

Figure 5.6 – Some results.

Figure 5.6 shows that the normal force on the bars is constant and the value is agreed with the analytical solution (158kN, approximately) obtained by the follow expression:

$$P_s = P\frac{E_s A_s}{E_s A_s + E_c A_c} \quad \text{or} \quad P_s = \delta_s \frac{E_s A_s}{L} \tag{5.1}$$

As demonstrated, the embedded technique used for the bar and frame finite elements present satisfactory results for the situations in which the structure is requested under uniaxial action. It was also verified that there is no difference between the simulations performed with the fiber represented by bar or frame elements.

5.2.2 Cantilever beam

Figure 5.7 shows a beam fixed in the left extremity under a uniform distribution load $(q = 50kN/m)$ for all its length. Such structure was analysed by Sampaio et al. (2015). The investigation of the embedded bar formuation under flexure is performed. The matrix and fiber properties are $E_m = 21GPa$, $\nu_m = 0$ and $E_f = 210GPa$, $\nu_f = 0$ and $A_f = 4cm^2$, respectively. The geometrical configurations are $L = 300\,cm$, $h = 20cm$, $b = 10cm$, $d = 3cm$, $h' = 14cm$.

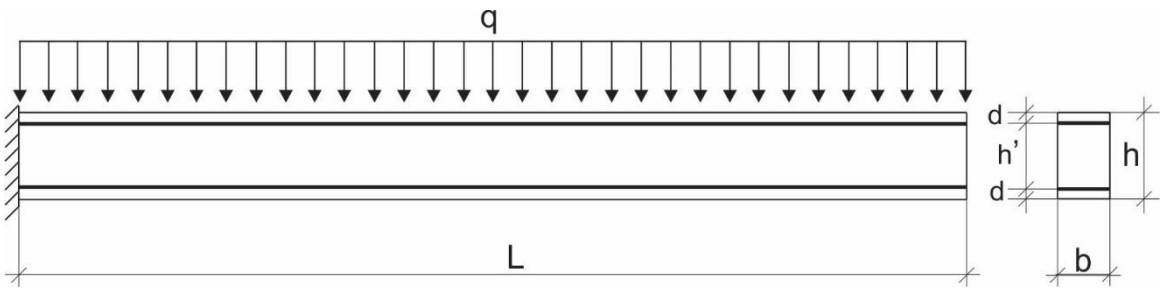

Figure 5.7 – Beam reinforced with fibers.

To such an example, the reinforcements were simulated by linear and cubic approximation bar finite elements, respectively represented in the Figure 5.8 with the nomenclature B1 and B2. For for the reinforcements represented by frame elements only the cubic approximation was considered. The results obtained from the simulations was compared with the answers presented by Sampaio (2014) and Sampaio et al. (2015). Although the frame element presents additional flexural and shear stiffness for this particular example such stiffness has not relevant effect, as can be seen in Figure 5.8 and Figure 5.9.

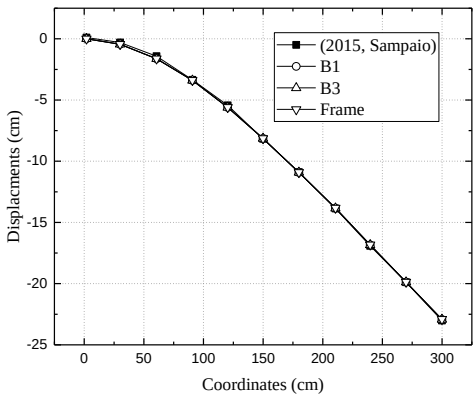

Figure 5.8 – The final position of the beam.

Figure 5.9 shows the distribution of vertical displacement for cases of the beam with and without reinforcements. As expected, the displacement of the beam without reinforcement is larger than beam reinforced, i.e., the embedded formulation plays consistent results. It also verified that identical values of displacements were obtained for the analysis with the reinforcements represented by bar and frame elements.

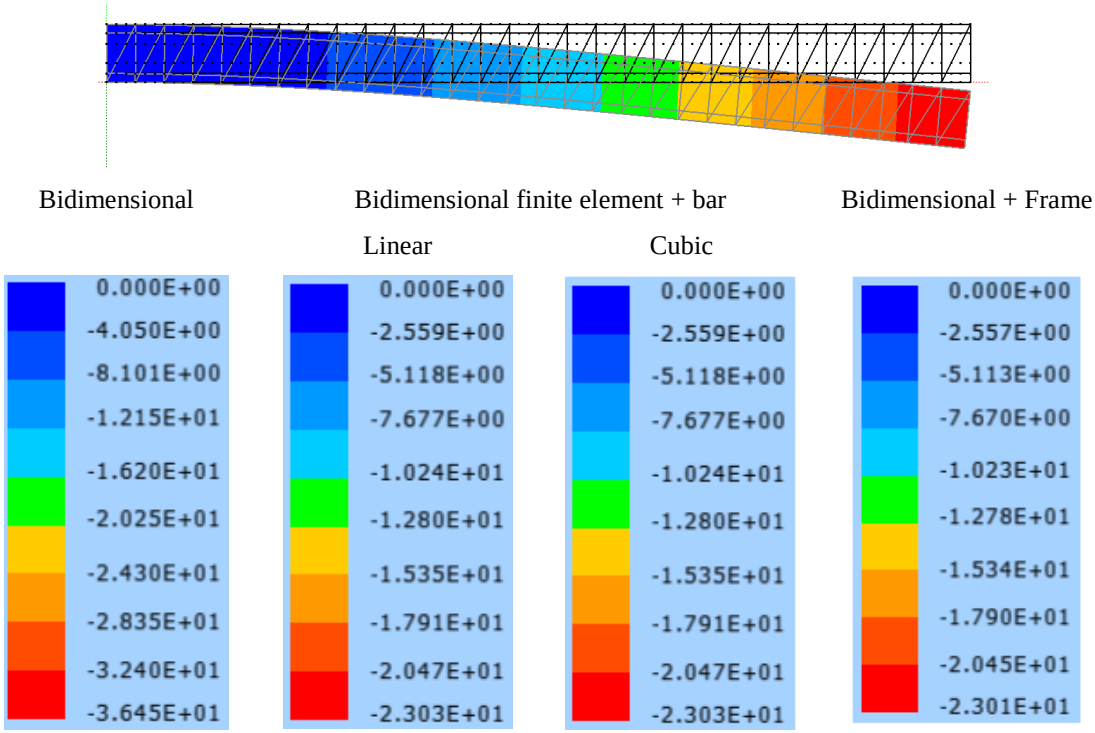

Figure 5.9 – Vertical displacement distribution.

Figure 5.10 shows that the uniaxial internal force distribution for the superior fiber represented by different finite elements has satisfactory results with the answer obtained by analytical formulation written in Eq (5.2).

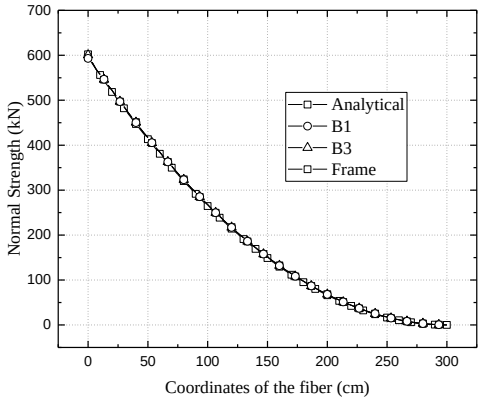

Figure 5.10 – Uniaxial internal force in the superior bar.

$$F_n = \pm \frac{3qh' E_f A_f}{E_m b h^3 + 6 E_f A_f h'^2} (x - L)^2 \qquad (5.2)$$

5.3 Elastoplastic examples

The one-dimensional plasticity model presented in chapter 4 item 4.1.2 is discussed with the following three examples.

5.3.1 Elastoplastic Models

The first example to discuss the plasticity formulation implemented concern of a simple tensile bar of length (L) equal 100mm, Figure 5.11. The elasticity modulus (E) equal 210GPa was adopted and the cross section area (A_0) 122.72mm².

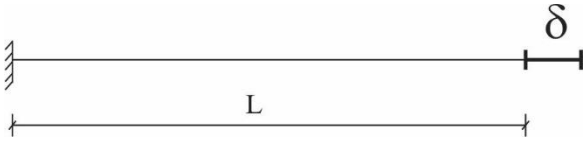

Figure 5.11 – Tensile bar.

The elastoplastic perfect behaviour was adopted with the tensile strength (σ_y) 500MPa, which corresponds of maximum internal force equal 61.36 kN. The bar was discretized by 10

linear finite elements. Twenty (20) steps of displacement (δ) of 0.05mm was applied on the right extremity of the bar.

Figure 5.12a and b shows the trajectory of equilibrium for the situation in which the bar is under tension and compression actions, respectively. For both numerical simulations, the maximum force value is agreed with the theoretical value estimated.

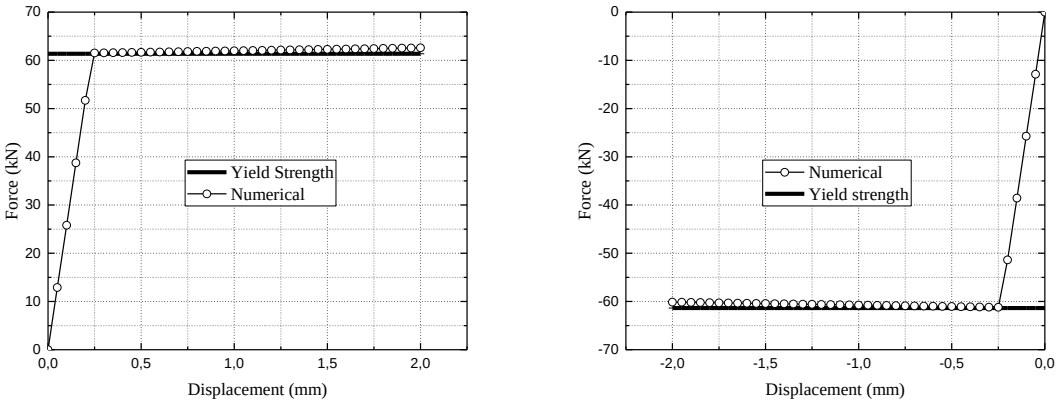

(a) (b)

Figure 5.12 – Curve force versus displacement (a) Traction bar and (b) Compression bar

5.3.2 Elastoplastic truss analysis

The Figure 5.13 shows the lattice geometry used to verify the elastoplastic model in a configuration in which more than 1 bar reaches its yielding from different load applied in the structure. The cross section area $A = 100mm^2$, the elastic modulus $E = 210GPa$ and the elastoplastic behaviour with the tensile strength equal $\sigma_y = 500MPa$ for all bars were adopted.

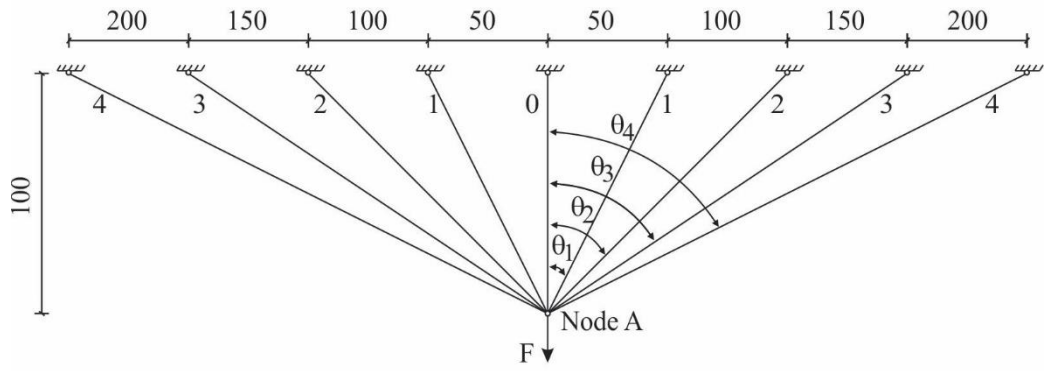

Figure 5.13 – Truss. Unity (mm)

The symmetry of the structure was taken account for the numerical analysis, see Figure 5.14a. Therefore, the value of properties of the vertical bar (bar 0) was divided per 2 ($EA_0 = EA/2$). Each bar was represented by 1 cubic finite element bar. The analysis was performed by displacement control with 40 steps of 0.05 mm vertically applied on the meeting node of the bars. Figure 5.14b shows that the curve force versus displacement obtained with the numerical simulation agrees with the analytical response.

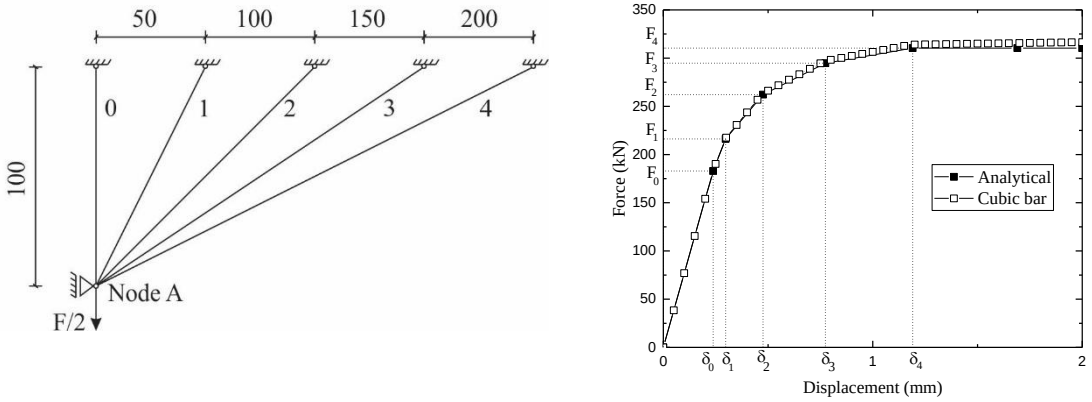

(a) (b)

Figure 5.14 – (a) Symmetric truss and (b) Curve: Force versus Displacement.

The equilibrium and compatibility equations were used to define the coordinates of the analytical curve. The critical points (slope change) are determined with the follows expressions:

$$F_i = \sigma_y A\left(1+2\sum_{k=1}^{m-1}\cos\theta_k + \frac{2}{\cos^2\theta_i}\sum_{k=m}^{n}\cos^3\theta_k\right) \tag{5.3}$$

$$\delta_i = \frac{\sigma_y L_0}{E}\sec^2\theta_i \tag{5.4}$$

where: i refers to the bar that has begun the plastic regime; k is the index summation; m is the number of bars that is in the plastic regime; n is the number of inclined bars for the symmetric structure; and, L_0 the length of the bar 0.

The bar 0 is the first bar to reach the plastic regime and there after the bars 1, 2, 3 and 4, sequentially. Therefore, the coordinates (F_0, δ_0) define the end of elastic regime of the structure and the equations (5.3) and (5.4) can be thus simplified and written as:

$$F_E = F_0 = \sigma_y A\left(1+2\sum_{k=1}^{n}\cos^3\theta_k\right) \tag{5.5}$$

$$\delta_E = \delta_0 = \frac{\sigma_y L_0}{E}\sec^2\theta_i \tag{5.6}$$

The peak load of the structure is defined when all bars is in plastic regime. This point occurs when starts the yielding of the bar 4. Therefore the equations (5.3) and (5.4) are defined as:

$$F_U = F_4 = \sigma_y A\left(1+2\sum_{k=1}^{m-1=n}\cos\theta_k\right) \tag{5.7}$$

$$\delta_U = \delta_4 = \frac{\sigma_y L_0}{E}\sec^2\theta_4 \tag{5.8}$$

The Figure 5.14b shows that once the peak load is reached the load remains constant while the strain level increases.

Figure 5.15 shows the level of stress in all bars always 1 load step before and after each bar reach its respective yielding regime. As can be seen the bars 0, 1, 2, 3 and 4 reach theirs limit tensile stress from load steps 5, 7, 10, 16 e 24, respectively.

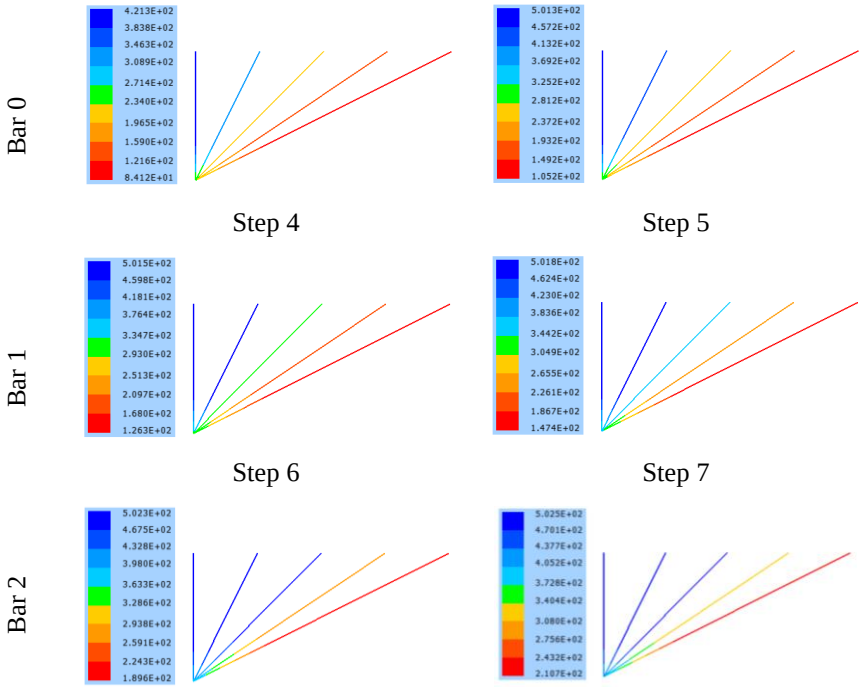

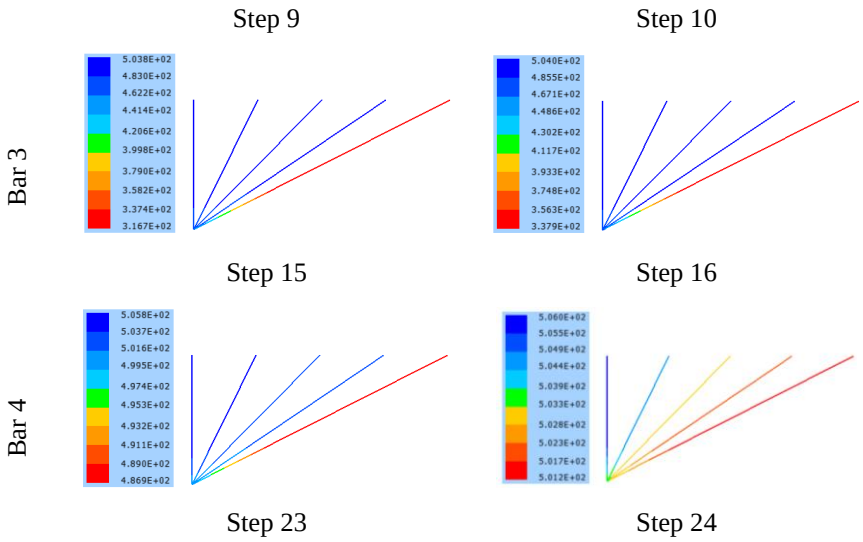

Figure 5.15 – Stresses. Unities (N/mm²)

5.3.3 Elastoplastic truss analysis: Traction and compression

Figure 5.16 shows geometry of the lattice structure analyzed. The main objective of the following example consists of the validation of the elastoplastic algorithm implemented in the situation in which in the structure there are bars under compressive and tensile regime.

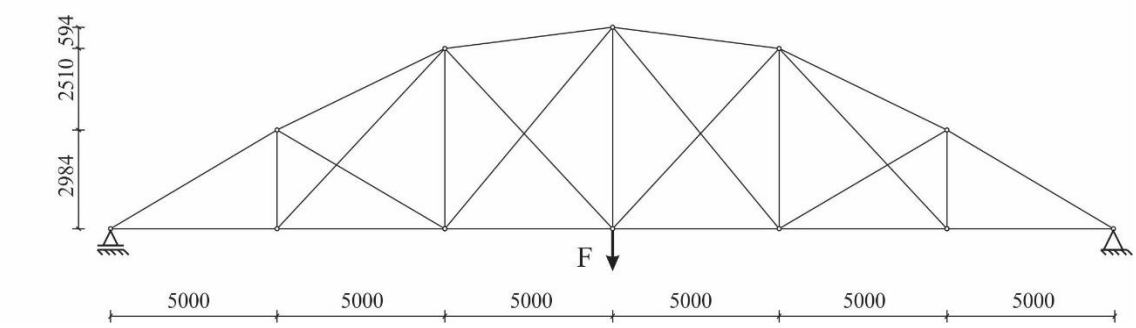

Figure 5.16 – Truss. Unities (mm)

Figure 5.17 shows the symmetry of the structure used to perform the numerical analysis and the area of the bars considered. The numbers inside the circle and triangles are the nodal numeration and the finite element number, respectively. Each bar of the structure was represented by one linear finite element of bar. Vertically in the node 4 it was applied 100 displacement increments of 1mm at the indicate direction and the equilibrium was reached with energy tolerance equal 0.001. The elasticity modulus is the same for all bars with value equal

210 GPa. The perfect elastoplastic with the tensile strength equal 100 MPa was taken into account.

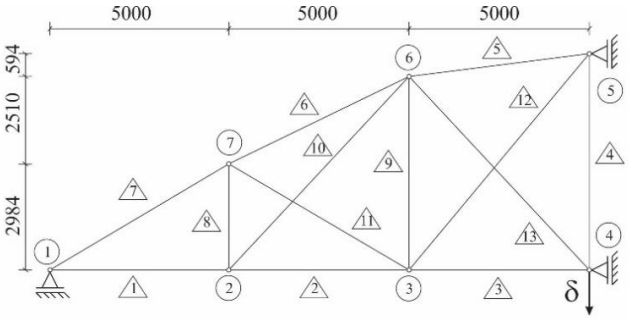

Finite element number	Area (mm²)
1,3,5,6 and 7	3303.219
2	2290.318
4,8,9,10,11,12 and 13	1045.159

Figure 5.17 – Symmetry of the structure, boundary conditions, nodal numeration and finite elements number. Unities (mm).

Figure 5.18 shows the final configuration position of the structure and the respective internal force of the bars. As can be seen, the horizontal bars 1, 2, and 3 are compressed while the elements 7, 6, and 5 are stretched.

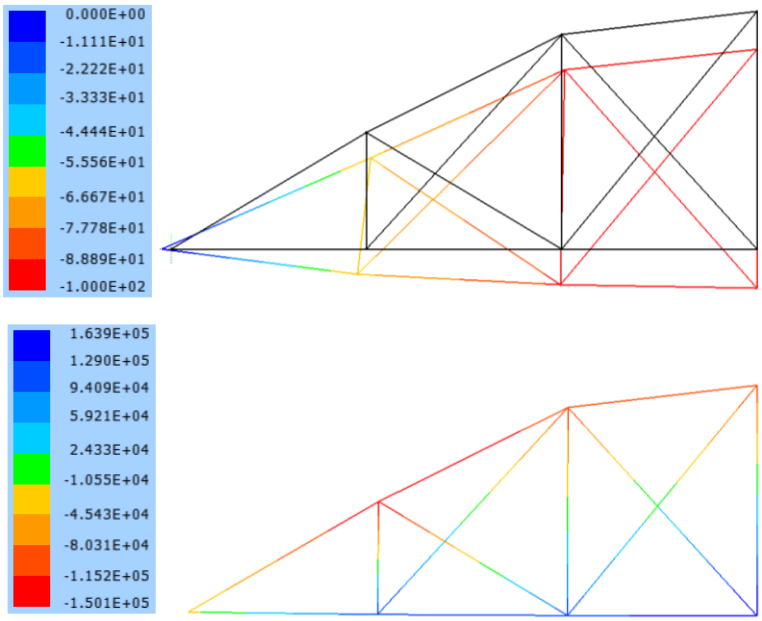

Figure 5.18 – Final configuration (a) Displacement with increased scale 100 times. Unities(mm). (b) Internal force. Unities (N)

Figure 5.19 shows the force versus displacement curve for the node 4 of the structure. Due to the symmetry used in the simulation the forces values obtained from the analysis was multiplied per 2.

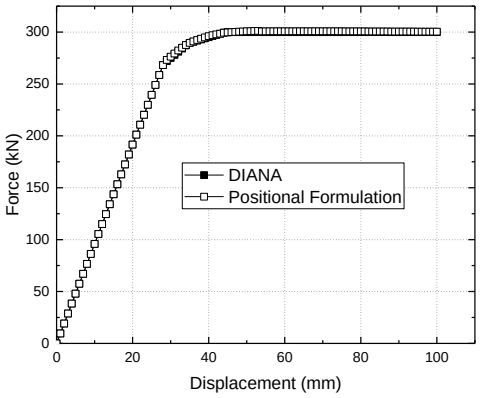

Figure 5.19 – Force versus displacement curve.

It verifies that the equilibrium trajectory is agreed with the results obtained from the code DIANA® (2017). The L2TRU finite element was used to perform the analysis in this commercial code. The same properties previously cited as well the increment of displacement and the tolerance criterion were adopted. The elastoplastic perfect model with the Von Mises criteria was also taken into account. The elastoplastic regime starts from 260kN (increment 28), approximately, and the maximum load that the structure supports occurs with the value equal 300kN (increment 45). From Table 12 the bars 2 and 6 determined the collapse of the structure as can be seen the yielding condition in tensile and compressed regime were respectively reached. Table 12 also shows that the Piola Kirchhoff and Cauchy stress are equals to the same increment of displacement applied which justifies the addictive strain decomposition for the plastic model.

Table 12 - Bar stress for the last displacement of load.

Finite element	Stress (MPa) Increment 28		Stress (MPa) Increment 45		Stress (MPa) Last Increment	
	Piola Kirchhoff	Cauchy	Piola Kirchhoff	Cauchy	Piola Kirchhoff	Cauchy
1	68.0938	68.1159	76.1783	76.2059	76.6886	76.7166
2	99.7186	99.7659	100.098	100.231	100.640	101.038
3	81.4593	81.4908	94.6546	94.6972	98.0583	98.1175
4	63.5426	63.5618	83.4103	83.4435	94.2478	94.2901
5	-93.1501	-93.1088	-100.522	-100.425	-97.7903	-97.6349
6	-81.5344	-81.5027	-99.9940	-99.9398	-100.468	-100.201
7	-79.2098	-79.1799	-88.5099	-88.4725	-88.7059	-88.6684
8	-3.24049	-3.24054	-24.0981	-24.0953	-25.1210	-25.1180
9	20.0505	20.0524	21.3051	21.3073	32.9765	32.9817
10	-49.7028	-49.7016	31.5551	31.5598	31.4865	31.4912
11	17.5364	17.5378	48.4875	48.4987	47.6770	47.6878
12	-37.6299	-37.6232	-59.9620	-59.9449	-75.4666	-75.4394
13	87.0638	87.0999	80.2886	80.3193	65.8978	65.9184

5.4 Plane stress plasticity

Some aspects of the plane-stress plasticity model presented in chapter 4 item 4.1.3 are discussed with the follows three examples.

5.4.1 Elastoplastic model bar (Frame)

The bar of the Figure 5.20 has length (L) 1000mm and the measure of the cross section (b,h) equal 50mm and 100mm, respectively.

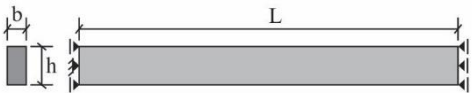

Figure 5.20 – Bar model.

This uniaxial bar model was analyzed by three different numerical configurations, Figure 5.21. Two elements the bi-quadratic quadrilateral and the cubic frame were used to test

the plane stress-projected plasticity model. Figure 5.21 show the model discretized by 98 quadrilateral elements and 10 cubic finite elements, respectively. Two configurations of boundary conditions were assumed to the analysis with the quadrilateral elements. In the case a.1 the transversal cross-section strains are free while in the case a.2 these strains are restricted. The latter case was assumed to compare with the results from frame elements once its kinematic does not allow the strain in the transversal cross-section. For the analysis with the frame element, case (b), all degrees of freedom were constrained on the left extremity and on the right extremity only the horizontal direction was restricted to enable the displacement application.

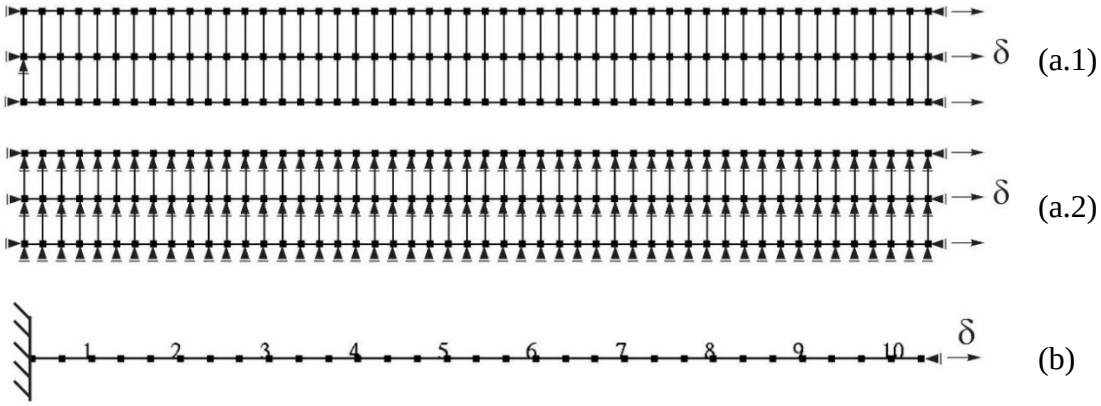

Figure 5.21 – Bar discretization.

The Figure 5.22 shows analysis of the bar for the three configurations previously discussed. The results consist of the bar under the perfect elastoplastic behavior with traction and compressive hypothesis. The poisson presumed for all analysis were 0.0. According to the elastic branch it can be seen the same stiffness for all simulations. Once the bar reaches the yielding stresses, defined by the force 1200kN, only the quadrilateral finite element with the boundary conditions configuration showed in Figure 5.21a.1 follow the typical elastoplastic perfect behavior. For the simulation performed by the other elements the trajectory of equilibrium continues showing an unrealistic stiffness (locking), even after reaching the maximum plasticity load.

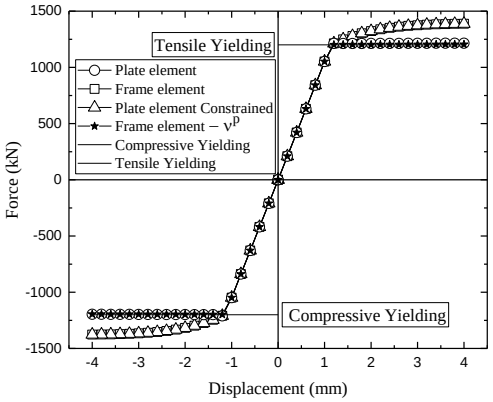

Figure 5.22 – Curve Force versus Displacement.

Such behavior occurs because the frame as long as the quadrilateral elements in the case a.2 have a state in which it is not allowed the transversal strain on the cross-section of the bar. So to release the frame element locking it was assumed the value 0.5 for the poisson on the Von Mises criteria (ν^p). When this value is assumed it is verified in accordance with Figure 5.22 that the curve presents results agreed with the analytical answer. To improve the convergence of the model only the diagonal terms from the elastoplastic tangent matrix $\mathfrak{C}^{ep}$ from Eq. (4.65) was considered.

5.4.2 Cantilever beam: plastic hinge

The plastic hinge formation is discussed with the cantilever beam presented in Figure 5.23.

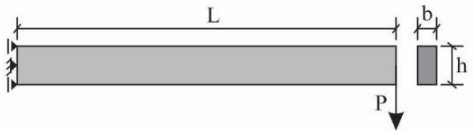

Figure 5.23 – Beam.

The length (L) 1000mm and the cross-section dimensions (b) 50mm and (h) 100mm were used. The elasticity modulus (E) considered is equal 210GPa. It was adopted the perfect elastoplastic with the yield stress (σ_y) equal 240MPa. The final 30 mm of displacement was applied in 15 steps of 2mm. The energy criteria equal 0.001 is used to assure the static equilibrium. The beam was discretized with 10 finite elements and the number of integration points assumed was 4x3.

Figure 5.24 shows the curve force-displacement for the right extremity of the beam. It observes that both analytical and numerical results present initially an elastic behavior. With 10mm of displacement, the structure presents loss of stiffness, which physically is associated with the begun of the plastic hinge process formation. The ultimate load analytically estimated in 30kN is reached for an equal displacement 15mm.

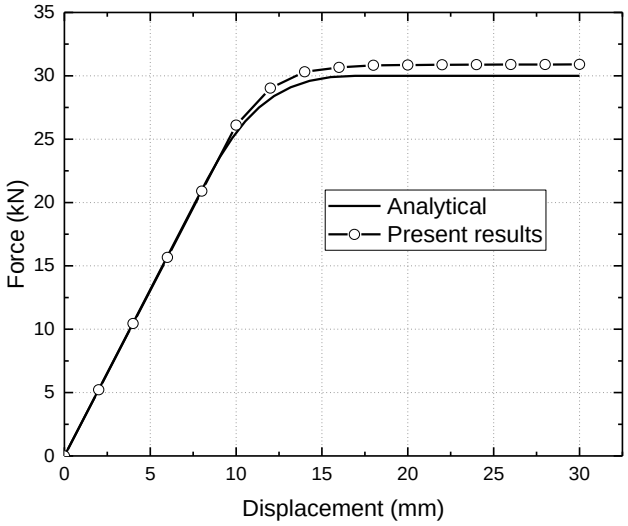

Figure 5.24 – Curve Force-Displacement on the right extremity.

The analytical expression that relates the load on the right extremity of the beam and the vertical displacement at the same point is presented by Lubliner (2006) and has the follow form:

$$P = \frac{\sigma_y b}{L}\left(c^2 - \frac{y^{*2}}{3}\right) \tag{5.9}$$

$$\delta = \delta_E \left(\frac{P_E}{P}\right)^2 \left[5 - \left(3 + \frac{P}{P_E}\right)\sqrt{3 - \frac{2P}{P_E}}\right] \tag{5.10}$$

where y^* is the distance between the longitudinal axes of beam and the fiber coordinate in the cross section where the yielding stress σ_y is already reached. The elastic displacement and ultimate elastic force (δ_E and P_E, respectively) are calculated for the case when the bottom and the top face of cross-section has reached the yielding criteria and therefore the stress distribution remains still linear.

$$P_E = \frac{2\sigma_y b c^2}{3L} \tag{5.11}$$

$$\delta_E = \frac{\sigma_y L^2}{3Ec} \tag{5.12}$$

5.4.3 Elastic-Plastic of Pure bending

A beam under a pure bending testing it was used to verify the behavior of the formulation which more than 1 cross section starts the elastoplastic regime for the same load applied in the structure.

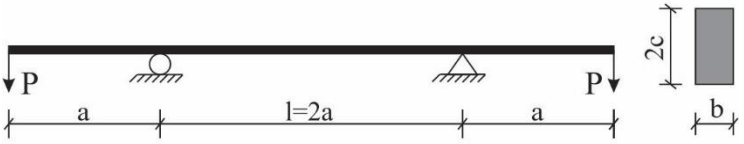

Dimensions (mm)	
a	2000
2c	100
b	50

Figure 5.25 – Beam.

The elasticity modulus (E) 210GPa was adopted to the analysis, the yield stress (σ_y) 200MPa and the perfect elastoplastic analysis was considered. In order to facilitate the analysis the symmetry of the structure it was taken into account, Figure 5.26. The analysis was performed under displacement control vertically applied in the left extremity. Thus, it was used 30 steps of 10mm. The energy tolerance considered was 0.001.

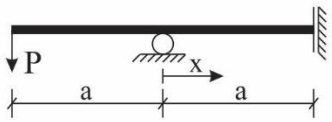

Figure 5.26 – Symmetry of the structure.

The structure was discretized by 4, 10 and 20 finite elements. The number of integrations points (IP) per elements was varied between 12, 30, 56 and 90 points. The distribution of integration points was done following the nomenclature 4x3, 6x5, 8x7 and 10x9 which corresponds to the number of points per element in the longitudinal and vertical direction, respectively.

Figure 5.27 presents the bending moments distribution for various load levels. The results are for analysis performed with 4 finte elements. The load values correspond to the steps 1, 5, 10, 15 and 30. It observes that the results plotted agree with the bending moment distribution expected. Between 0 and 200cm, the moment variation is linear while for the central span its value is constant. It also verifies that for the last two steps the beam is already in the plastic regime and therefore no moment variation between them is presented.

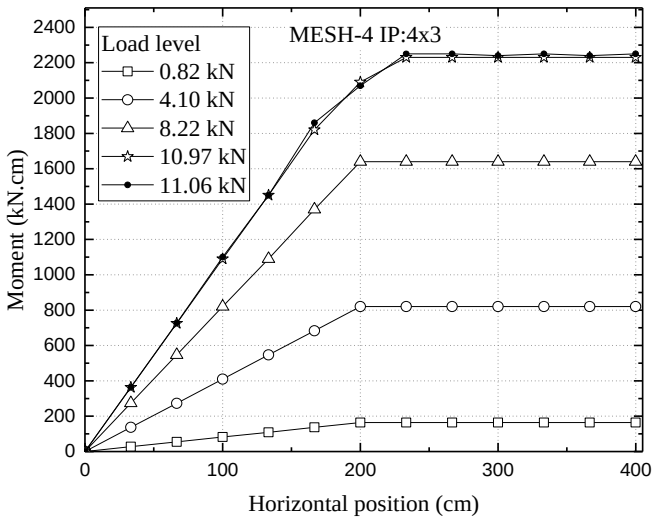

Figure 5.27 – Bending moments diagrams for some load levels.

Figure 5.28 shows two analyses of Force-Displacement relationship at the point of displacement application.

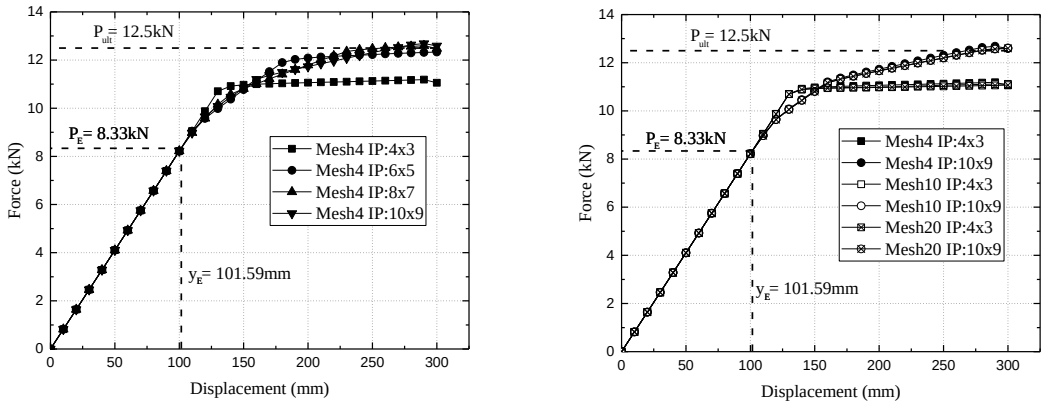

(a) (b)

Figure 5.28 –Force versus Displacement curve: (a) Changing the number of integration points and (b) Comparison with different mesh discretization.

Figure 5.28a presents the force-displacement curves for the structure discretized by 4 finite elements with different number of integration points. As can be seen, the equilibrium trajectory changed according to the number of integration points considered. For the analysis done with IP:4x3 the elastic regime is followed until the load equal 11kN, approximately, which is bigger than the analytical solutions 8.33kN. Once ended the elastic regime the curve presents the horizontal yielding tensile that defines the collapse of the structure. The ultimate load reached is smaller than the analytical resulted 12.5kN. On the other hand, for the analysis performed with more integration points, the elastic regime becomes close to the analytical answer as well the ultimate load. It verifies that once starts the plastic regime the stiffness of the structure is gradually reduced as long the displacement increase. This behaviour happens because the vertical number and distribution of the integration points at the cross section of the finite element, Figure 5.29.

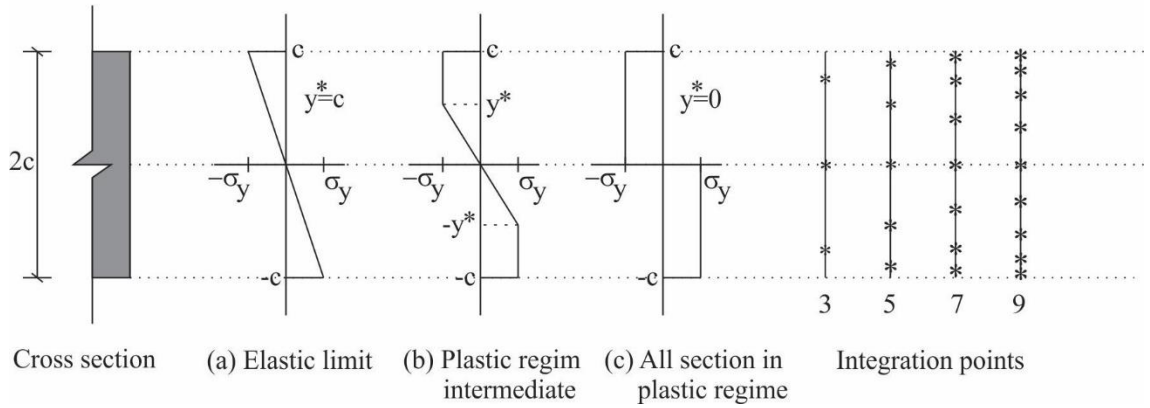

Figure 5.29 – Plastic mechanism of a cross section in pure bending.

When the element has only 3 integration points in the cross-section the elastoplastic behaviour is determined only by one integration point, if we take into account the symmetry of the section. Therefore, once reached the yielding tensile all section is considered under plastic state and thus the transition of the curve force-displacement between the elastic and plastic state is abrupt as previously discussed. However, for the section that presents more than one integration point verifies that the yielding criteria for each point considered is reached for different levels of displacements and thus justifies the gradual reduction of the stiffness of the structure.

The Figure 5.29b shows the h-refinement test performed to verify the convergence of the analysis. According to the three meshes used, the results obtained were the same. This

behaviour characterizes that the numerical convergence is reached even for a discretization with 4 elements. Curves with IP:4x3 and IP:10x9 were also plotted and all results were the same if it is compared the results obtained between different meshes.

The analytical answer to determine the end of elastic answer as well the yielding tensile was performed following the configurations presented in the Figure 5.29 and the configuration of the structure, Figure 5.25. In the transition between the elastic limit and the beginning of the plastic state (a) only the top and the bottom surface at the cross-section has the yielding tensile reached and therefore a linear distribution of stress can be assumed. For this case, it is possible write:

$$P_E = \frac{2}{3a}\sigma_y bc^2 \quad \text{and} \quad y_E(-a) = \frac{P_E a^2}{6EI}(2a+3l) \tag{5.13}$$

The calculation of the ultimate load takes all integration points of the cross-section under the plastic regime (c) and is predicted as:

$$P_{ult} = \frac{\sigma_y bc^2}{a} \tag{5.14}$$

5.5 Plasticity in the fibers

The embedded theory for the coupling technique between the matrix-fiber elements considering the elastoplastic behavior for the fibers is following validated.

5.5.1 Bar with axial load

The steel reinforcement bar located at the centre of the bar presented in Figure 5.30 is used to verify the coupling matrix-fibers with the fibers under elastoplastic behavior. The properties and the geometrical dimensions are ilustred at the same figure.

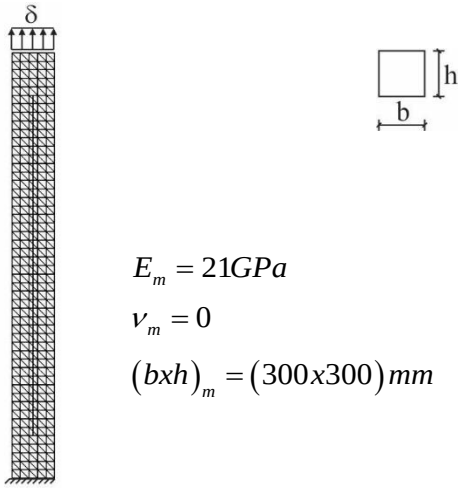

Figure 5.30 – Uniaxial bar.

The convergence in energy equal 0.001 was adopted to check the equilibrium. The total displacement of 10mm was progressively applied in 10 steps on the top extremity of the structure. Next, the results to the simulation performed with elastic and elastoplastic behaviors for the steel reinforcement bar are discussed.

Figure 5.31 shows the force-displacement curves measured at the top extremity of the reinforcement bar. The steel reinforcement bar was simulated by the bars finite elements as well as the two frame finite elements. It verifies that all curves agree betweem them. The analysis performed with the plastic behavior for the bar presents the maximum force equal 90.48kN which correspond to the tensile strength yield adopted.

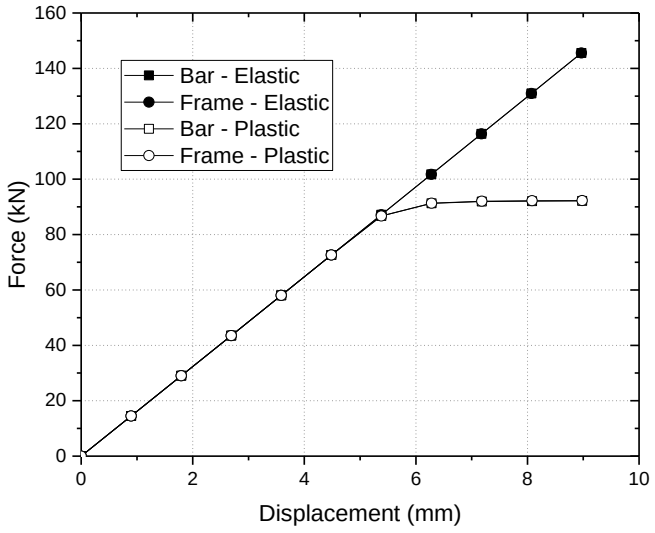

Figure 5.31 – Force-Displacement curve for the reinforcement bar.

Figure 5.32 shows the vertical displacement at the last increment displacement for the all analysis performed. As noted, all analysis results at similar strain distribution. There is a non-uniforme strain distribution only at the regions next to the extremity of the reinforcement bar while for all other cross-section the strain is more regular. Comparing the different reinforcement formulation verifies that all results are the exactly the same value of strain. Differences appears only when it is compared the values of the strain for the analysis performed with the reinforcement bar with elastic and plastic behaviors.

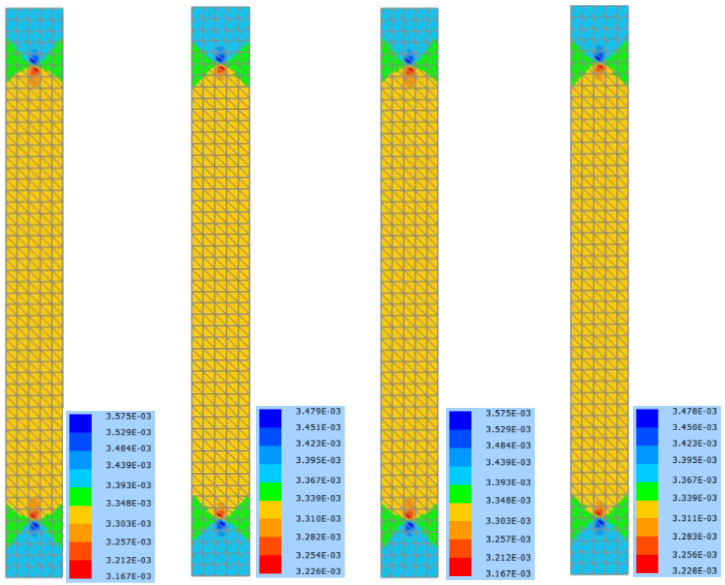

Figure 5.32 – Vertical strain distribution for the last step load.

5.5.2 Cantilever beam with plasticity in the fiber

To verify the elastoplastic behavior on the fibers for the matrix-fiber coupling formulation the same reinforced cantilever beam previously discussed in the topic 5.2.2 was considered. Excepting the tensile yield assumed for the reinforcement equal 500MPa, all other properties and geometrical dimensions previously described remains the same. The bar and frame elements were used to simulate the reinforcement bars of the structure.

Figure 5.33 shows the final displacement position of the cantilever beam analysed. For all results, the matrix elements were represented by the two-dimensional finite elements with

cubic approximation and assuming elastic physical behavior. The same cubic approximation was taken into account for the finite elements that represents the reinforcement bars. Such a figure confront the values of simulations performed for the situation of the structure without reinforcement bars and with the reinforcements represented by bar and frame finite elements under the elastic and elastoplastic model.

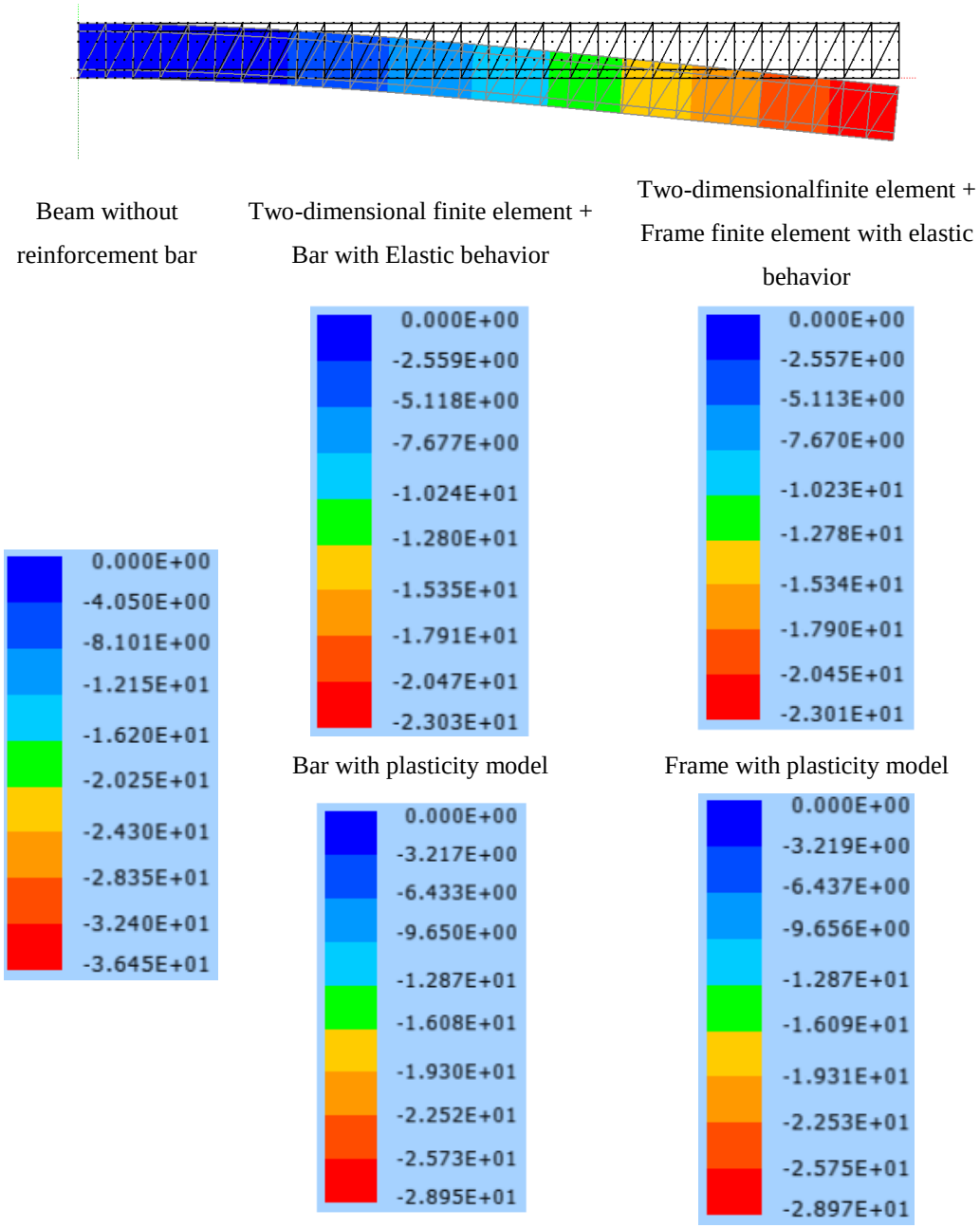

Figure 5.33 – Final displacement position.

As can be seen the consideration of the elastoplastic model for the reinforcement bars increase the value of the final displacement from -23,03cm to -28,95cm. However, such an amount remains less than the final displacement of the structure without reinforcements (-36,45cm).

Figure 5.34 shows the normal strength distribution throughout the reinforcement bars for all analysis considered. It verifies that the top and bottom reinforcements present the normal strength distribution consistent with the analytical expression written in (5.15). It also observes that, with the elastoplastic model assumption, the top and bottom reinforcements until the coordinate 150cm reach the yield stress, and therefore present plastic behavior. For values of coordinates bigger 150cm the reinforcements are under the elastic regime and therefore the normal strength distribution follows the expected behavior described by Eq. (5.15).

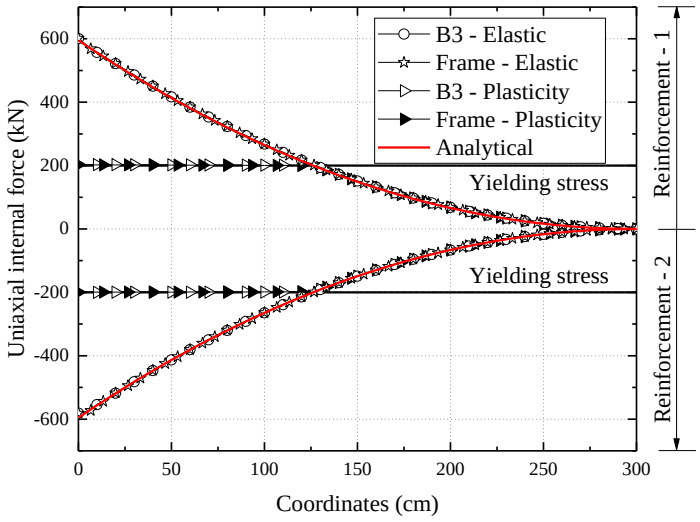

Figure 5.34 – Uniaxial internal force in both reinforcements.

$$F_n = \pm \frac{3qh' E_f A_f}{E_m b h^3 + 6 E_f A_f h'^2} (x - L)^2 \qquad (5.15)$$

5.6 Damage models examples

The general characteristics of the two damage models proposed in chapter 4 items 4.2 and 4.3 are discussed with the following examples.

5.6.1 Behavior of the softening

The behavior of the smeared damage model described on the topic 4.2 and the verification of the correct implementation is following discussed. To do so the quadrilateral geometry with the boundary, mesh discretization and loading configuration showed in the Figure 5.35 is assumed.

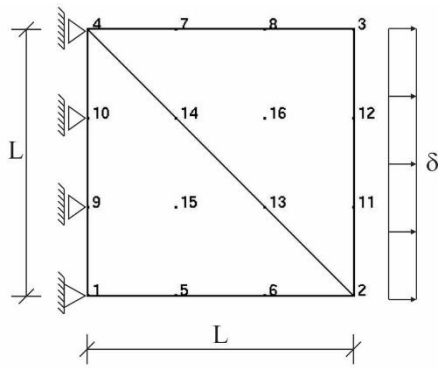

Figure 5.35 – Geomtry of the structure.

The equilibrium of the problem was reached with the value of the energy criterion equal 0.001. The initial value of the elastic modulus (E) supposed for the problem was 10.000MPa and the length L equal 1mm. The parameters responsible to describe the post peak behavior are the fracture energy, characteristic length and the shape of the softening curves. The same values 0.01N/mm and 0.707mm of fracture energy and the characteristic length were respectively adopted for all analysis. The end of elastic regime is defined with the value of the tensile strength equal 3MPa.

Figure 5.36a shows the equilibrium trajectory of such structure assuming linear, bilinear and multilinear softening curves, while Figure 5.36b presents the stress-strain curve for loading and unloading conditions, only for the linear softening shape.

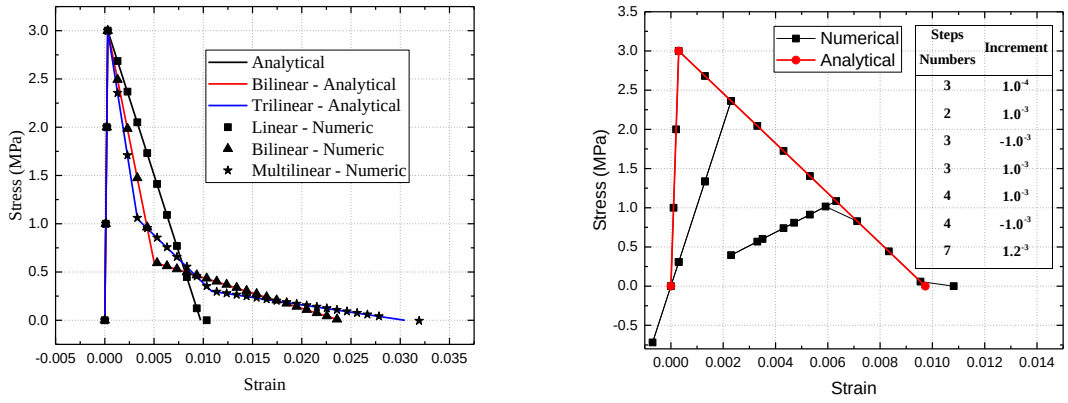

(a) (b)

Figure 5.36 – (a) Differents softening curve shapes subjected only loading process and (b) Load and unloading analysis with linear softening curves.

The analytical curves plotted into the Figure 5.36a and b refer to results obtained for alfa and beta coefficients presented in Table 13.

Table 13 – Parameters for the softening' curves.

Linear			Bilinear			Trilinear		
i	α_i	β_i	i	α_i	β_i	i	α_i	β_i
1	1.00	1.00	1	1.00	1.00	1	1.00	1.00
2	0.00	0.00	2	0.20	0.20	2	0.35	0.35
			3	0.00	0.00	3	0.10	0.10
						4	0.00	0.00

The analysis was performed with the displacement control. For all curves of Figure 5.36a before reaches the tensile strength it was adopted 3 increment of 1.0^{-4} mm and in the softening branch for the linear, bilinear and trilinear curves were assumed 10, 25 and 30 steps of 1.0^{-3}mm, respectively. For the curve plotted into Figure 5.36b the increment of displacement is showed at the same figure.

Figure 5.36a shows that assuming the same values of fracture energy and characteristic length with different shapes of softening curves changes the value of the ultimate strain. For the linear softening curve, the ultimate strain recorded was 0.0097 while for the trilinear and multilinear cases were 0.0239 and 0.0305, respectively.

Figure 5.36b shows that once initiated the damage process the stiffness of the structure decrease and under a loading and unloading process there is no accumulation of inelastic strain.

The damage process occurs only when the tensile strength is reached, and, once gotten the stiffness of the structure is affected for both tension and the compression configuration.

5.6.2 Strain localization – Mesh Sensitivity

The follow example addresses the mesh sensitivity discussion for smeared model implemented over a situation with failure localization zone. To do so a specimen under uniaxial traction and dimensions 50x25x25mm³ (length x height x thickness, respectively) was adopted. The elasticity modulus (E) equal 21GPa and Poisson null were used to the analysis. It was applied 60 increment of displacement equal 0.002mm on the right side of the bar while on the left extremity remained constrained. The energy control equal 0.001 was assumed to determine the equilibrium convergence. Three different meshes constructed with quadrilateral elements were tested, as illustrated in the Figure 5.37. A smaller tensile strength 3.5MPa was considered for the hatched elements to force the strain localization while the others ones its value was 7.0MPa. The linear softening and the fracture energy supposed equal 0.1N.mm/mm were taken into account. The curves force-displacement measured at the right extremity is showed in Figure 5.37a. Different values of characteristic length (h) in accordance with the bandwidth softening were assumed to provide the mesh objectivity. Figure 5.37b shows once initialized the strain localization the middle element of the bar undergoing softening while the others unloads elastically.

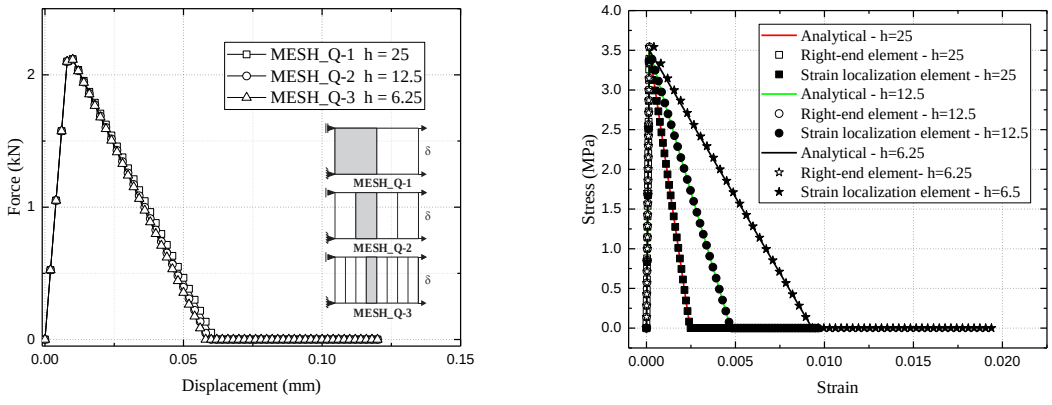

(a) (b)

Figure 5.37 – Results of the analysis.

5.6.3 Beam notched under three point support

The follow example consists of a beam notched under three point supports, Figure 5.38. This is a standard test done in laboratory to determine the fracture energy (G_f) of the material. The test involves a beam supported in its extremities under a load applied to the middle of the length.

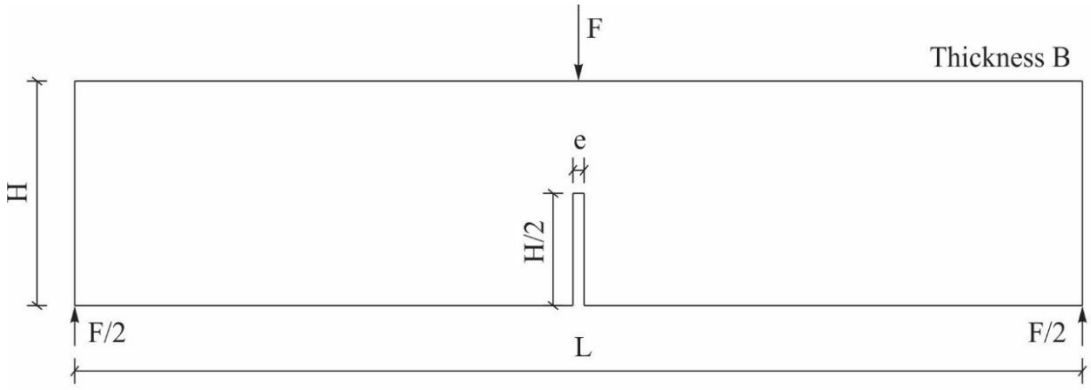

Figure 5.38 – Beam notched.

Table 14 presents the dimensions of the beam and properties of the concrete used to the follows simulations. All dimensions, properties and experimental test results were withdrawn of the work performed by Reinhardt and Kormeling (1983).

Table 14 – Geometry and Properties.

Heigth (H):	100mm
Thickness (B):	100mm
Length (L):	450mm
Elasticity Modulus (E):	20GPa
Poisson (ν):	0.20
Tensile stress (fct):	2.4MPa
Fracture Energy (Gf):	0.113N/mm

The mesh discretization was done by finite triangular cubic elements, Figure 5.39. Each element has 7 hammer points. It was applied 100 increments of 0.01mm. The convergence adopted was 0.0001 in force and displacement and 0.001 in energy. However, during the analysis it was verified that the first convergence reached for all increments was in energy.

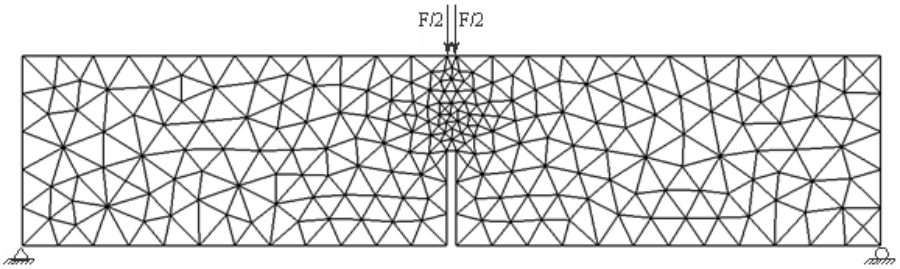

Figure 5.39 – Mesh.

Softening curve shape discussion

Taking into account the rotate crack model the structure was analyzed with three different softening curves assuming the same ultimate strain ε_{ult} equal 7‰, approximately. Figure 5.40 shows the three softening curves adopted and the parameters values α_i and β_i used in the models. Although the ultimate strain ($\varepsilon_{ult} = k_{ult}$) and the fracture energy (G_f) are the same for the three curves as can be seen the area under the curves (G_f/h) are different due to the crack band parameter. The crack band (h) adopted for the linear, bilinear and multilinear softening curves were 13mm, 34mm and 44mm, respectively. The bilinear softening was assumed according to prescription suggested by CEB FIB Model Code (2010) while the multilinear softening was adjusted to the Hordijk et al. (1986) softening curve.

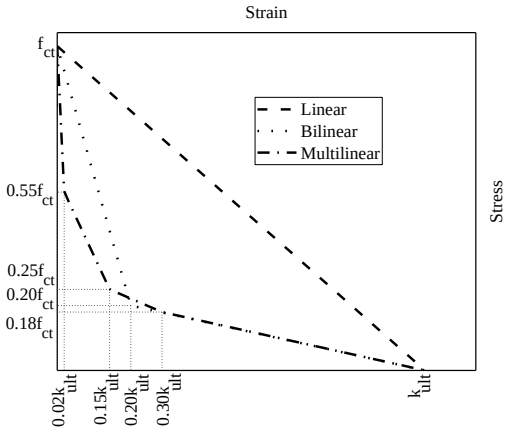

Figure 5.40 – The three softening branch adopted.

Figure 5.41a shows in the final configuration that the collapse of the structure occurred vertically to the point of load application. The figure presented refers to the last increment of

displacement with the scale 10 times increased. According to Figure 5.41b the equilibrium trajectories obtained by the numerical solutions are agreed with the experimental results, i.e. the same global stiffness with a linear branch, follow to the peak load and the softening branch. The elastic behaviors for the three simulations are similar until the value of force equal 1200N, approximately. Following, the concrete starts to present more clearly its degradation and reaches the peak load for different values of force and displacement. So, as can be seen the softening curve has direct influence over the dissipation rate of energy represented by the crack activation and consequently the global collapse of the structure. The dissipation rate of energy in the analysis decreased according to the following order of softening curve: linear, bilinear and multilinear. This behavior is agreed with the total area under the softening curves that was presented in Figure 5.40. Figure 5.41b still shows that the slopes for all curves in the post-peak branch are the same, which indicate that in this stage, the major crack is entirely open and therefore the shape of the softening curve has no more influence.

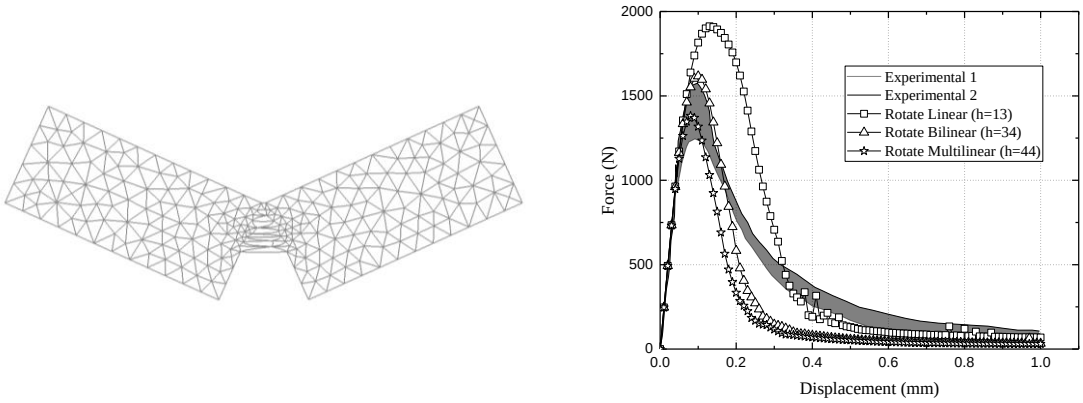

(a) (b)

Figure 5.41 - Last increment of load and the scale 10 times increased and (b) Equilibrium of the structure.

Figure 5.42a shows that the crack zone occurs on the middle of the beam upper the region notched. It can be also seen that the integration points located on the vertical direction of the notch presents enable cracks with the biggest intensities (blue color). The Figure 5.42b shows a zoom of the crack zone for the simulations performed by the three softening curves and the legends that refers to the parameter (k) of the model.The intensity of the crack activation (k) is related to the degree of stiffness degradation of the material, which is evaluated in the integration points of the finite elements. From a physical point of view, Figure 5.42 shows a

preferred path for the crack opening, illustrated by the cracks with the blue color. Such characteristic indicates the formation of a macro-crack that starts on the top of the notch and has its propagation vertically until the point of the load application. The cracks in red color are associated with the micro-crack diffuses that is a characteristic of a typical damage zone.

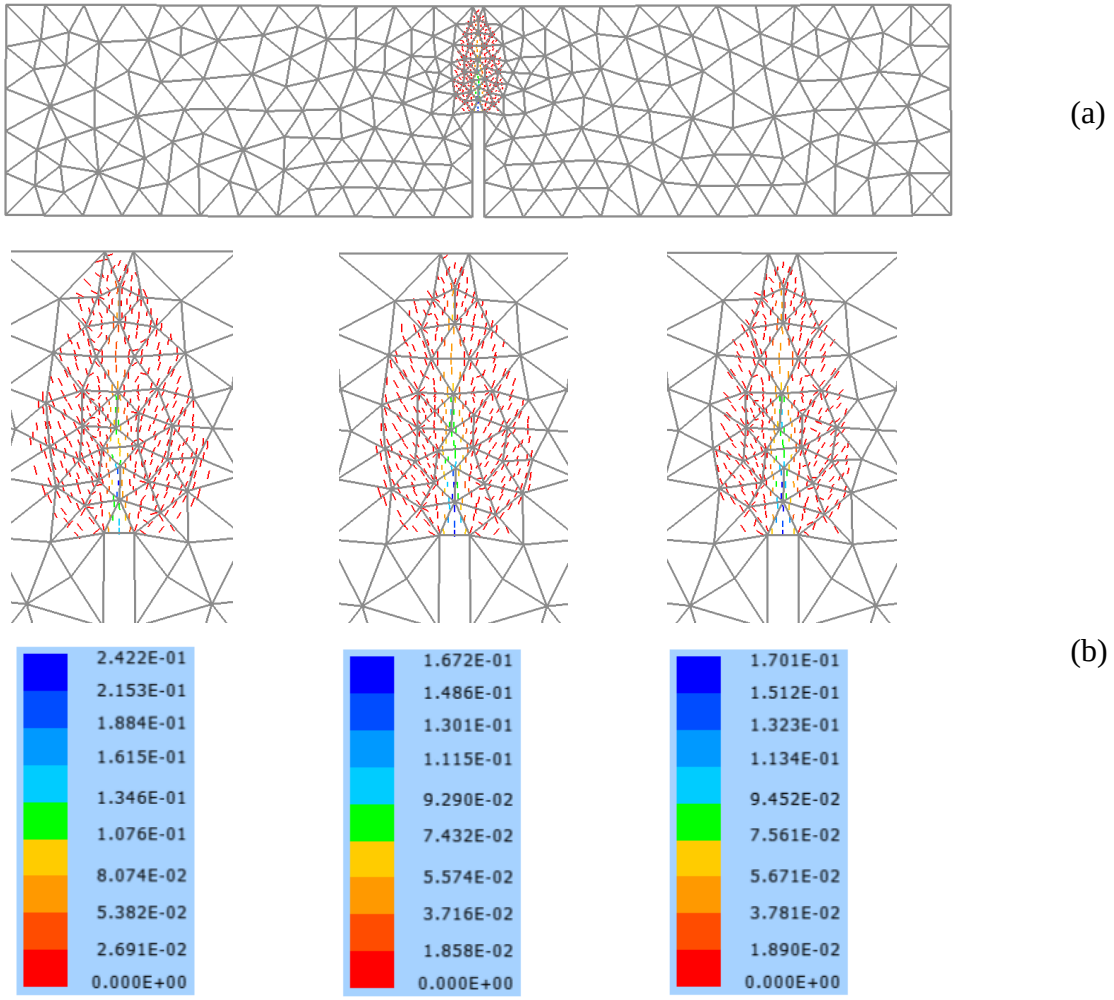

Figure 5.42 – Crack patterns. (a) All beam and (b) Detailed crack for the different softening curves: (b.1) Linear, (b.2) Bilinear and (b.3) Multilinear. Unities(mm).

Rotate and Fixed crack model confrontation

Figure 5.43 shows that the curves resulted from the simulation with the rotate as well fixed models before the peak load is similar for all analysis. However, the peak load reached from the fixed crack analysis are bigger than the results obtained from the rotate model for the same softening curve and the same crack band. The behavior of the post-peak obtained with the

fixed model distances more from the experimental results than the answer done by the rotation model. The stiffness degradation direction of the integrations points of the the finite elements, which the cracks are enabled, is the explanation for this behavior, as is follow written.

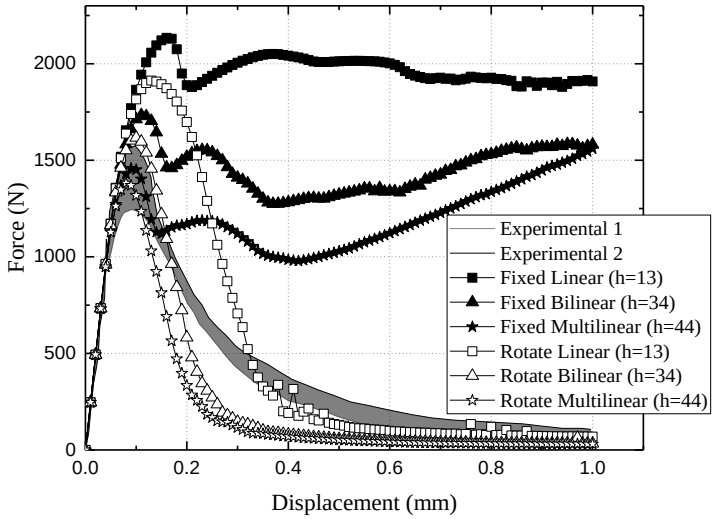

Figure 5.43 – Fixe-Rotate comparison.

Figure 5.44a shows the crack zone configuration for the analysis performed with the fixed crack model. It can be seen the cracks pattern is similar those obtained from the rotate model presented in Figure 5.42. However, according to Figure 5.44b the cracks located precisely on the middle of the beam has vertical direction and as long they move away from the notched the cracks presents others directions. For the upper part of the beam, the cracks have horizontal direction, which is resulted from the compressive zone. Such behavior characterizes that the direction of the stiffness degradation of the finite elements does not offer a way that enable a propagation of the major crack in the vertical direction, differently from the simulation performed with the rotatate model. In conclusion, this explains why the equilibrium trajectory discussed with Figure 5.43 does not show the softening behavior obtained from the experimental test and the results from the rotate model simulation.

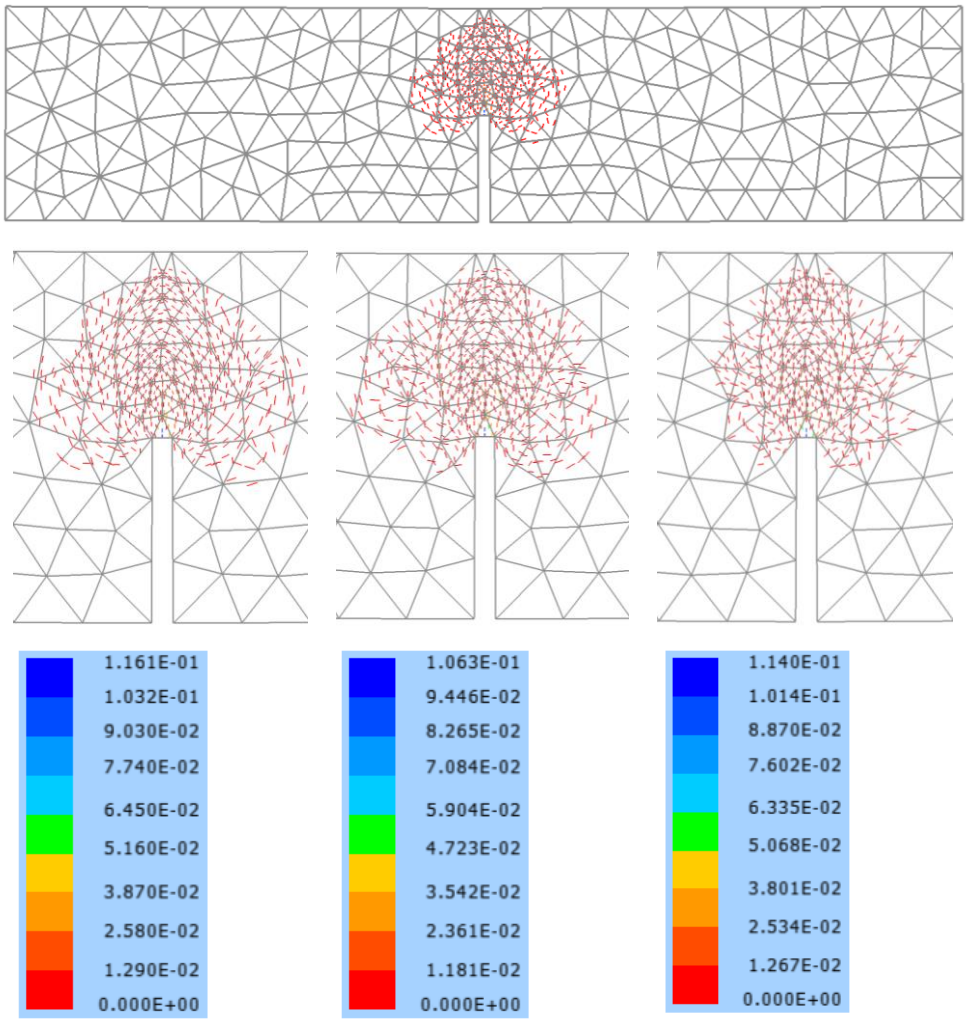

Figure 5.44 – (a) Crack zone of the beam Linear Softening and (b) Detailed crack for the different softening curves: (b.1) Linear, (b.2) Bilinear and (b.3) Multilinear. Unities(mm).

5.6.4 Damage model plane state

The follows example discuss the behavior under loading and unloading cases of the damage model described in topic 4.3. To do so a quadrilateral configuration, with dimension L equal 1mm, composed by two triangular finite elements was considered, Figure 5.45. In such example, the increment of load is applied at the right edge while the left edge of the structure is constrained. The Table 15 presents all material properties taken into account.

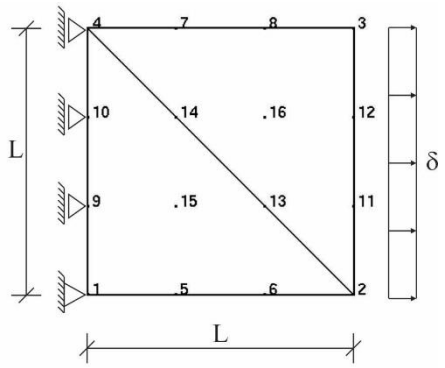

Table 15 – Material properties.

Elasticity modulus (GPa):	10
Compressive strength(fc) (MPa):	10
Tensile strength (ft) (MPa):	3
Fracture energy (Gf) (N/mm):	0.010
Equivalent length (h):	0.707

Figure 5.45 – Configuration of the example and properties of the material.

The linear softening behavior is adopted to simulate the material after the maximum tensile strength. The compression behavior is linear elastic until reached the yield of compressive stress, and it stays with this value for any strain calculated. The equilibrium was accept for value of energy equal 0.001.

Figure 5.46 shows the Stress-Strain relationship with the increment of loads applied at the left edge of the structure.

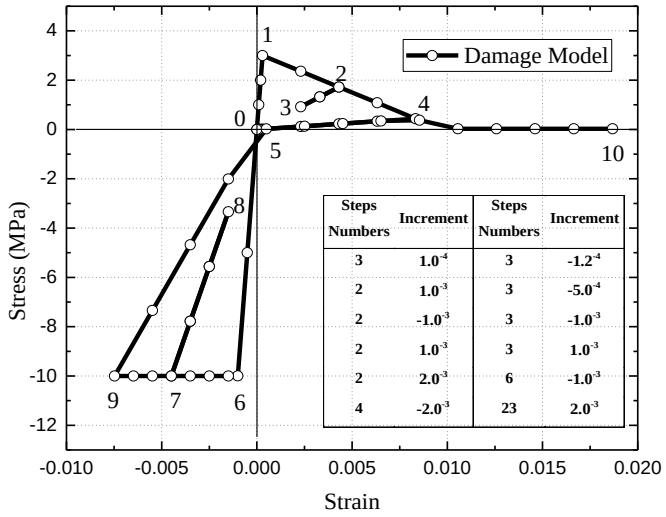

Figure 5.46 – Stress-Strain relationship.

At the beginning, the material presents an elastic linear regime, which correspond the branch between the points 0-1. In the point 1 the tensile strength is reached and the stress starts to decrease as long the material is stretched, in other words the damaging process is initialized. In the point 2 the structure is elastically discharged until the point 3 and next is reloaded until point 4. It should be noted that during the reloading process after point 3 the damage of the

material restarts to increase only after the tensile stress reaches again the value previously obtained in point 2. The inclinations of the branches between the points 1-2 and 2-4 are the same due to the linear softening curve adopted. At the point 4 stage, the structure is completely discharged until point 5. Between the points 5 and 6 the material presents a linear elastic behaviour under compression. It emphasizes that the material initially presents a linear elastic behaviour even though in traction it has already been damaged. Next, the linear curve continues until 10MPa, which correspond to the compressive strength of the material. At point 7 the material is discharged until 8 and subsequently recharged again until point 9. From point 9 the structure is stretched again and as can be seen the compressive stress linearly decrease. At point 5 the material returns to have tensile stresses with the same damage level already presented when the structure was being under tensile action. Then, the structure continues to be stretched until point 10 when the values of stress are null, this fact indicates the complete failure of the material.

5.7 Reinforced concrete beams

Two under and over reinforced concrete beams are follow investigated to verifies the implementation of the embedded theory, used to couple the matrix-fibers elements, working together with the physical nonlinearities models discussed in this thesis.

5.7.1 Under-Reinforced beam under four point flexural test

The results of the experimental four-point flexural test beam studied in this section were picked up in Tavares (2006) and Tavares et al. (2008). For this under-reinforced beam, the crushing of the material in the transversal section of the maximum flexural moment does not have a significant effect on the failure of the structure. The Figure 5.47 shows the geometrical dimensions for the beam as long the positions of the reinforcement bars.

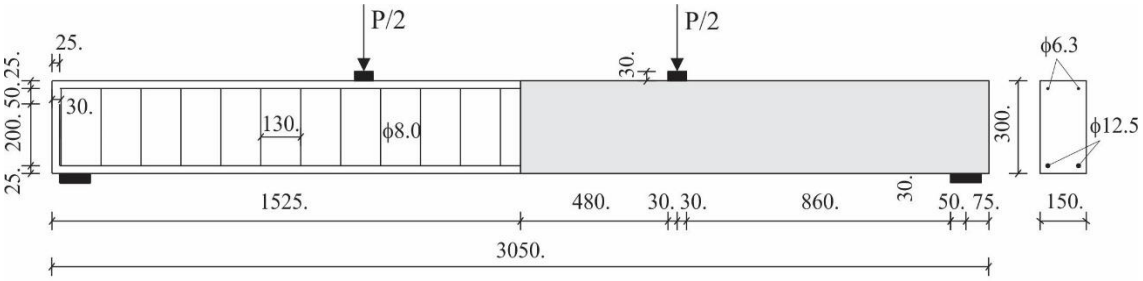

Figure 5.47 – Beam configuration. Unities (mm).

The materials properties used in this simulation are summarized in Table 16.

Table 16 – Material properties.

Steel		Concrete	
Diameter (mm)	Yield Stress (MPa)		
6.3	551	Elasticity modulus (GPa)	38
8	572	Compressive strength (fcc) (MPa)	44.00
12.5	597	Tensile strength (fct) (MPa)	3.17
-	-	Fracture energy (Gf) (N/mm)	0.144

The fracture energy was estimated according CEB FIB Model Code (2010) with the follow expression.

$$G_f = 73\left(f_{ck} + \Delta f\right)^{0.18} \Rightarrow G_f = 73(44)^{0.18} \Rightarrow G_f = 0.144 N/mm \qquad (5.16)$$

For the numerical simulation, it was taking into account the symmetry of the structure. The displacement control was applied with 80 steps of 0.25mm. The cubic triangular elements for the concrete and cubic elements for the steel were used, as follow illustrated:

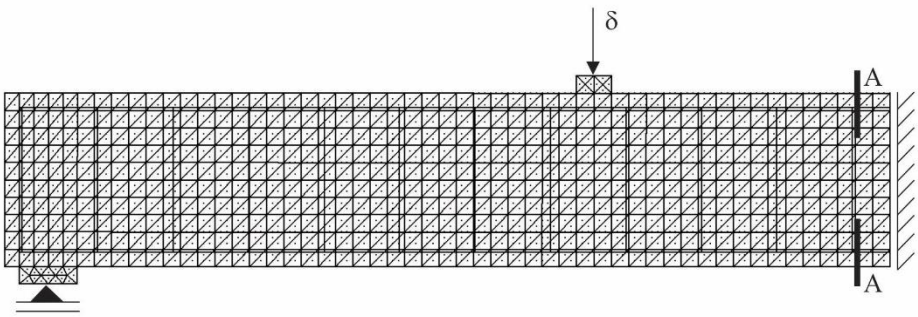

Figure 5.48 - Symmetrical structure.

The numerical analysis was performed with the two damage models presented in itens 4.2 and 4.3. Remembering that the first model taking into account the degradation of the material once reached Rankine criteria, while the second one assumes the degradation for tension and compression forces for the two directions of bi-dimensional problems. For each of damage models, the influence of the steel reinforcement of the beam was analyzed with the bar and frame finite elements. At last, for all previous consideration two shape of softening curves linear and multilinear were considered being the multilinear case calibrated in accord with the Hordijk et al. (1986) curve, Eq. (5.17).

$$\frac{f(k)}{f_{ct}}\begin{cases}\left(1+\left(c_1\frac{k}{k_{ult}}\right)^3\right)e^{\left(-c_2\frac{k}{k_{ult}}\right)}-\frac{k}{k_{ult}}\left(1+c_1^3\right)e^{\left(-c_2\right)} & if\ \left(0<k<k_{ult}\right)\\ 0 & if\ \left(k_{ult}<k<\infty\right)\end{cases} \qquad (5.17)$$

Figure 5.49 shows the values of parameters (α,β) of the multilinear softening curve. The crack band length or equivalent length (h) equal 120 mm was estimated considering the ultimate strain for the steel approximately equal 0.002.

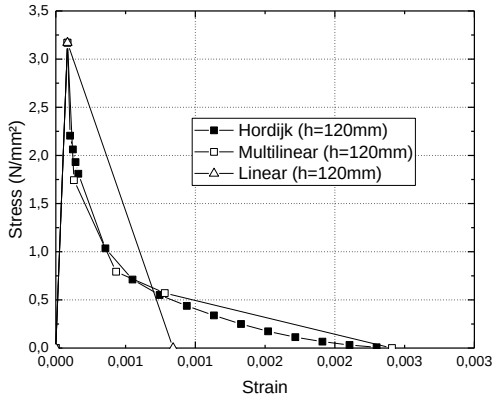

(a)

i	α_i	β_i
1	1.00	1.00
2	0.55	0.30
3	0.25	0.15
4	0.18	0.02
5	0.00	0.00

(b)

Figure 5.49 – (a) Softening curves and (b) Parameters of the multilinear softening curves.

Figure 5.50 shows that all numerical results are well agree with the equilibrium trajectory obtained from the experimental test. The curve values are the deflection measured at the bottom face of the symmetry cross-section and the load taken from the point of displacement application. It observes that all curves present three branches with different slopes. The first

branch, for the displacement between 1 and 2.5mm refers to the elastic behavior of the beam. The second one it starts with the cracking moment value and finish when the beam reachs the maximum force. The slope of the second branch changes, which physically represents a reduction of the structural stiffness. Lastly, the last branch starts with displacement 12.5 mm, approximately, and the horizontal trajectory indicates that the steel reaches its yield strength and therefore the collapse of the structure is achieved.

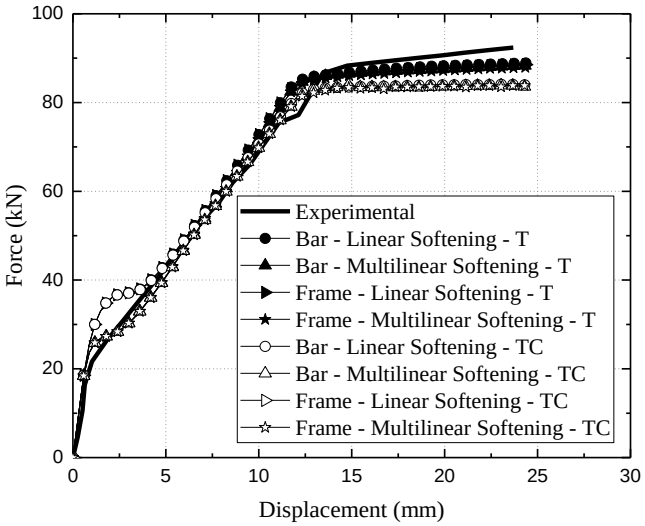

Figure 5.50 – Load versus Displacement.

According to Figure 5.50 it can be seen that for both damage models adopted, here symbolized by T of tension and TC of tension-compression, similar equilibrium trajectories are obtained. This means that the crushing of concrete does not present a substantial effect on the global collapse of the structure and therefore the failure of the beam happens under tensile stresses during flexure.

The shape of the softening curve is related with the energy release ratio during the damage process of the structure. In accordance with the Figure 5.50, the adoption of the linear or multilinear softening had direct influence in the cracking moment of the beam. For the analysis performed with the linear softening the intensity of force applied at the instant of the cracking moment was equal 37kN, that is bigger than 23 kN, which was the value reached for the multilinear softening cases.

Regarding the type of the finite element considered to represent the steel reinforcement, the equilibrium trajectory plotted showed there is no difference between the results obtained with the analysis performed with the bar and frame finite elements. In other words, the

contribution of the shear and the bending stiffness of the bar are not relevant to the global behavior of this structure, as already expected.

The SecTrans software developed by Haach (2010) was used to calculate and compare the moment-curvature diagram obtained with the results of the finite element analysis, Figure 5.51. The input data for the concrete were the elastic modulus, the tensile strength with linear softening and compressive strength with Parabola-Rectangle diagram. To represent the steel were considered only the tensile strength equal 597MPa and the elastic modulus. All other values correspond to the same presented in Table 16.

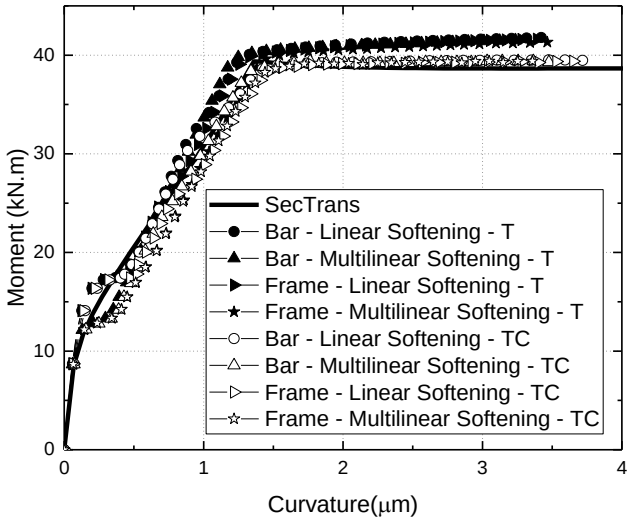

Figure 5.51 – Moment-Curvature diagram

Figure 5.51 indicates a satisfactory agreement between the curves of moment-curvature plotted. The same three branches presented for the load-displacement graphics are also visualized in the moment-curvature diagram. As can be seen depending of the softening curve adopted the cracking moment varies between 12.5kN and 17.5kN and the ultimate capacity supported by the beam correspond to the value of moment approximately equal 40 kN.m.

The Figure 5.52 and Figure 5.53 show some results for the analysis performed with the bar finite element representing the steel reinforcement, the damage model only taking into account the degradation due to the traction criteria with the linear softening curve, (Bar – Linear Softening - T).

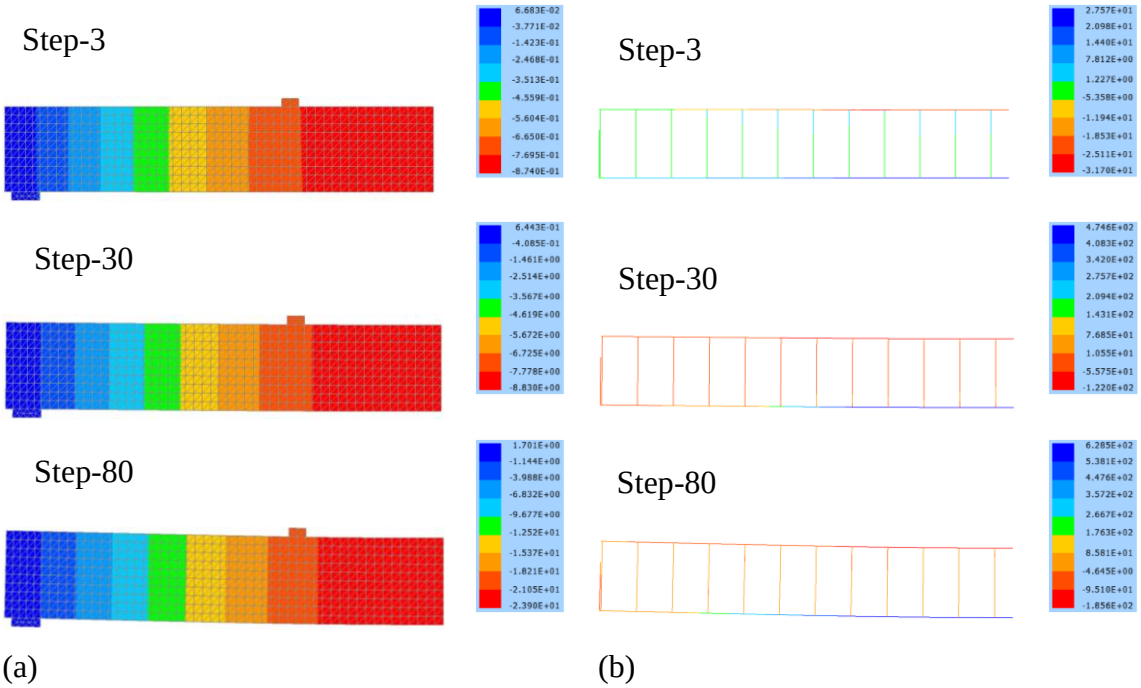

Figure 5.52 – (a) Vertical displacement (mm) and (b) Cauchy stresses (N/mm²).

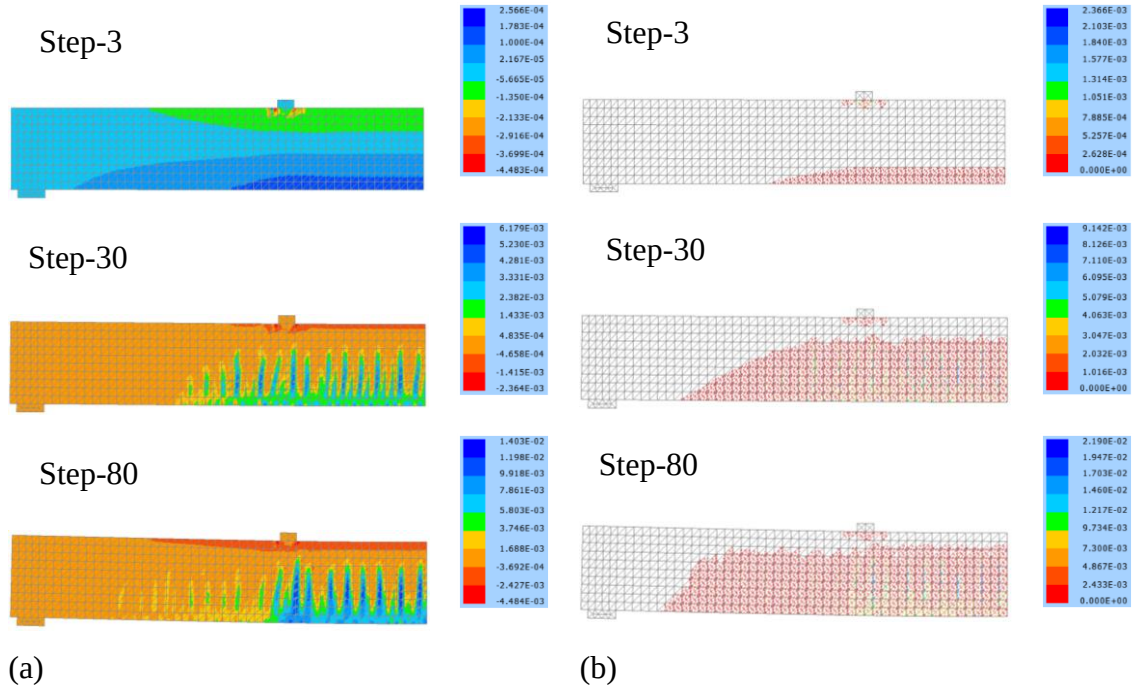

Figure 5.53 – (a) Horizontal strain and (b) cracking pattern.

According to displacement configuration the largest displacement occurs for sections located on the middle third of the beam. Such value increase as long as the load displacement

is applied, the maximum values of displacements in the three steps presented are -0.87, -8.83 and -23.90 mm, respectively.

Excepting the upper longitudinal bar all steels present tension stresses. The bottom longitudinal bar is the bar most requested to tension being the only one that reaches the plastic behaviour, as can be seen in the step 80. Such plastic behavior happens in the same region that the beam has the most significant vertical displacements.

The tension and compressive regions of the beam it verified with the plot of horizontal strain distribution. As showed, the cross-sections located between the application of the load and the right extremity of the beam present similar strain configuration. In such region, the bottom and upper cross sections are under tension and compressive regime, respectively. Differently, of the step-3, that presents a uniform strain distribution; in the steps 30 and 80, it can be seen vertical regions with the most significant strain. The plot of the cracking pattern show that such region present the most advanced damaging process.

5.7.2 Over-Reinforced beam under four point flexural test

Figure 5.54 shows the configuration of the beam under four-point bending test considered to be investigated. The difference between this example and the beam analysed in the previous section 5.7.1 is that this one is over-reinforced and therefore it was designed to collapse into domain 4. Such consideration suggests that the crushing of the material in the transversal section of the maximum flexural moment have a significant effect on the failure of the structure, differently of the previous beam.

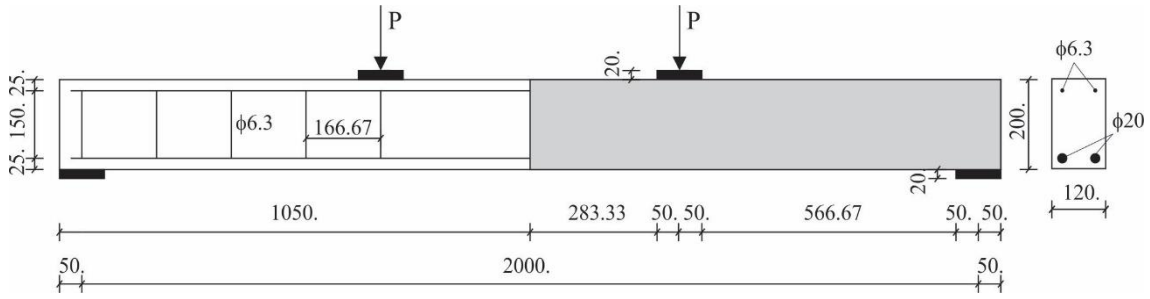

Figure 5.54 – Beam.

The symmetry of the structure was taken into account to execute the numerical simulation, as shows the Figure 5.55. The analysis were performed with displacement control,

80 steps of 0.5mm was applied. The convergence of the model was assumed with the energy criteria equal 0.001.

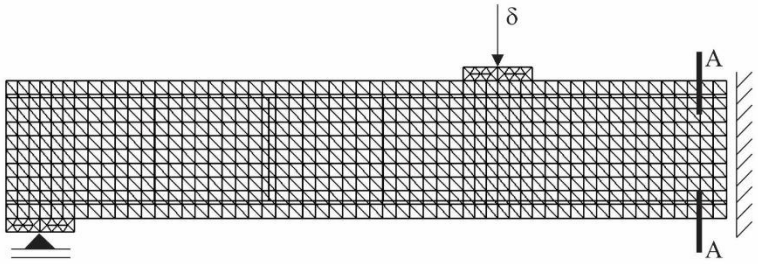

Figure 5.55 – Numerical model.

The physical properties of steel consist on the yield plasticity strength (f_y) equal 500MPa and the elasticity modulus of 210GPa. The elasticity modulus of the concrete was considered equal 20GPa and its tensile behaviour after the tensile strength (f_{ct}) 2.2MPa following a linear softening branch with fracture energy equal (G_f) 0.139Nmm/mm. The compressive behaviour it is linear until the compression yield (f_{cc}) with the value equal 20MPa. The equivalent length (h) adopted was 60mm.

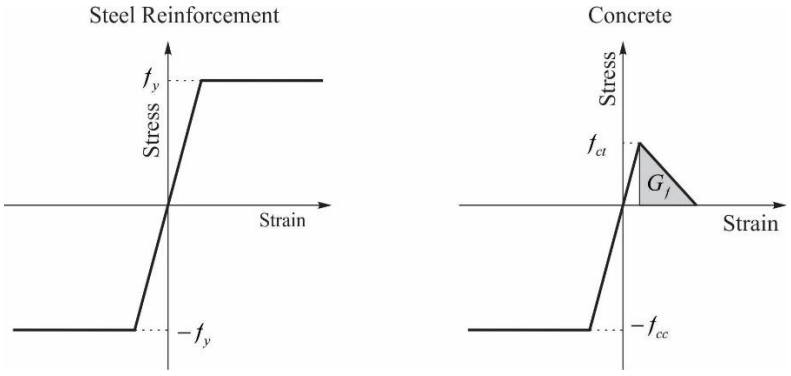

Figure 5.56 – Material Physical behaviour.

Figure 5.57 shows the curves of force versus displacement. The forces were computed from the displacement point application while the displacements were picked on the bottom of the mid-span length.

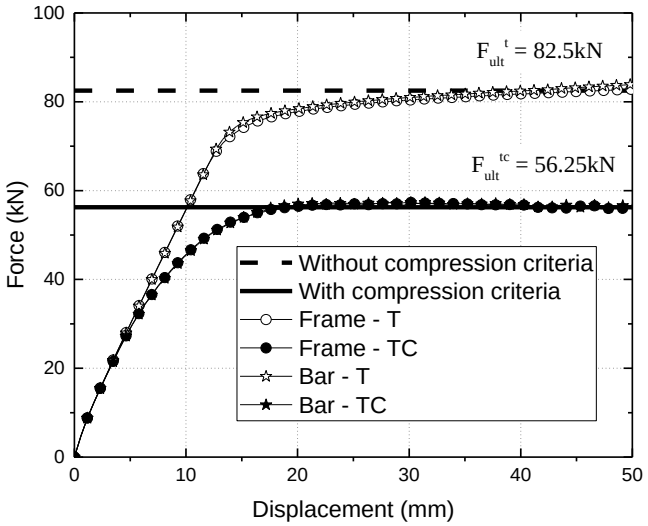

Figure 5.57 – Equilibrium trajectory.

As can be observed in Figure 5.57, two types of curves were obtained from the simulations performed with the beam in question. Curves with the yield around to 82.5kN and others with 56.25kN, which results in 31.82% of difference between them. The curves with the highest yield consider only the degradation of the material associated to the traction criteria, i.e. there is no stiffness penalization for the compression strength. On the other hand, the curves related to the yield 56.25kN take into account the criteria under tension and compression regime to evaluate the stiffness degradation of the concrete. So, faced this results it can be concluded, as expected, that the crushing of the concrete has a significant effect in the failure prediction of this structure.

The two estimative of ultimate forces showed in the Figure 5.57 were calculated with the equilibrium of transversal section subjected to the maximum flexural moment. The two estimative differs from each other due to the consideration or not of the crushing concrete. Such equations are follow written.

$$M = \frac{F_{ult}^{tc} L}{3} = A_{s'} f_y \left(d - d'\right) + f_{cc} b_w x \left(d - 0.5x\right) \tag{5.18}$$

$$M = \frac{F_{ult}^{t} L}{3} = A_s f_y d \tag{5.19}$$

where, $A_{s'}$ and A_s are the area of the cross-section for the upper and bottom longitudinal bars, respectively; d the distance between the upper surface of the transversal section until the bottom longitudinal bars; d' the distance between the upper surface of the transversal section

until the upper longitudinal bars; L the length of the beam; b_w the width of the transversal section; f_{cc} the compressive strength of the concrete; f_y the yield plasticity strength; χ the neutral axis depth; F_{ult}^{t}. and F_{ult}^{tc} are the ultimate forces with and without the compressive criterion, respectively.

Still according to the Figure 5.57, for both damage models the steel reinforcements were simulated with the bar and frame finite elements. According to the curves, it could be verified that independently of the finite element used the equilibrium trajectory obtained presents the same behavior. The previous observation implies that the steel reinforcement bars of the structure are mainly subjected to the uniaxial forces and in this sense, the flexural and shear effects can be neglected.

Next, a general discussion between the results obtained by the two damage models used in the analysis is performed. It was only considered the results with the model simulated for the steel reinforcement bar represented by the bar finite element once, as already discussed, the using of the bar or frame elements does not affect the global behavior of this structure.

Figure 5.58 shows the final displacement configuration of the beam. It verifies that the displacement pattern is similar for both cases and the intensity differs less than 1% between them. Taking into account only the damage criteria in traction (a) the maximum displacement was equal 48.60 mm while for the damaging criteria in traction and compression (b) it was 49.14 mm.

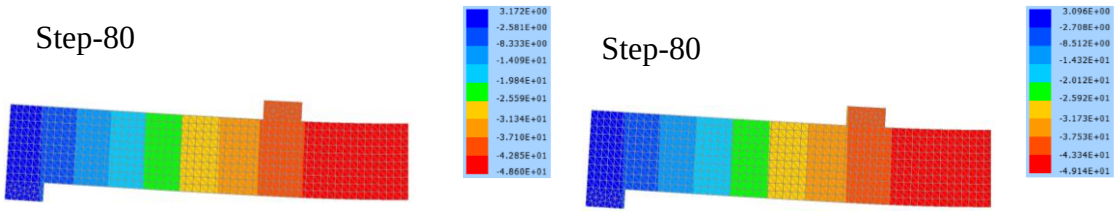

(a) T (b) TC

Figure 5.58 – Vertical displacement (mm)

Figure 5.59 shows the stresses distribution of the beam for the increment of load in the steps 3, 30 and 80. It observes that the highest stress value occurs on the third middle span that was the sector with the highest displament. In such region, the top and bottom face of the cross section presents compressive and tensile efforts, respectively. In the step 3, the damage process

initiated does not affect the global linear elastic behavior of the structure. Therefore, there is no substantial difference between the stress distribution calculated with the both damage models (a and b). At step 20, the neutral axle depth for the mid-span cross section for the beam simulated by the model (a) is lesser than the neutral axle depth of the model (b). Such difference occurs because in the model (b) some points at top face reach the yield compressive strength, defined as 20MPa, and therefore a larger compressed region is necessary to satisfy the equilibrium of the section. Step 80 shows cleary the difference between the compressive and traction stress distribution obtained with the two models. For the model (a) the value of the compressive stress on the top face of the most required cross section is around 85MPa while for the model (b) is 20MPa.

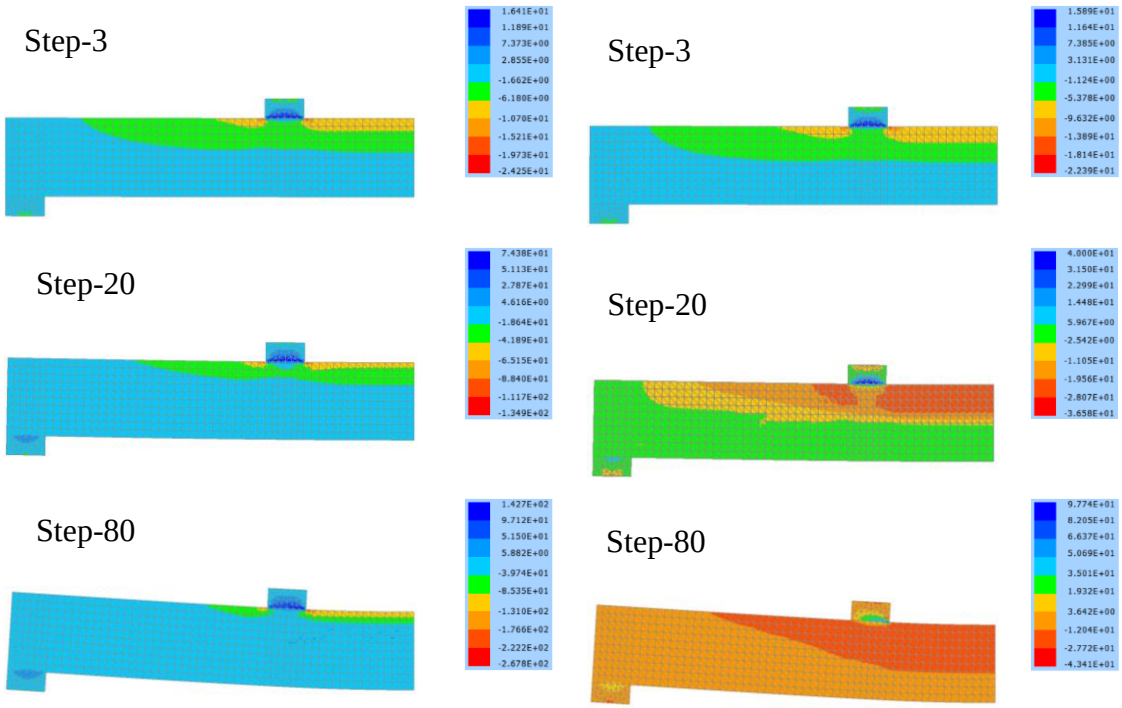

Figure 5.59 – Horizontal Cauchy stresses (N/mm²)

Figure 5.60 shows the evolution of cracking patterns for same steps 3, 20 and 80. Step 3 shows the appearance of the first cracks at the region of the highest flexural moment. The same crack patterns is observed for both model (a and b) however, as long as the increment of displacement is increased some differences can be observed. At step 20 it verifies that more cracks appear in the beam and major cracks are concentrated where the cracking was initiated.

At step 8, the model (a) compared with the model (b) presents both a larger area of the cracked region and larger values of crack opening.

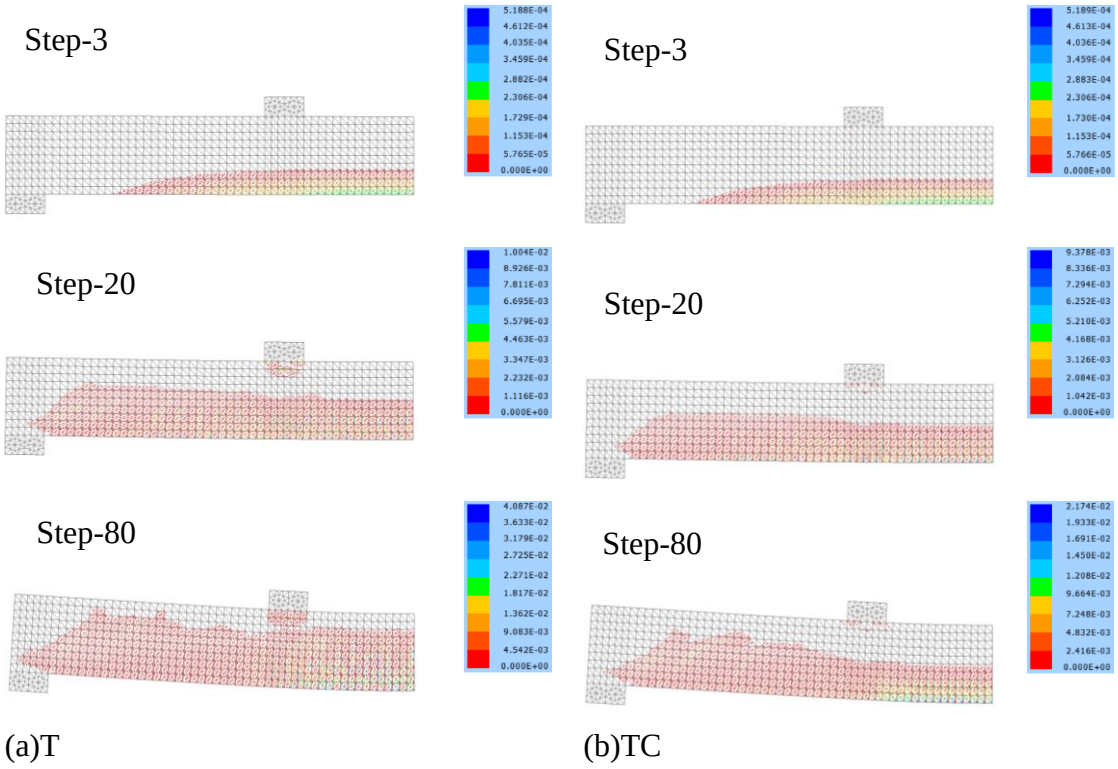

Figure 5.60 – Cracking pattern.

The stresses of the steel reinforcement bars are presented in the Figure 5.61. It verifies that only the upper longitudinal steel reinforcement bar presents compressive behavior while all the others have a tensile stress. Similar to the previously results the stress distribution at step 3 is equivalent for both analysis (a and b). In step 20, the upper longitudinal steel reinforcement is already in a plastic regime. This happens because, by this stage, the damaging process due to compressive forces is already initialized and therefore such reinforcement is more requested to satisfy the equilibrium of the cross-section. At last step, differently from model (b), which both longitudinal bars is under plastic behavior, the model (a) only the bottom longitudinal bar reaches the yield tensile strength. The previous behavior happens because in the model (a) the damaged region due traction forces presents crack openings that are more significant than that occurs in the model (b).

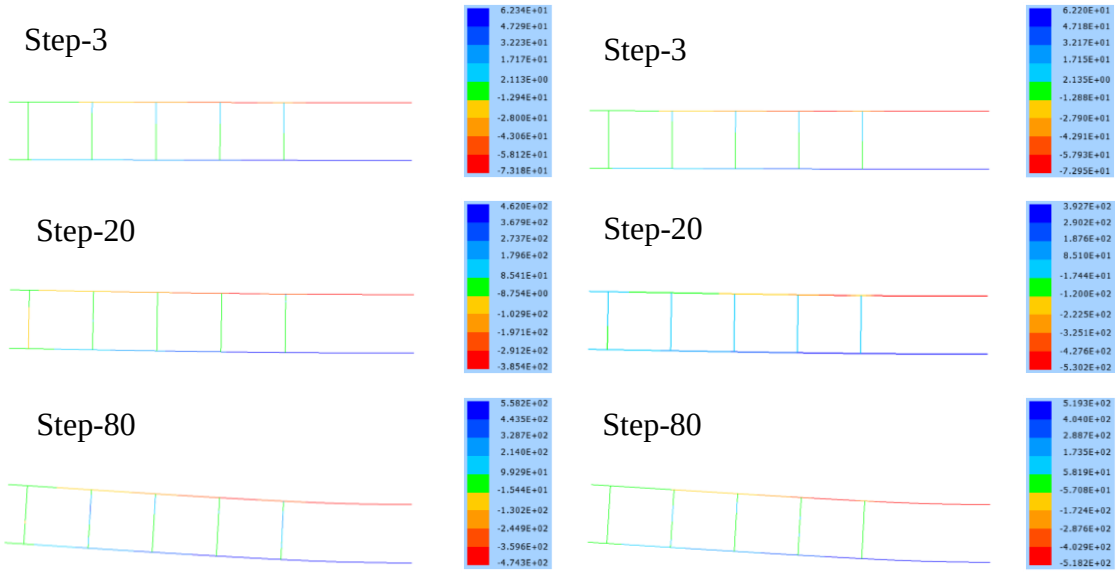

Figure 5.61 – Cauchy Stresses (N/mm²).

5.8 Dowel action

Sørensen et al. (2017) performed an experimental study to investigate the initiation of the dowel action, at small shear displacements, followed by catenary action in the reinforcement bar at large displacement. Figure 5.62 shows the test setup perfomed in their study. The test setup composed by two independents cubic blocks of edge dimensions 200mm linked only by a longitudinal rebar. Steel plates placed on the top and bottom surfaces guarantee the adequate distribution of the vertical force applied in the test. The boundary conditions and the location of the load application ensures that the preferential shear displacement action occurs vertically on the midle of the longitudinal bar.

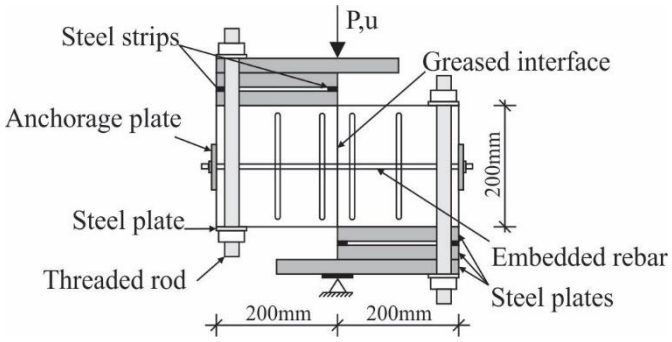

Figure 5.62 – Test setup. Adapted from (Sørensen et al. 2017).

Figure 5.63 shows the numerical model adopted to simulate such structure. All analysis follow discussed were performed with displacement control (u) applied on the top of the steel plate. The boundary condition applied in the corner of the bottom plate steel assures the constrained of displacement in the horizontal and vertical directions. The boundary condition considered between the two blocks of concrete enables the relative vertical displacement and constraint the stresses horizontal distribution between them.

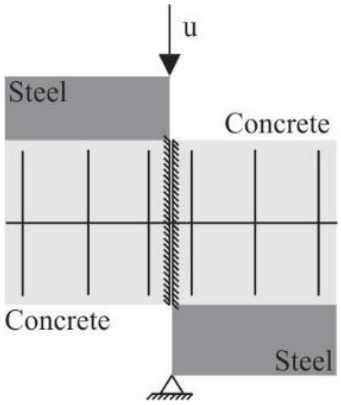

Figure 5.63 – Numerical modeling.

The present problem involves aspects of localized rupture characterized by the dowel action of the longitudinal bar, at small shear displacements, followed by catenary action under the large strain domain. Such characteristic defines by itself the complexity of this analysis. First, the localized rupture effects are physically understood as a discrete phenomenon and the finite element method is developed assuming strain continuity. Thus, the introduction in the constitutive laws of the physical nonlinearities formulation could lead to numerical problems for specific analysis. Such problem redouble with the use of the additional techniques as the embedding of fibers in the matrix elements. Second, the geometrical non-linear effects can be sharply raised with the significative influence of the physical non-linearities. At last, the theories linked to materials that present small and large strain effects diverge mathematically from each other when such effects are significative. In this sense, for the same structure, different results are possibly obtained.

The definition and classification of the small or larger strain is not so evident. Such classification is complex once there is no numerical value of deformation that clarify these two domains. Specifically, two strain measures were adopted to performed the analysis of such

structure, the Green strain, as already employed in the previously analysis, and the so-called the Engineering strain.

The formulation of the two-dimensional, bar and frame finite elements with the application of Green strain was already presented in chapter 3. Following, it is discuss the expressions related to the finite elements with the adoption of the Engineering strain measure. To do so, the Engineering strain measure for the uniaxial and bidimensional cases is first written as a function of the positions. At last, it is following presented the expressions to the calculation of the internal force and the Hessian matrix for the two-dimensional, bar and frame finite elements.

5.8.1 Strain measures written as a function of the positions

The following topics presents the definition of the strain measures as a function of the positions.

Uniaxial strain

For the uniaxial case, the Eq.(3.25) defines the Green strain as a function of the modulus of the tangent vectors and consequently the nodal position of the nodes of the bar finite element, as follow rewritten.

$$ {}_f E = \frac{1}{2}\left(\frac{\left|\overrightarrow{{}_f T}^{\Omega}\right|^2 - \left|\overrightarrow{{}_f T}^{\Omega^0}\right|^2}{\left|\overrightarrow{{}_f T}^{\Omega^0}\right|^2} \right) = \frac{1}{2}\left(\frac{\left|\overrightarrow{{}_f T}^{\Omega}\right|^2}{\left|\overrightarrow{{}_f T}^{\Omega^0}\right|^2} - 1 \right) $$

or

$$ {}_f E = \frac{1}{2}\left\{ \frac{\left[\left(\frac{d\ {}_f\phi_p(\eta)}{d\eta} {}_f Y_1^p \right)^2 + \left(\frac{d\ {}_f\phi_p(\eta)}{d\eta}\ {}_f Y_2^p \right)^2 \right]}{\left[\left(\frac{d\ {}_f\phi_p(\eta)}{d\eta}\ {}_f X_1^p \right)^2 + \left(\frac{d\ {}_f\phi_p(\eta)}{d\eta}\ {}_f X_2^p \right)^2 \right]} - 1 \right\} \tag{5.20} $$

In this same sense, according to the definition of longitudinal strain, the strain measure for the uniaxial case can also be written as:

$$ {}_f\varepsilon = \left(\frac{\left| \overrightarrow{{}_fT^{\Omega}} \right| - \left| \overrightarrow{{}_fT^{\Omega^0}} \right|}{\left| \overrightarrow{{}_fT^{\Omega^0}} \right|} \right) = \left(\frac{\left| \overrightarrow{{}_fT^{\Omega}} \right|}{\left| \overrightarrow{{}_fT^{\Omega^0}} \right|} - 1 \right) $$

or

$$ {}_f\varepsilon = \left\{ \frac{\left[\left(\frac{d\,{}_f\phi_p(\eta)}{d\eta} {}_fY_1^p \right)^2 + \left(\frac{d\,{}_f\phi_p(\eta)}{d\eta} {}_fY_2^p \right)^2 \right]^{1/2}}{\left[\left(\frac{d\,{}_f\phi_p(\eta)}{d\eta} {}_fX_1^p \right)^2 + \left(\frac{d\,{}_f\phi_p(\eta)}{d\eta} {}_fX_2^p \right)^2 \right]^{1/2}} - 1 \right\} \tag{5.21} $$

Bidimensional strain

For two-dimensional cases, as already defined in Eq.(3.6) the Green strain tensor written as a function of the right stretch Cauchy tensor (C) or the gradient configuration function (A) is:

$$ E = \frac{1}{2}\left(C - I\right) = \frac{1}{2}\left(A^T A - I\right) \tag{5.22} $$

From the relationship between the configuration function and the displacement function the gradient of the configuration function called as A can be written as a function of the gradient of displacement ($\nabla\vec{u}$) as follow presented:

$$ A = \nabla\vec{u} + I \tag{5.23} $$

Therefore, replacing Eq.(5.23) in (5.22) the Green strain tensor expressed as a function of the gradient of the displacements is:

$$ E = \frac{1}{2}\left(\nabla\vec{u}^t + \nabla\vec{u} + \nabla\vec{u}^t.\nabla\vec{u}\right) = \frac{1}{2}\left(\nabla\vec{u}^t + \nabla\vec{u}\right) + \frac{1}{2}\left(\nabla\vec{u}^t.\nabla\vec{u}\right) \tag{5.24} $$

The first term is commoly defined as the small strain and called as Linear or Engineering strain. Thus, replacing the relationship (5.23) in (5.24) the Engineering strain written as a funcition of the gradient of the configuration function results:

$$\varepsilon = \frac{1}{2}\left(\nabla\vec{u}^{t} + \nabla\vec{u}\right) = \frac{1}{2}\left\{A^{t} + A - 2I\right\} = \frac{1}{2}\left\{\left[A^{1}.\left(A^{0}\right)^{-1}\right]^{t} + \left[A^{1}.\left(A^{0}\right)^{-1}\right] - 2I\right\} \tag{5.25}$$

Remembering that the gradient of the configuration function is calculated with the nodal position of the finite element considered.

The Engineering strain defined in (5.25) is used in the internal force and Hessian matrix calculation of the two-dimensional and the frame finite elements. It verifies that this expression is the same for both finite elements. However, the gradient of the configuration function A is different for each one once its definition depends on the Kinematic of the element, as described in the chapter 3.

The Internal force and the Hessian matrix expressions for the bar finite element and the bidimensional finite elements with the Engineering strain is following presented.

5.8.2 Finite elements with the unidimensional formulation

The use of the Engineering strain defines the strain energy density (${}_{f}u$) as:

$${}_{f}u = \frac{1}{2}\,{}_{f}\mathbb{E}\,{}_{f}\varepsilon^{2} \tag{5.26}$$

where ${}_{f}\mathbb{E}$ is the tangent elasticity modulus.

The integration of (5.26) over the initial volume gives:

$${}_{f}U = \int_{{}_{f}V_0} {}_{f}u\, d\,{}_{f}V_0 \tag{5.27}$$

Internal Force

The variation of the elastic strain energy as a function of nodal position of the elements defines the internal force vector, as following described:

$${}_{f}F_{\alpha}^{i} = \frac{\partial\,{}_{f}U}{\partial\,{}_{f}Y_{\alpha}^{i}} = \int_{V_0^{f}} \frac{\partial\,{}_{f}u}{\partial\,{}_{f}\varepsilon}\frac{\partial\,{}_{f}\varepsilon}{\partial\,{}_{f}Y_{\alpha}^{i}}\, d\,{}_{f}V_0 = \int_{V_0^{f}} \frac{\partial\,{}_{f}u}{\partial\,{}_{f}\varepsilon}\frac{\partial\,{}_{f}\varepsilon}{\partial\left|{}_{f}\vec{T}^{\Omega}\right|}\frac{\partial\left|{}_{f}\vec{T}^{\Omega}\right|}{\partial\,{}_{f}Y_{\alpha}^{i}}\, d\,{}_{f}V_0 \tag{5.28}$$

where:

$$\frac{\partial\, {}_f u}{\partial\, {}_f \varepsilon} = {}_f \sigma = {}_f \mathbb{E}\, {}_f \varepsilon \tag{5.29}$$

$$\frac{\partial\, {}_f \varepsilon}{\partial\, {}_f Y_\alpha^i} = \frac{\partial\, {}_f \varepsilon}{\partial \left| {}_f \vec{T}^{\Omega} \right|} \frac{\partial \left| {}_f \vec{T}^{\Omega} \right|}{\partial\, {}_f Y_\alpha^i} = \left| {}_f \vec{T}^{\Omega^0} \right|^{-1} \left(\frac{d\, {}_f \phi_p(\eta)}{d\eta}\, {}_f Y_\alpha^p \right) \frac{d\, {}_f \phi_i(\eta)}{d\eta} \left| {}_f \vec{T}^{\Omega} \right|^{-1} \tag{5.30}$$

According to the Energetic conjugates assumption, the variation of the strain energy density as a function of Engineering strain defines the Cauchy stress (${}_f \sigma$), as shows the Eq.(5.29).

The integral solution of the Eq.(5.28) is performed in the dimensioneless coordinates domain with the Gauss-Legendre quadrature, as follows described:

$${}_f F_\alpha^i = \sum_{k=1}^{npg} {}_f \sigma \left(\frac{d\, {}_f \phi_p(\eta)}{d\eta}\bigg|_{\eta=\eta_k} {}_f Y_\alpha^p \right) \frac{d\, {}_f \phi_i(\eta)}{d\eta}\bigg|_{\eta=\eta_k} \left| {}_f \vec{T}^{\Omega^0} \right|^{-1} \left| {}_f \vec{T}^{\Omega} \right|^{-1} {}_f c_k\, {}_f J_0(\eta_k)\, {}_f A_0 \tag{5.31}$$

where npg are the numbers of Gauss points, η the isoparametric coordinates, ${}_f c_k$ theirs respective weights, ${}_f A_0$ it is the initial cross-section of the bar and the Jacobian ${}_f J_0(\eta)$ expressed as:

$${}_f J_0(\eta) = \left| \vec{T}^{\Omega_0} \right| = \sqrt{\left(\frac{dx_1}{d\eta} \right)^2 + \left(\frac{dx_2}{d\eta} \right)^2} \tag{5.32}$$

Hessian Matrix

The second derivative of the strain energy density defines the Hessian matrix as:

$${}_f H_{\alpha\beta}^{ij} = \frac{\partial^2\, {}_f U}{\partial\, {}_f Y_\alpha^i \partial\, {}_f Y_\beta^j} = \int_{{}_f V_0} \frac{\partial\, {}_f u}{\partial\, {}_f Y_\alpha^i \partial\, {}_f Y_\beta^j} d\, {}_f V_0 = \int_{{}_f V_0} \frac{\partial}{\partial\, {}_f Y_\beta^j} \left(\frac{\partial\, {}_f u}{\partial\, {}_f Y_\alpha^i} \right) d\, {}_f V_0 \tag{5.33}$$

Applying the chain rule to solve the expression inside the integral defined in (5.33) it is possible to write:

$$\frac{\partial}{\partial\, {}_f Y_\beta^j} \left(\frac{\partial\, {}_f u}{\partial\, {}_f \varepsilon} \frac{\partial\, {}_f \varepsilon}{\partial\, {}_f Y_\alpha^i} \right) = \frac{\partial}{\partial\, {}_f Y_\beta^j} \left({}_f \sigma \frac{\partial\, {}_f \varepsilon}{\partial\, {}_f Y_\alpha^i} \right) = \frac{\partial\, {}_f \sigma}{\partial\, {}_f Y_\beta^j} \frac{\partial\, {}_f \varepsilon}{\partial\, {}_f Y_\alpha^i} + {}_f \sigma \frac{\partial^2\, {}_f \varepsilon}{\partial\, {}_f Y_\beta^j \partial\, {}_f Y_\alpha^i} \tag{5.34}$$

where:

$$\frac{\partial\, {}_f\sigma}{\partial\, {}_fY_\beta^j} = \frac{\partial}{\partial\, {}_fY_\beta^j}\left({}_f\mathbb{E}\, {}_f\varepsilon \right) = {}_f\mathbb{E}\, \frac{\partial\, {}_f\varepsilon}{\partial\, {}_fY_\beta^j} \tag{5.35}$$

$$\frac{\partial^2\, {}_f\varepsilon}{\partial\, {}_fY_\beta^j \partial\, {}_fY_\alpha^i} = \frac{\partial^2\, {}_f\varepsilon}{\partial \left| {}_f\vec{T}^{\Omega} \right| \partial \left| {}_f\vec{T}^{\Omega} \right|} \frac{\partial^2 \left| {}_f\vec{T}^{\Omega} \right|}{\partial\, {}_fY_\beta^j \partial\, {}_fY_\alpha^i} = 0 \tag{5.36}$$

The integral solution of Hessian matrix (5.34) is also done with the Gauss-Legendre quadrature. Thus, replacing the expressions (5.35) and (5.36) into (5.33) the numerical integration is follow specified:

$${}_fH_{\alpha\beta}^{ij} = \sum_{k=1}^{npg} \left(\frac{{}_f\mathbb{E}}{\left| {}_f\vec{T}^{\Omega^0} \right|^{-2} \left| {}_f\vec{T}^{\Omega} \right|^{-2}} \left(\left. \frac{d\, {}_f\phi_p(\eta)}{d\eta} \right|_{\eta=\eta_k} {}_fY_\beta^p \right) \left. \frac{d\, {}_f\phi_j(\eta)}{d\eta} \right|_{\eta=\eta_k} \left(\left. \frac{d\, {}_f\phi_p(\eta)}{d\eta} \right|_{\eta=\eta_k} {}_fY_\alpha^p \right) \left. \frac{d\, {}_f\phi_i(\eta)}{d\eta} \right|_{\eta=\eta_k} {}_fc_k\, {}_fJ_0(\eta_k)\, {}_fA \right) \tag{5.37}$$

5.8.3 Finite elements with the bidimensional formulation

The strain energy density (u)for the bidimensional formulation is expressed as:

$$u = \frac{1}{2}\varepsilon : \mathfrak{C} : \varepsilon \quad \text{or} \quad u = \frac{1}{2}\varepsilon_{ij}\mathfrak{C}_{ijkl}\varepsilon_{kl} \tag{5.38}$$

The integration of (5.26) over the initial volume gives:

$$U = \int_{V_0} u dV_0 \tag{5.39}$$

Internal Force

The first derivative of the strain energy defines the internal force as:

$$F_\alpha^{\beta\,\mathrm{int}} = \frac{\partial U}{\partial Y_\alpha^\beta} = \int_{V^0} \frac{\partial u}{\partial Y_\alpha^\beta} dV^0 = \int_{V_0} \frac{\partial u}{\partial \varepsilon} \frac{\partial \varepsilon}{\partial Y_\alpha^\beta} dV_0 \tag{5.40}$$

In accordance with the Energetic conjugate assumption, the first term ($\partial u/\partial \varepsilon$), i.e. the variation of the energy-strain density as function of Engineering strain, defines the Cauchy stress and therefore it is possible writes the Eq. (5.41). The second term ($\partial \varepsilon / \partial Y_\alpha^\beta$) is developed in (5.42).

$$\sigma = \frac{\partial u}{\partial \varepsilon} \quad \text{or} \quad \sigma_{ij} = \frac{\partial u}{\partial \varepsilon_{ij}} \tag{5.41}$$

$$\frac{\partial \varepsilon}{\partial Y_\alpha^\beta} = \frac{1}{2}\left[\left(\frac{\partial A^1}{\partial Y_\alpha^\beta} A^{0^{-1}}\right)^{-1} + \left(\frac{\partial A^1}{\partial Y_\alpha^\beta} A^{0^{-1}}\right)\right] \tag{5.42}$$

For the two-dimensional finite elements the terms $\partial A^1 / \partial Y_\alpha^\beta$ are exactly the same defined in the Eqs. (3.17) and (3.18) of chapter 3 in topic 3.1. On the other hand, for the frame finite element, $\partial A^1 / \partial Y_\alpha^\beta$ is the expressions written in the Eqs. (3.74), (3.75) and (3.76) in topic 3.3.

Hessian Matrix

The second derivative of the strain energy density defines the Hessian matrix as:

$$H_{\alpha\beta\gamma\tau} = \frac{\partial^2 U}{\partial Y_\alpha^\beta \partial Y_\gamma^\tau} = \int_{V^0} \frac{\partial^2 u}{\partial Y_\alpha^\beta \partial Y_\gamma^\tau} dV^0 \tag{5.43}$$

The development of the term $\partial^2 U_e / \partial Y_\alpha^\beta \partial Y_\gamma^\tau$ gives:

$$\frac{\partial^2 U}{\partial Y_\alpha^\beta \partial Y_\gamma^\tau} = \frac{\partial}{\partial Y_\gamma^\tau}\left(\sigma_{ij} \frac{\partial \varepsilon_{ij}}{\partial Y_\alpha^\beta}\right) = \left(\frac{\partial \sigma_{ij}}{\partial Y_\gamma^\tau} \frac{\partial \varepsilon_{ij}}{\partial Y_\alpha^\beta} + \sigma_{ij} \frac{\partial^2 \varepsilon_{ij}}{\partial Y_\alpha^\beta \partial Y_\gamma^\tau}\right) = \frac{\partial \sigma_{ij}}{\partial Y_\gamma^\tau} \frac{\partial \varepsilon_{ij}}{\partial Y_\alpha^\beta} \tag{5.44}$$

where ($\partial \varepsilon_{ij} / \partial Y_\alpha^\beta$) was already presented in (5.42) and the term ($\partial^2 \varepsilon_{ij} / \partial Y_\alpha^\beta \partial Y_\gamma^\tau$) is null.
The derivative of Cauchy stress is:

$$\frac{\partial \sigma_{ij}}{\partial Y_\gamma^\tau} = \mathfrak{C} \frac{\partial \varepsilon_{ij}}{\partial Y_\gamma^\tau} \tag{5.45}$$

Remembering that $\partial \varepsilon_{ij} / \partial Y_\gamma^\tau$ is already known in (5.42).

Figure 5.64 shows the three mesh adopted to the simulation of the structure. The two-dimensional finite elements and the elements used to represent the steel rebars have cubic

approximation. The difference between the Meshes 1 and 2 refers to the numbers of finite elements of the longitudinal rebars. For the Mesh 1 was adopted 5 elements, while for the Mesh 2 was used 7 finite elements. The Mesh 3 corresponds to the refinement of the two-dimensional elements and in such situation the longitudinal rebars was refined with 7 elements.

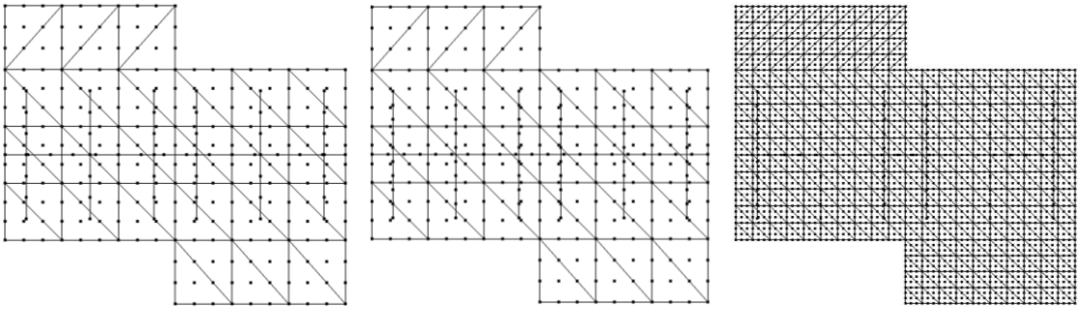

(Mesh - 1) (Mesh - 2) (Mesh -3)

Figure 5.64 – Mesh refinement.

The numerical analysis of such experimental study consists of two stages. The first one assumes the elastic behavior for the two blocks and the elastoplastic behaviors for the steel rebars. For the second stage, beyond the elastoplastic formulation taken for the steel bars the two-dimensional damage model is used to represent the degradation process of the concrete in the two blocks. In both stages is analyzed the influence of the mesh refinement as well as the use of the Green and Engineering Strain.

For all analysis, the Yield stresses and diameters of the stirrups and the longitudinal bars are the same and equals 614MPa and 8mm, respectively. The elasticity modulus initially adopted for all reinforcements were 210GPa. However to consider the bond slip effect the strategy to represent such phenomena with the changing of the constitutive law of the steel rebar was assumed, as described in (Terán and Haach 2018). Therefore, for some results the initial elasticity modulus supposed for the longitudinal rebar was 31.960MPa.

Elastic regime for the two blocks and Elastoplastic behaviours for the steel rebars

Figure 5.65 shows the typical final position configuration for the two blocks of concrete and the steel reinforcement obtained for all analysis following discussed. As can be seen, occurs only the vertical displacement of the two blocks. The finite element that represents the longitudinal bar and link the two blocks is the most requested. In the final position, such element

reach the Yield stress only in the region that the reinforcement bar link the two blocks, Figure 5.65b.

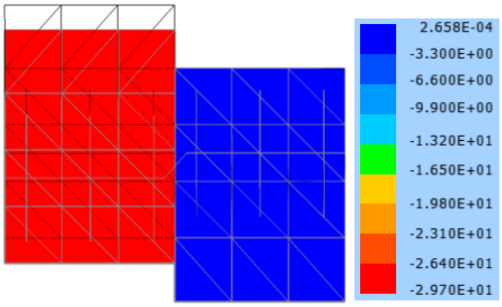

(a) The two block and the reinformenct bars. Unities (mm)

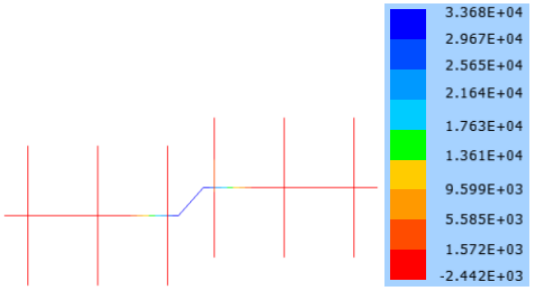

(b) Normal strength of the reinforcement bars. Unities (N)

Figure 5.65 – Final displaced position

Figure 5.66 shows the trajectory of equilibrium for the simulations performed with the rebars simulated with frame and bar finite elements confronted with the experimental curve obtained from the experimental test. Such analysis consider the elastic behaviour for the two blocks and elastoplastic behaviours for the steel rebars. The graphs plotted in the right and left column correspond to the analysis with the elasticity modulus of the longitudinal rebar assumed as 210GPa and 31.960MPa, repectively. The set of graph shows the influence of the three-mesh initilially assumed (Figure 2.5). In each graph, the results of the simulation performed with the Green and Engineering strains are also plotted.

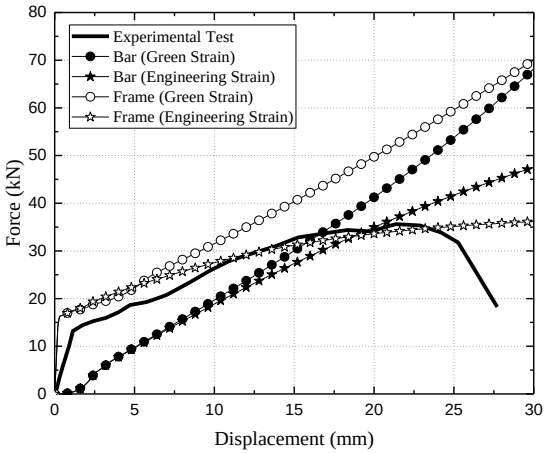

Mesh - 1 (E_s =210GPa)

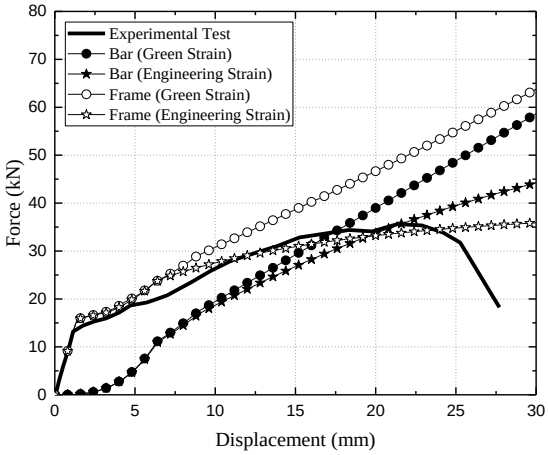

Mesh - 1 (E_s =31960MPa)

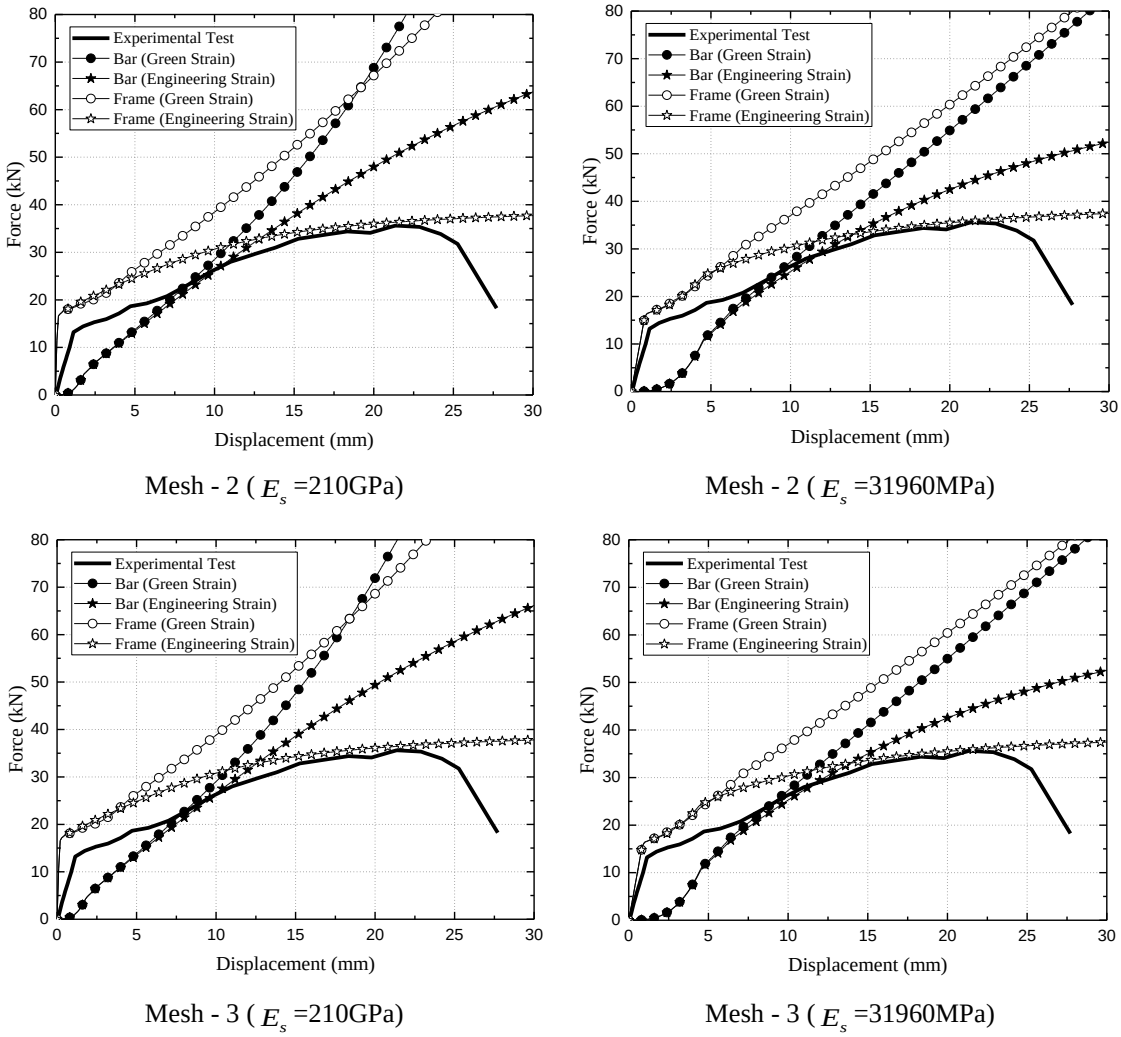

Figure 5.66 - Force versus displacement curve. Cubic approximation for the finite elements.

The experimental curve gotten from Sørensen et al. (2017) shows that the initial stiffness of the structure changes at the value of load equal 15kN. From the test observation, such changing of configuration occurs with the plastic hinge formation in the longitudinal rebar. After the plastic hinge formation, the longitudinal rebar presents a catenary action behavior and therefore justifies the growth of the load capacity of the structure until the peak load value of 35kN, approximately. The peak load represents the rupture of the bar with a combination of the shear and uniaxial actions.

According to Figure 5.66, all curves plotted from the simulations performed with bars elements does not presents stiffness at the beginning of the displacement. Such result is already waited once the bar finite element only present uniaxial stiffness. The structure stiffness increase only after 2.5mm of displacement (for the analysis with E_s =31.960MPa) and this

occurs due to the catenary action of the bar. In other words, at this stage, the bar finite element has only efforts at its longitudinal axle. On the other hand, the results provided with the simulations executed with frame elements shows that even for the first load steps the structure already presents initial stiffness. For the curves plotted with E_s =210GPa, it observes that the stiffness of the structure is bigger than the stiffness obtained from experimental test. For results calculated with E_s =31.960MPa the initial stiffness are well agrees with the experimental curve. Therefore, from such observation it concludes that the bond slip effect has a significant influence in the behaviour of the present structure. The initial stiffness of the structure is constant until the value of load equal 18kN and 15kN, for the analysis with E_s equal 210GPa and 31.960MPa, respectively. At this load level, the curve shows a changing of inclination that indicates the formation of the plastic hinge in the reinforcement bar. For values of load bigger than 18kN and 15kN, the catenary action of the reinforcement bar determines the stiffness of the structure.

From the previous observation, it has been proved that the element only with uniaxial stiffness does not represent well the problem and therefore it is not adequate to be used in such analysis. So, it was proposed the use of the frame element, which presents beyond the uniaxial, the shear and bending stiffnesses, to circumvent such a problem. Such element was embedded in the two-dimensional finite elements (matrix elements) with the coupling technique described in topic 3.4 in the present work. As shown, such a solution strategy contemplates a satisfactory procedure to solve the problem and therefore an essential scientific contribution in the analysis of dowel action problems.

Still according to Figure 5.64, for the three meshes adopted the initial behavior of the curves do not present a significant difference between them. The considerable difference occurs when the structure is under catenary action effect. The results obtained from the Meshes (2 and 3) are similar, and both diverge from the answer of the Mesh 1. Therefore, for the present analysis the mesh refinement of the longitudinal rebar has more influence on the trajectory of equilibrium of the structure than the two-dimensional finite element. The divergence of the results occurs mainly for the curves plotted with the use of Green Strain.

In general, the results of the analysis performed with the frame finite element and the adoption of the Engineering strain measure provides results closer to the experimental curve. The force values for all curves plotted with the simulations performed with the use of Green strain increase indefinitely. Such behavior continues even though after all integrations points

on the shear section have already reached the plasticity yield on the catenary action configuration. The curves plotted with the use of Engineering strain also shows a growth of the load after the plastic hinge formation but such curves trend to a peak load value.

Two-dimensional damage model for the two blocks and Elastoplastic behaviours for the steel rebars

The compressive strength (f_{cc}) of the concrete specified by Sorenren et al. (2017) is equal 48MPa. The estimation of the values of elasticity modulus (E_c), tensile strength (f_{ct}), and fracture energy (G_f) according to CEB-FIB Model Code (2010) results in 38.180MPa, 3.96Mpa and 0.150N/mm, respectively. Figure 5.67a shows the damage criteria to characterize the non-linear physical behaviour of the two blocks. The multilinear softening curve was calibrated with the Hordijk et al. (1986) curve for an ultimate strain equal 0.002. Figure 5.67b also shows the admensional coordinates (α, β). The value of the equivalent length (h) adopted was 170mm.

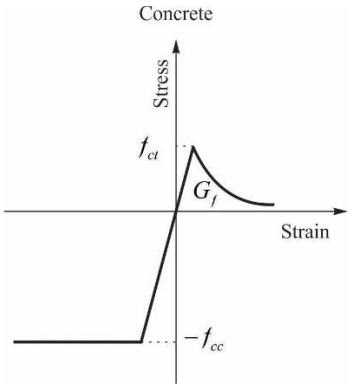

(a)

i	α_i	β_i
1	1.00	1.00
2	0.70	0.60
3	0.30	0.20
4	0.10	0.05
5	0.10	0.00

(b)

Figure 5.67 – (a) Damaging criteria and (b) Parameters of the multilinear softening curves.

Figure 5.68 shows the non-linear behavior of the force-displacement curves resulted from the numerical simulations performed with the use of Bimodular damage models applied to the two blocks of concrete. In general, it observes that the trajectories of equilibrium obtained in such situation are similar to these already commented in Figure 5.66, determined with the two blocks under elastic regime. The final cracking configuration of the structure simulated with the use of Engineering strain and frame finite elements for the steel rebars are presented

inside of the graphs. It verifies that the cracking patterns appear in the region next to the shear displacement of the longitudinal rebars and the refinement of the mesh linked to the two-dimensional finite element enable a better representation of the cracking propagation (Mesh–3). Therefore, it concludes that for such simulation although the two blocks present regions where the damaging process starts such areas are restricted and do not offer an essential effect in the global equilibrium of the structure. Thus, indeed the structural behavior of this structure is directly associated with the dowel action phenomena.

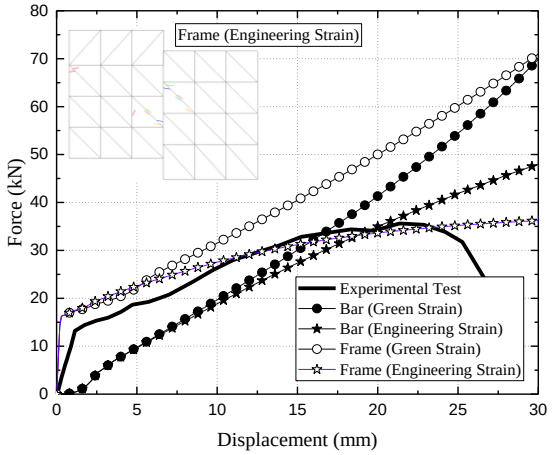

Mesh – 1 (E_s = 210GPa)

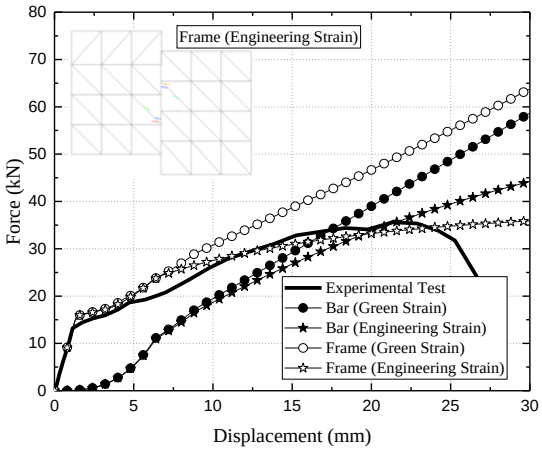

Mesh – 1 (E_s = 31.960MPa)

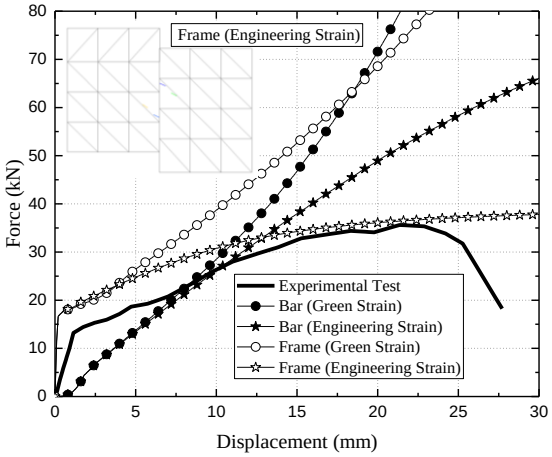

Mesh – 2 (E_s = 210GPa)

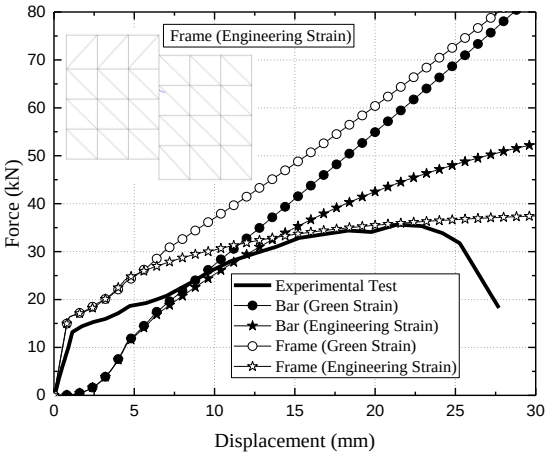

Mesh – 2 (E_s = 31.960MPa)

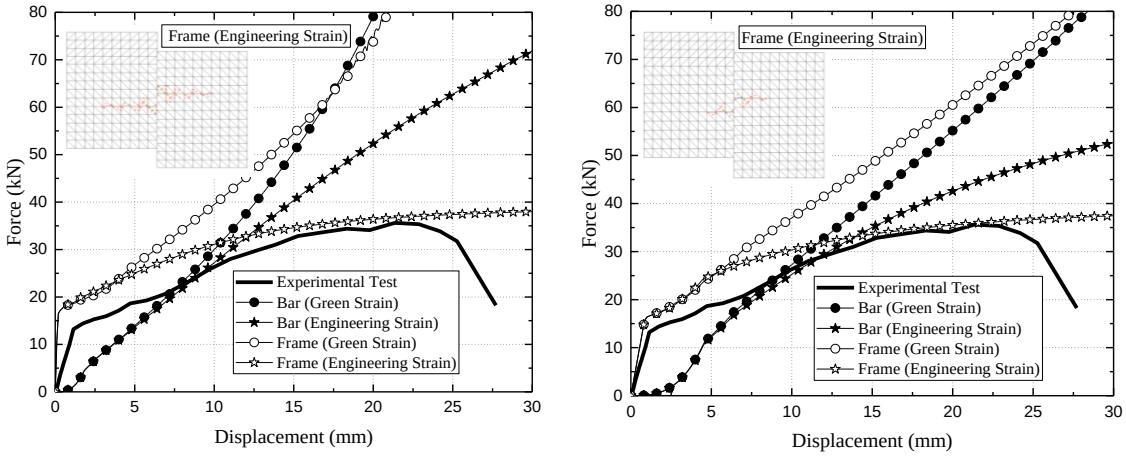

Mesh – 3 (E_s = 210GPa) Mesh – 3 (E_s = 31.960MPa)

Figure 5.68 - Force versus displacement curve. Cubic approximation for the elements.

5.9 Summary

This chapter dealt with numerous examples of validation and analysis of the formulations discussed in the present thesis. From them, the two-dimensional, bar and frame finite elements formulations were tested and certified. The plasticity theory represented by the one-dimensional and the plane-stress approach was verified as well as the characteristics of the two damage models developed. Regarding the discussions performed over all examples it was possible to formulate the following general conclusions:

a) The code developed provided coherent results for all analysis performed and therefore can be used to carry out other structural investigations of new structures;
b) The geometrical nonlinear formulation implemented provided satisfactory results for the examples analyzed;
c) The physical nonlinear approaches discussed and proposed in this work produced adequate results in the analysis. It shows to be possible their application with the positional finite element method technique;
d) The consideration of the flexural and the shear stiffnesses beyond the uniaxial stiffness in the reinforcement bar for the analysis of the structures subjected to Dowel action mechanism is essential to carry on suitable investigations.

6 CONCLUSION AND FINAL REMARKS

In such study one program (2D) of finite element method with positional formulation approach, implemented in Fortran language and considering the physical and geometrical nonlinearities to simulate some generic structures was developed. In accordance with the main objective of the present work. Three finite positional elements constitute the code developed named in this thesis as two-dimensional, bar and frame elements. The formulation and the strategy of implementation of such elements were presented in details. Some examples of structures were used to validate the formulation presented. The results were compared with commercial codes, analytical results and experimental tests, being the last one acquired from the literature. Overall, with the analysis the main conclusion of this thesis is the formulation proposed is adequate to represent the mechanical behavior of structures with differents geometries, boundary conditions and displacement/load aplications. Such conclusion shows the consistency and accuracy of the theory proposed.

6.1 About the embedded theory

The embedded theory for the matrix-fiber coupling was used with the three-finite positional elements initially implemented. The two-dimensional elements symbolize the matrix elements while the bar and frame elements the fibers one. The coupling technique presented was developed with the additive composition of the total potential energy of the matrix-fiber elements and posterior variation of this energy in relation with the positions of the matrix elements. It should be emphazise that the coupling between the two-dimensional and the frame finite elements constituted the one of the novelty of this thesis. Regarding the results obtained with such formulation it was possible to formulate the following conclusions:

a) The results obtained from such strategy was suitable with the examples explored. For all analysed examples the additional stiffness of the fiber elements contribute to the

global structural behavior. Therefore, this coupling technique made the analysis of reinforced structures possible.

b) Besides the coupling between the two-dimensional and the frame elements consider the angular rotation as an additional variable in the global system, it could be observed that the benefits of this procedure still relates the fact that the users does not need to worry about the nodal connection.

c) The frame finite elements as fibers representation can be adopted to simulate structures in which the shear mechanism is not a relevant effect in its global behavior. Examples 5.2.1 and 5.2.2, showed in chapter 5, certified that the fibers represented as bar or frame elements provided the same answers for the analysis of structures subjected to uniaxial effects. Similar observation occured for the examples 5.2.2, 5.5.2, 5.7.1 and 5.7.2, which correspond to structures that the fibers are principally under uniaxial requesting from flexural action.

d) The fiber with the uniaxial, flexural and shear stiffnesses are essential to analyze the dowel action mechanism. As discussed in example 5.8 the initial stiffness of such problem were adequately represented when the frame element was considered.

e) The typical mechanism of the plastic hinge formation on the reinforcement bar could only be observed for the rebar represented by the frame finite element.

6.2 About the physical nonlinearities

In this thesis, two physical nonlinearities formulation was adopted to represent the physical behaviors of the materials: the elastoplastic and the damage models. From the results of the examples 5.3.1, 5.3.2, 5.3.3, 5.4.1, 5.4.2, 5.4.3, 5.5.1, 5.5.2, 5.6.1, 5.6.2, 5.6.3, 5.6.4, 5.7.1, 5.7.2 and 5.8, discussed in chapter 5, it was possible to formulate the following conclusions:

a) The one-dimensional and the plane-stress plasticity theory are suitable to represent the physical behavior of the fibers.

b) The consideration of the additive decomposition of strain enable the use of the computational code in the analysis of structures with the material presenting small strain.

c) The ultimate load value for the structure simulated in the example 5.6.3 diverges with different shapes of the softening curve adopted for the so-called *damage model with the smeared crack approach*.

d) The variation (fixed-rotation) of the *damage model with the smeared crack approach* can provide different results for the same structure analyzed with the same input data. As demonstrated, similar results are obtained in the cases where the preferential plan of rupture does not change during the analysis, which occurs for uniaxial cases. On the other hand, as treated in the example 5.6.3, it was showed that the trajectory of equilibrium of the three point experimental test can present several deviations. Such deviations depends on the damage models adopted, such as fixed or rotate. It was observed that the main variation occurred from the different shapes of equilibrium curves obtained for beyond peak load values.

e) Both *Damage model with the smeared crack approach* and *Bimodular damage model* developed are classified as anisotropic damage models because the evolution of the degradation of the structure is not the same for different principal stress directions.

f) The adoption of the compression criteria for the matrix elements, such as assumed in the *Bimodular damage model*, constitute an important aspect to adequately simulate some structures such as the over-reinforced beams.

g) The adoption of any physical nonlinear model influence the results of the structure analyzed. At this sense, to avoid any problems with numerical simulations the knowledge of the model used is of fundamental importance to perform realistic analysis.

Finally, from the last three examples 5.7.1, 5.7.2 and 5.8 that covered simultaneously the application of all formulations discussed in this thesis it was possible to formulate the following conclusion:

a) The application of the embedded theory together with the elastoplastic and damage models in the positional finite element method provides a satisfactory analysis of reinforced structures.

b) The consideration of the flexural and shear stiffnesses beyond the uniaxial stiffness in the reinforcement of the bars in structures requested mainly by shear effects, which results in the dowel action mechanism, is essential to perform adequate analysis.

6.3 Projections for future research

During the development of the present study, it was possible to verify that the all themes covered to perform the current research comprehend a large field of study that still needs to be developed and therefore refined to make feasible the adequate analysis of specific structures. Thus, some proposals for future research are presented below:

1) Exploring the capacity of the computational code developed with differents structures;
2) Implementation of three-dimensional finite elements, such as solid and plate elements, to evaluate structures in 3D;
3) Expansion of the elastic plastic and damage formulations proposed for the simulation of three-dimensional structures;
4) Parallelization technique for the calculus optimizations of the computational code;
5) Implementation of the arch-length method to enable the resolution of structures that presents snap-back effects in the curves of equilibrium trajectory.
6) Implementation of numerical techniques, such as the Line search method to improve the convergence of the iterative process of the Newton Raphson method already used.
7) Study and implementation of the elastoplastic models for large strains with the adoption of multiplicative decomposition of the deformation gradient tensor.
8) Exploration and implementation of other traditional damage models (such as the isotropic, orthotropic and anisotropic models) and posterior comparaison with the model proposed;
9) Study of differents Constitutive Laws applied in the analysis with consideration of geometrical nonlinearity;
10) Exploration of the technique of the embedded theory applied at this study for three-dimensional cases;

REFERENCES

Abaqus 6.13. (2013). “Abaqus Analysis user’s manual.”

Aguiar, E. A. B. (2010). “Comportamento de chumbadores grauteados de ligações viga-pilar parcialmente resistentes a momento fletor.” Universidade de São Paulo (USP).

Aguiar, E. A. B., Bellucio, E. K., and El Debs, M. K. (2012). “Behaviour of grouted dowels used in precast concrete connections.” *Structural Concrete*, 13(2), 84–94.

Ahmad, S., Bhargava, P., and Chourasia, A. (2018). “Shear transfer strength of uncracked interfaces : A simple analytical model.” *Construction and Building Materials*, Elsevier Ltd, 192, 366–380.

Arafa, M., and Mehlhorn, G. (1998). “A modified discrete model in the nonlinear finite element analysis of prestressed and reinforced concrete structures.” *2nd Int. PhD Symposium in Civil Engineering*, Budapest, 1–10.

Areias, P., Msekh, M. A., and Rabczuk, T. (2016). “Damage and fracture algorithm using the screened Poisson equation and local remeshing.” *Engineering Fracture Mechanics*, Elsevier Ltd, 158, 116–143.

Ashour, A. F. (1997). “Tests of Reinforced Concrete Continuous Deep Beams.” *ACI Structural Journal*, 94(1), 3–12.

Assan, A. E. (2003). *Método dos Elementos Finitos*. Editora da Unicamp, Campinas.

ATENA 5.6. (2016). “ATENA Program Documentation Part 1 Theory Manual.”

Azócar, D., Elgueta, M., and Cecilia, M. (2010). “Automatic LEFM crack propagation method based on local Lepp – Delaunay mesh refinement.” *Advances in Engineering Software*, Elsevier Ltd, 41(2), 111–119.

Balakirshnan, S., and Murray, D. W. (1986). “Finite Element Prediction of reinforced concrete behaviour.” PhD Thesis - University of Alberta.

Barbato, M. (2009). “Efficient finite element modelling of reinforced concrete beams retrofitted with fibre reinforced polymers.” *Computers and Structures*, Elsevier Ltd, 87, 167–176.

Barenblatt, G. I. (1962). “The Mathematical Theory of Equilibrium Cracks in Brittle Fracture.” *Advances in Applied Mechanics*, (H. L. Dryden, T. von Kármán, G. Kuerti, F. H. van den Dungen, and L. B. T.-A. in A. M. Howarth, eds.), Elsevier, 7, 55–129.

Barzegar, F. (1988). “Layering of RC membrane and plate elements in nonlinear analysis.” *Journal of Structural Engineering, ASCE*, 114(11), 2474–2492.

Barzegar, F. (1989). “Analysis of RC membrane elements with anisotropic reinforcement.” *Journal of Structural Engineering, ASCE*, 115(3), 647–665.

Barzegar, F., and Maddipudi, S. (n.d.). “Three-Dimensional Modeling of Concrete Structures. II: Reinforced Concrete.” *Journal of Structural Engineering, ASCE*, 123(10), 1347–1356.

Barzegar, F., and Maddipudi, S. (1994). “Generating Reinforcement in FE Modeling of Concrete Structures.” *Journal of Structural Engineering, ASCE*, 120(5), 1656–1662.

Bazant, Z., and Oh, B. (1983). “Crack band theory for fracture of concrete.” *Materials and Structures*, 16, 155.

Bazant, Z. P. (1985). “Fracture in Concrete and Reinforced Concrete.” *Mechanics of Geomaterials*, Z. P. Bazant, ed., John Wiley & Sons, Ltd, 259–303.

Bazant, Z. P., and ASCE, F. (1983). “Comment on orthotropic models for concrete and geomaterials.” *Journal of Engineering Mechanics*, 109(3), 849–865.

Bazant, Z. P., ASCE, F., and Cedolin, L. (1983). “Finite element modeling of crack band propagation.” *Journal*, 109(17618), 69–92.

Bazant, Z. P., and ASCE, M. (1976). “Instability, Ductility, and Size Effect in Strain-Softening Concrete.” *Journal of the engineering mechanics division*, (April).

Bazant, Z. P., and Planas, J. (1998). *Fracture and Size Effect in Concrete and Other Quasibrittle Materials*. CRC Press, London.

Behbahani, A. E., and Al., E. (2015). “Plastic-damage smeared crack model to simulate the behaviour of structures made by cement based materials.” *International Journal of Solids and Structures*, 73–74, 20–40.

Belytschko, T., Liu, W. K., Moran, B., and Elkhodary, K. I. (2014). *Nonlinear Finite Elements for Continua and Structures*. John Wiley & Sons, Ltd, United Kingdom.

Bencardino, F., Condello, A., and Ombres, L. (2016). “Numerical and analytical modeling of concrete beams with steel , FRP and hybrid FRP-steel reinforcements.” *COMPOSITE STRUCTURE*, Elsevier Ltd, 140(40), 53–65.

Bonet, J., and Wood, R. D. (2010). *Nonlinear continuum mechanics for finite element analysis*. Cambridge University Press.

Bonet, J., Wood, R. D., Mahaney, J., and Heywood, P. (2000). “Finite element analysis of air supported membrane structures.” *Computer Methods in Applied Mechanics and Engineering*, 190(5–7), 579–595.

De Borst, R. (1986). “Non-linear analysis of frictional materials.” Delft University of Technology.

De Borst, R. (2002). “Fracture in quasi-brittle materials : a review of continuum damage-based approaches.” *Engineering Fracture Mechanics*, 69, 95–112.

De Borst, R., and Nauta, P. (1985). “Non-orthogonal cracks in a smeared finite element model.” *Engineering Computations*, 2, 35–46.

Bouziadi, F., Boulekbache, B., Haddi, A., and Djelal, C. (2018). “Experimental and finite element analysis of creep behaviour of steel fibre reinforced high strength concrete beams.” *Construction and Building Materials*, Elsevier Ltd, 173, 101–110.

Carrazedo, R. (2009). “Estudo e desenvolvimento de código computacional para análise de impacto entre estruturas levando em consideração efeitos térmicos.” Tese (Doutorado em Engenharia de Estruturas) - Departamento de Engenharia de Estruturas. Escola de Engenharia de São Carlos, Universidade de São Paulo, São Carlos, 2009.

CEB - FIB Model Code. (2010). “Model Code 2010 - Final draft, Volume 1.”

Cedolin, L., and Bazant, Z. P. (1980). “Effect of finite element choice in blunt crack band analysis.” *Computer*, 24, 305–316.

Cervenka, J., and Papanikolaou, V. K. (2008). “Three dimensional combined fracture–plastic material model for concrete.” *International Journal of Plasticity*, 24, 2192–2220.

Cervenka, V. et al. (1996). “Mesh Sensitivity Effects in Smeared Finite Analysis of Concrete Fracture.” *Fracture Mechanics of Concrete*, AEDIFICATIO Publishers, Freiburg, 10.

Cervenka, V., and Gerstle, K. (1971). “Inelastic analysis of reinforced concrete columns.” *IABSE*, 31(11), 32–45.

Chang, T. Y., ASCE, M., Taniguchi, H., Chen, W. F., and Asce, M. (1987). “Non-linear finite element analysis of reinforced concrete panels.” 113(1), 122–140.

Chen, W. F. (2007). *Plasticity in Reinforced Concrete*. J. Ross Publishing, Fort Lauderdale.

Chiaruttini, V., Riolo, V., and Feyel, F. (2013). “Advanced remeshing techniques for complex 3D crack propagation.” *13th International Conference on Fracture*, Beijing.

Chudoba, R., Jerábek, J., and Peiffer, F. (2009). “Crack-Centered Enrichment for Debonding in Two-Phase Composite Applied to Textile Reinforced Concrete.” 7(4), 309–328.

Coda, H. B. (2018). *O Método dos elementos finitos posicional : sólidos e estruturas – não linearidade geométrica e dinâmica*. (EESC-USP, ed.), São Carlos.

Coda, H. B., and Greco, M. (2004). “A simple FEM formulation for large deflection 2D frame analysis based on position description.” *Computer Methods in Applied Mechanics and Engineering*, 193(33–35), 3541–3557.

Coda, H. B., and Paccola, R. R. (2007). “An alternative positional FEM formulation for geometrically non-linear analysis of shells: Curved triangular isoparametric elements.” *Computational Mechanics*, 40(1), 185–200.

Coda, H. B., and Paccola, R. R. (2008). “A positional FEM Formulation for geometrical non-linear analysis of shells.” *Latin American Journal of Solids and Structures*, 5(3), 205–223.

Coda, H. B., and Paccola, R. R. (2010). “Improved finite element for 3D laminate frame analysis including warping for any cross-section.” *Applied Mathematical Modelling*, Elsevier Inc., 34(4), 1107–1137.

Cornelissen, H. A. W., Hordijk, D. A., and Reinhardt, H. W. (1986). “Experimental determination of crack softening characteristics of normalweight and lightweight concrete.” *HERON*, 31(2), 45–56.

Crisfield, M. A. (1991). *Non-linear finite element analysis of solids and structures: Essentials*. John Wiley & Sons, Inc., New York, NY, USA.

Crisfield, M. A. (1997). *Nonlinear Finite Element Analysis of Solids and Structures: Advanced*

topics. (John Wiley & Sons Ltd, ed.), New York, NY, USA.

Crisfleld, M. A., and Wills, J. (1989). "Analysis Of R/C Panels Using Different Concrete Models." *Journal of Engineering Mechanics*, 115(3), 578–597.

Cunha, V. M. C. F., Barros, J. A. O., and Sena-cruz, J. M. (2012). "A finite element model with discrete embedded elements for fibre reinforced composites." *Computers and Structures*, 95, 22–33.

Dashti, F., Dhakal, R. P., and Pampanin, S. (2017). "Numerical Modeling of Rectangular Reinforced Concrete Structural Walls." *Journal of Structural Engineering*, 143(6), 04017031.

Dawari, V. B., and Vesmawala, G. R. (2014). "Application of Nonlinear Concrete Model for Finite Element Analysis of Reinforced Concrete Beams." *International Jounal od Scientific & Engineering Research*, 5(9), 776–782.

Dei Poli, S., Di Prisco, M., and Gambarova, P. G. (1992). "Shear response, deformations, and subgrades stiffness of a dowel bar emdedded in concrete." *ACI Structural Journal*, 89(6), 665–675.

DIANA 10.2. (2017). "User's manual release." TNO DIANA, Delft, Netherlands.

Dugdale, D. S. (1960). "Yielding of Steel Sheets Containing Slits." *Journal of Mechanics and Physics of Solids*, 8, 100–104.

Dunne, F., and Petrinic, N. (2005). *Introduction to Computational Plasticity*. Oxford University Press, Oxford.

Džolev, I. M., Cvetkovska, M. J., Lađinović, Đ. Ž., and Radonjanin, V. S. (2018). "Numerical analysis on the behavior of reinforced concrete frame structures in fire Numerical analysis on the behaviour of reinforced concrete frame structures in fire." *Computers and Concrete*,

21(6), 637–647.

Echegaray-Oviedo, J., Navarro-Gregori, J., Cuenca, E., and Serna, P. (2017). “Modified push-off test for analysing the shear behaviour of concrete cracks.” *Strain*, 53(6), 1–17.

Eftekhari, M., Karrech, A., Elchalakani, M., and Basarir, H. (2018). “Multi-scale Modeling Approach to Predict the Nonlinear Behavior of CNT- reinforced Concrete Columns Subjected to Service Loading.” *Structures*, Elsevier, 14, 301–312.

El-Ariss, B. (2007). “Behavior of beams with dowel action.” *Engineering Structures*, 29, 899–903.

El-Mezaini, N., and Citipitioglu, E. (1991). “Finite element analysis of prestressed and reinforced concrete structures.” *Journal of Structural Engineering, ASCE*, 117(10), 2851–2864.

Elices, M., Guinea, G. V., and Planas, J. (1992). “Measurement of the fracture energy using three-point bend tests : Part 3 - Influence of cutting the P-Delta tail.” *Materials and Structures*, 25, 327–334.

Elwi, A. E., and Hrudey, T. M. (1989). “Finite Element Model for Curved Embedded Reinforcement.” *Journal of Engineering Mechanics*, 115(4), 740–754.

Elwi, A. E., and Murray, D. W. (1980). “Nonlinear Analysis of Axisymmetric Reinforced Concrete Structures.” (87), 155.

Fédération Internationale du Béton-fib. (2008). “Structural connections for precast concrete buildings.” fib Bulletin-43.

Feenstra, P. H. (1993). “Computational Aspects of Biaxial Stress in Plain and Reinforced Concrete.” Delft University of Technology.

Felix, E. F. (2018). “Modelagem da Deformação do Concreto Armado Devido à Formação dos Produtos de Corrosão.” Dissertação (Mestrado em Engenharia de Estruturas) - Departamento de Engenharia de Estruturas. Escola de Engenharia de São Carlos, Universidade de São Paulo, São Carlos, 2018.

Figueira, D., Sousa, C., Calçada, R., and Neves, A. S. (2016). “Push-off tests in the study of cyclic behavior of interfaces between concretes cast at different times.” *Journal of Structural Engineering*, 142(1), 1–10.

Filippou, F. C. (1990). “Finite Element Analysis of Reinforced Concrete Structures Finite Element Analysis of Reinforced Concrete Structures.” *Matrix*, 14(November), 717–725.

Foster, R. M., Asce, S. M., Morley, C. T., and Lees, J. M. (2016). “Modified push-off testing of an inclined shear plane in reinforced concrete strengthened with CFRP fabric.” *Journal of Composites for Construction*, 20(3), 1–10.

Frenay, J. W., Reinhardt, H. W., and Walraven, J. C. (1992a). “Time-dependent shear transfer in cracked concrete: Part I.” *Journal of Structural Engineering*, 117(10), 2900–2918.

Frenay, J. W., Reinhardt, H. W., and Walraven, J. C. (1992b). “Time-dependent shear transfer in cracked concrete: Parte II.” *Journal of Structural Engineering*, 117(10), 2919–2935.

Friedel, L. F. O. (2016). “Análise de estruturas planas reforçadas com fibras ativas viscoelásticas e matriz com modelo constitutivo hiperelástico : aplicações gerais em engenharia e biomecânica.”

Girard, C., and Bastien, J. (2002). “Finite-Element Bond-Slip Model for Concrete Columns under Cyclic Loads.” *Journal of Structural Engineering, ASCE*, 128(12), 1502–1510.

Guinea, G. V., Planas, J., and Elices, M. (1992). “Measuement of the fracture energy using three-point bend tests: Part 1 - Influence of experimental procedures.” *Materials and Structures*, 25, 212–218.

Haach, V. G. (2010). “SecTrans.” http://www.set.eesc.usp.br/portal/pt/softwares/27-pesquisa/softwares/444-sectrans, São Carlos.

Hanson, J. H., and Ingraffea, A. R. (2003). “Using numerical simulations to compare the fracture toughness values for concrete from the size-effect , two-parameter and fictitious crack models.” *Engineering Fracture Mechanics*, 70, 1015–1027.

Hariri-ardebili, M. A., Seyed-Kolbadi, S. M., and Mirzabozorg, H. (2013). “A smeared crack model for seismic failure analysis of concrete gravity dams considering fracture energy effects.” *Structural Engineering and Mechanics*, 48(1), 2013.

Hawileh, R. A. (2015). “Finite element modeling of reinforced concrete beams with a hybrid combination of steel and aramid reinforcement.” *Materials and Design*, Elsevier Ltd, 65, 831–839.

He, S., Fang, Z., and Mosallam, A. S. (2017). “Push-out tests for perfobond strip connectors with UHPC grout in the joints of steel-concrete hybrid bridge girders.” *Engineering Structures*, Elsevier Ltd, 135, 177–190.

He, X. G., and Kwan, a. K. H. (2001). “Modeling dowel action of reinforcement bars for finite element analysis of concrete structures.” *Computers and Structures*, 79(6), 595–604.

Heiza, K. M. (2013). “New finite-element approach for reinforced concrete beams.” *Magazine of Concrete Research*, 65(1), 1–13.

Hettich, T., Hund, A., and Ramm, E. (2008). “Modeling of failure in composites by X-FEM and level sets within a multiscale framework.” 197, 414–424.

Hillerborg, A., Modéer, M., and Petersson, P. E. (1976). “Analysis of crack formation and crack growth in concrete by means of fracture mechanics and finite elements.” *Cement and Concrete Research*, 6, 773–782.

Holzapfel, G. A. (2000). *Nonlinear Solid Mechanics - A continuum approch for engineering*. John Wiley & Sons, Ltd, United Kingdom.

Hordijk, D. A. (1991). "Local approach to fatigue of concrete." University of Technology.

Hsu, T. T. C., Mau, S. T., and Chen, B. (1987). "Theory of shear transger strength of reinforced concrete." *ACI Structural Journal*, 84(2), 149–160.

Hu, H., Lin, F., and Jan, Y. (2004). "Nonlinear finite element analysis of reinforced concrete beams strengthened by fiber-reinforced plastics." *Composite Structures*, 63, 271–281.

Husain, H. M., Oukaili, N. K., and Muyhammed, H. S. (2009). "Dowel action between two concretes." *Journal of Engineering*, 15(2), 3583–3605.

Ingraffea, A. R., and Saouma, V. (1985). "Numerical modeling of discrete crack propagation in reinforced and plain concrete." *Fracture mechanics of concrete: Structural application and numerical calculation*, G. C. Sih and A. DiTommaso, eds., Springer Netherlands, Dordrecht, 171–225.

Jendele, L., and Cervenka, J. (2006). "Finite element modelling of reinforcement with bond." *Computers and Structures*, 84(28), 1780–1791.

Jetteur, P. (1986). "Implicit integration algorithm for elastoplasticity in plane stress analysis." *Engineering Computations*, 3(3), 251–253.

Jirasek, M. (2011). "Damage and Smeared Crack Models." *Numerical Modeling of Concrete Cracking*, M. G. Hofstetter G., ed., Springer, Vienna.

Jirasek, M., and Zimmermann, T. (1998). "Rotating Crack Model with Transition to Scalar Damage." *Journal of Engineering Mechanics*, 124(3), 277–284.

Jirásek, M., and Zimmermann, T. (2001). "Embedded crack model : I . Basic formulation."

International Journal for Numerical Methods in Engineering, 1269–1290.

Jongvivatsakul, P., Attachaiyawuth, A., and Pansuk, W. (2016). "A crack-shear slip model of high-strength steel fiber-reinforced concrete based on a push-off test." *Construction and Building Materials*, Elsevier Ltd, 126, 924–935.

JSCE. (2010). "Guidelines for Concrete No. 15: Standard Specifications for Concrete Structures - 2007 'Design.'" Japan Society of Civil Engineers.

Kim, W., and White, R. N. (1999). "Hypothesis for localized horizontal shearing failure mechanism of slender RC beams." *Journal of Structural Engineering*, 125(10), 1126–1135.

Kormeling H. A., R. H. W. (1983). "Determination of the fracture energy of normal concrete and epoxy modified com

Kwan, A. K. H., and Ma, F. J. (2016). "Crack width analysis of reinforced concrete under direct tension by finite element method and crack queuing algorithm." *Engineering Structures*, 126, 618–627.

Kwan, A. K. H., and Ng, P. L. (2013). "Modelling dowel action of discrete reinforcing bars for finite element analysis of concrete structures." *Computers and Concrete*, 12(1), 19–36.

Lee, J., and Lopez, M. M. (2014). "An Experimental Study on Fracture Energy of Plain Concrete." *International Journal of Concrete Structures and Materials*, 8(2), 129–139.

Lee, J. S., Choi, I., and Cho, H. (2004). "Modeling and detection of damage using smeared crack model." *Engineering Structures*, 26, 267–278.

Lemaitre, J. (1996). *A Course on Damage Mechanics*. Springer-Verlag Berlin Heidelberg.

Lemaitre, J., and Chaboche, J. L. (2000). *Mechanics of solid materials*. Cambridge University

Press, United Kingdom.

Lemaitre, J., and Desmorat, R. (2005). *Engineering Damage Mechanics*. Springer-Verlag Berlin Heidelberg.

Li, P., Tan, N., and Wang, C. (2018). “Nonlinear bond model for the dowel action considering the fatigue damage effect.” *Advances in Materials Science and Engineering*.

Liu, J., and Foster, S. J. (1998). “Microplane model for the finite element analysis of reinforced concrete tied columns. Studies from the School of Civil and Environmental Engineering Volume 368 de UNICIV report, ISSN 0077-880X.” School of Civil and Environmental Engineering, University of New South Wales, 1998.

Lubliner, J. (2006). *Plasticity Theory*. Pearson Education, New York, USA.

Maciel, D. N. (2008). “Análise de problemas elásticos não lineares geométricos empregando o método dos elementos finitos posicional.” *SET/EESC*, Doutor, 162.

Maekawa, K., Gebreyouhannes, E., Mishima, T., and An, X. (2006). “Three-dimensional fatigue simulation of RC slabs under traveling wheel- type loads.” *Journal of Advanced Concrete Technology*, 4(3), 445–457.

Maekawa, K., and Qureshi, J. (1996a). “Embedded bar behavior in concrete under combined axial pullout and transverse displacement.pdf.” *J. Materials, Conc. Struct., Pavements*, 30(532), 183–195.

Maekawa, K., and Qureshi, J. (1996b). “Computational model for reinforcing bar embedded in concrete under combined axial pullout and transverse displacement.” *J. Materials, Conc. Struct., Pavements*, 31(538), 227–239.

Maekawa, K., and Qureshi, J. (1997). “Stress transfer across interfaces in reinforced concrete due to aggregate interlock and dowel action.” *J. Materials, Conc. Struct., Pavements*,

34(557), 159–172.

Mansur, M. A., Vinayagam, T., and Tan, K.-H. (2008). “Shear transfer across a crack in reinforced high-strength concrete.” *Journal of materials in civil engineering*, 20(4), 294–302.

Markou, G., and Papadrakakis, M. (2012). “An efficient generation method of embedded reinforcement in hexahedral elements for reinforced concrete simulations.” *Advances in Engineering Software*, Elsevier Ltd, 45, 175–187.

Marques, G. C. S. C. (2006). “Estudo e desenvolvimento de código computacional baseado no método dos elementos finitos para análise dinâmica não linear geométrica de sólidos bidimensionais.” Dissertação (Mestrado em Engenharia de Estruturas) - Departamento de Engenharia de Estruturas. Escola de Engenharia de São Carlos, Universidade de São Paulo, São Carlos, 2006.

Martin, J., Stanton, J., Mitra, N., and Lowes, L. N. (2008). “Experimental Testing to Determine Concrete Fracture Energy Using Simple Laboratory Test Setup.” *ACI Materials Journal*, (104), 575–584.

Mattiasson, K. (1981). “Numerical results from large deflection beam and frame problems analysed by means of elliptic integrals.” *International Journal for Numerical Methods in Engineering*, 17(May 1980), 145–153.

Mattock, A. H., and Hawkins, N. M. (1972). “SHEAR TRANSFER IN REINFORCED CONCRETE- RECENT RESEARCH.” *PCI Journal*, 1(July-August), 55–75.

Mehta, P. K., and Monteiro, P. J. M. (2008). *Concreto: microestrutura, propriedades e materiais*. São Paulo:IBRACON.

Miller, K. S. (1981). “On the Inverse of the Sum of Matrices.” *Mathematics Magazine*, 54(2), 67–72.

Moradi, A. R., Soltani, M., and Tasnimi, A. A. (2012). “A Simplified Constitutive Model for Dowel Action across RC Cracks A Simplified Constitutive Model for Dowel Action across RC Cracks.” *Journal of Advanced Concrete Technology*, 10, 264–277.

Morales-alonso, G., Cendón, D. A., Gálvez, F., and Sánchez-gálvez, V. (2015). “Influence of the softening curve in the fracture patterns of concrete slabs subjected to blast.” *Engineering Fracture Mechanics*, Elsevier Ltd, 140, 1–16.

Moura, C. A. (2015). “Aplicação de formulação baseada no Método dos Elementos Finitos Posicional na análise bidimensional elástica de compósitos particulados.” Dissertação (Mestrado em Engenharia de Estruturas) - Departamento de Engenharia de Estruturas. Escola de Engenharia de São Carlos, Universidade de São Paulo, São Carlos, 2015.

Mourlas, C., Papadrakakis, M., and Markou, G. (2017). “A computationally efficient model for the cyclic behavior of reinforced concrete structural members.” *Engineering Structures*, Elsevier Ltd, 141, 97–125.

Mousa, S., Mohamed, H. M., Benmokrane, B., and Ferrier, E. (2018). “Flexural behavior of full-scale circular concrete members reinforced with basalt FRP bars and spirals: Tests and theoretical studies.” *Composite Structures*, Elsevier, 203, 217–232.

NBR 6118. (2014). “Projeto de estruturas de concreto - Procedimento.” ABNT, Rio de Janeiro.

NBR 7222. (2011). “Concreto e argamassa - Determinação da resistência à tração por compressão diametral de corpos de prova cilíndricos.” ABNT, Rio de Janeiro.

Ngo, D., and Scordelis, A. C. (1967). “Finite element analysis of reinforced concrete beams.” *Journal of the American Concrete Institute*, 64, 152–163.

Nilson, A. H. (1968). “Nonlinear analysis of reinforced concrete by the finite element method.” *Journal Proceedings*, 65(9), 757–766.

Nogueira, G. V. (2015). “Formulação de elemento finito posicional para modelagem numérica de pórticos planos constituídos por compósitos laminados : uma abordagem não linear geométrica baseada na teoria Layerwise.” Dissertação (Mestrado em Engenharia de Estruturas) - Departamento de Engenharia de Estruturas. Escola de Engenharia de São Carlos, Universidade de São Paulo, São Carlos, 2015.

Oliver, J. (1989). “A Consistent Characteristic Length for Smeared Cracking Models.” *International Journal for Numerical Methods in Engineering*, 28, 461–474.

Oliver, J., and Huespe, A. E. (2004). “Continuum approach to material failure in strong discontinuity settings.” *Computer Methods in Applied Mechanics and Engineering*, 193, 3195–3220.

Oliver, J., Linero, D. L., Huespe, A. E., and Manzoli, O. L. (2008). “Two-dimensional modeling of material failure in reinforced concrete by means of a continuum strong discontinuity approach.” 197, 332–348.

Owen, D. R. J., Figueiras, J. A., and Damjanic, F. (1983). “Finite element analysis of reinforced and prestressed concrete structures including thermal loading.” *Computer Methods in Applied Mechanics and Engineering*, 41, 323–366.

Owen, D. R. J., and Hinton, E. (1980). *Finite elements plasticity: Theory and Practice*. (Pineridge Press Limited, ed.), Swansea.

Özcan, D. M., Bayraktar, A., Abdurrahman, S., Haktanir, T., and Türker, T. (2009). “Experimental and finite element analysis on the steel fiber-reinforced concrete (SFRC) beams ultimate behavior.” *Constructions and Building Materials*, 23, 1064–1077.

Paccola, R. R., Sampaio, M. S. M., and Coda, H. B. (2014). “Fiber-matrix Contact Stress Analysis for Elastic 2D Composite Solids.” *Latin American Journal of Solids and Structures*, 583–611.

Park, R., and Paulay, T. (1975). *Reinforced concrete structures*. John Wiley & Sons, New York, USA.

Pascon, J. P. (2012). “Sobre modelos constitutivos não lineares para materiais com gradação funcional exibindo grandes deformações: implementação numérica em formulação não linear geométrica.” Tese (Doutorado em Engenharia de Estruturas) - Departamento de Engenharia de Estruturas. Escola de Engenharia de São Carlos, Universidade de São Paulo, São Carlos, 2012.

Pereira, D. P. (2015). “Análise não linear geométrica de sólidos elásticos tridimensionais reforçados com fibras através do método dos elementos finitos.”

Phillips, D. V., and Zienkiewicz, O. C. (1976). “Finite element non-linear analysis of concrete structures.” *Proceedings of the Institution of Civil Engineers*, ICE Publishing, 61(1), 59–88.

Piscesa, B., Attard, M. M., and Khajeh, A. (2018). “3D Finite element modeling of circular reinforced concrete columns confined with FRP using a plasticity based formulation.” *Composite Structures*, Elsevier, 194(February), 478–493.

Planas, J., Elices, M., and Guinea, G. V. (1992). “Measurement of the fracture energy using three-point bend tests : Part 2--Influence of bulk energy dissipation.” *Materials and Structures*, 25, 305–312.

Qin, R., Zhou, A., and Lau, D. (2017). “Effect of reinforcement ratio on the flexural performance of hybrid FRP reinforced concrete beams.” *Composites Part B*, Elsevier Ltd, 108, 200–209.

Radtke, F. K. F., Simone, A., and Sluys, L. J. (2010a). “A partition of unity finite element method for obtaining elastic properties of continua with embedded thin fibres.” (September), 708–732.

Radtke, F. K. F., Simone, A., and Sluys, L. J. (2010b). “A computational model for failure analysis of fibre reinforced concrete with discrete treatment of fibres.” 77, 597–620.

Radtke, F. K. F., Simone, A., and Sluys, L. J. (2011). “A partition of unity finite element method for simulating non-linear debonding and matrix failure in thin fibre composites.” (October 2010), 453–476.

Rahal, K. N., Khaleefi, A. L., and All-Sanee, A. (2016). “An experimental investigation of shear-transfer strength of normal and high strength self compacting concrete.” *Engineering Structures*, Elsevier Ltd, 109, 16–25.

Ramírez, C. Q. (2018). “Análise não linear geométrica de músculos esqueléticos via método dos elementos finitos posicional.” Tese (Doutorado em Engenharia de Estruturas) - Departamento de Engenharia de Estruturas. Escola de Engenharia de São Carlos, Universidade de São Paulo, São Carlos, 2018.

Randl, N. (2007). “Load Bearing Behaviour of Cast-in Shear Dowels.” *Beton- und Stahlbetonbau*, 102, 31–37.

Rashid, Y. R. (1968). “Ultimate strength analysis of prestressed concrete pressure vessels.” *Nuclear Engineering and Design*, 7(4), 334–344.

Reis, M. C. J. (2012). “Análise não linear geométrica de pórticos planos considerando ligações semirrígidas elastoplásticas.” Dissertação (Mestrado em Engenharia de Estruturas) - Departamento de Engenharia de Estruturas. Escola de Engenharia de São Carlos, Universidade de São Paulo, São Carlos, 2012.

Reis, M. C. J., and Coda, H. B. (2014). “Physical and geometrical non-linear analysis of plane frames considering elastoplastic semi-rigid connections by the positional FEM.” 1163–1189.

RILEM, T. (1985). “Determination of the fracture energy mortar and concrete by means of three-point bend test on notched beams.” *Materials and Structures*, (T.-50-F. F. M. of C. RILEM Draft Recommendation, ed.), 18(106), 285–290.

Rots, J. G. (1988). “Computational modelling of concrete fracture.” Delft University of Technology.

Rots, J. G., and De Borst, R. (1987). “Analysis of Mixed-Mode Fracture in Concrete.” *Journal of Engineering Mechanics*, 113(11), 1739–1758.

Rots, J. G., Nauta, P., Kusters, G. M. A., and Blaauwendraad, J. (1985). “Smeared crack approach and fracture localization in concrete.” *Heron*, 30(1).

Saatci, S., and Vecchio, F. J. (2009). “Nonlinear Finite Element Modeling of Reinforced Concrete Structures under Impact Loads.” *ACI Structural Journal*, 106(5), 717–725.

Sagaseta, J., and Vollum, R. L. (2011). “Influence of aggregate fracture on shear transfer through cracks in reinforced concrete.” *Magazine of Concrete Research*, 63(2), 119–137.

Sampaio, M. S. M. (2014). “Análise não linear geométrica de cascas laminadas reforçadas com fibras.” Tese (Doutorado em Engenharia de Estruturas) - Departamento de Engenharia de Estruturas. Escola de Engenharia de São Carlos, Universidade de São Paulo, São Carlos, 2014.

Sampaio, M. S. M., Paccola, R. R., and Coda, H. B. (2015). “A geometrically nonlinear FEM formulation for the analysis of fiber reinforced laminated plates and shells.” *Composite Structures*, Elsevier Ltd, 119, 799–814.

Sanches Júnior, F., and Venturini, W. S. (2007). “Damage modelling of reinforced concrete beams.” *Advances in Engineering Software*, 38, 538–546.

Sanches, R. A. K. (2006). “Análise bidimensional de interação fluido-estrutura: Desenvolvimento de código computacional.” Dissertação (Mestrado em Engenharia de Estruturas) - Departamento de Engenharia de Estruturas. Escola de Engenharia de São Carlos, Universidade de São Paulo, São Carlos, 2006.

Sanches, R. A. K. (2011). “Sobre o acoplamento fluido-casca utilizando o Método dos Elementos Finitos.” Tese (Doutorado em Engenharia de Estruturas) - Departamento de Engenharia de Estruturas. Escola de Engenharia de São Carlos, Universidade de São Paulo, São Carlos, 2011.

Sánchez, J. A. G. (2013). “Uma formulação em elementos finitos para a análise dinâmica e estática linear de risers incluindo o contato com o leito do mar.” Tese (Doutorado em Engenharia de Estruturas) - Departamento de Engenharia de Estruturas. Escola de Engenharia de São Carlos, Universidade de São Paulo, São Carlos, 2013.

Santos, J., and Henriques, A. A. (2015). “New finite element to model bond-slip with steel strain effect for the analysis of reinforced concrete structures.” *Engineering Structures*, 86, 72–83.

Sato, Y., and Naganuma, K. (2007). “Discrete-like crack simulation by smeared crack-based FEM for reinforced concrete.” *Earthquake Engineering and Structural Dynamics*, 36, 2137–2152.

Silva, W. Q. (2010). “Análise não linear geométrica do acoplamento solo-estrutura através da combinação MEC-MEF.” Dissertação (Mestrado em Engenharia de Estruturas) - Departamento de Engenharia de Estruturas. Escola de Engenharia de São Carlos, Universidade de São Paulo, São Carlos, 2010.

Silva, W. Q. (2014). “Sobre análise não linear geométrica de edifícios considerando o empenamento dos núcleos estruturais e a interação solo-estrutura.” Tese (Doutorado em Engenharia de Estruturas) - Departamento de Engenharia de Estruturas. Escola de Engenharia de São Carlos, Universidade de São Paulo, São Carlos, 2014.

Simão, W. I. D. S. (2003). “Modelos de armadura e aderência para análise não-linear de estruturas de concreto armado.” 126.

Simo, J. C., and Hughes, T. J. R. (1998). *Interdisciplinary Applied Mathematics*. (J. E. Marsden, L. Sirovich, and S. Wiggins, eds.), Springer.

Simo, J. C., and Taylor, R. L. (1985). “Consistent tangent operators for rate-independent elastoplasticity.” *Computer methods in applied mechanics and engineering*, 48, 101–118.

Singh, B., and Chintakindi, S. (2012). “An appraisal of dowel action in reinforced concrete beams.” *Institution of Civil Engineers*, 166(SB5), 257–267.

Soetens, T., and Matthys, S. (2017). “Shear-stress transfer across a crack in steel fibre-reinforced concrete.” *Cement and Concrete Composites*, Elsevier Ltd, 82, 1–13.

Sørensen, J. H., Hoang, L. C., Olesen, J. F., and Fischer, G. (2017). “Testing and modeling dowel and catenary action in rebars crossing shear joints in RC.” *Engineering Structures*, Elsevier Ltd, 145, 234–245.

Soroushian, P., Obaseki, K., Rojas, M., and Najm, H. S. (1987). “Behavior of bars in dowel action against concrete cover.” *ACI Structural Journal*, 84(2), 170–176.

de Souza Neto, E. A., Peric, D., and Owen, D. R. J. (2008). *Computational Methods for plasticity - Theory and applications*. John Wiley & Sons, Ltd, United Kingdom.

Spiliopoulos, K. V., and Lykidis, G. C. (2006). “An efficient three-dimensional solid finite element dynamic analysis of reinforced concrete structures.” *Earthquake Engineering and Structural Dynamics*, (February 2005), 137–157.

Suidan, M., and Schnobrich, W. . (1973). “Finite Element analysis of reinforced concrete.” *ASCE Journal of the Structures Division*, 99, 2109–2122.

Tavares, D. H. (2006). “Análise teórica e experimental de vigas de concreto armadas com barras não metálicas de GFRP.” Sao Paulo.

Tavares, D. H., Giongo, J. S., and Paultre, P. (2008). “Behavior of reinforced concrete beams reinforced with GFRP bars.” 1(3), 285–295.

Terán, J. R. D., and Haach, V. G. (2018). “Equivalent stress-strain law for embedded reinforcements considering bond-slip effects.” *Engineering Structures*, 1–7.

Thybo, A. E. A., Michel, A., and Stang, H. (2017). “Smeared crack modelling approach for corrosion-induced concrete damage.” *Materials and Structures*, Springer Netherlands, 50(2), 1–14.

Timoshenko, S. (1956). *Strength of materials: Advanced Theory and Problems - Part II*. D. Van Nostrand Company, Inc., Princeton, New Jersey.

Vanalli, L., Paccola, R. R., and Coda, H. B. (2008). “A simple way to introduce fibers into FEM models.” *Communications in Numerical Methods in Engineering*, (January 2007), 585–603.

Vecchio, F. J. (1990). “Reinforced concrete membrane element formulations.” *Journal of Structural Engineering, ASCE*, 116(3), 730–750.

Vintzeleou, E. N., and Tassios, T. P. (1986). “Mathematical models for dowel action under monotonic and cyclic conditions.” *Magazine of Concrete Research*, 38(134), 13–22.

Vintzeleou, E. N., and Tassios, T. P. (1987). “Behavior of dowels under cyclic deformations.pdf.” *ACI Structural Journal*, 84(1), 18–30.

Volokh, K. Y. (2013). “Characteristic length of damage localization in concrete.” *Mechanics Research Communications*, Elsevier Ltd., 51, 29–31.

Waseem, S. A., and Singh, B. (2018). “Strut-and-tie model for shear strength of reinforced concrete ‘ push-off ’ specimens.” *Structures and Buildings*, 171(SB4), 295–305.

Wight, J. K., and MacGregor, J. G. (2012). *Reinforced concrete: Mechanics and Design*. Pearson.

Xia, J., Xiao, Y., Mackie, K. R., Al-ramahee, M., and Mirmiran, A. (2015). “Dowel action and shear strength contribution of high strength rebar embedded in ultra-high performance fiber reinforced concrete.” *Engineering Structures*, Elsevier Ltd, 83, 223–232.

Xu, J., Wu, C., Li, Z.-X., and Ng, C.-T. (2015). “Numerical analysis of shear transfer across an initially uncrack reinforced concrete member.” *Engineering Structures*, Elsevier Ltd, 102, 296–309.

Yang, K., and Ashour, A. F. (2007). “Structural behaviour of reinforced-concrete continuous deep beams with web openings.” *Magazine of Concrete Research*, 59(10), 699–711.

Yankelevsky, D. Z. (1985). “New finite element for bond-slip analysis.” *Journal of Structural Engineering, ASCE*, 111(7), 1533–1542.

Yu, J., Zhan, K., Li, L., and Yu, K. (2018). “Using XFEM to model the effect of different axial compression on the hysteretic behaviour of the flexure - dominant RC columns.” *Structural Design of Tall and Special Buildings*, 27, 1–12.

Zhang, Y., Lu, M., and Hwang, K. (1994). “Finite element modeling of reinforced concrete structures.” *Finite Elements in Analysis and Design*, 18(1–3), 51–58.